The Structural and Geomorphic Development of Active Collisional Orogens, from Single Earthquake to Million Year Timescales, Timor Leste and New Zealand

A thesis submitted in fulfillment of the requirements for the degree of Doctor of Philosophy in Geology in the University of Canterbury by

Brendan Duffy

November 2012

FOR MY WIFE

NICCI

AND OUR DAUGHTERS

CIARA

AND

ISABELLA

I COULDN'T HAVE DONE THIS WITHOUT YOU!

AND FOR MY INSPIRATIONAL LATE MOTHER IN LAW,

GAYE-LYNN FLORENCE DOWLING

(SEPTEMBER 1950 TO JULY 2011)

FRONTISPIECE

These striking stone walls serve the multiple purposes of retainment, drainage diversion and cooling for the waters of the Marobo Hot Springs near Maliana, Timor Leste. The hot springs are driven by deep circulation of meteoric waters in active faults (Lawless et al. 2005).

ABSTRACT

The structure and geomorphology of active orogens evolves on time scales ranging from a single earthquake to millions of years of tectonic deformation. Analysis of crustal deformation using new and established remote sensing techniques, and integration of these data with field mapping, geochronology and the sedimentary record, create new opportunities to understand orogenic evolution over these timescales. Timor Leste (East Timor) lies on the northern collisional boundary between continental crust from the Australian Plate and the Banda volcanic arc. GPS studies have indicated that the island of Timor is actively shortening. Field mapping and fault kinematic analysis of an emergent Pliocene marine sequence identifies gentle folding, overprinted by a predominance of NW-SE oriented dextral-normal faults and NE-SW oriented sinistral-normal faults that collectively bound large (5-20km^2) bedrock massifs throughout the island. These fault systems intersect at non-Andersonian conjugate angles of approximately 120° and accommodate an estimated 20 km of orogen-parallel extension. Folding of Pliocene rocks in Timor may represent an early episode of contraction but the overall pattern of deformation is one of lateral crustal extrusion sub-parallel to the Banda Arc. Stratigraphic relationships suggest that extrusion began prior to 5.5 Ma, during and after initial uplift of the orogen. Sedimentological, geochemical and Nd isotope data indicate that the island of Timor was emergent and shedding terrigenous sediment into carbonate basins prior to 4.5 Ma. Synorogenic tectonic and sedimentary phases initiated almost synchronously across much of Timor Leste and <2 Myr before similar events in West Timor. An increase in plate coupling along this obliquely converging boundary, due to subduction of an outlying continental plateau at the Banda Trench, is proposed as a mechanism for uplift that accounts for orogen-parallel extension and early uplift of Timor Leste. Rapid bathymetric changes around Timor are likely to have played an important role in evolution of the Indonesian Seaway.

The 2010 M_w 7.1 Darfield (Canterbury) earthquake in New Zealand was complex, involving multiple faults with strike-slip, reverse and normal displacements. Multi-temporal cadastral surveying and airborne light detection and ranging (LiDAR) surveys allowed surface deformation at the junction of three faults to be analyzed in this study in unprecedented detail. A nested, localized restraining stepover with contractional bulging was identified in an area with the overall fault structure of a releasing bend, highlighting the surface complexities that may develop in fault interaction zones during a single earthquake sequence. The earthquake also caused river avulsion and flooding in this area. Geomorphic investigations of these rivers prior to the earthquake identify plausible precursory patterns, including channel migration and narrowing. Comparison of the pre

and post-earthquake geomorphology of the fault rupture also suggests that a subtle scarp or groove was present along much of the trace prior to the Darfield earthquake. Hydrogeology and well logs support a hypothesis of extended slip history and suggests that that the Selwyn River fan may be infilling a graben that has accumulated late Quaternary vertical slip of <30 m. Investigating fault behavior, geomorphic and sedimentary responses over a multitude of time-scales and at different study sites provides insights into fault interactions and orogenesis during single earthquakes and over millions of years of plate boundary deformation.

CONTENTS

ACKNOWLEDGMENTS

During my PhD study I was supported by a Tertiary Education Commission Top Achiever Scholarship, for which I am grateful.

My supervisory team was excellent and provided both guidance and friendship. Mark Quigley provided the funding through his Marsden fast start grant. Uwe Ring provided invaluable insights into extrusional tectonics from a European perspective. Kari Bassett provided emergency stratigraphic logging training prior to my field season and subsequently provided an ever-listening ear and much insight into sedimentology. Kari's training significantly improved the quality of my logs. Almost as important as supervisory support was the moral support I received from two great office mates, Eric Bilderback and Tim Stahl. We each had such different projects but somehow always found time to listen to each other.

I thank the staff at SERN who provided me with letters to ease my path, both with local Suku Chiefs and with customs on the way out of Timor Leste. I also thank Aaron Benincasa of the University of Western Australia, who provided me with excellent logistic support during my first field season in Timor Leste. My first field season in Timor was funded by the Mason Trust and by Aaron's supervisors, Myra Keep and David Haig of the University of Western Australia. My fieldwork benefitted greatly from the field assistance provided by Andy Monteiro and Nabe. Andy was my first field assistant and is now pursuing his own geological career for which I wish him the best.

My second field season was made easier by the assistance of Atino Varela, Johny Rheis, Jonny Soares da Costa and Lamberto Fernandes. Lamberto exercised his wisdom and calm to save me from a couple of spots of bother. My second field season was severely impeded by terrible weather that denied access to key sections. During these challenges I was kept sane by Louise Moody, who described the field campaign in a beautifully understated way as "not ideal". I was lucky to spend several valuable days revisiting the type section with Jamie Shulmeister and Annie Nguyen. Annie subsequently did an excellent work up of the palynology, leading to our co-authoring an AGU poster and Geology paper. A chance meeting with Ron Harris on the Baucau Dili Road led me to a new and exciting section, and collaboration with Douwe Van Hinsbergen and Richard Bakker. Ron subsequently gave me valuable feedback at AGU that really sharpened my focus.

I would like to take this opportunity also to acknowledge the friendship and advice given me by Mike Audley-Charles. Mike gave me a lot of time from his well earned retirement to carry on a

detailed email discussion of many aspects of Timor's synorogenic geology. He also introduced me by email to Ron Harris, for which I am indebted to him.

As with any Canterbury geology PhD student doing fieldwork, nothing would have gone quite as smoothly without the work of the technical staff. Cathy and Vanessa helped me clear my samples through the biosecurity system. Rob Spiers produced numerous thin sections. Stephen Brown ran geochemical analyses and provided me with methodological details. Chris Grimshaw was ever helpful in the lab. I also thank the management of the College of Science, who bent the rules to allow me to finance myself whilst I was in Timor.

During my PhD I was lucky to become heavily involved in the science response to the 4 September 2010 Canterbury earthquake, which gave me the opportunity to work alongside people such as Kevin Furlong, Russ Van Dissen, Nicola Litchfield, Pilar Villamor and David Barrell. The work I did on the West segment of the Greendale fault and the fault bend was greatly aided by many people. Grant Sanford gave permission for his property survey to be used for earthquake science, and Craig McInnes enthusiastically shared the baseline survey data. Both Grant Sanford and Paget Milsom then provided access to their properties. It was very gratifying to have Craig accompany me to the field and confirm my results. Russ Van Dissen and David Barrell provided great mentoring and editorial help. David's whisky analogies were particularly useful and I think his advice has greatly improved my writing. Nic Carson, Jocelyn Campbell, Sharon Hornblow and Andy MacKenzie assisted with field work and the late John Beavan at GNS provided expert and friendly geodetic assistance, without which much of my work would have been meaningless. Tim Stahl was a legend, spending two days working on my behalf acquiring digital elevation data over a particularly interesting area, followed by hours reviewing my numerous manuscript iterations.

I thank the review and editorial team at *GSA Bulletin* who dealt with the kinematics manuscript (Chapter 4), and those at *Tectonics* who are dealing with my Timor extrusion manuscript (Chapter 2). I also thank my examiners, An Yin and Lorna Strachan, for their time and efforts.

Above all else, my thanks go to my family. Special thanks to my late mother-in-law, Gaye and her partner Dave for their encouragement. My wife Nicci is ever supportive of my endeavors; excited with me at the high points and commiserating during the low points. Nicci and my daughters Ciara and Isabella all put up with my forgetful nature and pre-occupation with great humor, and did me a great honor by recognizing me as a new species, *Homo forgetypus* in honor of my abysmal memory for everyday tasks. Nicci and the girls have been very supportive of my time away from home, and without that this would have been impossible. For their understanding of my

excitement during the 4 Sept 2010 earthquake, and my overwhelming need to go out and find the fault whilst our world was rocking, I am very grateful. During my thesis Nicci has dealt with the illness and death of her mum, Gaye, in addition to the trials and tribulations of the earthquakes and my thesis research. Thank you.

THESIS PROLOGUE

This thesis, which originally arose from a New Zealand Royal Society Marsden research grant to investigate the links between Timor tectonics, Indonesian oceanography and global climate, evolved in response to the circumstances of the Mw7.1 Canterbury earthquake of 4 September 2010. As a key member of the University of Canterbury – GNS Science surface rupture response team I spent more than three months collecting time-sensitive data that became two chapters of this thesis. The thesis is therefore separated into two parts, each devoted to understanding the significance and geological record of interaction of an array of reverse, strike-slip, and normal faults within a collisional orogen.

Scientific context

The first part of this thesis explores the timing of bathymetric changes in the Indonesian Throughflow, the only remaining tropical gateway between the world's oceans and a critical component of ocean-climate coupling (Schott & McCreary Jr 2001). Numerous authors have shown that the distribution of orogen-scale (10^2 km) bathymetry controls oceanographic circulation regimes (Berggren & Hollister 1977; Hay 1996; Cane & Molnar 2001; Hall 2009). Ocean gateways are thus recognized as a critical factor that influences global climatic phenomena (e.g. Mikolajewicz et al. 1993; Smith & Pickering 2003; Nathan & Leckie 2009; von der Heydt & Dijkstra 2011) and modulates their rates of change (e.g. Mudelsee & Raymo 2005). The Indonesian Throughflow is evolving in response to ongoing bathymetric changes that were brought about by the progressive and complex collision between Australia and Eurasia, which has taken place during the late Cenozoic (Hall 2002; Spakman & Hall 2010; Hall 2012). A major bottleneck in the Indonesian Throughflow is its exit route through the Timor region where Australia is presently colliding with the Banda Arc. The timing and rates of collisional orogenesis in the Indonesian Throughflow are therefore potentially relevant to global climate.

Timing is only one important aspect of the Timor arc-continent collision. Arc-continent collision is a principle method of accretion of material to continents and thus the growth of continental crust (Clift & Vannucchi 2004). Furthermore the accretion of an arc is only the first stage of ocean basin closure that must be followed eventually by continental collision. Fragmentary records of fossil arc-continent collision events abound in collisional orogens. The Banda arc-continent collision is therefore important, not only for its location but because it is one of the world's youngest collisional orogens and therefore a potentially useful analogue for fossil

collision zones. However, this utility is incomplete because the Banda orogen is not yet well understood.

Like any collision, the Banda arc-continent collision involves the contractional interaction of two plates. In the case of an arc-continent collision, the protagonists are an extended continental margin and an intra-oceanic arc, separated by a trench. Several questions can be asked about an arc-continent collision. These include:

a) When was contact initiated between the Australian continental margin and the Banda Forearc in the Timor orogen?
b) How can seemingly disparate depositional histories in Timor's orogenic basins be reconciled using a single orogenic model?
c) How do the forearc and the passive margin respond to collision, specifically, which is subducted and which is obducted/accreted (Afonso & Zlotnik 2011; Boutelier et al. 2012).
d) What drives extension in collisional orogens (e.g. Dewey 2005)?
e) How is uplift generated and topography created and distributed (e.g. slab rupture and buoyant rebound or crustal thickening)?

The majority of these questions can be summed up by asking:

"How do tectonic stresses, lithospheric structure, and topographic and bathymetric relief interact in a fundamentally contractional environment to cause the syn to post-collisional extension that is widely reported at many temporal and spatial scales from ancient and modern collisional orogens (Molnar & Tapponnier 1975; Dewey 1988; Ratschbacher et al. 1991a; Ratschbacher et al. 1991b; Hartz & Andresen 1997; Andresen et al. 1998; Taylor et al. 2003; Clift et al. 2004; Dewey 2005; Escalona & Mann 2011; Styron et al. 2011)?"

This general question, which remains unresolved in the Timor region of the Banda Arc, also has wider relevance to other collisional orogens such as the South Island of New Zealand (see Part 2). When it comes to answering the question, it is well known that the topographic expression of tectonic deformation in the landscape can provide insights into the kinematic development of orogens. Tectonic landscape development over orogenic timescales is commonly studied using high quality bathymetric and topographic datasets (Masson et al. 1991; Hooper et al. 2003; Ganas et al. 2005; Muller & Harding 2007; Pedley et al. 2010). Tectonic displacements and erosion not only shape topography, but also result in the creation and filling respectively of sedimentary basins. A great deal of research effort has gone into understanding how drainages interact with tectonics to shape the landscape (Burnett & Schumm 1983; Ouchi 1985; Schumm 1986; Leeder &

Alexander 1987; Alexander et al. 1994; Burbank et al. 1996; Campbell et al. 2003; Amos & Burbank 2007). These studies show that the rates and style of [topographic or bathymetric] landscape development of these sedimentary basins, their tectonic setting, and their relationship to the sediment distribution system control the rates at which accommodation space is created and filled, the depositional architecture of the fill, and the interaction between sediment distributary systems and underlying faults. Tectonic influences on landscape development can now be monitored at ever-decreasing time scales since the advent of high resolution remote sensing platforms that provide multi-temporal perspectives (Reigber et al. 1997; Kääb 2002; Simons et al. 2002; Beavan et al. 2010a; Mukoyama 2011; Oskin et al. 2012).

Thesis Format

This thesis uses the geomorphic, structural and sedimentological records of faulting to investigate the cause and effect relationships between tectonic stresses, lithospheric and/or crustal structure, topography and interactions among thrust and normal faulting at two different temporal and spatial scales. For Timor, the oceanographic implications are also considered.

Part one of this thesis is set in Timor Leste in Eastern Indonesia.

Timor, which is an orogenic wedge that occupies a forearc position in the zone of collision between the northward-subducting Australian continent and the oceanic arc on its northern margin (Audley-Charles 1968,1986b; Harris 1991), is the world's youngest arc-continent collision and thus provides the opportunity to study this process in a relatively immature and unmodified state. Uplift of the island of Timor is a major component of the bathymetric development of the Indonesian Throughflow. The tectonic development of the Indonesian Throughflow may have contributed to the Plio-Pleistocene climate transition, northern hemisphere glaciations and hominid evolution (Cane & Molnar 2001). The timing of collision in Timor is controversial (compare Haig & McCartain 2007; Audley-Charles 2011; Hall & Sevastjanova 2012, p.839) and limited field data (Kenyon 1974; Berry & Grady 1981; Keep et al. 2009; Keep & Haig 2010) and historical seismicity (Tjia 1981; McCaffrey 1988,1989) suggest that parts of this arc-continent collision are dissected by high angle transtensional faulting. This extension, including its topographic effects and its relationship to ongoing shortening demonstrated by GPS studies (Nugroho et al. 2009), has so far not been fully explained, although it is typically ascribed to slab rupture processes (Price & Audley-Charles 1983,1987; Charlton 1991; Sandiford 2008). In particular, the links between topography and structure have been hinted at but never fully investigated.

Chapter 1 presents new structural and stratigraphic constraints on the kinematics of extension in the synorogenic basins of Timor. It melds these data with DEM-based topographic

mapping to evaluate the extent to which the present topography and coastline geometry of Timor Leste is influenced by normal faulting. The consistency of kinematic indicators in Timor with similar structural styles in Tibet and the European Alps (Ratschbacher et al. 1991a; Taylor et al. 2003), and with new models linking ductile extrusion at depth with brittle faulting at the surface (Yin & Taylor 2008,2011), suggests that Timor has been extruded parallel to the strike of the arc-continent collision. A model is proposed linking the extrusion to underplating of an indenting continental plateau.

Chapter 2 investigates the style, timing and sediment provenance of Pliocene sedimentary sequences to characterize the sedimentary response to the arc-continent collision. I use lithostratigraphic analysis, geochemistry, petrography and Nd isotope analysis. Evolutionary trends in the geochemistry suggest that uplift initiated prior to 4.5 Ma, and was associated in the first instance with the subsidence and filling of syn-collisional, orogen-perpendicular graben. Evolution of the sedimentary fill indicates that the basin floor uplift equaled or exceeded graben subsidence leading to slow shallowing of the basin. Petrography indicates that the sediments in the synorogenic basins were derived from the uplifted forearc, with a small but significant component derived from Australian rocks. The Nd isotope characteristics of the interbedded mudstones indicate that they are derived dominantly from Australian shales, which are remobilized to form a tectonic mélange that is widespread throughout Timor. This mélange contains numerous blocks of Australian-affinity strata and these blocks probably provided the source for Australian affinity rocks in the synorogenic sandstones.

Chapter 3 synthesizes the information from Chapter 1 and Chapter 2 of this thesis with previously published datasets to suggest that Timor has played an important role in the development of the Indonesian Throughflow.

Part two of this thesis is set in Canterbury, New Zealand.

On the 4th September 2010, Canterbury experienced the Mw7.1 Darfield earthquake. Although no deaths were attributed to the mainshock, a violent Mw 6.3 aftershock struck just south of Christchurch at lunchtime on 22 February 2011, resulting in several building collapses and the deaths of 185 people, including many students. The consequences of that aftershock, in particular, will continue to be felt in Christchurch for many years, especially by those that lost family, homes and livelihoods. During prolonged closures of the University of Canterbury after the major earthquakes, I was fortunate to become involved in the science response to the Canterbury earthquake sequence. Apart from initial fault mapping, my greatest involvement was with research

into the releasing West segment of the Greendale fault that ruptured through to the surface during the Darfield earthquake.

Normal faulting was observed at a right bend on the Greendale fault during the Canterbury earthquake in New Zealand (Quigley et al. 2012b). Papers published soon after the earthquake described the extension as a releasing bend (Quigley et al. 2010a; Quigley et al. 2010b) possibly created by fracture propagation (Sibson et al. 2011a; Sibson et al. 2011b), but these interpretations did not completely account for the role of this 'releasing bend' in the complex rupture of up to seven faults in the Darfield earthquake (Beavan et al. 2012). The West segment is a dextral oblique normal fault in a transpressional setting and, in that respect, is similar to much of what I saw in Timor. I applied geodetic, topographic, structural, geomorphic and sedimentological data to understand the single event interactions of different-sense faults, and how these interactions may have contributed to basin evolution along the West segment of the Greendale fault.

Chapter 4 investigates geodetic and geomorphic consequences of fault interactions between the West and Central segments of the Greendale fault, and the Charing Cross blind thrust that initiated the earthquake. Differencing of multi-temporal LiDAR and cadastral survey data, together with mapping of avulsion flooding, indicate the complexity of the rupture process. The West segment is a separate fault that overlaps with the Central segment of the Greendale fault and, together with the Charing Cross blind thrust, forms a triple junction. The footwall of the West segment does indeed pull away from a releasing bend, but the hanging wall moves towards the triple junction, converging on a restraining bend and feeding material towards the Charing Cross fault. Documentation of complexities such as these at changes in fault strike may have implications for seismic hazard analysis as other research indicates the importance of apparent releasing bends in rupture arrest (Wesnousky 2006; Elliott et al. 2009; Ben-Zion et al. 2012)

Chapter 5 presents geomorphic and structural evidence for tectonic tilt and a penultimate rupture where the West segment of the Greendale fault crosses Late Holocene alluvium (Forsyth et al. 2008). The rivers that parallel the West segment show evidence of meander migration and slip-off terrace development that suggest gentle warping in this area. Comparison of modern river banks with archival cadastral survey data suggests that tilting was ongoing over the short history of European occupation of the Canterbury Plains, and can be detected even over the last 60 years. Historical air photography, specially acquired digital elevation data, and differencing of pre and post earthquake topographic data, all suggest that a low (30-60 cm), pre-existing scarp was present, and had previously caused avulsion of the Hororata River in a manner similar to that of the recent earthquake. At the location of a stepover in the modern scarp, an almost identical feature was detected in the pre-earthquake data. A review of well stratigraphy and previous hydrogeological

studies add weight to this evidence and suggest that this fault has a much shorter recurrence interval than has been proposed. Further geophysical investigations, trenching and surface dating will be required to flesh out this history.

Chapter 6 summarizes the key findings of this thesis.

Scientific contributions arising from this PhD and related work

It has always been my intention to write chapters with a view to submitting them as journal articles, so some minor repetition may appear in tectonic setting and regional geology of each chapter. However, where possible, much of the material in these sections has been written for topical relevance. There has been little overlap in the methodologies between each of the chapters.

At the time of thesis submission, Chapter 2, 3, 4 and 5 have been widely presented at conferences (Duffy et al. 2009; Duffy & Quigley 2010; Duffy et al. 2011a; Duffy et al. 2011b; Duffy et al. 2011c; Duffy et al. 2011d). Chapter 2 is in review at *Tectonics* (Duffy et al. (accepted manuscript)). Chapter 4 has been accepted for publication in *GSA Bulletin* and will be published in early 2013 (Duffy et al. 2013). Data collected for parts of Chapter 3 were included in a paper I co-authored in Marine Geology (Quigley et al. 2012a).

Some of the geochemical analyses in Chapter 3 were included in a paper I co-authored that will be published in *Geology* in February 2013 (Nguyen et al. 2013). My contribution to the Nguyen et al. paper included refining Annie Nguyen's (2011) thesis uplift rate determinations by applying my age model, re-interpreting the tectonic significance based on revised uplift rates, drafting all figures, writing the introduction and much of the discussion and handling most of the revisions. During this thesis I selectively cite either Nguyen et al. (2013) in discussion, or Nguyen (2011) where I make use of my own reinterpretation and figures.

During my time as a PhD scholar I have additionally contributed to and co-authored a number of papers on the Greendale fault rupture (Quigley et al. 2010a; Quigley et al. 2010b; Barrell et al. 2011; Van Dissen et al. 2011; Quigley et al. 2012b; Villamor et al. 2012), and given invited talks at conferences including AGU (Duffy et al. 2011d) about that event (Duffy 2011,2012). I have also co-authored an unrelated publication on relative dating of terraces that is presently being revised for resubmission (Stahl et al. in review).

Originality

The material presented in this thesis has benefitted from discussions with my supervisory team, colleagues and external collaborators who are duly acknowledged. In terms of data, I am indebted to Douwe van Hinsbergen and Yair Rosenthal for providing biostratigraphic and isotopic

age data for the Marobo and DSDP sections respectively (Chapter 3). Sebastien Leprince carried out the CosiCorr analysis that I use in Chapter 4. Other collaborators appear as co-authors on my submitted manuscripts, in acknowledgement of their supervisory input, valuable discussions and editorial input into the manuscripts. However, the manuscripts themselves were written entirely by myself. Apart from these debts, this thesis including all fieldwork, data collection, manipulation, interpretation, presentation and conclusions represents my own personal research.

PART ONE: THE PLIOCENE TO RECENT GEODYNAMIC EVOLUTION OF TIMOR

CHAPTER 1. ARC-PARALLEL EXTRUSION OF TIMOR

1.1 Abstract

Structural studies of synorogenic basins in Timor, using field and remote sensing techniques, provide new evidence for syn-collisional extension in the converging plate boundary zone between the Australian Plate and Banda Arc. Fault mapping and kinematic analyses were carried out at scales ranging from outcrop (<1m^2), to the dimensions of the active orogen in East Timor (~100 km^2). These analyses identify a predominance of NW-SE oriented dextral-normal faults, and NE-SW oriented sinistral-normal faults, that collectively bound large (5-20km^2) bedrock massifs throughout the island. These fault systems intersect at non-Andersonian conjugate angles of approximately 120°. Reconstructions of fault-dismembered massifs suggest that they accommodate an estimated 20 km of NE-directed extension across the Timor orogen. Major, sub-parallel ENE-oriented faults on the northern and southern sides of the Timor orogen exhibit normal-sinistral and normal-dextral kinematics, respectively. Folding of Pliocene rocks in Timor may represent an early episode of contraction, but the overall pattern of deformation is one of lateral crustal extrusion sub-parallel to the Banda Arc. Stratigraphic relationships suggest that extrusion began prior to 5.5 Ma, during and after pronounced rapid uplift of the orogen. This is linked to progressive coupling of the arc to an underthrust plateau on the Australian Plate. The coupling effect was probably enhanced by subduction of ocean crust bounding a subducting plateau that tore away from the margins of the buoyant plateau. GPS and seismicity to the west of Timor are consistent with the westward propagation of plate coupling and progressive implementation of this deformation regime. This study enables me to track the structural evolution of the upper crust during dramatic plate-boundary reorganizations accompanying the transition from subduction to collision. The deformation structures that are documented here suggest that both upper and lower plate deformation during incipient island arc-continent collision was largely controlled by the geometry and topography of the lower plate.

1.2 Introduction

Quantifying the timescales and mechanisms by which an arc-continent collision develops from a subduction system is an important part of understanding the evolution of collisional orogens, and the role of passive margin architecture in that process (e.g. Brown & Huang 2009). In principle the process of arc-continent collision should result in contractional deformation as the ratio of subduction velocity to convergence velocity declines (e.g. Davis et al. 1983). In practice, however, extension is reported from both ancient (Clift et al. 2004; Dewey 2005) and modern arc-continent collisions (Gorney et al. 2007; Escalona & Mann 2011) including the island of Timor in the Banda arc (Figure 1.1) (Price & Audley-Charles 1983,1987; McCaffrey 1996). Young arc-continent collisions are commonly diachronous, and the concepts of space-time equivalence

(Suppe 1984) suggest that they should provide an important analogue for interpretation of features including extension in fossil arc-continent collisions (Brown & Huang 2009). A wealth of models has been proposed elsewhere to account for extension of arc-continent collisions (Ave Lallemant & Guth 1990; Sacks & Secor Jr 1990; Cloos 1993; Pubellier & Cobbold 1996; Teng et al. 2000; Lister & Forster 2009), but the collisional and extensional history of many of these orogens remains controversial and unresolved.

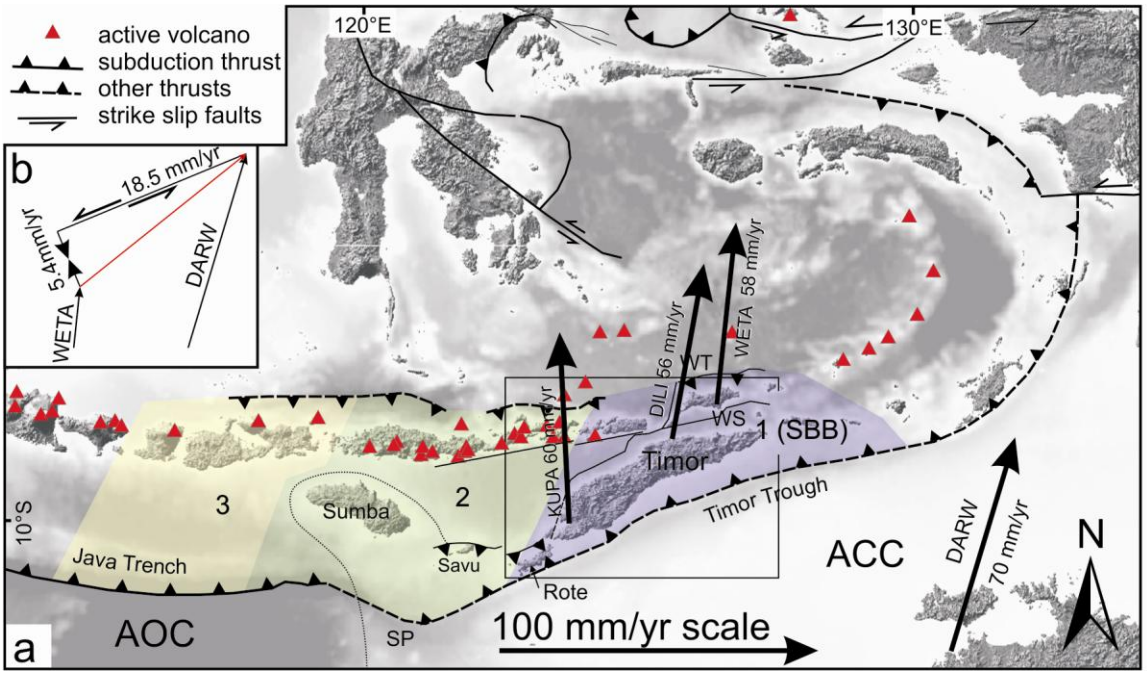

Figure 1.1. Tectonic setting of Timor and the Banda Arc. a) Plate boundary elements. Faults follow Hinschberger et al. (2005), modified after Rigg and Hall (2012) and Watkinson et al. (2011). GPS plate motion vectors shown relative to the Sunda Shelf: WETA – Wetar , KUPA – Kupang and DILI – Dili (after Genrich et al, 1996); DARW – Darwin (after Nugroho et al. 2009). Coupling zones (after Nugroho et al. 2009) range from 1 (maximum coupling – South Banda Block - SBB) to 3 (minimum coupling - eastern Java Trench). WT – Wetar Thrust; WS - Wetar Suture; ACC – Australian continental crust; AOC – Australian ocean crust; SP - Scott Plateau. b). The ~ 20 mm of differential movement between Darwin and Wetar resolves into trough-normal shortening (~5.4 mm/yr) and trough-parallel left-lateral shear components (~18.5 mm/yr).

The island of Timor lies in the outer arc region between the Timor Trough and the Banda arc (Figure 1.1). It is located close to the transition from subduction to collision of the Australian Plate with the Banda arc (Harris 1991,2011) and is the orogenic product of that collision (Audley-Charles 1968). The timing of the collision is highly controversial, and estimates presently range from ~8 to ~3 Ma (Keep & Haig 2010; Audley-Charles 2011). Geophysical and field observations, along with shallow seismicity show that Timor is actively extending (Berry & Grady 1981; Price & Audley-Charles 1987; McCaffrey 1988,1989; Charlton 1991; Charlton et al. 1991; Masson et al. 1991; Charlton 1997; Keep et al. 2009; Keep & Haig 2010) (Figure 1.2). The mechanism and effects of this extension are unclear. Small total displacements on the back-arc Wetar Thrust

(Silver et al. 1983) do not yet constitute subduction polarity reversal (Snyder et al. 1996b), which has been shown elsewhere to cause extension due to a reversal in basal shear stress (Pubellier & Cobbold 1996). Arc-parallel extension and strike slip faulting dominates historical seismicity in West Timor (McCaffrey 1988,1989) and is observed in pull apart basins in the Wetar Strait north of Timor (Masson et al. 1991). This arc-parallel extension is not caused by subduction zone curvature (McCaffrey 1996). Despite evidence for arc-parallel seismicity, most models that have been proposed imply arc-normal extension, which has been interpreted as both superficial thin-skinned (Grady & Berry 1977; Price & Audley-Charles 1983,1987) and basement-involved thick-skinned (Charlton 1997). Particular emphasis has been given to models that invoke slab rupture below Wetar (Price & Audley-Charles 1983; Milsom & Audley-Charles 1986; Price & Audley-Charles 1987; Charlton 1991,1997; Sandiford 2008; Ely et al. 2011), but this is contested on the basis of mantle tomography by Spakman and Hall (2010), who argue instead for delamination. However, the short wavelength variability in regional uplift of Quaternary reefs (Chappell & Veeh 1978; Rosidi et al. 1981; Jouannic et al. 1988; Hantoro et al. 1994; Cox 2009) is inconsistent with complete control by a deep uplift mechanism such as isostatic rebound of a delaminated or ruptured slab (Harris 2011), suggesting that active faulting and/or folding must play a role in Timor's ongoing uplift.

Timor Leste is considered to represent the most advanced stage of collision in the southern Banda Arc (Charlton et al. 1991; Harris 1991). The previously unstudied extensional structures that cut synorogenic rocks in Timor Leste offer a rare opportunity to track the structural evolution of the plate boundary zone that accompanied the initial transition from subduction to collision, and particularly to isolate the timing, kinematics, causes and effects of extension. However, Timor Leste has until lately been a politically challenging location for fieldwork and remains largely remote and poorly accessible. Previous tectonic models that explain Timor's extension have thus been based on limited field investigations.

This chapter investigates the structural evolution of Timor Leste by mapping deformation in synorogenic sedimentary sequences. It combines detailed outcrop investigations from three widely separated basins (Figure 1.2) with lineament analysis and re-interpretation of previous work. This work identifies the kinematics, extent and history of major extensional fault systems in Timor. Based on these data, a pure shear extrusion model is proposed for Pliocene to Recent regional extension that provides insight into the collisional geometry of Timor.

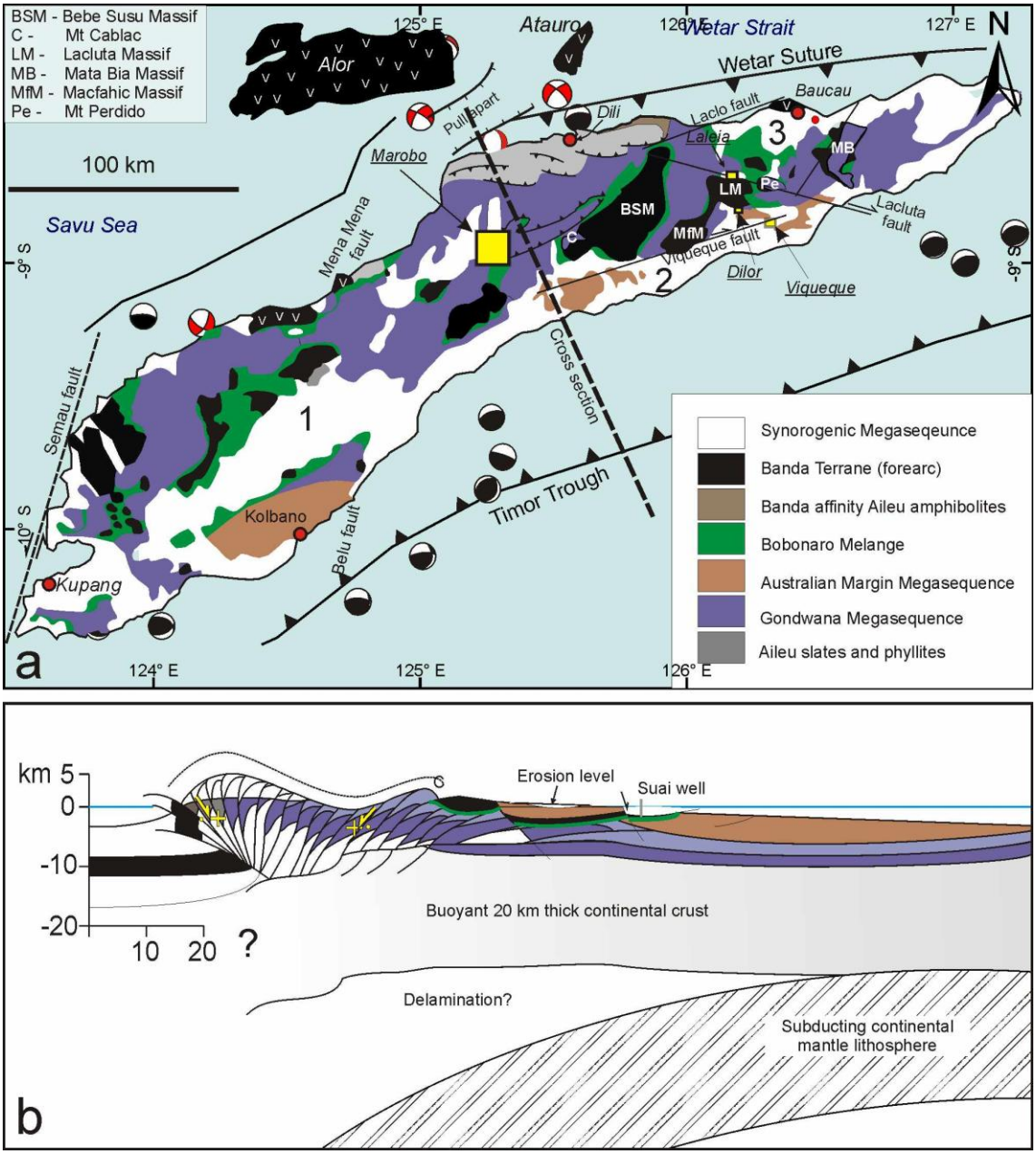

Figure 1.2: a) Geological sketch map of Timor, modified after Harris et al. (1998) and showing terrane distribution. Three main synorogenic basins are the Central basin of West Timor (1) and the Southern (2) and NE basins (3) of Timor Leste. Yellow boxes show study areas (Viqueque, Laleia, Marobo). Seismicity at <45km depth is taken from the global Centroid Moment Tensor catalog (Ekström et al. 2009) and plotted using 3DFocalMech (Labay & Haeussler 2007). Thrust solutions (black) are mostly confined to the deformation front south of Timor, whilst the remaining earthquakes are dominantly strike and normal slip (red). Pull apart basin west of Dili after Masson et al., (1991). b) Cross section through the highest topography of central Timor, adapted from Harris et al. (2000).

1.3 Geological setting and previous work

1.3.1 Geology of the Timor sector of the Banda Arc

The Australian plate in the Timor region is currently moving NNE at rates of ~70 mm/yr relative to the Sunda Shelf (Nugroho et al. 2009; DeMets et al. 2010) and its northern margin is being subducted under the greater Indonesian arc (Figure 1.1). Presently, the Australian continental slope collides with the Banda Arc and forearc and drives the arc northward along the backarc Wetar Thrust (Silver et al. 1983; Breen et al. 1989; Genrich et al. 1996; Snyder et al. 1996b). The collision of the Australian continental slope in the Timor region gives way westwards to subduction of the thinned Australian continental crust of the Scott Plateau below Sumba (dotted line Figure 1.1) (Shulgin et al. 2009) and thence to subduction of Australian ocean crust below the Sunda Shelf at the Java Trench (Planert et al. 2010). East from Sumba, the collision results in the development of a second, outer, non volcanic arc of continental material, including Timor, that occupies a forearc position between the volcanic arc and the Timor Trough (Von Der Borch 1979). GPS campaigns show that the outer and inner arc islands of Timor, Wetar and Alor (known collectively as the South Banda Block - SBB) are strongly coupled to Australia (Figure 1.1) (Genrich et al. 1997; Kreemer et al. 2000; Bock et al. 2003; Nugroho et al. 2009), but contraction is ongoing between Wetar and Darwin, Australia. This must be accommodated within the Timor orogenic wedge (Figure 1.2b). The coupling of Australia with the volcanic arc declines westward toward the subduction-collision transition (Nugroho et al. 2009).

1.3.2 Tectonostratigraphy of Timor

The island of Timor is formed of material derived mainly from Australian continental crust (Charlton 1987; Charlton & Suharsono 1990; Harris et al. 2000). The Permian to Jurassic rocks, known in Timor as the Gondwana Megasequence (Figure 1.2), rifted from the northern margin of eastern Gondwana during the Jurassic (Audley-Charles et al. 1988; Metcalfe 1996; Li & Powell 2001; Charlton et al. 2002) and were draped by a veneer of post-rift sediments deposited on the passive margin during Australia's northward drift (the Australian Margin Megasequence (Haig & McCartain 2007), or Kolbano Sequence (Audley-Charles et al. 1979; Charlton 1989)).

A décollement presently propagates through weak shales overlying the breakup unconformity as Australian continental material arrives at the Timor Trough (Figure 1.2b) (Karig et al. 1987; Breen et al. 1989). The Gondwana Megasequence below the décollement, together with minor amounts of the Australian Margin Megasequence, is underthrust and incorporated into stacked duplexes that underlie the Banda Terrane forearc basement and dominate the outcrop of the northern three quarters of Timor (Figure 1.2). The Aileu Metamorphic Complex on the north

coast of Timor is commonly considered to represent synorogenically metamorphosed Australian continental basement and thus the northernmost extent of Australian continental crust (Berry & Grady 1981; Berry & McDougall 1986). The Australian Margin Megasequence above the décollement is incorporated in the accretionary wedge (e.g. Harris 1991,2011)and exhumed on the south coast of Timor (e.g. Audley-Charles et al. 1979; Sawyer et al. 1993). Onshore, the accreted Australian Margin Megasequence is separated from the Gondwana Megasequence by the Banda Terrane forearc basement, which extends south of Timor where it is penetrated by exploration wells offshore of central Timor (Audley-Charles 1968; Charlton 2002; Harris 2011) (see Figure 1.2b). The weak shales below the décollement are overpressured in the collision zone and mobilized as the Bobonaro Mélange (Harris et al. 1998), referred to here as the Synorogenic Mélange (Haig et al. 2007).

1.3.3 Shallow seismicity of the Timor sector of the Banda Arc

Little onshore historical seismicity has been recorded in Timor Leste. Offshore, several thrust events occurred with M_w >5 at depths of 18-30 km below the northern flank of the Timor Trough (Figure 1.2a), suggesting slip on or close to the décollement. Immediately north of the Timor Leste capital city of Dili, a thrust event was recorded at ~ 30 km, along with extensional earthquakes at 16-20 km.

In West Timor, onshore earthquakes are generally transtensional and dominated by strike slip and normal earthquakes with T axes oriented E-W (Figure 1.2a) (McCaffrey 1988,1989). Charlton (1991) drew several major NE trending sinistral normal faults across West Timor. These include the Semau fault at the western end of Timor, where a Mw5.7 earthquake occurred near Kupang in the extreme west of Timor on 30 July 1975 (Figure 1.2a) (Tjia 1981). The remainder of these faults are not uniquely consistent with seismicity and do not appear as surface lineaments on digital elevation models or high resolution Google Earth satellite photography. As such they are generally excluded from geological maps of the island (e.g. Harris 2011). West Timor seismicity was interpreted by McCaffrey (1988,1989) as suggesting that orogen-parallel extension is now the dominant mode of deformation. This is supported by offshore sonar imaging of a major pull-apart basin between Alor and Timor, which appears to be created by eastward translation of Wetar relative to Alor (Masson et al. 1991). This structure coincides with normal faulting earthquakes studied by McCaffrey (1988) (Figure 1.2) and is thus active. Offshore seismicity surrounding West Timor is generally contractional.

1.3.4 Timing of collision

Collision is defined here as the first contact between the thinned Australian continental margin and the Banda Forearc. The timing and nature of this event in Timor is hotly debated. Audley-Charles (Audley-Charles 2011) argues for a collision ~3 Ma but Haig and Keep (Haig & McCartain 2007; Keep & Haig 2010) argue for an old collision at >8 Ma (see also Berry & McDougall 1986). The stratigraphic record of collision in the Kolbano area of West Timor (Figure 1.2) is bracketed by an unconformity between imbricated Early-Pliocene carbonates and undeformed Plio-Pleistocene equivalents (Audley-Charles et al. 1979; Sawyer et al. 1993; Charlton & Wall 1994). In Timor Leste, however, the bracket between ~8 Ma passive margin strata and unconformable ~5 Ma synorogenic strata is wider than in West Timor and does not lie within a single outcrop area (Haig & McCartain 2007). An 8 Ma cooling event in the Aileu Metamorphic complex (Figure 1.2) has been interpreted as a synorogenic metamorphic event (e.g. Berry & McDougall 1986; Keep & Haig 2010), but may have occurred as early as 10 Ma (Ely 2009), and has recently been linked to opening of the Banda Sea (Ely 2009; Audley-Charles 2011; Hall 2011). Several authors have suggested that Wetar exhibits isotopic signatures of contamination by subducted continental material since >4.7 Ma (e.g. Elburg et al. 2005; Herrington et al. 2011). However, such interpretations are complicated by a lack of geochemical data on the composition of subducted sediment. The cessation of volcanism at ~3 Ma (Abbott & Chamalaun 1981; Ely et al. 2011; Herrington et al. 2011) provides a youngest age for the collision but may, significantly post-date collision, as is seen in the Aegean (Ring et al. 2010) and in West Timor and Sumba where the adjacent arc is still active even though collision initiated there at least 3 and 2 Ma, respectively (Harris 2011).

1.3.5 Synorogenic geology of Timor

Onshore structural investigations (Harris 1991) and marine seismic surveys show that Timor is a doubly-vergent orogen with a strongly contractional offshore deformation regime (Richardson & Blundell 1996; Snyder et al. 1996b). The syn-collisional uplift of Timor has exhumed synorogenic marine sediments that were deposited in the forearc setting and are generally found only in contact with the Synorogenic Mélange, the Australian Margin Megasequence or the Banda Terrane (Figure 1.2). These sediments, referred to as the Synorogenic Megasequence (Haig et al. 2007), are distributed through three major basins, the Central Basin of West Timor, and the Southern and North East Basins of Timor Leste (Audley-Charles 1968; Kenyon 1974) (Figure 1.2). In Timor Leste, the Synorogenic Megasequence comprises a basal, late Miocene to Early-Pliocene chalky carbonate pelagite that grades up to a marl (the Batu Putih Formation of Hopper 1942). The Batu Putih Formation sediments were deposited at depths of up to 2500 m since 5.5 Ma (Haig 2012) and are overlain by Mid-Pliocene to Early-Pleistocene deep marine clastic sediments

(the Viqueque Formation (Audley-Charles 1968) or the Noele Marls of West Timor (Kenyon 1974). The Viqueque Formation in Timor Leste is overlain by shallow marine Pleistocene fan deltas (the Dilor Conglomerate), coral reefs (the Baucau Limestone) and fluvial gravels (the Ainaro Gravels) (Audley-Charles 1968).

1.3.6 Synorogenic deformation

Many of the Pleistocene coral reefs of the South Banda Block show evidence of rapid, but spatially variable uplift to elevations >600 m on both sides of the 3000 m deep Wetar Strait (Chappell & Veeh 1978; Rosidi et al. 1981; Vita-Finzi & Hidayat 1991; Merritts et al. 1998; Cox 2009; Ely et al. 2011). Despite this uplift and geophysical evidence for ongoing contraction, the synorogenic sediments of Timor are only gently deformed. Folding is observed, particularly in the Southern Basin, but most of the deformation comprises high angle faulting (Audley-Charles 1968). In West Timor, Barber et al. (1986) attributed much of the contractional deformation to diapir intrusion and mud volcanism localized along transtensional faults (see also Kenyon 1974). Although major Pleistocene normal faults have been recognized elsewhere in Timor, including the sinistral normal Laclo fault (Berry & Grady 1981; Harris 2011) and normal faults bounding the north sides of Mts Cablac (Keep et al. 2009) and Perdido (Keep & Haig 2010), the kinematics of this faulting has not been previously investigated in Timor Leste so the style of extension in Timor remains enigmatic.

1.4 Methods

1.4.1 Field mapping and kinematic analysis

Detailed structural mapping was carried out over a 25km^2 area surrounding the town of Viqueque in central Timor Leste, the type area of the Synorogenic Megasequence (Figure 1.2). This was followed by reconnaissance field mapping in the Laleia, Dilor and Marobo Basin areas, and the NE side of Mt Perdido. These latter areas were targeted based largely on GIS analyses (see below). Field observations including the orientations of bedding and faults were mapped at 1:10000 scale onto 2002 orthophotos and supplemented with stereoscopic analysis of 1950s aerial photos. Fault plane striation data were collected wherever possible, together with observations of displacements and of fault sense criteria (Petit 1987). Bedding and fault kinematic data were plotted using StereoWin (Allmendinger 2002) and FaultKinWin (Allmendinger et al. 2001) respectively.

1.4.2 GIS analyses

The lateral continuity of mapped structures was investigated using an overlaid combination of elevation and slope maps derived from a 3 arc second (90 m) SRTM v4.1 DEM (Jarvis et al.

2008). This approach highlighted linear and curvilinear topographic scarps that have been shown elsewhere to relate to crustal structure and zones of weakness, often reflected in the form of faults and fractures (e.g. Ganas et al. 2005; Masoud & Koike 2006; Demirkesen 2008; Rahiman & Pettinga 2008). Major normal faults, in particular, are typically marked by a topographic curvature anomaly arising at a change from background to steeper slopes (Jackson & Leeder 1994; Florinsky 1996; Ganas et al. 2005).

1.5 Synorogenic structure and kinematics of Timor Leste

This study splits Timor Leste into three structural geomorphic domains based on the dominance of distinct sets of structures. The domain boundaries and kinematic data are shown in Figure 1.3. Essentially, the domains comprise a NW extension domain where large-throw normal faults truncate and exhume the thrust stack that forms the NS contraction domain. In the NE extension domain, long transtensional fault traces dismember an overthrust sheet of Banda forearc, through which Gondwanan rocks are beginning to be exhumed in horst blocks.

1.5.1 NW extension domain

1.5.1.1 Structure and kinematics

The Marobo Basin of Central Timor (locality 1, Figure 1.3) lies immediately east of the Maliana Graben (Audley-Charles 1968), which is considered to be the easternmost limit of a 70 km long, orogen-parallel, synorogenic graben known as the Central basin of West Timor (Figure 1.2)(Brouwer 1942; de Waard 1956). The Marobo Basin fill includes > 30 m of Batu Putih Formation pelagic carbonates overlain by >700 m of submarine clastic sediments of the Viqueque Formation (Figure 1.4). The clastic sediments are composed dominantly of schistose lithics derived from the Banda Terrane.

The Marobo Basin is bounded to the west and east by rocks of the Gondwana Megasequence that crop out along Mt Loelaco and the Ilat Laun Ridge (Figure 1.4a). Bedding measurements within the Marobo Basin strike generally E-W and define a boat-shaped N-S syncline (Figure 1.4a&b). North-trending faults that cut synorogenic sediments in the Caiaco River (north from locality 618 in Figure 1.4) have dextral oblique normal displacements and striae (Figure 1.4c), and bound well-preserved graben structures in the active braided river bed, suggesting that they are recently active. The basin sediments are conically re-folded along the eastern boundary of the basin (Figure 1.4d) and the shear sense of refolding and the plunge of the cone axis is consistent with approximately N-S dextral normal shear sense (e.g. Becker 1995).

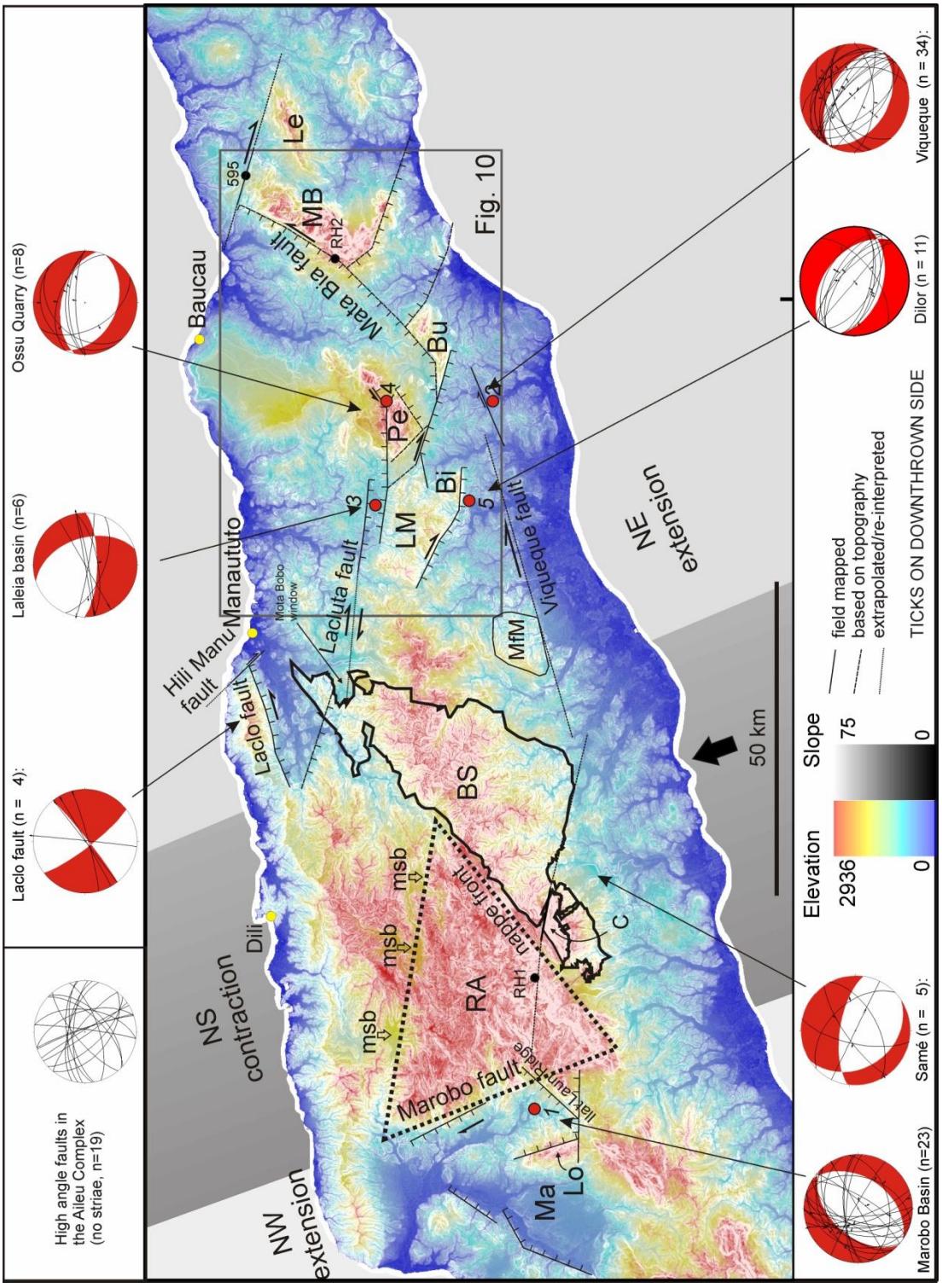

Figure 1.3: Combined SRTM elevation and slope map of Timor Leste, showing structural/geomorphic domains and lineaments regarded as the lateral continuations of major field-mapped transtensional faults. Hue represents elevation, tone represents slope. Shortening direction is indicated by heavy black arrow. Locality numbers: 1 – Marobo Basin; 2; Viqueque Basin; 3 – Laleia Basin; 4 – Perdido (MQ261); 5 – Dilor. Abbreviations: Bi – Mt Bibiliu; BS – Bebe Susu Massif; Bu – Mt Builo; C – Mt Cablac; Le – Legumau Massif; LM – Lacluta Massif; Lo – Mt Loelaco; Mat – Mata Bia Massif; msb – minor synorogenic basin; Pe – Mt Perdido; RA – Ramelau Arch (within dotted triangle). Faults and striae are summarized from following figures. Laclo fault and Aileu kinematic data from R. Harris (pers.comm).

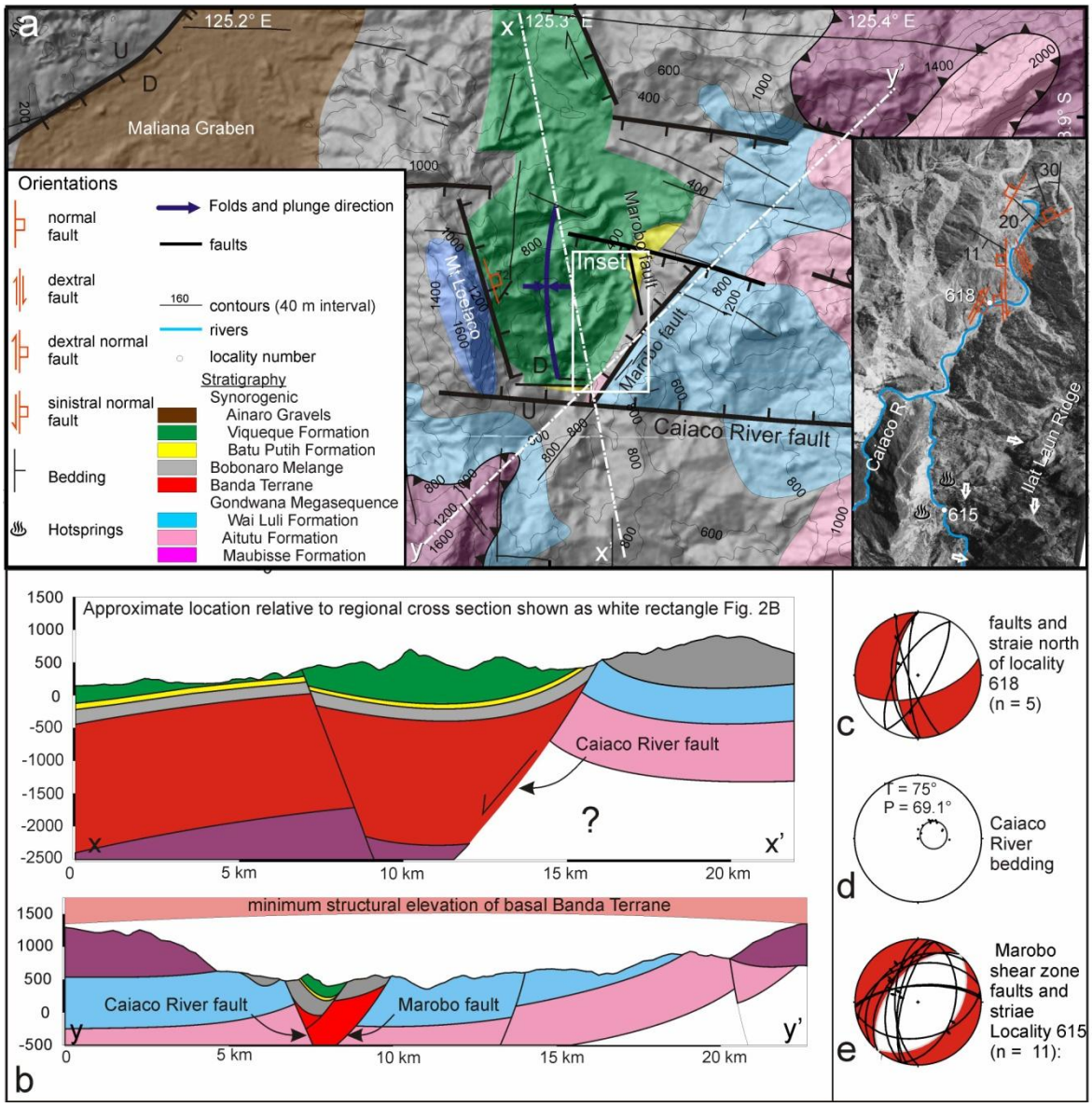

Figure 1.4: Reconnoissance map of the Viqueque Formation in the Marobo basin. For location see Figure 3. White rectangle shows area of investigation (see inset air photo); the remainder of the map is modified from Audley-Charles (1968). Arrows on air photo indicate fault traces visible on 1950's air photos. B) Cross sections drawn parallel to the syncline axis (X-X') and parallel to the strike of the Aileu-Maubisse Nappe (Y-Y'). Estimation of the throw on the graben bounding faults depends on inferring a thickness for the Banda Terrane (>2 km?) but is likely to exceed 4 km. C,D and E) structural data from the Marobo Basin. For discussion see text.

In the south of the Marobo Basin, a NE-striking line of hot springs are created by meteoric waters that are circulating deeply through active faults (Lawless et al. 2005). A few tens of metres south of the hot springs, at locality 615 (Figure 1.4), a gorge in the Caiaco River exposes a >50 m wide shear zone (Figure 1.5). The shear zone has a pervasive SC fabric with S horizontal and C picked out by multiple brittle faults that show normal displacement. The footwall rocks of the shear zone consist of Gondwanan Aitutu Formation limestones (Figure 1.5a). The faults in the

shear zone cut entirely through the Banda Terrane and are therefore not riedel shears associated with its emplacement (e.g. Yin & Kelty 1991).

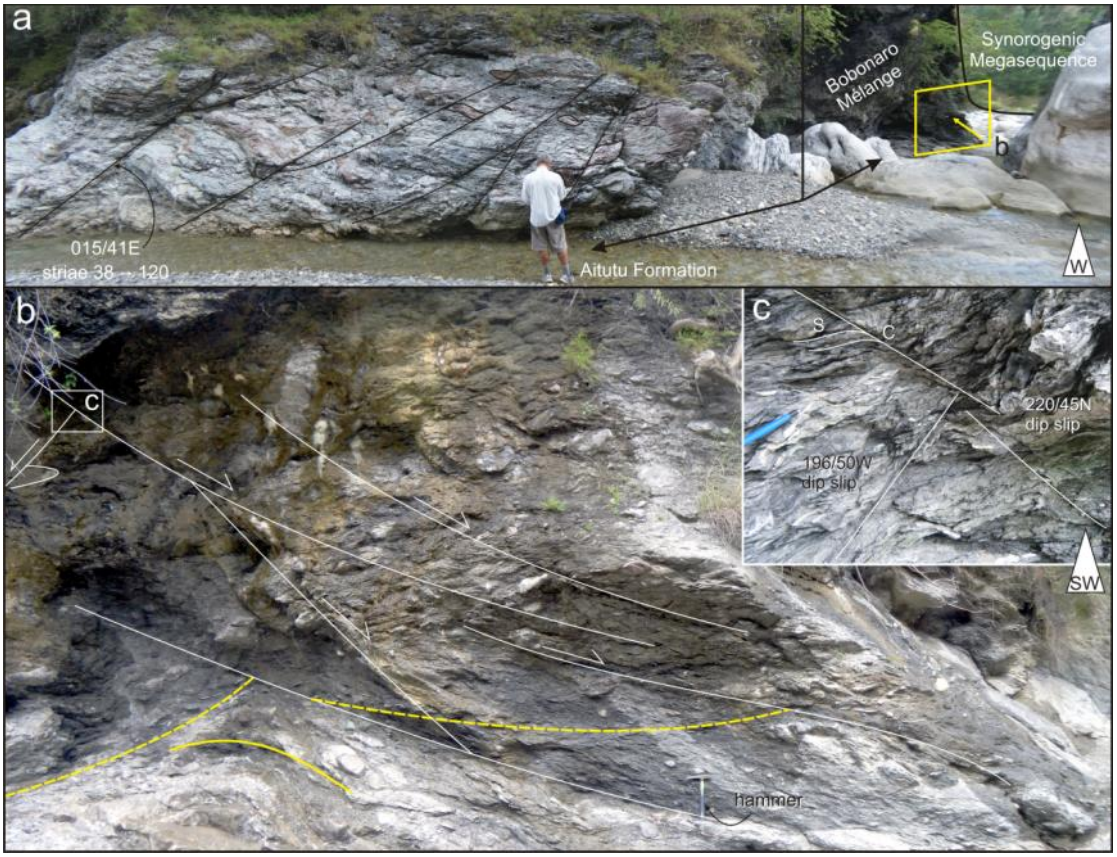

Figure 1.5. Structure of the Marobo shear zone, which provides good exposure of a fault with several km of high angle normal slip. a) Extended Aitutu Formation, showing boudinage and S-C fabric development and high angle brittle faulting in the footwall of the shear zone. Faults strike 015°, parallel with and dipping east towards the Ilat Laun Ridge. b) Shear zone in Synorogenic Mélange downstream (west) of the Aitutu Formation. White lines are normal faults, yellow lines are boudinaged layers. This outcrop shows a strongly developed SC fabric at a range of scales (b and c).

The normal faults in the Aitutu Formation strike approximately N-S and have dextral normal slip. They are sub-parallel with and dip towards the Ilat Laun Ridge (Figure 1.4a). The hanging wall rocks at the northern (downstream) end of the shear zone consist of rocks of the Synorogenic Mélange. Like the footwall rocks, the hanging wall rocks of the shear zone exhibit SC fabric at all scales (Figure 1.5c). The mélange has two sets of oppositely dipping faults, one equivalent to those seen in the footwall, and a second that has a more ENE/WSW orientation (Figure 1.4e). The net extension direction revealed by all faults is toward the NW (Figure 1.4e) but the rake rotates dependent on fault strike. E-W-striking faults show a sinistral component of strike slip and N-S faults show dextral slip.

Stratigraphic and structural relationships provide a means to estimate the minimum throw on the basin bounding faults. The basal Batu Putih Formation was deposited at depths <2500 m (Haig

2012) on top of an indeterminate thickness of the Synorogenic Mélange, which itself overlies Banda Terrane forearc rocks. The Marobo Basin slowly shallowed but remained at depths >1000 m (Haig 2012) while the Banda Terrane east of the basin was uplifted to above sea level and began eroding into the basin. The Banda Terrane east of the basin is now mostly eroded away and Gondwanan rocks of the underlying Maubisse and Aitutu Formations are exhumed to elevations higher than the synorogenic rocks in the basin (Figure 1.4b). This means that the Banda Terrane underlying the Marobo Basin is presently at a lower elevation than the base of the Maubisse nappe (Figure 1.4, Section x-x'). On this basis, the minimum displacement on the bounding normal faults is the sum of the thicknesses of the Banda Terrane and Maubisse nappe.

The Maubisse Formation is ~1 km thick (Audley-Charles 1968). The leading edge of the Banda Terrane forearc basement was probably wedge-shaped so its thickness is more difficult to estimate. However, it must have been thicker than 1.3 km, the thickness of the Bebe Susu Massif remnants of the Banda Terrane located SE of the Marobo Basin (Figure 1.3) (Audley-Charles 1968; Standley & Harris 2009) and may have been up to 9 km thick, the thickness of the forearc basement west of Sumba (Planert et al. 2010). The throw on the Marobo Basin bounding faults may therefore exceed 10 km, which is consistent with the brittle-ductile deformation observed in the Marobo shear zone.

1.5.1.2 Topographic evidence

The Marobo shear zone lies on an E-W topographic scarp (the Caiaco River fault, Figure 1.4) created by a ~20 m north-down step that is visible on aerial photographs and digital elevation models. Westwards from the shear zone, the Caiaco River fault truncates the southern end of the east-dipping strike ridge of Gondwanan limestones that forms Mt Loelaco.

Right lateral slip on faults within the Marobo Basin parallels both the strike of the basin and the trend of the western edge of the Ramelau Arch of central Timor (Figure 1.3). Eastwards across this discontinuity, referred to here as the Marobo fault, the elevation increases from ~100 m to ~1600 m over ~ 7 km. The Marobo fault is probably related to faulting that accommodates differential NW-directed subsidence of the Marobo Graben relative to the Ramelau Arch. The geometry of the Maliana Graben suggests that it has a similar structural style, but is bounded by a SE dipping bounding fault on its NW side (Figure 1.3).

1.6 N-S contraction domain of Central Timor

The Ramelau Arch of Gondwanan rocks dominates the high topography of Timor east of the Marobo Basin. The Ramelau Arch and Marobo Basin are separated by the Marobo fault (Figure 1.3). The Ilat Laun Ridge that bounds the eastern side of the Marobo Basin exposes virtually flat

lying Gondwanan Wai Luli Formation sandstone and mudstone beds that thrust southwards in km-scale exposures in the basin wall. These rocks form part of a nappe stack that has been interpreted as duplexes that were underplated below the Banda Forearc(Harris 1991; Snyder et al. 1996a; Harris et al. 2000; Harris 2011), and may have accommodated 50% shortening (Richardson & Blundell 1996) (Figure 1.2b). The stratigraphy within these nappes youngs southwards, which is consistent with duplexing of a lower plate passive margin. Nappe displacement has occurred since emplacement of the Banda Terrane, breaking through the Banda Terrane roof thrust and emplacing Gondwanan rocks over the Banda Terrane at Mt Cablac (Figure 1.2a) (Keep et al. 2009).

Although the Ramelau Arch consists of a nappe stack, its topography has a distinctly triangular shape (Figure 1.3). The Marobo fault forms the west side of the triangle, and the SE side is formed by the nappe fronts. The NE side of the triangle is marked by a series of minor synorogenic basins (msb - Figure 1.3), which lie on a NW-trending topographic discontinuity. NE of this line, the topography is lower than it is within the Ramelau Arch.

1.7 NE extension domain

Most of the data was collected east of the N-S contraction domain of central Timor. The boundary between the N-S contraction domain and the NE extension domain is presently unclear. However, east of the Ramelau Arch in central Timor Leste, the high topography is dominated by isolated massifs that include the Bebe Susu and Lacluta metamorphic massifs, and mixed-terrane massifs and mountains such as Mata Bia, Perdido, Builo and Bibiliu (Figure 1.2, Figure 1.3). The massifs are generally surrounded by Banda Terrane rocks and collisonal mélange (Barber & Audley-Charles 1976). The distribution of the massifs has been previously described as either erosional remnants of a once extensive nappe (Audley-Charles & Carter 1972), with nappes preserved in synformal structures created by post-emplacement en-echelon folding (Standley & Harris 2009), or as inherited Permian structures (Charlton 2002). This section describes the structure and kinematics from four areas in the NE extension domain (localities 2-5, Figure 1.3) that are strategically located relative to the massifs and slope anomalies. This section begins by describing contractional structures, which are reported here only from the Viqueque area but have been widely mapped throughout the Southern basin by Audley-Charles (1968). It then describes evidence for extensional and strike slip faulting.

1.7.1 Contractional structures

In the Viqueque Basin (locality 2, Figure 1.3) the Synorogenic Megasequence comprises the basal Batu Putih, which thins southward and is overlain by conglomerates and sandstones that fine southward. The Synorogenic Megasequence is gently folded by km-scale NE-SW folds (Figure

1.6). The folds are upright and the fold axes defined by poles to bedding on their limbs (Figure 1.6b&c) are approximately perpendicular to the regional shortening direction (Figure 1.1).

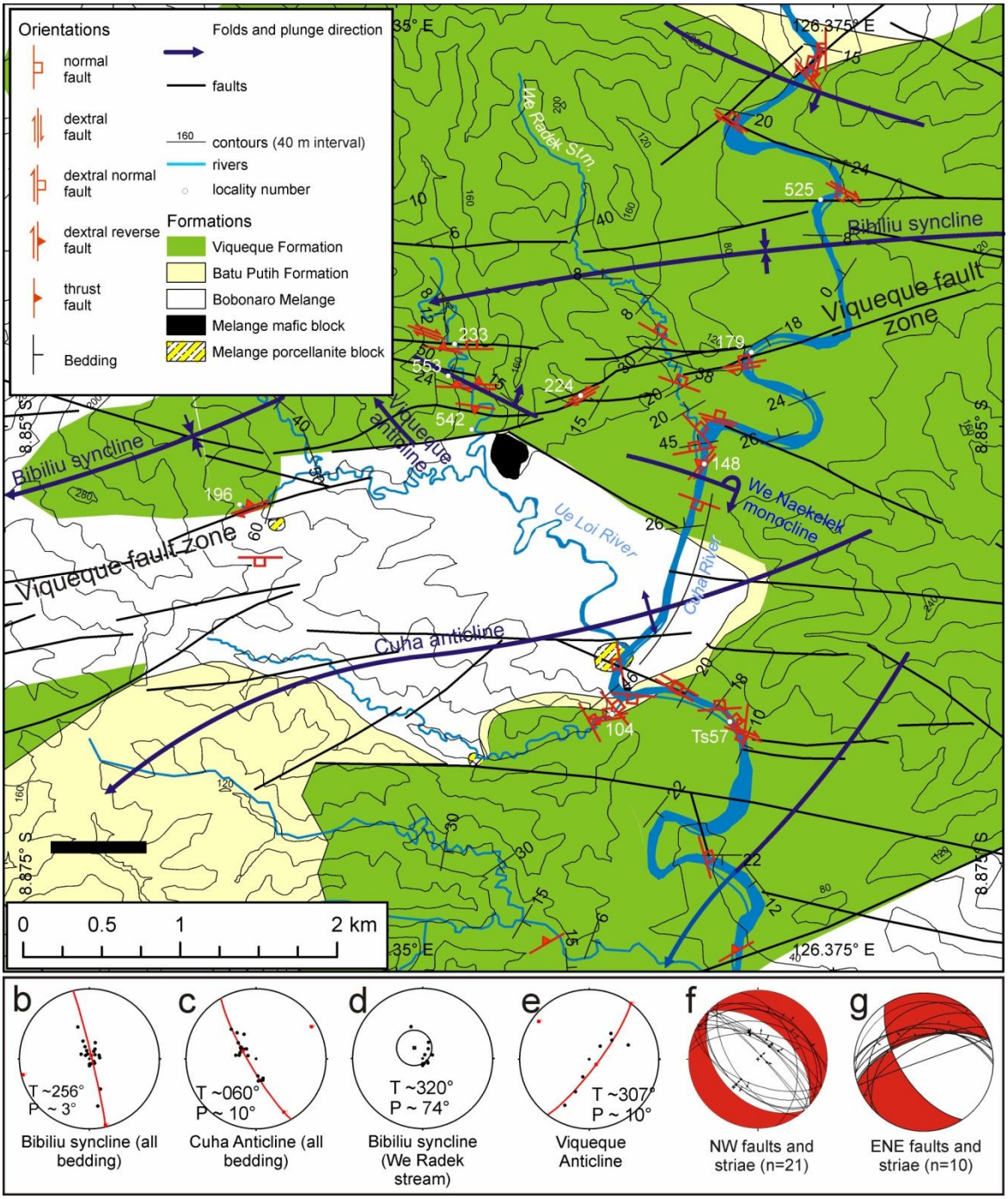

Figure 1.6: Structure of the Viqueque type area. a) geological map of the Viqueque area. Locality numbers shown white. b-e) Bedding orientation data for various parts of structures within the Viqueque area. f-g) Fault planes (lower hemisphere great circles), striations (arrows point in direction of motion of hanging wall) and average fault plane solutions (red) for NW-striking (f) and NE-striking faults (g) in the Viqueque area. For discussion see text.

The Bibiliu syncline in the Ue Loi River west of Viqueque is approximately cylindrical and plunges slightly SW toward 256° (Figure 1.6b). The Cuha anticline , south of and parallel with the Bibiliu syncline, plunges (at least locally) about 10° toward 060°, approximately opposite to the Bibiliu syncline (Figure 1.6c).

The NW-SE trending Viqueque anticline locally crossfolds the NE-trending structures at the location where the plunge reverses between the Bibiliu syncline and Cuha anticline. The axis of the NW end of the Viqueque anticline plunges 10° toward 307° (Figure 1.6f) and its NE limb conically refolds the Bibiliu syncline (Figure 1.6d). A structural dome at the intersection of the Cuha and Viqueque anticlines is cored by outcrop of the underlying Synorogenic Mélange. The contact between the mélange and the Synorogenic Megasequence is commonly underlain by the 'mixed block in clay' structural facies of the mélange (Harris et al. 1998), with large <200 m long blocks of porcellanite, chert, vesicular basalts and pillow lavas. These exotic blocks are only found for a few tens of stratigraphic meters below the base of the Batu Putih Formation. The core of the Viqueque anticline contains block-in-clay broken formation sandstones, which occur as lozenge-shaped boudins within a vertical fabric.

On the northeast limb of the Viqueque anticline, the north-dipping Synorogenic Megasequence beds abruptly steepen into a northeast verging, locally overturned monocline (the We Naekelek monocline - Figure 1.6). North of Viqueque the similar Buanu Rak monocline verges south on the north limb of the Bibiliu syncline (locality 528). The folding at locality 528 is accompanied by minor thrust fault displacement (<2 m). Between the We Naekelek and Buanu Rak monoclines the Bibiliu syncline is gentle and almost flat-bottomed.

1.7.2 WNW trending extensional faults

The boundaries of the massifs in the NE extension domain define two strong structural trends at WNW-ESE and NE-SW (Figure 1.3). The northern boundary of Lacluta Massif and the southern boundary of Mts Perdido and Builo lie on a major WNW-ESE scarp that extends from the south coast to the Laclo fault on the north coast where it appears to terminate (Figure 1.3a). This structural trend was investigated in several basins.

1.7.2.1 Viqueque Basin

The Viqueque Basin is located south of the prominent NW-trending scarp that forms the south face of Mt Builo (locality 2, Figure 1.3). Within the Viqueque Basin, the We Naekelek anticline and beds north of it for several hundred meters are pervasively crosscut by NW-striking faults. The faults are parallel to regional NW trending topographic scarps (Figure 1.3) and to the Viqueque anticline (Figure 1.6). Similar faults at the Viqueque Formation type section are located

immediately southeast and along axis of the Viqueque anticline (Figure 1.6) are also oriented generally NW-SE, parallel to the reach of the Cuha River in which they crop out. All of these faults have clear normal displacements, and striae are normal to slightly dextral (Figure 1.6f) The faults are pervasive but cannot be traced for more than a few tens of meters. Faults exposed at locality TS57 at the SE end of the type section take the form of a negative flower structure with dextral oblique normal faults bounding a central strike slip fault that parallels the type section reach of the Cuha River.

1.7.2.2 Laleia Basin

The synorogenic Laleia Basin, otherwise referred to as the Bere syncline (Audley-Charles 1968), lies 25 km NW of the Viqueque Basin and immediately north of a NW-striking topographic scarp that marks the northern side of the Lacluta Massif (locality 3 on Figure 1.3; Figure 1.7a). The Batu Putih Formation is only thinly present at the southern edge of the basin and is overlain by thick cross-bedded conglomerates emplaced northwards. This is in contrast to southwards emplacement of sediments in the Viqueque area. The contact between the Banda Terrane and the Batu Putih Formation in the Laleia Basin is obscured but north dipping faults immediately north of the contact strike 280-290° and have normal displacement (Figure 1.7b). The few striae observed in synorogenic strata had either pure strike-slip (unclear sense) or dextral oblique normal sense of slip (Figure 1.7c). However, a few tens of meters southwards into the outcrop of the Banda Terrane, horizontal striae can be seen on numerous 280°-striking faults within a vertical shear zone at locality 590 (Figure 1.7a). Crystallization on the lee side of asperities (e.g. Petit 1987) records dextral slip at this location.

On the north side of the Laleia Basin the synorogenic rocks dip southwards (Figure 1.7a&b) and a thick package of gently dipping Batu Putih Formation occupies the highest topographic position. South dipping faults with strikes of 258-290° throw conglomerates of the Viqueque Formation on the hanging wall down against older Batu Putih Formation rocks, demonstrating normal displacement. (Figure 1.7b). Gently west-plunging striae on the fault planes record dominantly dextral slip.

In the context of the observed dextral and normal faults, the Bere syncline is re-interpreted as a forced fold of the synorogenic cover rocks that has developed above a basement pull apart graben (Figure 1.7d). The pull-apart graben has formed in a right-stepover between separate segments of a dextral fault (the Lacluta fault) that bound the north and south sides of the basin. The southern segment is expressed as a topographic scarp that defines the northern boundary of the Lacluta Massif (Figure 1.3).

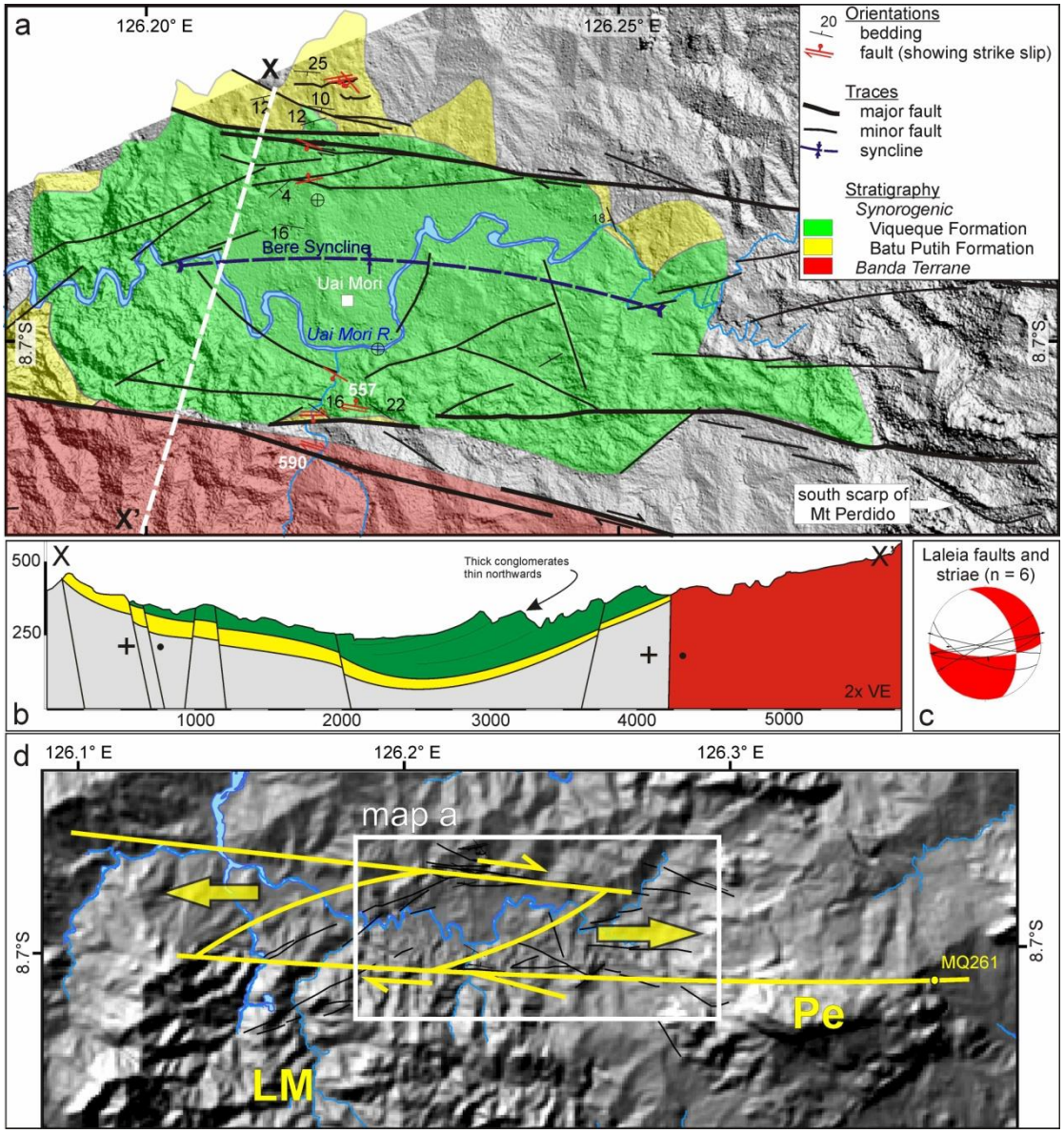

Figure 1.7: Reconnaissance geological map of the Laleia Basin. a) Detailed structure showing distribution of lithologies. Note dextral faults on both sides of the basin. b) Cross section showing forced folding of the Synorogenic Megasequence. c) Faults and striae from the Laleia Basin. d) Pull apart model for basin development, showing relationship to Mt Perdido and locality MQ261 (Figure 1.8).

1.7.2.3 Perdido

The southern segment of the Lacluta fault breaks eastwards into two strands (Figure 1.7a&d). The southern strand passes south of Mt Perdido (Figure 1.7d) and the northern strand passes across the north face of Mt Perdido (Figure 1.7D; locality 4 on Figure 1.3). There the northern strand projects through a roadside quarry (locality MQ261, Figure 1.8). Just north of this quarry Keep and Haig (2010) inferred an extensional forced fold that gently folded Pliocene coral limestones against the northern side of Perdido.

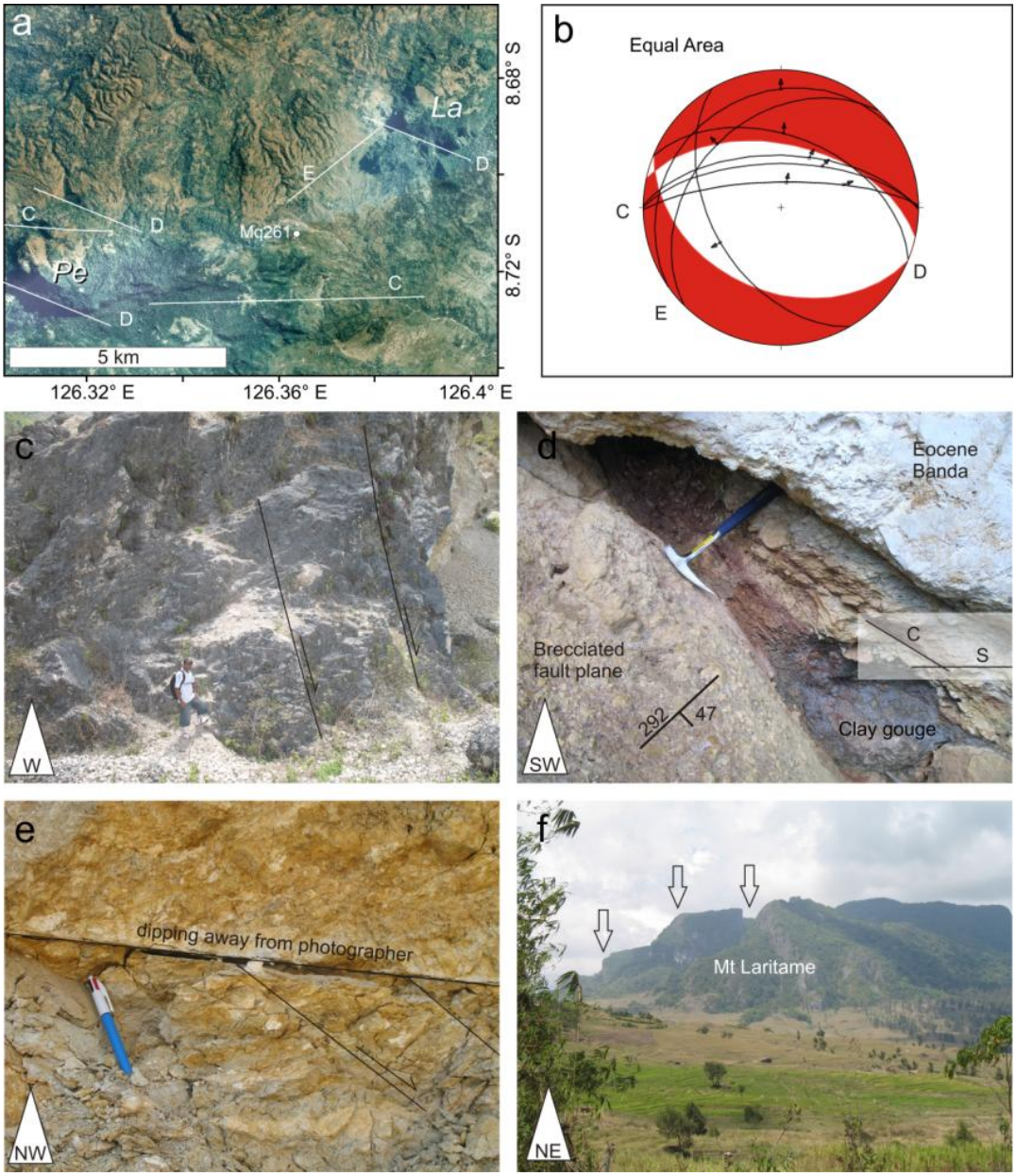

Figure 1.8: Quarry at locality Mq261 between Mts Perdido and Laritame in central Timor Leste. a) location of quarry and the orientation of distinct scarps associated with the two mountains. Letter designations refer to subfigures and also to the fault sets picked out in b), the striae and fault plane orientation data collected at Mq261. c-e) examples of the various fault sets. For discussion see text. f) View NE from quarry to Mt Laritame showing steep scarps that define fault set E.

Although the faults in the quarry do not involve synorogenic rocks, they nevertheless provide an opportunity to extend the mapping in the Laleia Basin and investigate the relationship between isolated massifs such as Mts Perdido and Laritame (Figure 1.8a). Several top-to-N faults were identified at MQ261 with strikes between 265 and 292 and a NE-SW extension direction (fault sets C and D, Figure 1.8b). Of these faults, set C (the E-W examples, which include the southern boundary of the Laleia Basin (Figure 1.7b), were all dextral normal (Figure 1.8b&c). Benincasa et al. (2012) recently interpreted Mt Perdido as a major pop-up on an E-W-striking

sinistral fault system. Their interpretation was based mainly on similarities between the strikes of fault sets developed around Mt Perdido, and similar fault sets developed in pop-ups elsewhere. Their interpretation requires several kilometers of E-W sinistral offset to produce a pop up structure with the volume of Mt Perdido. No sinistral E-W faults were observed around Perdido, or in the Laleia Basin west of Perdido, that would support such an interpretation.

A prominent NW-striking normal fault (set D, Figure 1.8d) juxtaposes hanging wall rocks of the Banda Terrane against Gondwana footwall rocks and has a well developed thick gouge with S-C fabric and a footwall breccia, suggesting a prolonged history of movement. Fault sets C and D at MQ261 parallel scarps that form the northern and southern boundaries of Mt Perdido and the southern boundary of Mt Laritame (Figure 1.8a).

More faults were observed that strike NE-SW and dip shallowly west (set E, Figure 1.8e), parallel with the scarps defining the western boundary of Mt Laritame and the eastern boundary of Mt Perdido. The scarps of Mt Laritame can be seen from the quarry as steeply dipping linear scarps (Figure 1.8f). At the quarry, set E was determined to be normal to dextral normal faults that crosscut E-W dextral normal faults of set C (Figure 1.8e).

The fault plane orientation and striation data at the MQ261 quarry suggest a pull-apart relationship between Mounts Perdido and Laritame and, although the striae are measured in basement faults, the extension direction is consistent with data from elsewhere in this domain (Figure 1.3). Mt Perdido is interpreted as a horst block that is displaced from the Lacluta Massif along the dextral oblique normal faults that are seen in the Laleia Basin. This interpretation opposes that of Benincasa et al. (2012).

1.7.2.4 Dilor

On the southern boundary of the Lacluta Massif (locality 5, Figure 1.3), the synorogenic rocks of the Viqueque Formation and the Dilor Conglomerate are downfaulted against rocks of the Gondwana Megasequence (Figure 1.9) (Audley-Charles, 1968). Although the contact between the synorogenic rocks and Gondwana Megasequence was not observed, pervasive normal faulting cuts turbidites of the Synorogenic Megasequence close to the fault (Figure 1.9b). The faults within the Synorogenic Megasequence strike parallel with Mt Bibiliu and striae reveal dextral oblique extension that is consistent with observations in Viqueque, the Bere syncline and north of Perdido.

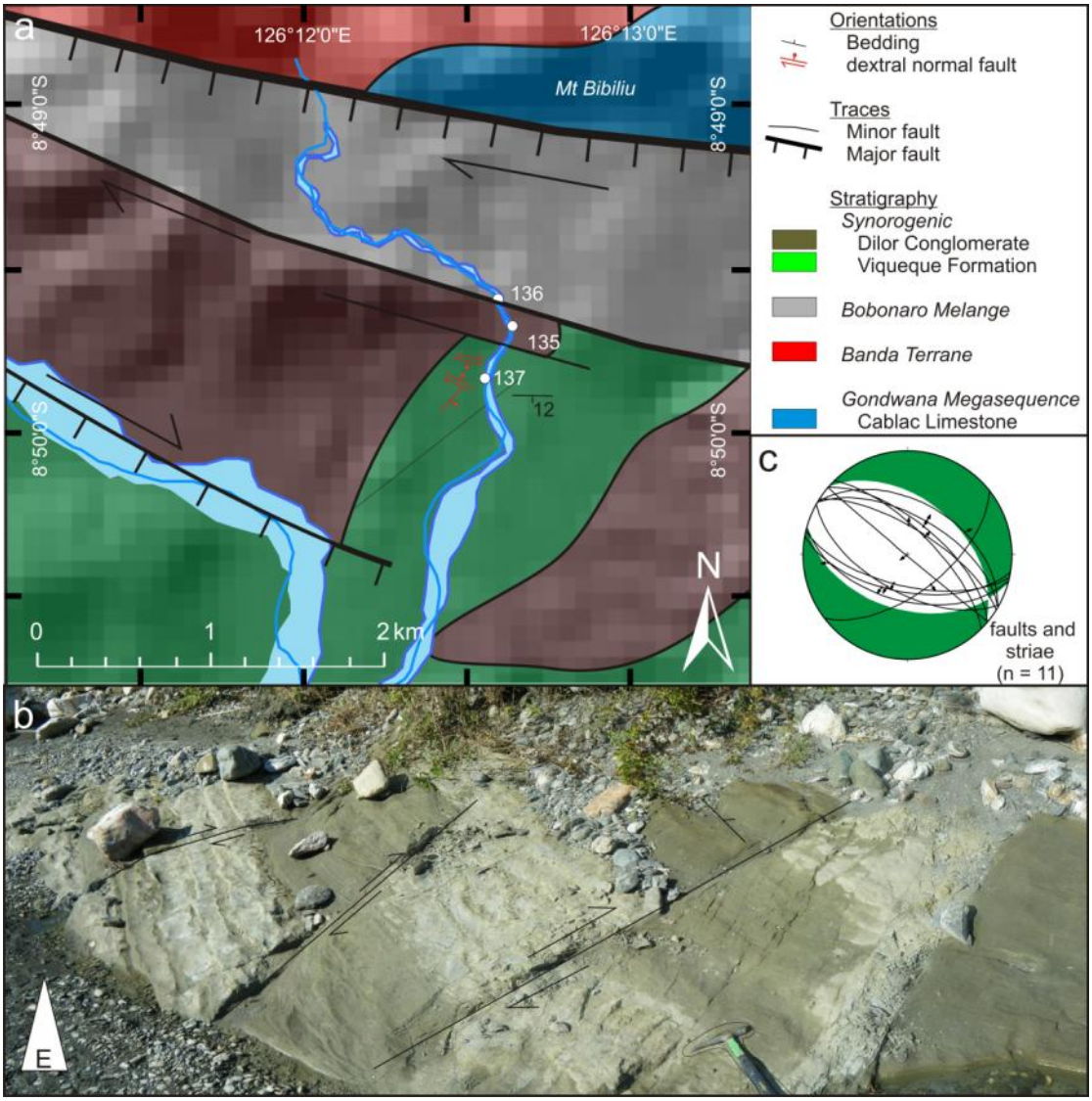

Figure 1.9: Normal faulting south of Mt Bibiliu on the southern side of the Lacluta Massif. a) Sketch map modified from Audley-Charles (1968). Note the flow of rivers along the normal faults. b) Photograph of dextral normal faults at locality 137. Photo faces east, beds dip south, faults strike SE, parallel to the face of Bibiliu.

1.7.3 Westward continuity of the Lacluta fault

The previous section has shown a consistent presence of NW-striking dextral oblique normal faults, including the Lacluta fault on the northern boundary of the Lacluta Massif. West of the Lacluta Massif, the Lacluta fault is shown cutting across the northern end of the Bebe Susu Massif (Figure 1.3), which does not appear to be dextrally offset. However, mapping by Standley and Harris (2009) shows that, the Banda Terrane of the Bebe Susu Massif south of the Lacluta fault is ~ 1 km thick, whereas north of the fault, only the basal Banda Terrane is preserved. A window north of the Lacluta fault (the Mota Bobo window - Figure 1.3) that exposes rocks of the Gondwanan Maubisse Formation was interpreted by Standley and Harris (2009) as erosional. An alternative explanation is that the Lacluta fault at the Bebe Susu Massif dips to the southwest and

its footwall exhumes Gondwanan rocks underlying the base of the Banda Terrane. The lack of dextral displacement of the Bebe Susu Massif suggests that the dextral displacement declines westwards.

1.7.4 WNW trending structures outside synorogenic basins

Approximately 50 km SW of the Lacluta fault, Keep et al. (2009) documented a north-dipping high angle normal fault that drops the Banda Terrane of the Bebe Susu Massif (BS Figure 1.3) down against Gondwanan rocks on the northern slopes of Mt Cablac (Ca on Figure 1.3a). This fault forms a clear trace on air photos that can be traced eastwards along the southern boundary of the Bebe Susu Massif and possibly westwards as a discontinuous series of en echelon structures that extend as far west as the Marobo graben (fine dotted line Figure 1.3).

40 km north of the Lacluta fault, the northern boundary of the Mata Bia Massif (Figure 1.3) forms a continuation of the Baucau coastline and parallels the Lacluta fault. E-W-striking dextral fault strands can be seen on aerial photographs at several localities north of Mata Bia. Field mapping in the occupied bed of a displaced stream at locality 595 showed that the outcrop in the dextrally offset stream is brecciated and has horizontal striae.

1.7.5 NE trending faults

Sharp NE trending scarps define the western edges of the Lacluta Massif, the Mata Bia Massif and Mt Builo. The western faces of Mata Bia and Builo occupy a single NE trending scarp (the Mata Bia fault) that parallels the extension direction observed in the NE extension domain (Figure 1.3). The two mountains are separated by a low slope area that is bounded both north and south by scarps that parallel the orientation of the NE-SW faults (Figure 1.3). It therefore seems likely that the Mata Bia fault operated as a sinistral normal fault that accommodated northward translation of the Mata Bia Massif. The ‘conjugate’ angle between the NE sinistral normal and WNW dextral normal faults is ~110° rather than 60° (Figure 1.3a).

1.7.6 ENE trending faults

Several ENE-striking faults crosscut the We Naekelek anticline in Viqueque at localities 553 and 148 (Figure 1.6), where they have dextral oblique striae and a mix of normal and thrust displacements (Figure 1.6G). Similar, steeply dipping ENE-striking faults also crop out at several other localities (Figure 1.10). The sense of displacement at these localities is top-down-to-the-NW and the magnitude of displacements, though presently unquantified, are larger than other observed normal faults. The fault at locality 179 strikes 260° across the Cuha River and dips 60°N, juxtaposing a >10 m thick footwall conglomerate against a hanging wall mudstone. Striae on the fault plane plunge toward 022°, demonstrating a dextral oblique normal sense of motion.

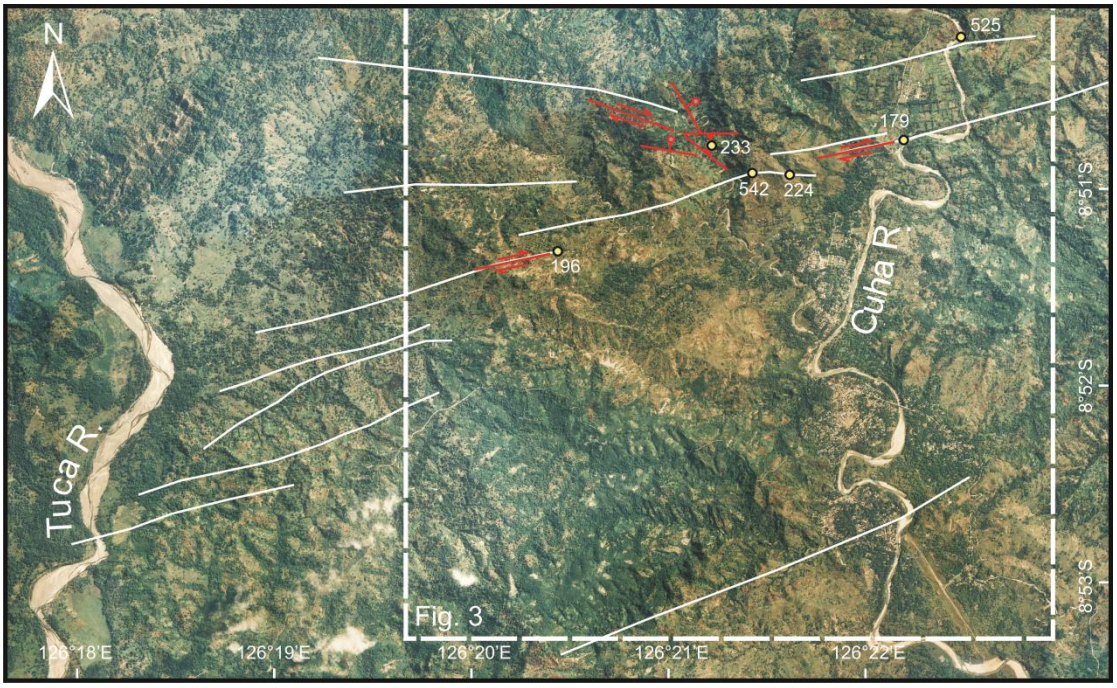

Figure 1.10: Map showing traces interpreted as discontinuous ENE-striking fault strands that make up the Viqueque Fault zone, and their relation to a typical WNW-striking fault.

The fault at locality 179 can be traced westwards on air photos, through a series of left steps that pass through localities 224, 542, and 196 (Figure 1.10). At locality 196 the western limb of the Viqueque anticline is re-folded tightly into a NE-plunging syncline against the outcrop of a 250° strike slip fault that juxtaposes sheared turbidite beds on the north side against mélange on the south side. Striae plunge 40° W, consistent with shortening at a restraining left step on a dextral fault. This set of ENE-striking faults appears to form a coherent fault system, referred to here as the Viqueque fault zone.

West of locality 179 (Figure 1.10), a strand of the Viqueque fault zone is exposed in the Ue Loi River at locality 233. From there, the fault continues westwards as a WNW-striking strike slip fault that diverges from the Viqueque fault zone and parallels the Viqueque anticline and the majority of normal faults (Figure 1.6f). Locality 233 is intensely faulted with pure dextral WNW (strike 290°), pure normal WNW (strikes 280°and 330°, top down to the north/northeast) and thrust faults observed (strikes 270° and 300°). The intersection of the WNW and ENE strands makes an angle of ~25°, a typical angle for Riedel shears. The local association of strike slip, extension and compression at locality 233 is consistent with fault interactions at the intersection of differently oriented but same sense (in this case dextral) strike slip faults (Sibson 1989; Duffy et al. 2013).

A probable strand of the Viqueque fault zone creates a dextral jog in the course of the Cuha River at locality 525 (Figure 1.10). The river has cut a gorge through the conglomerate on the downstream side of the fault. The main fault is not well exposed but can be inferred from the development of a graben ~30 m wide at the location of the dextral jog. Minor normal faults in the conglomerate on the south side of the fault strike 120° and dip 80° to the south, similar to the WNW-striking riedel shears seen at locality 233 (previous paragraph). The striae at locality 525 trend toward 228°, once again recording dextral displacement. Southwest of locality 196, the Viqueque fault zone crosses the Tuca River at what appears to be a similar dextral jog (Figure 1.10).

West of the Tuca River, the Viqueque fault zone can be traced as a slope anomaly that extends for more than 50 km along strike (Figure 1.3). Its termination is still enigmatic. Release of the slip on the Viqueque fault zone appears to displace the Macfahic massif from the Bebe Susu massif (Figure 1.3). However, fault striae from near Samé (Figure 1.3) indicate that the Viqueque fault zone probably extends much further west than the Bebe Susu massif, possibly to a point south of the Marobo basin.

The Viqueque fault zone is parallel to the normal (Berry & Grady 1981), *sinistral* oblique (Harris 2011) Laclo Fault on the north side of Timor (Figure 1.3). The Laclo Fault appears to truncate the western end of the Lacluta fault and is itself is truncated at its NE end by an almost vertical faulted contact with the Hili Manu peridotite (Berry & Grady 1981) (the Hili Manu fault, Figure 1.3). The Lacluta fault appears to truncate the eastern end of the Viqueque fault zone (Figure 1.3).

The Hili Manu fault strikes approximately 100°, parallel to the 100° strike of the latest deformation event in the Aileu Complex (Berry 1981; Berry & Grady 1981). Its striae plunge shallowly east, which was interpreted by Berry and Grady (1981) as indicative of a probable left-lateral fault. On the basis of its similarity with fault orientation and slip data from synorogenic basins, and its dextral offset of the Laclo River, it is reinterpreted here as a probable dextral normal fault. The mutual truncation of ENE and WNW-striking faults suggests that both sets are contemporaneous.

1.7.7 Large scale fault dip

Major normal faults are commonly located at the base of high mountain fronts (e.g. Jackson & Leeder 1994; Wdowinski & Zilberman 1997; Ganas et al. 2005). DEM profiles (Figure 1.11) show that all the massifs in the NE extension domain have steep, high western (Figure 1.11b) and southern boundaries (Figure 1.11c), with lower scarp elevations on their northern and eastern

sides. This suggests that the major faults generally dip south or west, with footwall uplift to the north and east. Most of the profiles, particularly Mata Bia (Figure 1.11C, cross section H-H') show evidence for internal north-dipping faults within the massifs that reduce and possibly reverse the tilt created by footwall uplift.

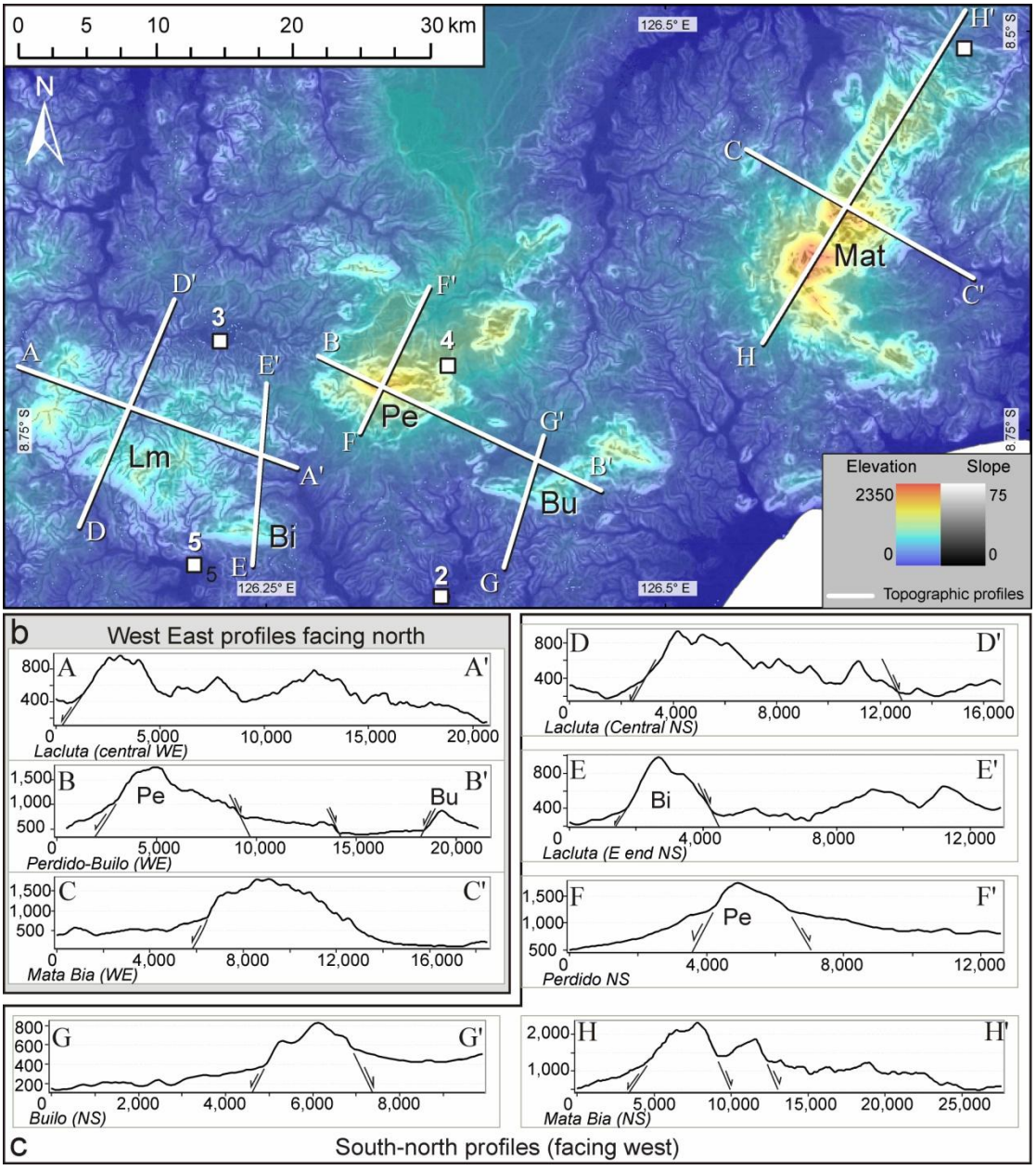

Figure 1.11: Scarp morphology of massifs of central Timor Leste. a) SRTM combined slope and elevation map. Hue is indicative of elevation. Brighter areas have steep slopes. Locality numbers: 2; Viqueque Basin; 3 – Laleia Basin; 4 – Perdido (MQ261); 5 - Dilor. Heavy black arrow shows extension direction of Viqueque normal faults. Bi – Mt Bibiliu; Bu – Mt Builo; Lm – Lacluta Massif; Mat – Mata Bia Massif; Pe – Mt Perdido. b) W-E profiles of the massifs show that the steepest, highest NE-trending scarps are all located on the western faces and topography declines eastwards, suggesting that the major normal faults are west-dipping. c) N-S profiles of the massifs show that all have their steepest scarps bounding their southern side, suggesting that the Viqueque and Dilor basins lie on the hanging wall of a major south-dipping fault system.

A southwest dip on the major NW-SE faults is also supported by the widespread exhumation of Gondwana rocks, and the absence or poor preservation of Viqueque Formation clastic synorogenic rocks on the north side of the Lacluta fault (even the Laleia Basin lies within the fault zone), compared with widespread preservation of the Banda Terrane and clastic synorogenic sediments on the hanging wall to the south.

1.8 Discussion

1.8.1 Kinematic model for conjugate strike-slip faulting and arc-parallel lateral extrusion

Extension and strike slip faulting in the NE extension domain (Figure 1.3) occurs mostly on NE sinistral and WNW dextral oblique strike slip faults. These have a conjugate angle of 110 ° and are mostly located between the ENE striking, opposing sense Laclo and Viqueque faults (Figure 1.12a). Structural observations within the fault-bounded massifs across Timor suggest that they have fold orientations that are consistent with each other and with the present stress regime (Standley & Harris 2009). This is inconsistent with vertical-axis block rotations during bookshelf-type strike-slip faulting, and also precludes differential rotation of once optimally-oriented antithetic faults during large scale strike slip tectonics. Subduction obliquity is also not responsible for arc-parallel extension in Timor that is apparent in seismicity (McCaffrey 1988,1989), offshore structures (Masson et al. 1991), and in the faulting of the Synorogenic Megasequence (McCaffrey 1996). An explanation may be found in similar fault geometries documented in other collisional orogens around the world including the European Alps, Tibet and Mongolia (Ratschbacher et al. 1991a; Ratschbacher et al. 1991b; Frisch et al. 1998,; Bistacchi & Massironi 2000; Walker et al. 2008; Styron et al. 2011).

Based on similarities between these orogens and Timor, I propose a paired general shear (PGS) model for Timor, based on the model of Yin and Taylor (2011). In the PGS model, brittle surface extension is coupled to ductile extrusion at depth between opposite-sense shear zones, which are oriented perpendicular to the shortening direction (Figure 1.12b-c). In Timor, these shear zones break to the surface as the Viqueque and Laclo strike slip fault zones (Figure 1.12a-b). Extrusion between these ENE-striking fault zones is localized on their Riedel shears, which include the Lacluta and Mata Bia faults. These Riedel shears must dip towards their master fault to join it at depth, which creates a series of fault-bounded blocks that are both tilted (e.g. Figure 1.11) and shuffled in the extrusion direction (Figure 1.12B). ‘Extension’ is therefore the surface expression of shortening at depth.

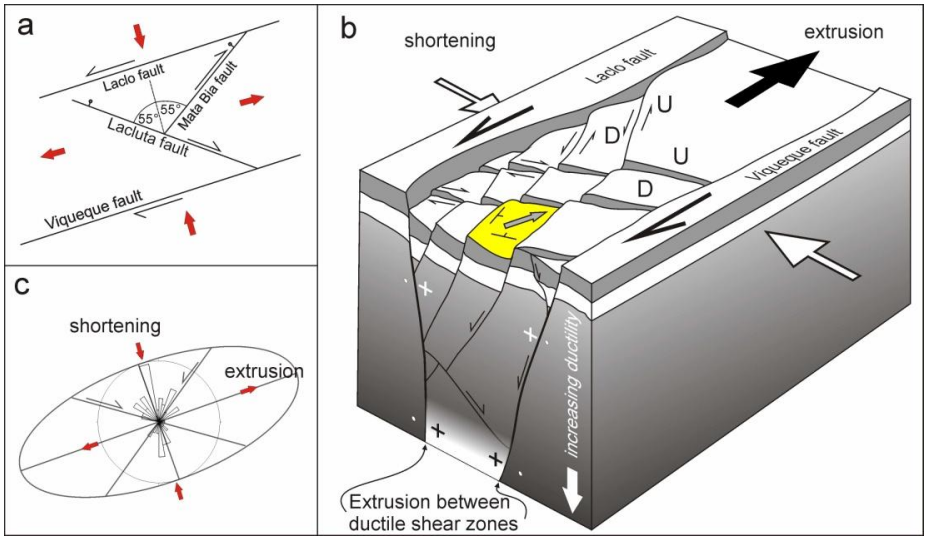

Figure 1.12: a) Relationship between the orientations of cross-cutting Riedel shears and bounding opposite-sense strike slip faults in Timor. b) Block diagram showing cross-cutting Riedel shears dipping towards the parent faults, creating a series of fault bounded blocks that are tilted in the extrusion direction. The yellow highlighted surface shows how slip on the Riedel shears back-tilts the block in the extrusion direction. c) Relationship between the shortening direction given by poles to bedding in Viqueque and the extrusion direction.

1.8.2 Reconstruction of a dismembered massif

Restoration of transtensional deformation is problematic because a great deal of movement occurs out of plane. However, a restoration is necessary to constrain paleogeography so this study attempts to restore the extrusion of Timor, within observational bounds. The topography of eastern Timor Leste is here considered to be expression of the arc-parallel extrusion of the island, as was done for extrusion of the Eastern Alps in Europe(Frisch et al. 1998) (Figure 1.13b). On this basis, the displacement on the various major structures is sequentially collapsed in 3 steps, beginning with the modern configuration (Figure 1.14a). A block including Perdido, Mata Bia and Builo are translated west along the Lacluta fault to restore Perdido against the Lacluta Massif (Figure 1.14b). The gap between Builo and Perdido is then collapsed, also along the Lacluta fault, making Builo part of the Lacluta Massif (Figure 1.14c). Finally, the gap between Mata Bia and Builo is collapsed along the Mata Bia fault (Figure 1.14d). This restoration accounts for ~20 km of extrusion.

The motions implied by reconstruction of the Banda Massif are in good agreement with striae recorded in this study. It is likely that the Mata Bia Massif could be restored further west across the north side of Perdido, parallel to the Lacluta fault (Figure 1.14d). This would be consistent with dextral striae on high angle faults parallel to the Lacluta fault at MQ261 (Figure 1.8) and would increase the total extrusion recorded in the dispersal of the Banda Massif to ~ 30 km. It would, however, require westward restoration of the Baucau Plateau. No field evidence presently exists to support such a restoration but if the Hili Manu fault is involved, this restoration would collapse the western edge of Manaututo Bay. In support of this speculation, the restoration

as shown partially collapses the distinctly telescopic linear elements of the Timor coastline. If these elements are structurally controlled, the extrusion may account for as much as 50% of the land area of Timor Leste.

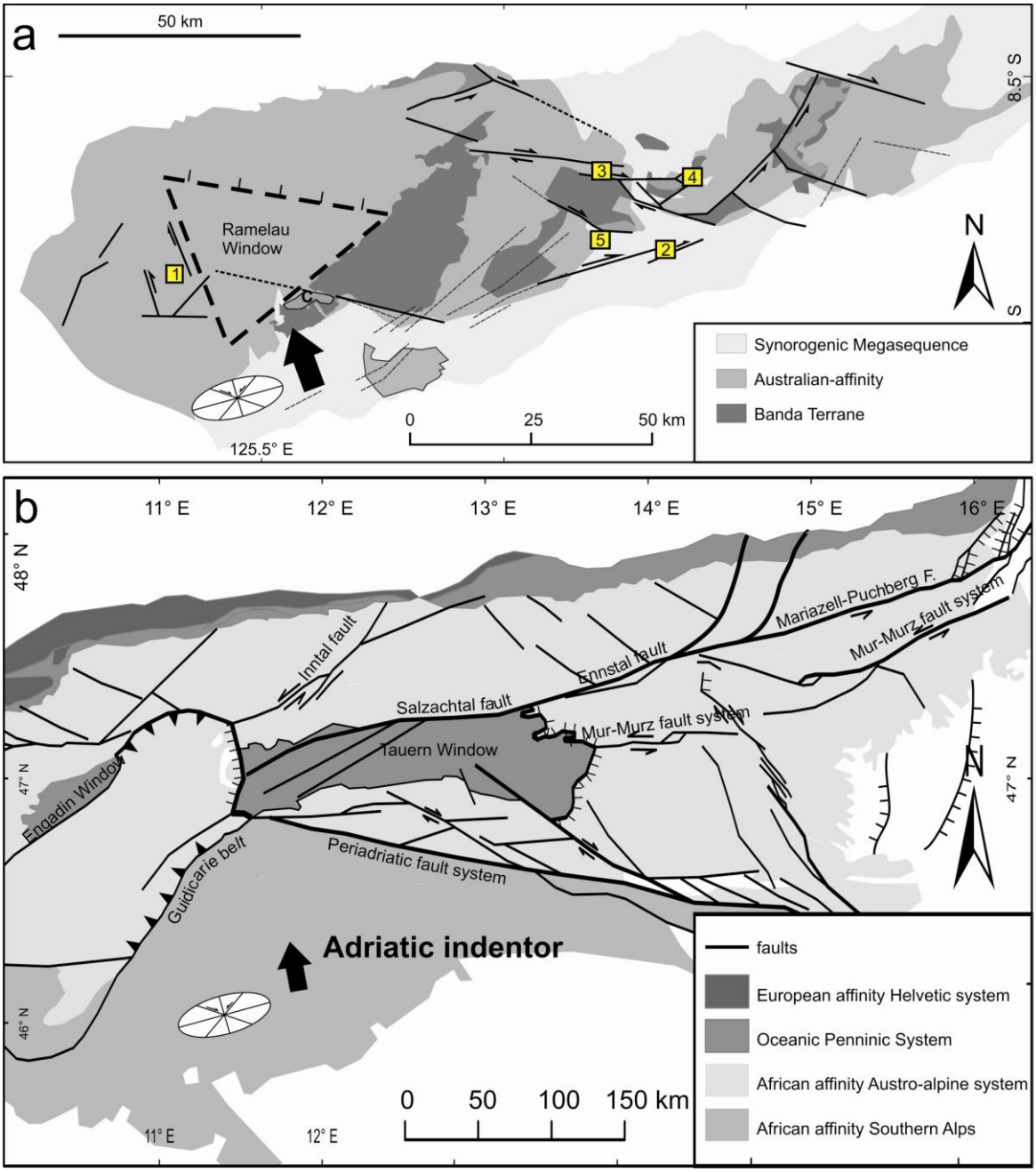

Figure 1.13. Regional transtension along conjugate strike slip faults. Shortening direction in both figures indicated by heavy black arrow. a) Faulting in Timor. Numbers denote basins indicated on Figure 1.3. Note the orientation of faults relative to the telescope-like geometry of the coastline. Fine dotted lines are faults mapped by Audley-Charles (1968) along the south coast that seem compatible with the present study b) Comparative generalized tectonic map of the European Alps, showing dismemberment and extrusion of the Eastern (Austroalpine) Alps associated with strike slip extrusion along structures similar to those observed in Timor. The Austroalpine rocks are being extruded eastward along non-Andersonian conjugate strike slip faults (Ratschbacher et al. 1991a; Frisch et al. 1998).

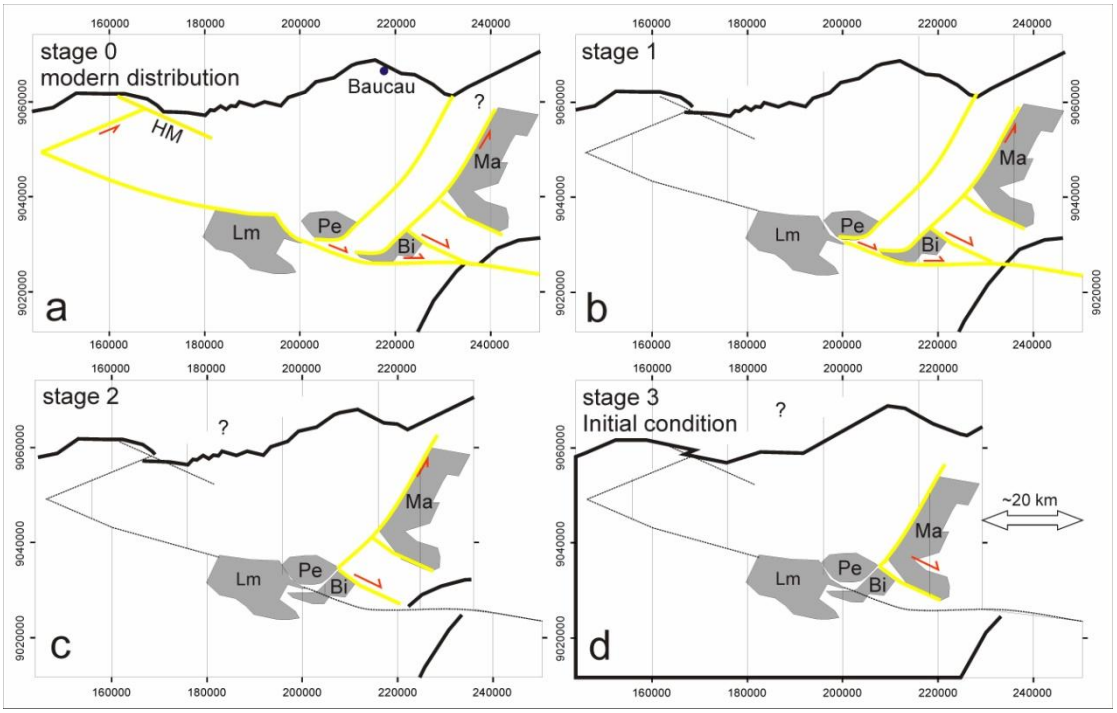

Figure 1.14: Three stage palinspastic reconstruction of central Timor Leste showing accumulation of at least 20 km of extension through fault separation only of the major fault blocks identified in this study. Note that it is not possible based on the data to hand, to account for out of plane displacement due to normal faulting.

1.8.3 Origin of contractional structures and relevance of diapirism

The discussion so far has focused on extension. The synclines in the Marobo and Laleia study sites have been shown to be forced folds over basement grabens (Figure 1.4; Figure 1.7). The only compressional structures, therefore, are those observed in the Viqueque Basin (Figure 1.6), where WSW-plunging km-scale folds are generally considered to be evidence of compressional shortening. These folds may reflect early deformation in a contractional setting, such as presently exists in the Timor Trough south of Timor (see earthquakes Figure 1.2a). However, seismic reflection studies show that synorogenic sediments immediately south of Timor (Veevers 1971; Crostella & Powell 1975), in the accretionary prism west of Timor and the Savu Sea (van der Werff 1995a,b), and in the Wetar Strait (Masson et al. 1991) presently accumulate in grabens, including the >3 km deep Suai graben (Crostella & Powell 1975, their Fig. 10), offshore of south central Timor. It seems likely that these settings are analogous to the depositional setting of the Synorogenic Megasequence.

Charlton (2002) suggests that the only contraction in the Suai Graben is caused by the reactive diapiric rise of mélange into the footwall of the graben bounding fault. Similar extensional diapirism provides the most likely explanation for the Viqueque anticline crossfold in the Viqueque Basin (Figure 1.6). The trend of the Viqueque anticline parallels the WNW trending

normal faults. The overhanging We Naekelek monocline on the NE limb of the Viqueque anticline (Figure 1.6) is a feature that is characteristic of diapirism and is known in diapiric literature as a flare (e.g. Giles & Lawton 2002). Flaring, together with the widespread occurrence of exotic blocks on the margin of the Viqueque anticline are consistent with observations of diapirism in West Timor (Kenyon 1974; Barber et al. 1986; Charlton 1991; Harris et al. 1998), the Suai Graben (Crostella & Powell 1975) and elsewhere (Talbot & Von Brunn 1987; Orange 1990; Giles & Lawton 2002). Shale diapirism is common in extensional settings due to the reactive rise of overpressured shales into space created in the footwall of extensional faults (Vendeville & Jackson 1992b; Van Rensbergen et al. 1999). Reactive space-filling is typically followed by active intrusion of diapirs once the overburden is sufficiently thinned. This deforms the overburden and results in the creation of features such as the shale flare observed here. The along axis transition from diapiric folding to normal faulting seen at the Viqueque type section (Figure 1.6) is also characteristic of diapir collapse during extension (Vendeville & Jackson 1992a). Much of the contractional deformation in synorogenic sediments in Timor Leste can therefore be attributed to extensional diapirism, rather than regional tectonic crustal shortening.

1.8.4 Inception age of extension and timing with respect to large scale tectonic evolution of the Timor orogen

Understanding the timing of inception of the extensional tectonic regime is critical to evaluating the probable mechanisms. Most faults in Timor Leste were mapped only within the Synorogenic Megasequence and are thus only constrained to post-deposition (i.e. Pleistocene or younger). The best estimate of the age of inception of normal faulting in Timor is provided by the structural relationships in the Marobo Basin. The Batu Putih Formation there records pelagic deposition in a deep basin, at 2500 m to 1000 m depth, beginning around 5.5 Ma (Haig 2012). Meanwhile, the Timor forearc was being uplifted from below the Batu Putih Formation to above sea level and seems to have emerged at slow uplift rates by ~4.5 Ma (Nguyen et al. 2013). This slow uplift preceded a period of rapid uplift that commenced around 3 Ma, possibly due to the arrival of the Australian continental slope at the subduction trench (Bowin et al. 1980). This rapid uplift event at ~3 Ma coincided with the onset of clastic sedimentation in the Viqueque area. Conglomerates in the Marobo Basin began depositing at ~3.5 Ma (see section 2.3.3.2), approximately 0.4 Ma earlier than in the Viqueque Basin. Subsidence of the Marobo Basin was therefore syn-collisional rather than post-collisional, and preceded the arrival of the continental slope. Since the onset of deep marine clastic sedimentation post 3.3 Ma, the pelagic basin sediments have been uplifted to 400 m above sea level but the graben remains active, indicating that regional uplift exceeds basin subsidence.

In the NE extensional domain, the Laclo fault has exhumed the Aileu Metamorphic Complex (Berry & Grady 1981). White mica $^{40}Ar/^{39}Ar$ age determinations show that the Aileu Metamorphic Complex only cooled to around 420°C at 5.4 Ma (Berry & McDougall 1986; Harris 2011). Apatite fission tracks further show that the same rocks were rapidly exhumed from the partial annealing zone (80–120°C) at rates of <3mm/yr over <4 m.y. (Harris et al. 2000). Taken together, these data indicate the inception of rapid extrusion in the NE domain since ~4Ma. This is the same age that extrusion was inferred from other data and arguments associated with a plane strain reconstruction of the orogen (Fig. 3 of Harris 1992).

1.8.5 Comparisons of geological and geophysical deformation regimes

GPS data show that the volcanic arc within the South Banda Block is strongly coupled to the Australian plate (Genrich et al. 1997; Bock et al. 2003; Nugroho et al. 2009) (Figure 1.1), and that the coupling decreases systematically westwards (Nugroho et al. 2009). GPS data is at extremely low resolution and almost absent within Timor. However, the decrease in coupling is reflected in global GPS velocities of islands within the Banda Arc (Figure 1.15), which are parallel to the arc and increase eastwards, revealing an arc-parallel extensional regime. Bock et al. (2003), showed that the strain rate increases westwards to a peak near the subduction-collision transition (Figure 1.15). Coupling changes therefore appear to extend the arc, as has been previously inferred in the Caribbean (Gorney et al. 2007).

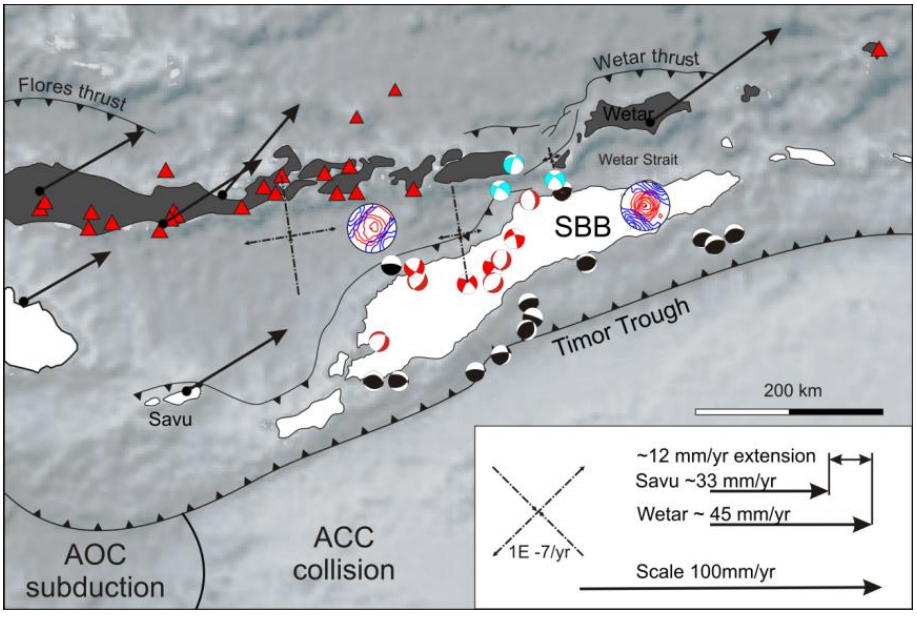

Figure 1.15: Summary of GPS and seismicity data for the Timor region arc and forearc. Heavy black arrows show global GPS velocities relative to ITRF 2000 (Nugroho et al. 2009), which increase eastward due to coupling. Fine dotted arrows show extensional strain fields developed by Bock et al. (2003), which increase westward. Global CMT catalog moment tensor solutions are shown for comparison with Kamb contour plots of P (red) and T (blue) axes of fault slip measurements.

The island of Timor itself cannot presently be considered part of the forearc for coupling purposes, because the overthrust forearc is completely dismembered and is passively carried on Australian continental crust. Nevertheless, historical seismicity in West Timor (Figure 1.15) led McCaffrey (1988,1989) to conclude that orogen-parallel extension dominates deformation within the Timor collision zone. McCaffrey suggested that shortening of the upper crust is accommodated by slip on sinistral transtensional faults such as those mapped by Charlton (1991) (see Figure 1.2a), which are the focus of active diapirism and mud volcanism in West Timor(Barber et al. 1986; Harris et al. 1998). The slip data from the NW extension domain is consistent with most historical seismicity in Timor (red solutions in Figure 1.15). The consistency of the mapped structures in the Marobo Basin with modern patterns of seismicity strongly suggests that the Marobo Basin is an active graben. This is borne out by young scarp development in the modern bed of the Caiaco River.

Earthquakes in the Wetar Strait (blue solutions Figure 1.15), which occur in the vicinity of a graben imaged by Masson et al. (1991), lie within the forearc region, yet are consistent with slip data from the NE extension domain (Figure 1.3). However, faults in the NE extension domain lack historical seismicity and have subdued surface expression. At greater depths than shown here, seismicity and seismic tomography suggest that the thick buoyant continental crust resists subduction, and is either delaminating or in the process of rupturing (Ely & Sandiford 2010; Sandiford 2010; Spakman & Hall 2010; Audley-Charles 2011; Ely et al. 2011).

1.8.6 Pliocene to Recent geodynamic evolution of Timor

The structures mapped in Timor, particularly in the NE extension domain, bear a marked resemblance to structures associated with the extrusion of the European Alps (e.g. Figure 1.13) and, to a lesser extent, Tibet. They are also virtually identical to lateral escape structures formed in analogue models of the transition from subduction to collision (Boutelier et al. 2012), and are reminiscent of structures formed in the upper plate during subduction of asperities such as seamounts in both analogue models (Dominguez et al. 1998; Dominguez et al. 2000) and field examples (Pedley et al. 2010).

Each of these is an example of crustal response to indentation. The structures in the Eastern (European) Alps that are analogous to the faults in the NE extension domain lie on the foreland side of the Adriatic indenter (Figure 1.13) and are caused by extrusion off the flanks of the indenter(Ratschbacher et al. 1991a; Ratschbacher et al. 1991b). Tibetan extrusion occurs in response to the indentation of India into Eurasia (Molnar & Tapponnier 1975). However, In both the Alps and Tibet (England & Houseman 1989; Tapponnier et al. 1990; England & Molnar 1993; Taylor et al. 2003; Yin & Taylor 2011) the extrusion is post-collisional and aided by a weak

middle/lower crust and the unconfined eastern boundaries of both orogens (Pannonian Basin and South China Sea). Although extrusion in Timor appears to be syn-collisional, and the spatial and temporal scales and tectonic settings of collision and extrusion in Timor, Tibet and the European Alps are vastly different, the similarities in the geometry of faulting suggest that the underlying mechanism is similar (e.g. Yin & Taylor 2011). Based on observations presented here and interpretation of published data, the following scenario is envisaged for the geodynamic evolution of Timor Leste.

This study follows Harris (1992) and Snyder et al. (1996a) in suggesting that collisional processes initiated when a narrow outlying Timor Plateau arrived at the subduction trench and was underthrust (Figure 1.16a). The low density continental material resisted subduction and was duplexed and thickened (Figure 1.16b), which locally domed the forearc over a core of buoyant continental material (Figure 1.2b) (Snyder et al. 1996a), whilst subduction continued either side. Stretching of the domed upper plate would have caused extension of the forearc basement that was contemporaneous with the duplexing of the buoyant plateau (Figure 1.2B; Figure 1.16b). At the same time, the doming increased the coupling of the buoyant underthrust plateau with the overlying forearc, and accelerated that part of the forearc to a velocity approaching that of the Australian continent. This acted to both create an arc-parallel extension regime that was focused in the vicinity of the Marobo Basin at the western (trailing) end of the underthrust plateau.

Coupling and doming led to initial uplift of east Timor and the creation of differential topography by extension on normal faults. These include the bounding faults of the Marobo Basin, and possibly the southern basin. A similar effect may be presently occurring west of Timor, where the island of Sumba is being uplifted on normal faults above the buoyant, subducted Scott Plateau (Fortuin et al. 1997; Fleury et al. 2009). This extensional regime, rather than the unlikely hypothesis of 1 Myr of locked subduction (Keep & Haig 2010), was responsible for the preservation of gently deformed synorogenic sediments that accumulated in extensional basins. Subduction locking, had it occurred, would have been equivalent to the effect of the much larger collision between the Australian plate with the Ontong Java Plateau (Knesel et al. 2008). This is both unlikely and not recorded by high resolution dating of Australian intraplate volcanism (Cohen et al. 2011). Peri-collisional extension of the forearc also occurred at the western (trailing) end of the underthrust plateau as documented by the late Miocene Ocussi volcanics (Harris 1992). Analagous magmatic events may include Paleogene magmatism in Tibet prior to initiation of slip on the Ailao Shan-Red River shear zone (Chung et al. 1997).

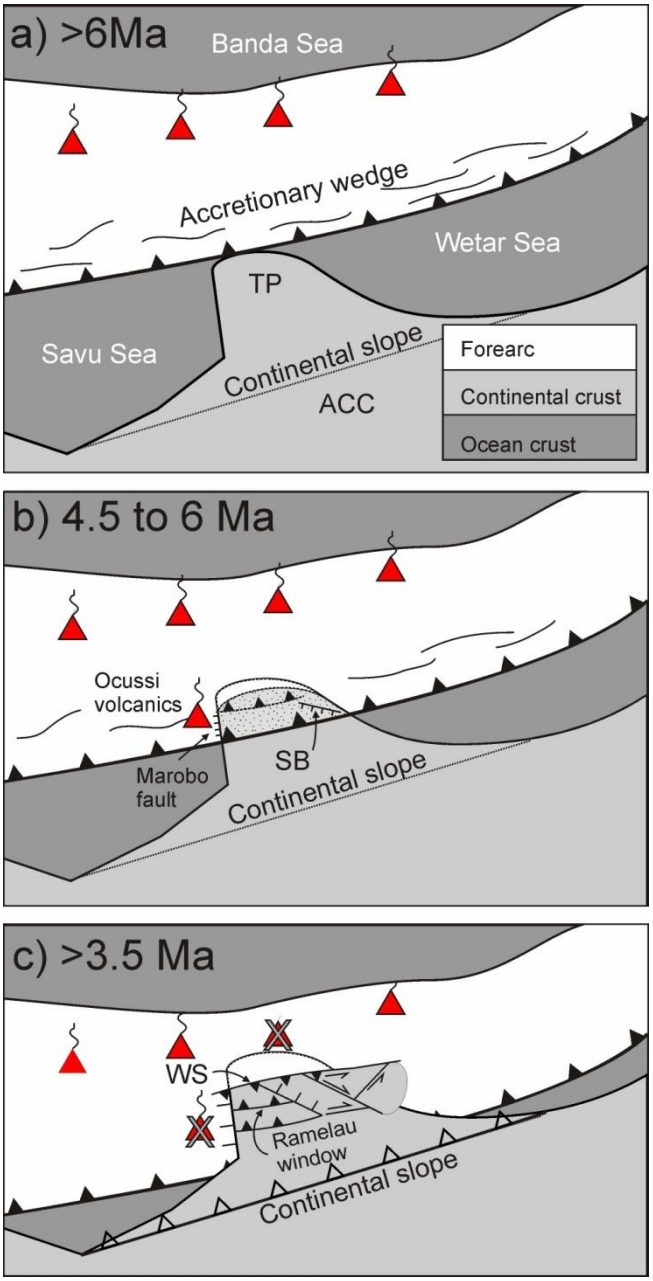

Figure 1.16. Schematic representation of the geodynamic development of Timor Leste (c.f. Harris 1992, his Fig. 3). Smoking triangles are active volcanoes. ACC - Australian Continental crust. a) The Timor Plateau arrives at the subduction trench. b) The Timor Plateau begins to be underplated (stippled) and shortened by duplexing on south-facing thrusts. The plateau resists subduction and delaminates from the continental mantle lithosphere. Extension of the duplexed plateau and overthrust forearc is initiated along the Marobo fault as the ocean crust and Timor's lower lithosphere continue to subduct. The uplifted forearc begins shedding sediment into synorogenic grabens. c) Subduction of dry continental mantle lithosphere results in cessation of volcanism on Wetar. Rebound of the buoyant, delaminated plateau and continued convergence lead to the thrusting of the duplexed plateau over the forearc along the Wetar Suture that lies north of Timor Leste. Erosion and extension of the uplifted forearc exposes the duplexed plateau in the Ramelau Arch (window). The indenting Timor Plateau extrudes eastwards over adjacent forearc basement.

Meanwhile, as the underthrust plateau resisted subduction, convergence continued and slab pull acted to subduct the oceanic lithosphere either side of the plateau, along with the delaminated, dry, lower continental crust of the plateau (Spakman & Hall 2010; Audley-Charles 2011). This

resulted in the extinction of volcanism on Wetar and Atauro, immediately north of the plateau, around 3 Ma (Abbott & Chamalaun 1981; Ely et al. 2011; Herrington et al. 2011) (Figure 1.16c). Continued convergence also back-folded the domed forearc and began to thrust the thickened plateau northward over the forearc along the Wetar Suture (Price & Audley-Charles 1983,1987) (Figure 1.2; Figure 1.16c).

The delamination and subduction of the crust below and on either side of the Timor Plateau would have had two effects. Firstly, it would have removed any lateral support for the underthrust plateau, which was already weighted down by the forearc and being compressed between the Australian continent to the south and the backfolded forearc to the north. Secondly, it would have allowed the influx of hot mantle wedge material below the Timor Plateau. The weakened plateau crust, above which the forearc was already extending, responded by extruding, perpendicular to shortening, into the free space created by coupling-related extension and by the subduction of adjoining oceanic crust. The extension is therefore focused on embayments in the colliding passive margin (e.g. Harris 1992)The extrusion of the NE extension domain created a distinctive fault pattern that is consistent with east-directed extrusion. The same pattern is seen in both a real example of east directed extrusion (the Eastern Alps, see Figure 1.13B) (Ratschbacher et al. 1991a; Frisch et al. 1998) and in analogue modeling of a collision subduction transition (Boutelier et al. 2012).

Contemporaneous extrusion of the Timor Plateau, and arc-parallel extension of the forearc, rapidly exhumed the Timor Plateau along normal faults. In this context, the Ramelau Arch of Timor is interpreted as an extensional window, bounded by normal faults and similar in many respects to the Lautern Window of the Eastern Alps (Figure 1.13b). Like the Lautern Window (Ratschbacher et al. 1991a), the highest topography in the Timor orogen is found in the Ramelau Window (Figure 1.3).

This new model for collision in Timor suggests that collision propagated both east and west from Timor Leste. This is compatible with the irregular geometry of the Australian passive margin, and with a general westwards propagation of collision. A similar scenario presently exists where the Scott Plateau creates an ‘early’ collision at Sumba (Fortuin et al. 1997) that locally propagates east to Savu and Rote (Harris et al. 2009; Roosmawati & Harris 2009) (Figure 1.1). Like the collision in Timor, this is locally counter to the regional westward propagation of the collision (Harris 1991). This study therefore serves to reinforce the practice of geologists who look to Sumba as a time-for-space analogy for Timor (e.g. Audley-Charles 1985,2004). Underthrusting of a Sumba-style point ‘indenter’ south of Wetar explains the early onset of extension, and the change in dominant obliquity sense either side of central Timor, from sinistral oblique in West Timor

(Charlton et al. 1991), to dextral oblique in eastern Timor Leste (this study). Similar but more subdued extrusion of Taiwan has been documented with GPS that has also been interpreted as being due in part to indentation (Hu et al. 2007).

Nugroho et al. (Nugroho et al. 2009) note that modern GPS relative motion vectors are consistent with the models of DeMets (1994), which suggests that they reflect long term trends. On this basis, the consistency between modern seismicity and GPS vector azimuths (Figure 1.15) is used as a guide to evaluating the timing and rates of extrusion. Wetar is strongly coupled to the Timor orogen, so although it lies in the arc it is used as a proxy for the GPS velocity of Timor. Averaged across the 575 km between Savu and Wetar, Nugroho's (2009) 12 mm/yr differential velocity between those locations (Figure 1.15) yields an extensional strain rate of 0.2 E-07/yr. This strain rate probably increases westward from Wetar, reaching rates of ~0.7 E-07/yr near the modern subduction-collision transition (Figure 1.15) (Bock et al. 2003). These modern GPS derived strain rates can account for about 11.5% (or 66km) of stretching over that distance during 5.5 Myr, which is the minimum lapsed time since the inception of orogen-parallel extension in the Marobo Basin. Of this it has been shown that approximately 20 km was localized in the NE extension domain of Timor Leste.

1.9 Conclusions

Field mapping and kinematic analysis indicates that Timor Leste is extending parallel to the arc by slip on non-Andersonian conjugate transtensional faults. Extension of the Timor arc-continent collision is interpreted to have resulted from collision of an outlying plateau that arrived south of Wetar and was bounded by ocean crust to both west and east. Data from the Marobo Basin show that the onset of extension was rapid and involved both the upper and lower plate. Data from eastern Timor Leste show that extension there was parallel to the arc and accommodated by general shear on conjugate strike slip faults. This study proposes that doming of the forearc above the thickened, buoyant, underplated continental plateau locally increased the coupling of the arc and caused arc-parallel extension in the upper plate. Continued shortening of the plateau, coupled with subduction of the plateau's bounding oceanic crust, caused extrusion of the plateau towards its unconstrained margins. The extrusion episode is recorded by intersecting, opposite-sense Riedel shears, such as the Lacluta and Mata Bia faults, that dip towards the major arc-parallel Laclo and Viqueque strike slip faults. The extrusion in Timor is of a similar style to extrusion documented at much larger scales in the European Alps and Tibet. It is also consistent with analogue models of the transition from subduction to arc-continent collision (Keep 2000; Boutelier et al. 2012) and with theoretical and analogue models of extrusion (Yin & Taylor 2011).

Many modern island arc-continent collisions, including Taiwan and Timor, are diachronous along the length of the orogen (e.g. Suppe 1984; Harris 1991; Roosmawati & Harris 2009). This gives rise to the concept of space-time equivalence (Suppe 1984), in which the history of development of older parts of the orogen is inferred by examining along strike analogues. This assumes a regular progression and neglects short wavelength variability in the geometry of the colliding margin. This study has shown that the detailed pre-collisional crustal geometry of the lower plate (e.g., indenter presence and shape) exerts an important influence on the structural evolution of both upper and lower plate crust during collision. Models of the subduction-collision transition (e.g. Keep 2000; Boutelier et al. 2012) are therefore applicable, not only to the regional diachronicity of collision, but also to local irregularities in the margin that create a series of indenters bounded by small areas of oceanic crust.

CHAPTER 2. SEDIMENTARY RESPONSE TO COLLISION AND EXTRUSION IN TIMOR LESTE

2.1 Abstract

The island of Timor is the product of collision between the Australian continent and the Banda Arc but the timing and nature of that collision are controversial. New sedimentological , geochemical and Nd isotope data from three basins including two widely-separated, well-dated sections of the Synorogenic Megasequence of Timor Leste improve constraints on the timing and effects of arc-continent collision in the Timor sector of the Banda Arc. The carbonate sediments accumulated in grabens such as the Marobo graben that formed due to simultaneous crustal shortening and extensional exhumation. Increasing muddy sediment flux at the base of the sections indicates that the island of Timor was emergent and shedding terrigenous sediment into carbonate basins prior to 4.5 Ma. Uplift was rapid and created an extreme relief that resulted in an abundant supply of coarse detritus to synorogenic basins. The basins containing the sections were filled by debris flow dominated sediment transport processes. In the westernmost Marobo Basin, a lack of organic debris suggests that the shoreline was steep and the shelf narrow to non-existent. In contrast, the easternmost Viqueque Basin was filled by debris flows derived from collapse of a gravelly delta that entrained fringing reefs and mangrove swamps and deposited them in deep sea debrites. The Laleia gravelly delta basin provides an example of a source area for the Viqueque deposits. Clastic sedimentation began at 3.5 Ma in the Marobo Basin of central Timor, ~0.5 Ma earlier than in the Viqueque Basin in eastern Timor, and 1 Ma earlier than in the Central basin of West Timor, which is consistent with early collision of an outlying plateau in the central part of Timor.

2.2 Introduction

Arc-continent collisions are inherently unique and display a large degree of variability in their collisional parameters including structure, composition and behavior of both the upper and lower plates (e.g. Afonso & Zlotnik 2011; Brown et al. 2011; Harris 2011). Erosion of the arc-continent collision supplies sediments to synorogenic basins. The structural context and lithology of synorogenic basins can therefore be expected to provide information on their depositional setting (Hong 1997; Bayona et al. 2011), and the sediments themselves provide a petrographic and geochemical record of the evolution of their source (Vroon et al. 1995; Dewey & Mange 2000; Clift et al. 2004). Analysis of the depositional setting and detailed provenance of well-dated sections in a young orogen, where the source and sediment are still contiguous, should therefore provide insights into the rates and processes of early orogenesis, including the timing of tectonic phases (De Smet et al. 1990), along strike lithological variability (Floyd et al. 1990) and erosional unroofing (DeCelles et al. 1998). These are fundamentally important inputs for constraining the tectonic evolution and paleogeography of an arc-continent collision.

The Australian continental shelf presently travels NNE at ~ 70 mm yr-1 relative to the Sunda Shelf (Genrich et al. 1996; Kreemer et al. 2000; Bock et al. 2003) (Figure 2.1A). Subduction north of Australia led to development of the Banda volcanic arc north of Timor since 12 Ma (Abbott and Chamalaun, 1981), as the greater Indonesian Arc propagated across the Banda embayment that separates NW Australia and the Sula Spur of Papua New Guinea (Spakman & Hall 2010). The Australian continental slope has now reached the subduction zone and begun colliding with the Banda Arc in the Timor region. The island of Timor in the outer southern Banda Arc (Figure 2.1A) presently comprises Australian basement and passive margin rocks, tectonically overlain by Banda forearc basement (Figure 2.1B & C). The plate boundary is presently in the process of transferring to the backarc Wetar Thrust (Silver et al. 1983; Breen et al. 1989; Genrich et al. 1996; Nugroho et al. 2009). The oblique geometry of the collision results in an overall regional westward propagation of the collision at ~100 km Myr-1 (Harris 1991).

The tectonic history of Timor is strongly debated including the timing, rates and structural style of key phases of the collision (Keep & Haig 2010; Audley-Charles 2011; Harris 2011). The collision initiated sometime prior to 3.4Ma in West Timor (Audley-Charles 1986a) and has been suggested to have occurred as late as >8Ma (Keep & Haig 2010). Duffy ((accepted manuscript) – see previous chapter) proposed that underthrusting of a continental plateau beneath Timor Leste led to upwarping of the forearc basement and extrusion and extensional exhumation of the underthrust plateau. Thus only remnants of the exhumed forearc basement are preserved, whilst several kilometers of its thickness has been eroded away and incorporated in the sedimentary fill of synorogenic basins. Some of these sediments have been exhumed and are widely exposed in the major synorogenic basins of Timor (Audley-Charles 1968; Kenyon 1974) (Figure 2.1B), where they can be expected to preserve a record of the collisonal evolution of Timor.

This study therefore examines the lithostratigraphy and provenance, including petrography and geochemical stratigraphy, of a carbonate, marl and siliciclastic coarsening up succession in three synorogenic basins in Timor Leste (Figure 2.1B). The biostratigraphy of two basins is well constrained (Haig & McCartain 2007; Bakker 2011; Haig 2012), which facilitates the dating of lithostratigraphic changes and evolutionary trends. The data are compared with equivalent units located westwards along the strike of the orogen, in West Timor and at the DSDP 262 drill site in the Timor Trough to provide a temporal perspective on the evolution of the Timor arc-continent collision zone.

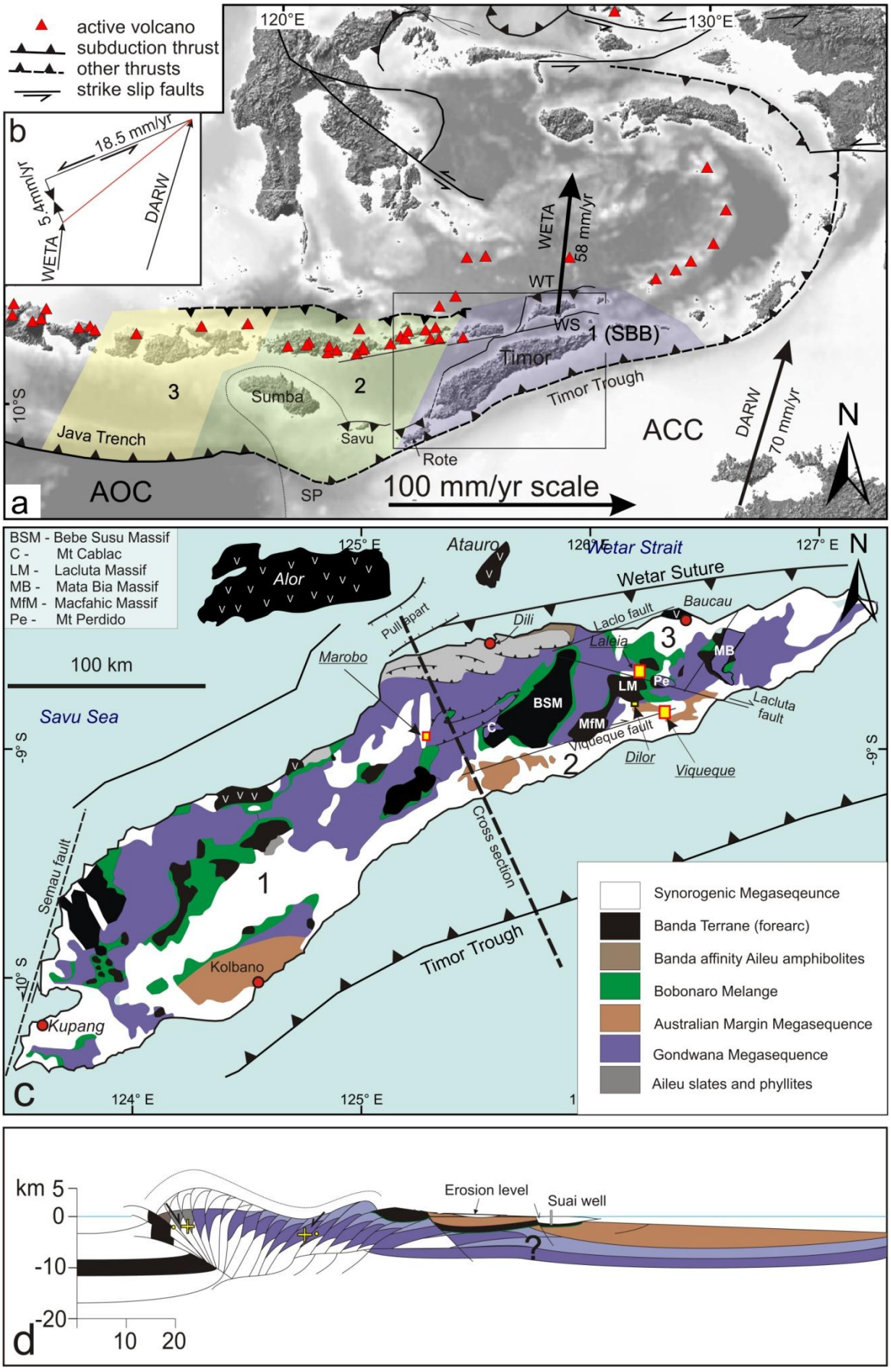
active volcano
subduction thrust
other thrusts
strike slip faults
120°E
130°E
b
18.5 mm/yr
5.4mm/yr
DARW
WETA
WETA
58 mm/yr
WT
WS
1 (SBB)
Timor
Timor Trough
3
Sumba
2
10°S
Java Trench
Savu
Rote
ACC
DARW
70 mm/yr
N
a
AOC
SP
100 mm/yr scale
BSM - Bebe Susu Massif
C - Mt Cablac
LM - Lacluta Massif
MB - Mata Bia Massif
MfM - Macfahic Massif
Pe - Mt Perdido
125° E
Atauro
Wetar Strait
127° E
N
Alor
Wetar Suture
Baucau
Pull Apart
Dili
Laclo fault
Laleia
3
MB
Marobo
LM
Pe
100 km
BSM
Lacluta fault
Savu Sea
C
MfM
Viqueque fault
-9° S
Dilor
Viqueque
2
Cross section
Semau fault
1
Timor Trough
Kolbano
-10° S
Kupang
c
124° E
125° E
Synorogenic Megaseqeunce
Banda Terrane (forearc)
Banda affinity Aileu amphibolites
Bobonaro Melange
Australian Margin Megasequence
Gondwana Megasequence
Aileu slates and phyllites
km 5
0
-10
-20
10
20
Erosion level
Suai well
?
d

Figure 2.1: (Previous page) Regional and local tectonics of Timor. A) Plate boundary elements. Faults follow Hinschberger et al. (2005), modified after Rigg and Hall (2012) and Watkinson et al. (2011). GPS plate motion vectors shown relative to the Sunda Shelf: WETA – Wetar (after Genrich et al, 1996); DARW – Darwin (after Nugroho et al. 2009). Coupling zones (after Nugroho et al. 2009) range from 1 (maximum coupling – South Banda Block - SBB) to 3 (minimum coupling - eastern Java Trench). WT – Wetar Thrust; WS - Wetar Suture; ACC – Australian continental crust; AOC – Australian ocean crust; SP - Scott Plateau. B). The ~ 20 mm of differential movement between Darwin and Wetar resolves into trough-normal shortening (~5.4 mm/yr) and trough-parallel left-lateral shear components (~18.5 mm/yr). B) Geological sketch map of Timor, modified after Harris (2006) and showing terrane distribution. Three main synorogenic basins are the Central basin of West Timor (1) and the Southern (2) and NE basins (3) of Timor Leste. Yellow boxes show study areas (Viqueque, Laleia, Marobo). C) Cross section through the highest topography of central Timor, modified after Harris et al. (Harris et al. 2000).

2.2.1 Tectonostratigraphic framework of Timor

The island of Timor comprises two separate nations. The name Timor is therefore used here to refer to the island landmass, whilst the political names West Timor and Timor Leste are used to refer to the western (Indonesian) and eastern (independent Timorese) parts of the island. This political subdivision is both convenient and geologically relevant.

The tectonostratigraphy of Timor has been the subject of considerable research efforts, which are summarized by Audley-Charles (1968) and Sawyer et al. (1993) and slightly modified and simplified by Haig and co-workers (Haig et al. 2007; Haig et al. 2008; Benincasa et al. 2012). Essentially, five subdivisions are recognized (Haig et al. 2007); the Australian-affinity Gondwana Megasequence and Australian Margin Megasequence; the Synorogenic Mélange; the Banda Terrane and the Synorogenic Megasequence (Figure 2.2).

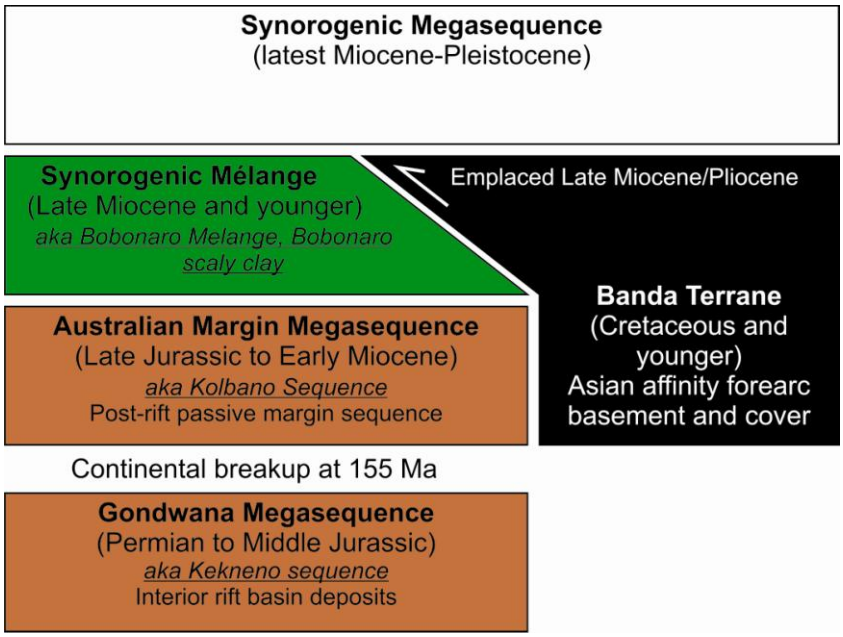

Figure 2.2: Tectonostratigraphic divisions of Timor (based on Haig et al. 2007).

2.2.1.1 Gondwana Megasequence

The oldest division is the Gondwana Megasequence (Haig et al. 2007), which ranges from the Permian through the Lower Jurassic. The Gondwana Megasequence, also known as the Kekneno Sequence (Simons 1940), occupies much of the northern three quarters of modern day Timor (Figure 2.1). Much of the Gondwana Megasequence was deposited in an interior rift basin on the northern margin of Gondwana during the Permian and Triassic (Metcalfe 1996; Charlton et al. 2002). The Permian succession comprises basinal mudstones, sandstones and shallow marine limestones.

Both siliciclastics and limestones are intercalated with basaltic volcanics and volcaniclastics (Charlton et al. 2002), but the limestones of the Maubisse Formation are intercalated with <500 m thickness of rift-related basalts (Gageonnet & Lemoine 1958; Audley-Charles 1968; Berry & Jenner 1982). The Maubisse Formation contains distinctive fauna and lithologies including crinoidal and fusulinid limestones, many of which are silicified (Barkham 1993; Charlton et al. 2002) in a manner that is characteristic of Paleozoic fossils (Schubert et al. 1997). The Maubisse Formation was originally interpreted as allochthonous (Brouwer 1942; Gageonnet & Lemoine 1958; Audley-Charles 1968) but subsequently found to relate laterally to age-equivalent siliciclastics (Grady & Berry 1977). Triassic lithologies include deep water shelf limestones that are contemporaneous with deltaic and turbidite successions, and with shallow water, commonly oolitic, carbonate bank limestones (Haig et al. 2008; Charlton et al. 2009). The Jurassic of Timor consists mainly of well-bedded blue marls and calcilutites that grade upwards into shales, locally surmounted by conglomerates (Audley-Charles 1968; Charlton et al. 2009). The Gondwana Megasequence is thoroughly discussed by Charlton et al. (2002; 2009).

2.2.1.2 Australian Margin Megasequence

The Australian Margin Megasequence (Haig et al. 2007), also known as the Kolbano Megasequence (Audley-Charles et al. 1979; Charlton 1989), was deposited at the outer edge of a continental terrace off the NW shelf of Australia, which formed by subsidence after continental break up at 155 Ma (Charlton 1989). The Australian Margin Megasequence is extremely fine grained. It consists of red shales, radiolarites and red, pink and white bedded cherts that pass upwards or laterally into white, extensively slumped planktic foraminiferal calcilutites that make up most of the sequence (Audley-Charles 1968; Charlton 1989; Sawyer et al. 1993).

2.2.1.3 Banda Terrane

The Asian-affinity Banda Terrane is widely distributed as klippen throughout Timor. It is a diverse unit of forearc crystalline basement and cover rocks, below which the Australian passive margin was partly subducted. It moved into a forearc position after being rifted from the Banda

Ridges during the opening of the Banda Sea (Harris 2006; Hall & Sevastjanova 2012) and is lithologically complex but similar in composition to the Banda Ridges (Honthaas et al. 1998; see Harris 2006, p. 212-220). The crystalline basement is known in Timor Leste as the Lolotoi Metamorphic Complex (Audley-Charles 1968), which is the equivalent of the Mutis Complex of West Timor (Standley & Harris 2009). The Lolotoi Metamorphic Complex is composed of regionally metamorphosed sedimentary and eruptive rocks. Common lithologies include medium pressure and temperature greenschists and amphibolite facies metabasites, quartz mica, sericite chlorite and garnet-bearing metapelitic schists and graphitic phyllites. Amphibolites and garnet bearing rocks have all been affected by retrograde metamorphism (de Roever 1940). Earle (1980) recorded a stacking relationship that, if it holds true beyond the Booi Massif of West Timor, may provide an unroofing signal. He found in order from bottom to top, polymetamorphic amphibolites and pelitic gneisses, monometamorphic gabbros and amphibolites, and serpentinite and tremolite schist.

The Lolotoi/Mutis Complex is overlain by a mixed volcaniclastic and carbonate cover sequence (the Cretaceous Palelo Group and the Late Paleocene and Eocene Metan Formation) (de Roever 1940; de Waard 1954; Audley-Charles 1968; Earle 1981; Brown & Earle 1983; Sopaheluwakan et al. 1989; Harris 2006). The base of the Palelo Group includes unusual radiolarian cherts (Earle 1983) and Standley and Harris (2009) reported an oolitic grainstone from the Palelo Group of the Bebe Susu Massif.

The Metan Formation of West Timor was correlated with the Dartollu and Barique Formation of Timor Leste (Audley-Charles 1968) by Carter et al. (1976). The Dartollu Limestone is an Eocene biocalcarenite (Audley-Charles 1968, p. 22) that includes calcareous algal and *Alveolinea* limestones. In West Timor it contains limestones with volcanic clasts and a large foraminiferal assemblage that includes the shallow tropical *Assilina*, *Pellatispira*, and *Biplanispira* genera (Rosidi et al. 1981). The Barique Formation is dominated by basic and dacitic vitric tuffs, with interbedded sandstones and lavas. Dacite lavas are common and overlie much of the Mutis Complex of West Timor (Harris 2006). The lavas are commonly altered to chlorite and carbonate. Dark greenish black, veined serpentinites are common and occasionally contain large clear crystals of olivine (Audley-Charles 1968). Diorite dikes commonly intrude the full thickness of the Banda Terrane (van West 1941; Earle 1980; Rosidi et al. 1981) .

2.2.1.4 Synorogenic Mélange

The Synorogenic Mélange (Haig et al. 2007) was previously referred to as the Sonnebait Series by the Dutch geologists (Simons 1940; Brouwer 1942; de Roever 1942) and as the Bobonaro Scaly Clay (Audley-Charles 1968). Audley-Charles (1968) and Carter et al. (1976)

interpreted the Bobonaro Scaly Clay of Timor Leste as an olistostrome but for some time now it has been recognized as a tectonic mélange, variously known as the Bobonaro or Synorogenic Mélange (Harris et al. 1998; Haig et al. 2007). The Synorogenic Mélange occurs widely around the base of the Banda Terrane nappe and is a matrix rich scaly clay unit sourced from mud-rich Australian continental margin sequences that are diapirically remobilized during accretion (Barber et al. 1986; Harris et al. 1998; Harris 2011). The Synorogenic Mélange of Timor Leste contains ~10% quartz (Audley-Charles 1965). In West Timor, the clays sourced from the Lower Jurassic to Cretaceous Australian-affinity rocks that bound the breakup unconformity, are smectite rich. Illite, kaolinite and chlorite rich clays are correlated with the Permian to Upper Triassic Gondwanan Megasequence rocks (Harris et al. 1998). The Synorogenic Mélange commonly contains blocks of both Australian and Banda affinity, although different structural associations have different block provenance (Harris et al. 1998).

2.2.1.5 Synorogenic Megasequence

The syn-collisional uplift and erosion of proto-Timor was accompanied by deposition of the Synorogenic Megasequence of Timor Leste , which is now well exposed in exhumed basins on the south side of Timor (Audley-Charles 1968; Haig et al. 2007) (Figure 2.1). In general terms, the Synorogenic Megasequence comprises a gently deformed, generally coarsening up succession that began depositing in the latest Miocene (Table 2.1). It consists of an Early-Pliocene basal chalk and marl, known as the Batu Putih Formation (Hopper 1942; Kenyon 1974), which is overlain by a clastic succession. The clastic succession is dominated by Mid to Late Pliocene deep marine sandstones and conglomerates known as the Viqueque Formation. The Batu Putih Formation and Viqueque Formation are the focus of this study. The Synorogenic Megasequence also includes Viqueque Formation age-equivalent coral debris flows (the Lari Guti Formation) and Pleistocene fan delta conglomerates and siltstones (the Dilor Conglomerate). The Synorogenic Megasequence is capped by the Baucau Limestone, a Pleistocene reef limestone that is commonly uplifted to elevations of >600 m on both sides of the Wetar Strait north of Timor (Chappell & Veeh 1978; Rosidi et al. 1981; Vita-Finzi & Hidayat 1991; Merritts et al. 1998; Cox 2009; Ely et al. 2011).

2.2.2 Synorogenic geology of Timor

The terranes of Timor have been assembled by slip on a series of décollements (Figure 2.1C). The Gondwana Megasequence is the basement of an outlying plateau (Harris 1992; Snyder et al. 1996a; Duffy et al. (accepted manuscript)) that was underthrust and duplexed below the Banda Terrane forearc basement. The Australian Margin Megasequence cover detached from the underthrust complex along a décollement that propagates along the breakup unconformity (Figure 2.1C), and was accreted to the front and top of the Banda Terrane forearc (Charlton et al. 1991;

Harris 1991; Harris et al. 2000). The Batu Putih Formation accumulated on top of the forearc and on the Australian Passive Margin sediments that had been incorporated in the accretionary wedge.

Subduction of seafloor adjacent to the underthrust plateau caused extensional exhumation of the underthrust, duplexed Gondwana Megasequence, and facilitated arc parallel extrusion of Timor along a system of oblique normal strike slip faults (previous chapter). Rapid Pliocene uplift of Timor (Nguyen et al. 2013) led to deposition of the clastic components of the Synorogenic Megasequence, overlying the carbonate Batu Putih Formation.

2.3 Lithofacies of the Synorogenic Megasequence

2.3.1 Nomenclature

The Batu Putih Formation chalks and marls were originally included in the Viqueque Formation by Audley-Charles (1968) and that practice has continued (e.g. Haig & McCartain 2007). However, the name Batu Putih Formation is widely used throughout West Timor, Savu and Rote in the Banda Arc (Harris et al. 2009; Roosmawati & Harris 2009). For the sake of consistency, this study adopts the name Batu Putih Formation for the basal chalks and marls of the Viqueque Formation, and restricts use of the name "Viqueque Formation" to the marine clastic detrital sediments that overlie the Batu Putih Formation.

The Viqueque Formation of Timor Leste thus defined is referred to as the Noele Marls in West Timor (Kenyon 1974, p. 143). However, the name Viqueque Formation is retained in Timor Leste because the Noele Marls is a lithostratigraphic unit that is defined as grey marls and subordinate sandstones, a description that is unfitting for the succession in Timor Leste. This study will continue to use the term Viqueque Formation and, where appropriate, relate facies within the clastic sediments to similar facies within the Noele Marls. The synorogenic nomenclature of Timor preferred in this study, along with other modern and historical usages, and possible confusions are summarized in Table 2.1.

Table 2.1: Synorogenic litho-stratigraphic nomenclature of Timor Leste and West Timor equivalents

Sequence name (defined by)	Formation name (defined by)	Rock types	Age	Facies	Notes / synonyms	West Timor Equivalent (defined by)
Synorogenic Megasequence (Haig et al. 2007)		Mildly deformed coarsening up succession deposited during Pliocene-Pleistocene emergence of the Timor landmass	Late Miocene to Pleistocene	Synorogenic	Historically referred to as the Autochthon (Audley-Charles 1968); Plio-Pleistocene series (Grunau 1953); Viqueque Series (Grunau 1956). Viqueque Formation (Sawyer et al. 1993); Named the Synorogenic Megasequence by Haig (2007) but subsequently referred to by Haig and McCartain (2007) as the Synorogenic Viqueque Megasequence, and by Quigley et al. (2012a) as the Viqueque Megasequence; Alternatively referred to as the Banda Orogen Sequence by Harris (2011)	Viqueque Group (Kenyon 1974)
	Ainaro Gravels (Audley-Charles 1968)			Alluvial gravels and fan deposits		Noilbesi Conglomerate (Kenyon 1974)
	Baucau Limestone (Audley-Charles 1968)		Pleistocene	Reef	Uplifted Pleistocene coral reefs of Baucau Limestone and equivalents are found throughout much of Timor and on the volcanic islands of the Banda Arc north of Timor (Chappell & Veeh 1978; Jouannic et al. 1988; Hantoro et al. 1994; Merritts et al. 1998; Cox 2009; Roosmawati & Harris 2009; Ely et al. 2011)	Soe Limestone (Kenyon 1974)
	Dilor Conglomerate (Audley-Charles 1968)	Cross-bedded conglomerate, silt and sand	Pleistocene	Fan delta	Kenyon (1974) compared it to the Noilbesi conglomerate of West Timor, although that unit appears to be non-marine (see Ainaro gravels). Similar but younger fan delta conglomerates interfinger with the Baucau Limestone east of Baucau on the north coast of Timor, where they are included with the Baucau Limestone by Audley-Charles 1968. They were referred to as Ainaro Gravels by Kenyon (1974) but are unequivocally marine (Mills 2011).	Possibly Obernaik member of the Noele Marls (Kenyon 1974, p. 135)
	Lari Guti Limestone (Audley-Charles 1968)	Coral detritus in cut and fill channels eroded into foraminiferal packstone (Benincasa et al. 2012)	Latest Pliocene to Early-Pleistocene (N22) (Keep & Haig 2010; Benincasa et al. 2012)	Channels at 500-1000 m (Benincasa et al. 2012)	Considered as a member of the Viqueque Formation by Benincasa (2012) due to age equivalence to Viqueque Formation. However it is of contrasting lithology, mappable extent and is not seen in contact with Viqueque Formation clastic sediments, so it is regarded here as a separate formation	Grouped with the Saboe Limestone by Kenyon (1974)
	Viqueque Formation (Audley-Charles 1968)	Interbedded Conglomerates, sandstones and mudstones		Mid-bathyal (Haig & McCartain 2007)	Redefined here to specifically exclude the basal Batu Putih Formation, in line with the Noele Marls of West Timor (Kenyon 1974). The term Samé Member was used by Kenyon (1974) to refer to all the Pliocene clastic sediments in the southern basin of Timor Leste. The name Viqueque Formation was also used by Sawyer (1993) to refer to the entire Synorogenic Megasequence.	Noele Marls (Kenyon 1974)
	Batu Putih Formation named by Hopper (1942) and formally adopted by Kenyon (1974).	White chalky calcilutites grading up to marls (Interbedded vitric tuffs reported but not observed in this study)	Latest Miocene to Early-Pliocene	Mid-bathyal open water limestone and marls (Haig & McCartain 2007; Haig 2012)	The name Batu Putih Formation is used throughout the Banda orogen (De Smet et al. 1990; Harris et al. 2009; Roosmawati & Harris 2009) and is preferred here for the basal chalks and marls of the Viqueque Formation	Batu Putih Formation (Hopper 1942; Kenyon 1974)

2.3.2 Methods

Lithofacies analysis of exhumed and core sediments underpins our understanding the geometry and depositional environment of sedimentary basins (Mutti 1985; Shanmugam & Moiola 1988; Reading & Richards 1994; Shanmugam 1997; Galloway 1998; Shanmugam 2000; Mulder et al. 2003), and provides potential to interpret the relative contribution of underlying processes such as erosion and tectonic uplift (e.g. Burbank 1992). Following an initial reconnaissance, several stratigraphic sections were measured, and lithological variations recorded in detail. These sections were all measured using a clinometer and abney level, supplemented by a meter stick. Thicknesses were not rounded and beds as small as 3 cm were measured. These sections provide a stratigraphic context for lithofacies analysis.

Samples were collected of both sandstone and mudstone intervals and their locations recorded on the stratigraphic column. Mudstone samples of the Caiaco River section were analyzed for foraminiferal content and biostratigraphy by Douwe van Hinsbergen and Bakker (2011). The Viqueque section had previously been measured by Haig and McCartain (2007), so my stratigraphic column was correlated with theirs. Time was limited but one clast count of 300 clasts was made at a conglomerate at the top of the Northern Cuha section in Viqueque.

Paleocurrents were measured where possible using a Suunto compass with the regionally appropriate declination. Most paleocurrents are measured from the foresets of cross bedding or ripple cross laminae. In one instance, a paleoslope was determined from the axial trace of a slump fold in the Marobo Basin. Most beds are gently dipping so no rotation was applied.

2.3.3 Lithologies

Stratigraphic sections were measured and described in three basins. In each basin, the Synorogenic Megasequence consisted of basal carbonates and marls of the Batu Putih Formation, overlain by clastic sediments. The following account provides a brief unified description of the Batu Putih Formation from all three basins. The Viqueque Formation, however, is described by basin, because it is highly variable in localized sub-basins.

2.3.3.1 The Batu Putih Formation

The Batu Putih Formation (Figure 2.3) was mapped in all 3 basins (Figure 2.1B). It is underlain in the Marobo and Viqueque Basins by Synorogenic Mélange. The mélange is widely exposed around Viqueque where it contains exotic blocks including pillow basalts, analcitized basalts, brittle radiolarites and interbedded light pink, red and white cherts. The radiolarites and cherts are similar to lithologies described from the Nakfunu and Menu Formations of the Australian Margin (Kolbano) Megasequence of West Timor (Sawyer et al. 1993), and from the

Cretaceous Wai Bua Formation of the Australian Margin Megasequence of Timor Leste (Audley-Charles 1968, p. 16). Structural mapping has shown that the mélange locally diapirically intrudes the Batu Putih and Viqueque Formations.

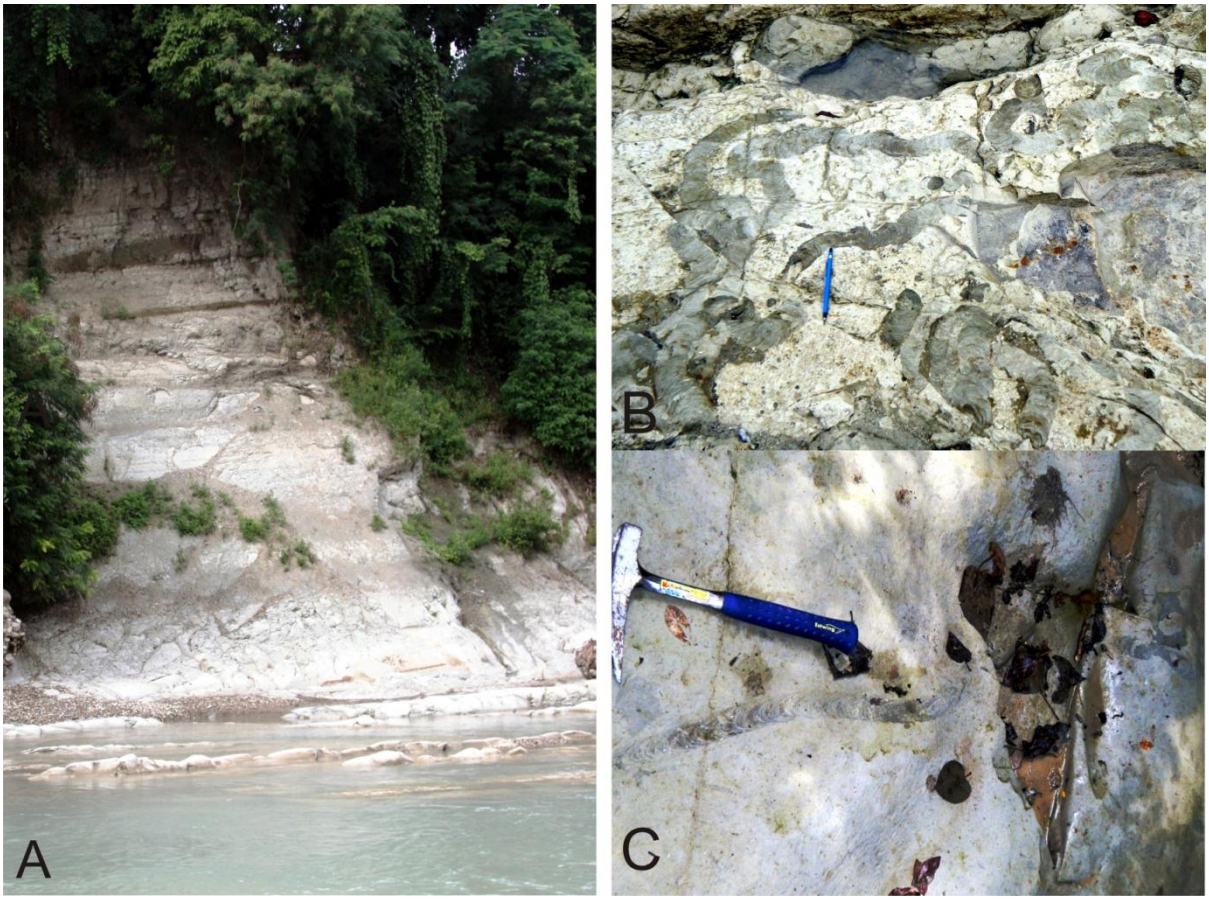

Figure 2.3: Bedding in the Batu Putih Formation in the Viqueque Basin, immediately below the Viqueque Formation type section in the Cuha River. B and C show trace fossils in the Batu Putih Formation at Laleia and Viqueque Basins respectively.

Coherent sections of the Batu Putih Formation were measured in the Caiaco River of the Marobo Basin and the Cuha River of the Viqueque Basin (Figure 2.1B). In each instance, the base of the section consists of less than 2 m of massive, creamy, chalky foraminiferal limestone. This basal limestone incorporates mélange clasts in its lowest few centimeters. Induration of the limestone varies between basins and is greatest in the Marobo Basin and least in the Viqueque Basin.

The basal limestone grades into >40 m of soft, light grey to blue foraminiferal marls (Figure 2.3A). Bedding in the chalk and marls is generally massive and indistinct, but becomes more distinct upsection (Figure 2.3A). A well bedded interval, containing dark mica crystals that weather to produce iron-stained halos, is present in both the northern Cuha and Type sections (Figure 2.12 1). Audley-Charles (1968) reported the presence of two vitric tuff beds in the marls of

the type section, but these were not observed. The marls thicken northwards in the Viqueque area from ~40 m at the type section to ~100 m at the Northern Cuha section (Figure 2.12 1).

The marls in all basins contain abundant feeding-trail trace fossils. The traces comprise tightly meandering to straight trails of oval to semi-circular meniscae, picked out by a concentrations of darker sediment and bounded by parallel sediment strings (Figure 2.3B and C). These characteristics are diagnostic of ichnogenus *Scolicia* (Uchman 1995), which are made by irregular echinoids.

2.3.3.2 The Viqueque Formation

As indicated in Table 2.1, the Viqueque Formation is limited here to the clastic detritus and specifically excludes the underlying carbonates and marls of the Batu Putih Formation dealt with above. Numbered lithofacies are presented in tabulated form for each basin. The first letter of the facies number indicates the basin, and the facies are numbered in order of decreasing grainsize (e.g. Mc2 = Marobo, conglomerate, 2nd coarsest; Vs3 = Viqueque, sandstone, 3rd coarsest). This numbering system is used throughout this section.

Marobo Basin

Lithologies

A single section was logged in the Marobo Basin and mapping was only carried out along the section. The section location is shown in Figure 2.4 and the measured section in Figure 2.5. The lithofacies of clastic sedimentary rocks logged within the section are summarized in Table 2.2.

The Marobo Basin fill consists of a variable succession of southwest to south-dipping conglomerates, pebbly sandstones, sandstones and mudstones (Table 2.2). The paleoflow directions measured in the section indicate that these sediments were emplaced towards the south and southwest (Figure 2.4; Figure 2.5).

The coarsest beds in the Marobo section are poorly sorted pebble to boulder conglomerates (Mc1,Table 2.2; Figure 2.6A & C). Mc1 facies are generally clast supported, inversely graded at their bases and change to normal grading upwards. They are mostly 2 to 3 m thick, although they can locally range up to 20 m thickness. The thicker Mc1 conglomerates have planar bases and are laterally continuous within the area studied. Thinner Mc1 beds are commonly channelized at the base. They are normally graded above the base, become more matrix supported upwards and contain floating intraclasts of up to 2 m diameter.

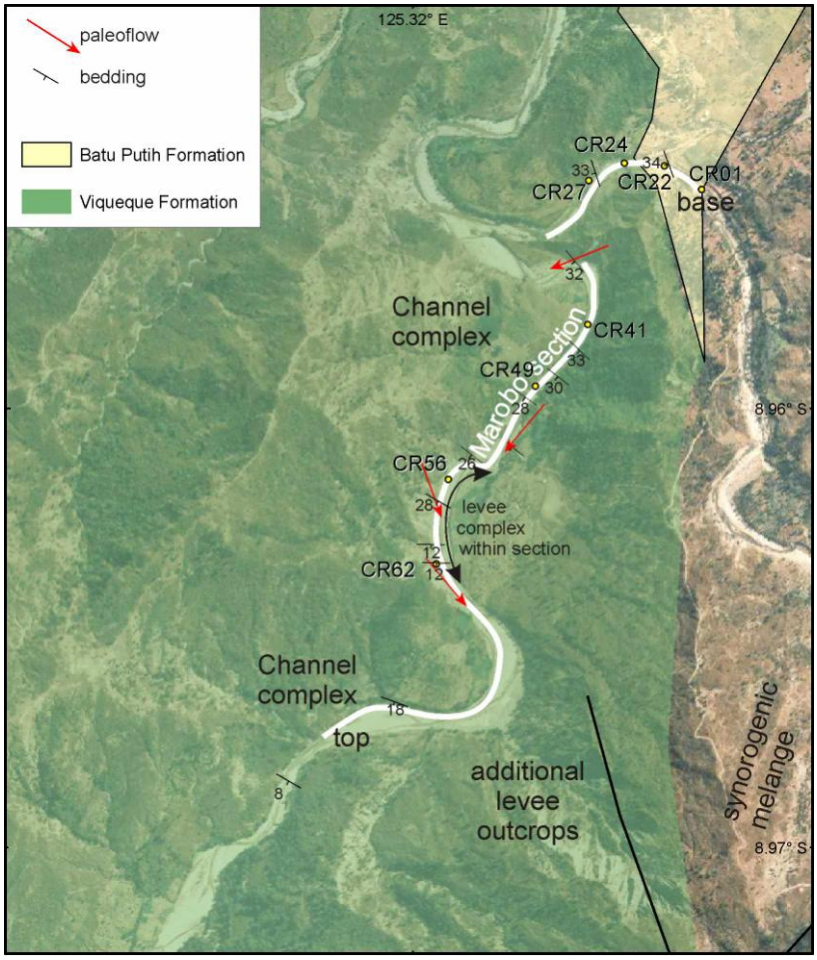

Figure 2.4: Reconnaissance scale only map showing the location of the Marobo Basin measured section (white line). For location see Figure 2.1.

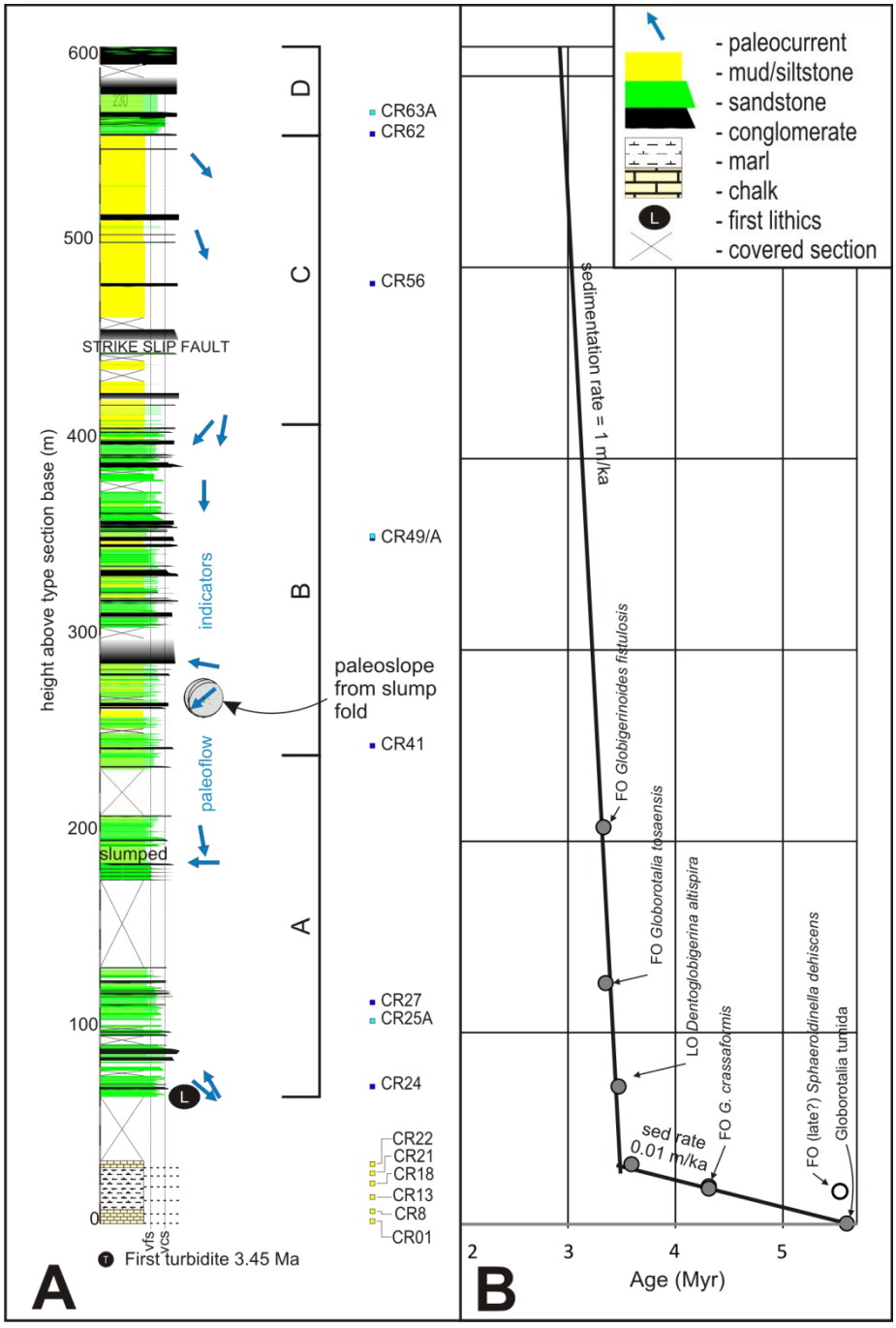

Figure 2.5: Summary stratigraphic column (A) and age model (B) for the Caiaco River section in the Marobo Basin. Age model based on data provided by Douwe van Hinsbergen. For a detailed stratigraphic column see Appendix 1.

Table 2.2: Lithofacies of the Marobo Basin

Facies	Lithology	Grain size	Textural features	Thickness	Sedimentary structures	Interpretation
Mc1	Thick bedded coarse conglomerate (Figure 2.6A)	Pebble to boulder	Clast supported, poorly sorted, crudely rounded to angular	Mostly <5 m, one example >20 m	Planar base. Locally inverse graded at base grading up to sandy matrix supported. Floating intrabasinal clasts up to 2 m diameter. Commonly channelized.	R2 and R3 gravels (Lowe 1982), deposited by cohesionless hyper-concentrated density flow (e.g. Mulder & Alexander 2001) in a channel complex.
Mc2	Disorganized conglomerate with basal sand injection (Figure 2.6C)	Pebble to boulder	v. poorly sorted, angular	<3 m	Inverse graded at base, disorganized above. Common coarse sand to granule injection at base and entrainment of broken stratigraphy.	Clastic injection and block transport suggests slide (Shanmugam 2006, p. 50)
Mc3	Medium bedded conglomerate (Figure 2.6B)	Granule to pebble	Clast supported poorly sorted granule to pebble	0.5-1.5 m	Load casted base. Graded, floating clasts. Commonly grades up to Ms.	High density turbidity current in a channel complex (S1 - Lowe 1982). See also Tripsanas (2008) facies association 7
Mc4	Stratified sandy gravel and pebbly sandstone	Coarse sand to cobble	Very poorly sorted, rounded to subangular. Upper levels contain bivalve and woody detritus	~0.03-1 m	Locally cross bedded or planar stratification. Occasionally imbricated. Overall normally graded but with layers of pebbles highlighting stratification in the pebbly sandstone. The pebbly sandstone subfacies appears transitional between the stratified sandy gravel and the sandstones of the Ms class.	S1 or S2 traction carpet (Lowe 1982). See also Pickering et al. (1989, facies A2.5 to A2.8) and Hein and Walker (1982).
Ms1	Medium bedded sandstones	Coarse to medium sand	moderately sorted subangular	0.1-0.5 m	The thicker sandstones have a massive to graded base with occasional cross bedding. Grading commonly follows an initial massive interval. They typically grade up to laminated sandstones (T b) and less commonly rippled and upper laminated intervals (T b –d) (Figure 2.7C). This facies almost always contains rip-up clasts.	Sandy debris flows (Shanmugam 2006), grading into turbidites Ta-d (Bouma 1962)
Ms2	Thin-bedded sandstone and siltstone	Silt to medium sand	Well sorted		Thinner sandstones typically occur as multiple thin packages of bioturbated, normally graded, climbing ripple cross laminated, medium sand, often containing intraclasts and interbedded with laminated fine sandstones, siltstones and occasionally mudstones. The siltstones are sometimes extremely contorted.	Channel leveé CCC turbidites (e.g. Walker 1985; Fergusson et al. 1989; Posamentier & Walker 2006, their Fig.8)
Mm1	Massive mudstone	Silty mud with occasional very fine sand and silt interbeds	Upper levels contain abundant foraminifera		Structureless to subtly graded, indistinctly laminated at base, otherwise bedding typically absent	Turbiditic and hemipelagic mud (Kneller 1995; Shanmugam 1997,2000; Posamentier & Walker 2006)
Mm2	Pebbly mudstone	Dominantly mud.	Chaotic, poorly sorted	<3 m	Folded and sheared/distorted, chaotic with truncations and isoclinal ptygmatic folding of sandstone beds (Figure 2.7)	Sediment slumps and cohesive debris flows (Shanmugam 2006; Di Celma 2011)

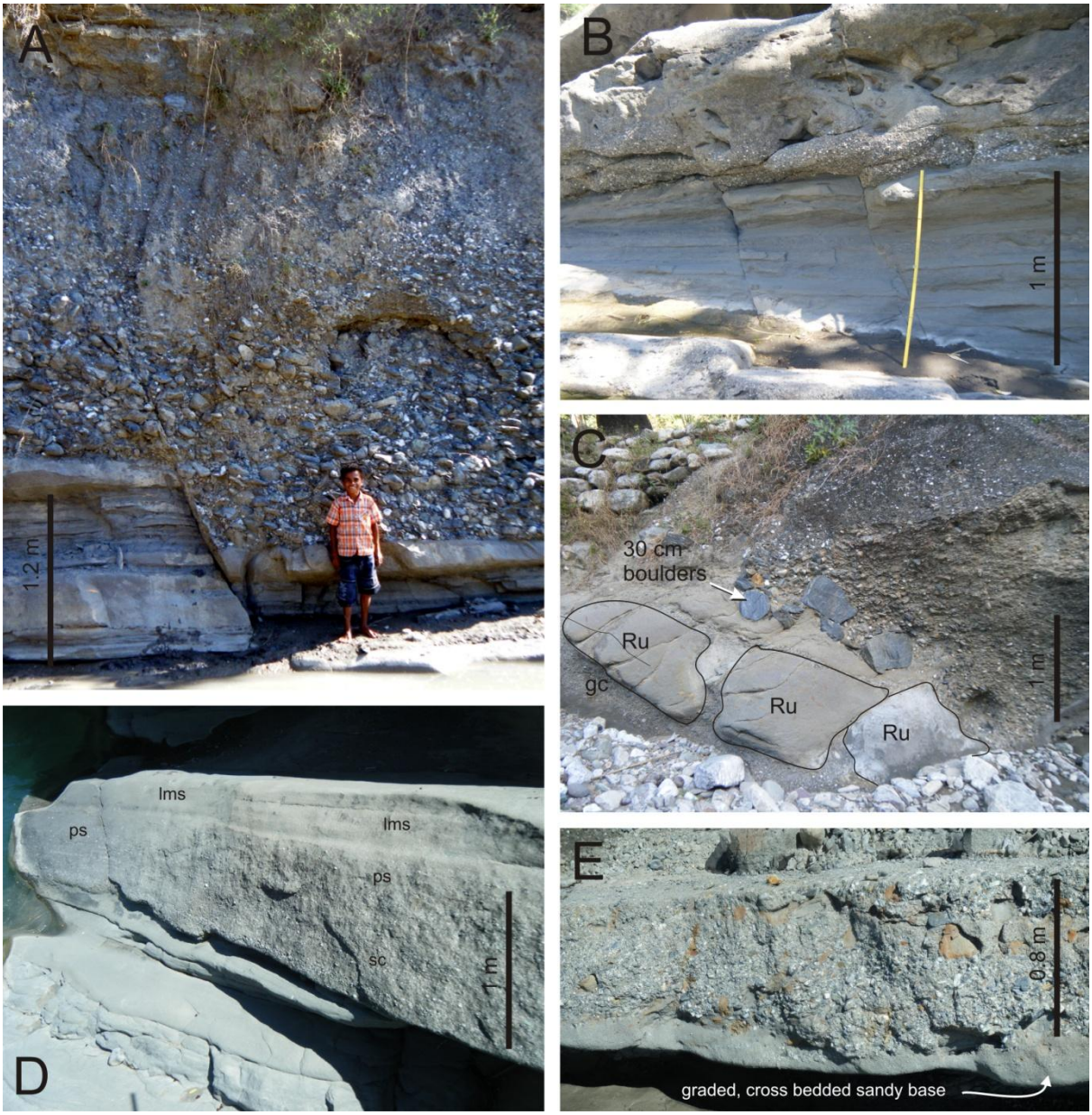

Figure 2.6: Conglomerates from the Marobo Basin. A) Mc1 – Thick bedded, clast supported, coarse cobble conglomerate grading up to sandy matrix supported pebble conglomerate. B) Mc3 – Medium bedded, graded, rounded pebble conglomerate. Holes in outcrop are sockets left by preferential erosion of floating rip up clasts. C) Mc2 – Angular, clast supported disorganized conglomerate, sometimes with rip up clasts at the base. Ripup clasts are broken and encased in a coarse sand to granule matrix (gc) that is part of the conglomerate. D) Mc4 – stratified sandy conglomerate (sc) grading laterally and vertically into laminated pebbly sandstone (ps) and laminated medium sand (lms). E) Mc5 – Cross bedded conglomerate.

Mc2 conglomerates are also clast supported, 2 to 3 m thick and inversely graded at their bases. However, Mc2 conglomerates have large blocks of underlying stratigraphy entrained at their base and are completely disorganized with no evidence of normal grading upwards. The basal blocks of Mc2 are dilated and encased in coarse sand to granules that were injected from the base of the conglomerate (Figure 2.6C). Other beds are frozen in the act of peeling the underlying stratigraphy (Figure 2.7A & B).

The Mc3 granule to pebble conglomerates (Table 2.2) are clast supported at their base, grade up to become matrix supported and generally contain floating intraclasts. However, they are more thinly bedded than Mc1 conglomerates, have load casted bases and usually grade upwards abruptly into coarse sandstones (Figure 2.6B).

The poorly sorted, crudely stratified sandy conglomerate and pebbly sandstones (Mc4,Table 2.2) are the most lithologically diverse facies in the Marobo Basin. These units typically have load structures at their base. Both planar and cross-bedded stratification were observed (Figure 2.6D & E), along with occasional subtle imbrication. Planar stratified beds rarely contain intraclasts, whereas they are commonly present in cross-bedded pebbly sandstones (Figure 2.6D & E). In several instances, planar stratified sandy gravels can be seen to grade both laterally and upwards into laminated pebbly sandstones and laminated medium sandstone (Figure 2.6D), indicating an overall normal grading. The laminae in the pebbly sandstones are picked out by stringers of granules and pebbles. Lateral gradation indicates a fining to the southwest, which is consistent with paleocurrent directions (Figure 2.4; Figure 2.5). Pebbly sandstones are thinnest at the top of the section, where they occur as laminated horizons of 3-5 cm thickness, interbedded with thinly-bedded medium sandstone of facies Ms2 (Table 2.2; Figure 2.8C).

Medium bedded coarse to medium sandstones (Ms1,Table 2.2) are common throughout the section. They commonly form the gradational tops of Mc3 and Mc4 facies (e.g. Figure 2.6D), in which case they are typically laminated. Where the Ms1 facies occurred as discrete beds they usually comprised a basal massive coarse sandstone with a planar to load casted base. The top of the massive sandstone grades into laminated medium sandstone. The grading often begins at the top of an initial massive interval rather than being graded from the base upwards. Where the massive layer is present it commonly contains horizons of ripped up intraclasts. Ripple cross lamination is less common than planar laminations but becomes more common towards the top of the section.

Numerous packages of thinly-bedded, flame structured, ripple cross laminated, reasonably well sorted siltstones and sandstones occur in the section (Ms2,Table 2.2). These beds commonly contain mudstone intraclasts, and have climbing ripples and grade up to convolutedly-laminated siltstones.

All the lithologies listed above are commonly interbedded with massive mudstones (Mm1,Table 2.2) that are typically subtly internally graded. Foraminifera are only common in the uppermost few cm of these mudstone units.

The Mc2 bed in Figure 2.7A overlies a pebbly mudstone (Mm2, Table 2.2; Figure 2.7A). The pebbly mudstone has a chaotic structure, which is internally sheared to form a southwest-verging fabric, and contains cobbles, pebbles and discontinuous folded layers of sandstone.

Woody and organic detritus are rare throughout most of the section but become common in the thinly-laminated pebbly sandstones that occur in the top 50 m of the measured section (Level D of Figure 2.5; see Figure 2.8C).

Stratigraphy

Amongst this coarse-grained basin fill, four distinct levels are identified (Figure 2.5A). The lower part of the clastic section up to ~240 m above base (Level A of Figure 2.5A) is dominated by thinly to medium-bedded conglomerates (Mc3), laminated pebbly sandstones (Mc4) that grade both down slope and upwards into laminated sandstones (Ms1), discrete Ms1 sandstones and interbedded Mm1 mudstones.

The measured section coarsens upwards and in Level B of Figure 2.5A, the Mc3 conglomerates are progressively replaced by thicker, clast supported, inverse to normally graded, often channelized Mc1 conglomerates and occasional disorganized Mc2 conglomerates. The thickest, coarsest example of Mc1 occurs at 275 m above the base (Figure 2.5; Figure 2.6A). This part of the section also exhibits abundant sheared pebbly mudstones (Mm2), bulldozing of strata by Mc2 conglomerates and folded sandstone beds (Figure 2.7).

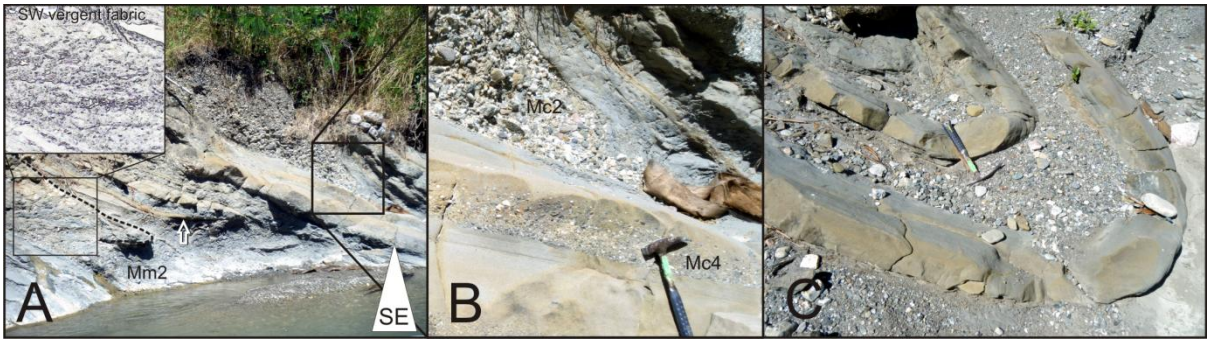

Figure 2.7: Slump structures in the Marobo Basin. A) Pebbly mudstone (Mm2) with contorted (dotted line) and truncated beds (arrow) overlain by pebbly sandstone (Mc4). Inset detail is edge enhanced image showing southwest vergent fabric in pebbly mudstone. B) Detail showing the pebbly sandstone grading up to a laminated sandstone, overlain to the right of the photo by Mm1 mudstone. An Mc2 conglomerate has partly peeled the mudstone off the top of the sandstone before freezing. C) slump folded Ms1 sandstone beds. The axis of the fold is interpreted as parallel to the strike of the paleoslope and was therefore used as a paleocurrent indicator (Figure 2.5), although other interpretations are possible (Strachan & Alsop 2006) .

At the top of Level B, the section fines up abruptly so that Level C of the Marobo section (Figure 2.5A) is dominated by thinly-bedded Ms2 sandstones that typically occur as multiple thin packages of bioturbated, normally graded, interbedded medium to fine sandstones, siltstones and

silty mudstones. Occasional thick Mc1 graded cobble to pebble conglomerates punctuate the interval.

Level D marks a return to coarse clastic sedimentation (Figure 2.5A) that laps onto and dips much less steeply than the underlying beds of Level C (Figure 2.8A). The base of Level D is dominated by stratified pebbly sandstones (Mc4) that prograde southwards across the slope formed by the top conglomerate of Level C (Figure 2.8A&B). These are overlain by and thinly interbedded with thin-bedded sandstones (Ms2) and finally overlain by a thick Mc1 conglomerate that forms the top of the measured section (although more section was logged by Bakker 2011). Although this conglomerate is very thick (apparent thickness >20 m) and is tentatively identified as Mc1, it contains numerous sandstone lenses particularly near the top. Level D contains abundant terrestrial plant detritus, along with broken and intact molluscan debris, which are noticeably absent in the underlying strata.

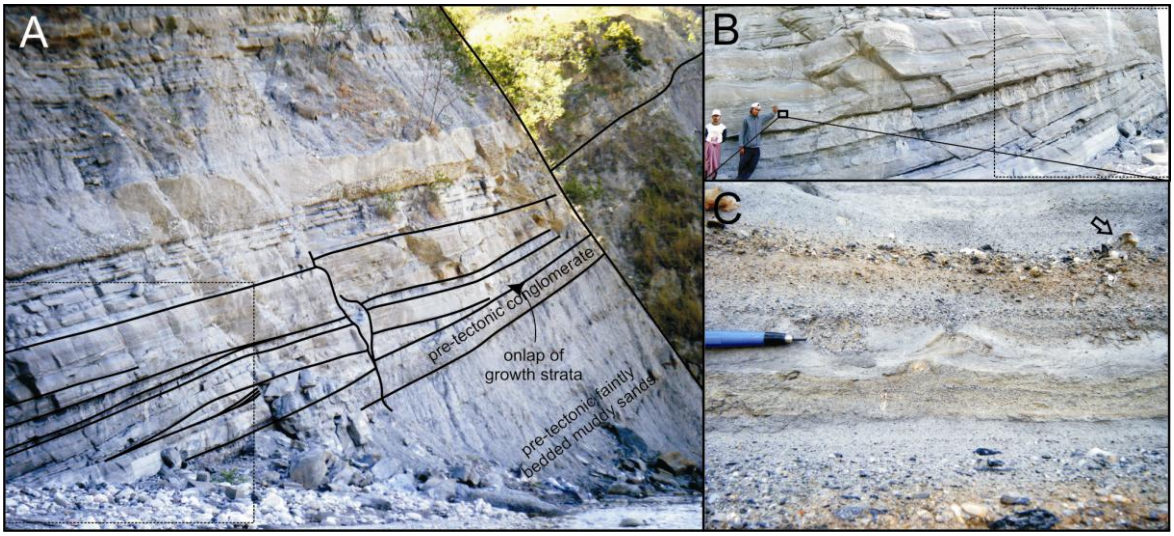

Figure 2.8: A) Contact between intervals C and D on Figure 2.5, interpreted as growth strata caused by an interval of faulting. B) Different perspective of same outcrop showing progradation of strata and the location of photograph C). Dotted rectangles in A and B show the same area. C) Detail showing flame structures in cross laminated, thinly-bedded sandstone (Ms2), intruding laminated pebbly sandstone that is rich with intact molluscs (arrow), broken shells and plant debris and overlying a stratified pebbly sandstone.

Interpretation of depositional setting

The facies associations that make up Levels A, B and D of Figure 2.5 are considered different parts of a single facies association. The commonly channelized Mc1 conglomerates that dominate level B and D are interpreted as gravels deposited by cohesionless debris flows in a channel complex on a coarse submarine fan (e.g. R2 [inverse graded] and R3 [normally graded] gravels of Lowe 1982). The sheared pebbly mudstones (Mm2), chaotically folded and truncated sandstones (Figure 2.7) and disorganized conglomerates with basal injection (Mc2) are lithofacies that are commonly associated with sediment slumps and cohesive debris flows (Shanmugam 2006;

Di Celma 2011), possibly sourced from failure of the channel margins or adjacent steep topography. The stratified sandy conglomerates and pebbly sandstones of interval A, with their crudely cross bedded or planar laminations, are typical of S1 and S2 traction carpet of high density turbidity currents (Lowe 1982; Pickering et al. 1989) and are interpreted to be relatively distal equivalents of the Mc1 conglomerates. The Ms1 sandstones and Mm1 mudstones represent the products of T_{a-d} sandy and T_e muddy turbidity currents respectively (Bouma 1962). On the basis of these facies, Levels A, B and D are interpreted here as a turbidite channel complex facies association. The Marobo association of coarse conglomerates, stratified and cross-bedded finer conglomerates and pebbly sandstones is similar to channel complex facies reported from other localities including the Cap Enragé Formation, Québec, Canada (Hein & Walker 1982) and gravel-dominated axial thalwegs in the Rosario Formation of Baja California in Mexico (Kane et al. 2009).

The change from conglomeratic channel deposits (Level B) to the thinly-bedded, bioturbated siltstones and sandstones punctuated with conglomerates (Level C) and back to conglomeratic channel deposits (Level D) suggests that the Level C sandstones and siltstones accumulated on the channel margins. They are typical of channel leveé deposits reported elsewhere (Walker 1985; Fergusson et al. 1989; Hubbard et al. 2009). Similar, minor examples can be found within the conglomeratic sections, particularly at the base of Level B. Those were probably minor leveés that accumulated from overspill of individual channel turbidites. However, the 150 m thickness of the Level C leveé deposits suggest that they were deposited as a feature that remained adjacent to the entire channel belt over a prolonged period. Reconnaissance observations indicate that the Level C leveé complex is laterally continuous eastwards, toward the basin's eastern bounding fault, while conglomerates of the channel complex dominate to the south and west. The paleoflow within this leveé complex is more southeasterly, compared with the southwest flow of the channel complex (Figure 2.4; Figure 2.5). These details and the large scale of the leveé complex are similar to observations in other elongate depocentres (e.g. Hubbard et al. 2009) and suggest that the leveé complex developed as a wedge on the eastern side of the basin.

Based on the descriptions of Kenyon (1974, p.63 & 93), the Marobo Basin sediments are similar to the Ofua and Nanfua sandstone members of the lowermost and uppermost Noele Marls respectively of West Timor.

Marobo Basin age model

The Marobo section age model (see Figure 2.5B) is derived from unpublished biostratigraphy by Dr. JW Zachariasse, kindly provided D. Van Hinsbergen. In summary, the base of the section in the Batu Putih Formation contains *Globorotalia tumida* and is thus younger than

5.59 to 5.57 Ma (Lourens et al. 2004; Wade et al. 2011). CR16 appears to be ~5.53 -5.54 Ma based on the first occurrence of *Sphaeroidinella dehiscens* (Lourens et al. 2004; Wade et al. 2011). However, this implies an extremely high sedimentation rate in the latest Miocene that is not in keeping with the pelagic carbonate nature of the sediments. It is more likely that the first occurrence of *dehiscens* is either delayed or was not detected. CR18 marks the first occurrence of *Globorotalia crassaformis*, which is dated at 4.31 Ma (Lourens et al. 2004; Wade et al. 2011). The last occurrence of *Sphaerodinellopsis* is detected in CR22 (3.59 Ma in Wade et al. 2011), while CR24 marks the last occurrence of *Dentoglobigerina altispira*, dated at 3.47 Ma in the Pacific (Wade et al. 2011). *Globorotalia tosaensis* first appears at level CR30, suggesting an age for that level of 3.35 Ma (Wade et al. 2011), and *Globigerinoides fistulosis* occurs upwards from CR 38, which is therefore considered to have an age of 3.33 Ma (Wade et al. 2011). The top of the section is older than 1.88 Ma (= LO of fistulosis in Lourens et al., 2004 and in Wade et al., 2011) and probably older than 1.93 Ma (= FO *truncatulinoides* in Lourens et al., 2004; Wade et al., 2011). The sedimentation rates suggested by dating of the lower turbidites (1m/ka) suggests that the top of the section may be not greatly less than 3Ma. Pre-turbidite sedimentation rates were around 0.01 m/ka.

Laleia Basin

Lithologies

Sample and outcrop locations for the Laleia Basin are shown on Figure 2.9. Only four lithofacies were recognized in a reconnaissance of the sedimentary rocks of the Laleia Basin. These are summarized in Table 2.3. No stratigraphic column was measured.

The Laleia Basin contains at least 270 m of clastic sediments that are dominated by weakly cross bedded, crudely rounded to angular, cobble conglomerates (facies Lc - Figure 2.10A). The cross beds dip toward the NE, away from the Lacluta Massif. The conglomerates are interbedded at 1.5 to 15 m intervals with ~30 cm thick sandstones (facies Ls1 - Figure 2.10A) that grade up from pebbly sandstone at their base to laminated medium sandstone. A thick sequence of thinly bedded, root casted, normally graded sandstones and mudstones overlies the conglomerates (facies Ls2 - Figure 2.10B&E). Coarse to medium graded sandstone and pebbly sandstone lenses (facies Ls3 - Figure 2.10B&D) interfinger with the Ls2 sandstones and mudstones, causing extensive soft sediment deformation. The base of sandstone lenses and channel fills contain a well preserved molluscan fauna (Figure 2.10E).

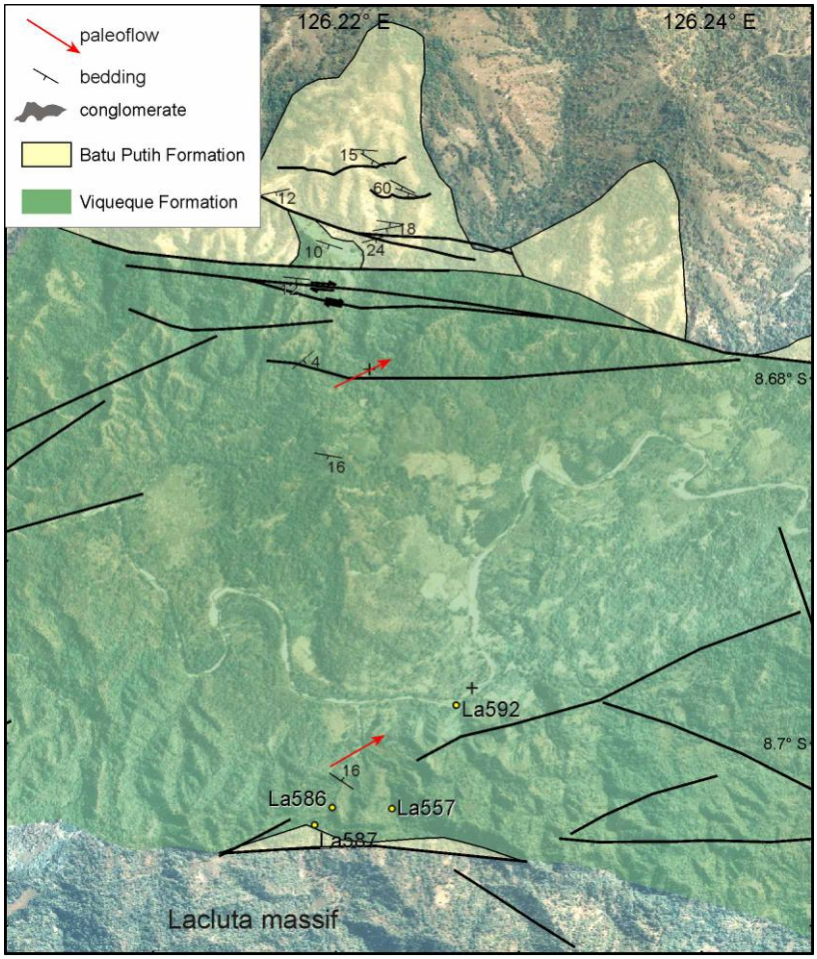

Figure 2.9: Map showing the location of outcrops referred to in text. No section was measured. For basin location see Figure 2.1.

Similar facies to those in Laleia occur on the south side of the Lacluta Massif near Dilor, the type area for the Dilor Conglomerate (Figure 2.10F). The Ls2 facies at that locality is intercalated with the conglomerate. Sandstone similar to Ls1 is present as discontinuous lenses within the conglomerate and a sample from this locality was found to contain reworked N18 foraminifera (D. Haig personal communication).

Table 2.3: Lithofacies of the Laleia Basin

Facies	Lithology	Grain size	Textural features	Thickness	Sedimentary structures	Interpretation
Lc	Cross bedded conglomerate	< cobble	Poorly sorted	1.5 m to 15 m	Faintly Cross stratified, otherwise massive. Interbedded with Ls1 (Figure 2.10a)	Gravelly delta dune deposits
Ls1	Parallel bedded sandstones	Fine to med sand	Moderately sorted	<0.5 m	Occasionally faintly cross bedded or normally graded.	Low flow or reworking of sediments, possibly beach?
Ls2	Normally graded sandstones and mudstones (Figure 2.10b)	Interbedded coarse sand to mud	Poorly sorted with abundant shelly and carbonaceous detritus	10-15 cm	Normally graded beds. Fluid escape structures and root casts throughout (Figure 2.10c). Soft sediment deformation where overlain by Ls3 (Figure 2.10d).	Intertidal delta plain or interdistributary bay mangrove environment (Michels et al. 1998; Fig. 10 in Allison et al. 2003)
Ls3	Very coarse sandstone	Coarse sand to granule	Poorly sorted. Typically has fossiliferous lag (Figure 2.10e)	<0.5 m	Lenses of normally graded sandstone, commonly present in scoured channels.	Sediment lobes and intertidal channels on the delta plain to interdistributary bay. (e.g. Allison et al. 2003)

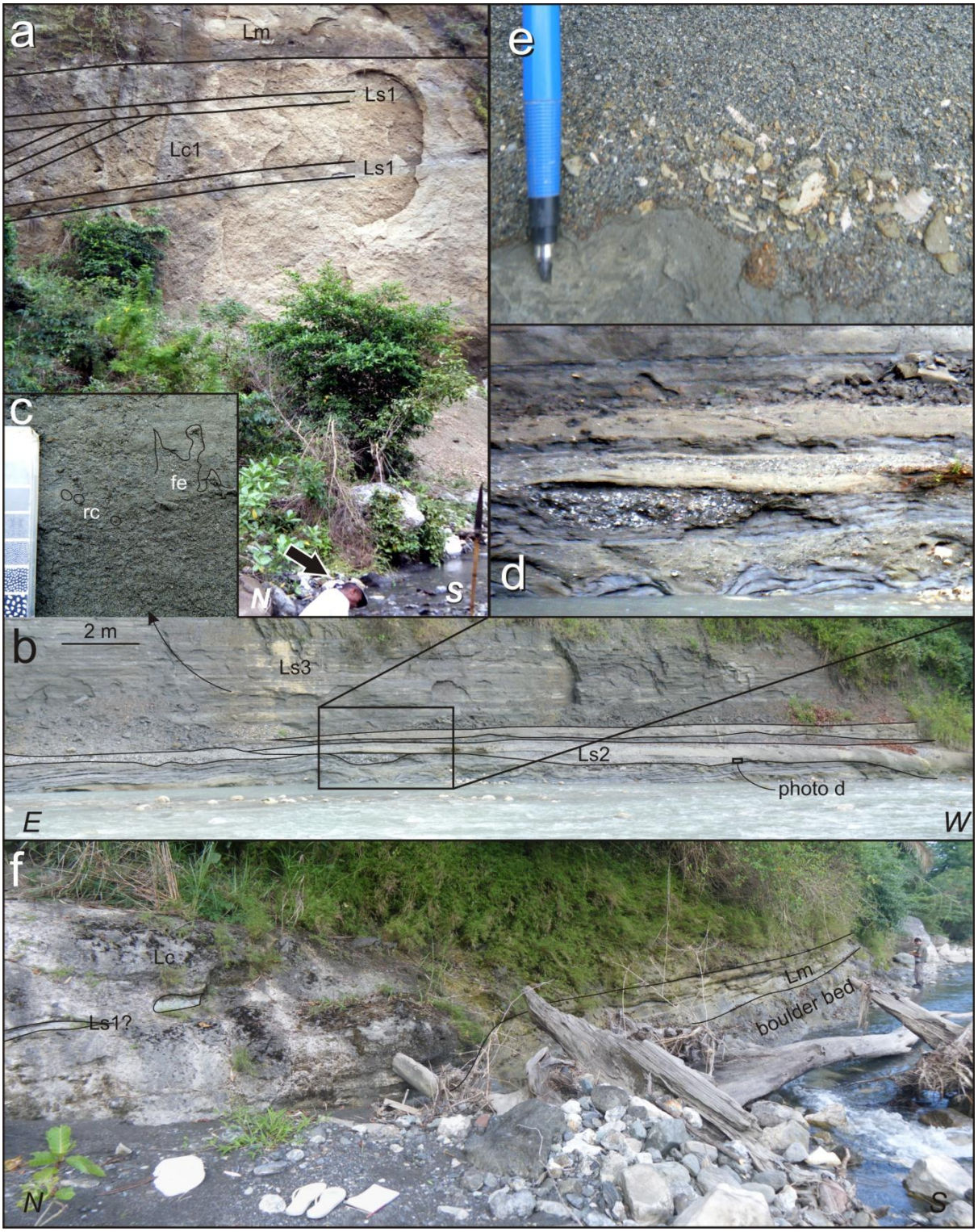

Figure 2.10: Sedimentary facies of the Laleia Basin. A) Locality La586 - Cross bedded conglomerates (Lc) with interbeds of sandstone (Ls) and overlain by flat lying mudstone (Lm). Note person for scale (arrow). B) Locality La592 - Muddy sandstones and siltstones of (Ls3), showing interfingering of pebbly sandstones. C) Detail of Ls3 showing root casts (rc), fluid escape structures (fe) and grading. D) Detail showing soft sediment deformation below coarse pebbly sandstone lens. E) Sand lenses contain abundant well preserved molluscan debris. F) Similar facies developed near Dilor south of the Lacluta Massif, the type area for the Dilor Conglomerate. The Ls1 silt bed at this locality contained reworked Globoratalia tumida foraminifera, indicating the presence of exhumed Batu Putih Formation carbonates in the hinterland.

Interpretation of depositional setting

The Dilor Conglomerate was interpreted by Audley-Charles (1968) as being a marine deltaic deposit. The cross bedded conglomerates of the Laleia Basin are consistent with this interpretation (Figure 2.27) and are similar to but generally smaller than foreset facies observed in Gilbert type fan deltas that form where gravelly sediments discharge into a body of standing water (e.g. McConnico & Bassett 2007). The graded beds of the overlying sandstones and mudstones (Ls3) indicate that they were deposited by settling in a subaqueous environment but the beds contain both marine fossils and root casts. Mangroves are marine plants that prefer intertidal, sheltered, low-energy muddy habitats (Blasco et al. 1996). The presence of root casts in a marine environment, together with the soft sediment deformation and the carbonaceous detritus, suggest that the sediments were deposited in mangrove swamps (Figure 2.27) such as presently occur on the north coast of Timor where the rivers discharge via tide dominated deltas into the Wetar Strait. The channels and lenses of granular coarse sandstones of Ls2 probably represent distributary intertidal channels and major sediment flux events respectively. Although the scale is clearly different, strong parallels can be drawn with the sedimentology of intertidal and mangrove environments of the Ganges Brahmaputra delta (Michels et al. 1998; Fig. 10 in Allison et al. 2003).

Nomenclature

The sediments of the Laleia Basin are presently grouped as part of the Viqueque Formation, a lithostratigraphic unit in which they do not appear to belong. Audley-Charles (1968) specifically defined the Viqueque Formation as being characterized by the appearance of siltstones and sandstones that become increasingly important up section. The Lc1 conglomerates are similar to Audley-Charles' (1968) Dilor Conglomerate and, based on Kenyon's (1974, p. 135) descriptions, they are lithostratigraphically equivalent to the conglomerate facies of the Obernaik Member of the Noele Marls in West Timor. The rhythmic, normally graded sandstones are equivalent to the coarser elements of shallow water facies developed above the conglomerates in the Obernaik Member, as well as in the Tanah Putih Marls of West Timor (Kenyon 1974, p.123 & 135). The clastic sediments of the Laleia Basin are therefore re-assigned as the Obernaik facies of the Dilor Conglomerate. The age of the Laleia Basin clastic succession is presently undetermined.

Viqueque Basin

Two stratigraphic sections were measured in the Viqueque area where the Viqueque Formation is widely exposed in the rivers and streams (Figure 2.11). The sections are shown in Figure 2.12A. One of these was the Type section as defined by Audley-Charles (1968). Data from

the measured sections were supplemented by widespread field observations during structural mapping (Chapter 1).

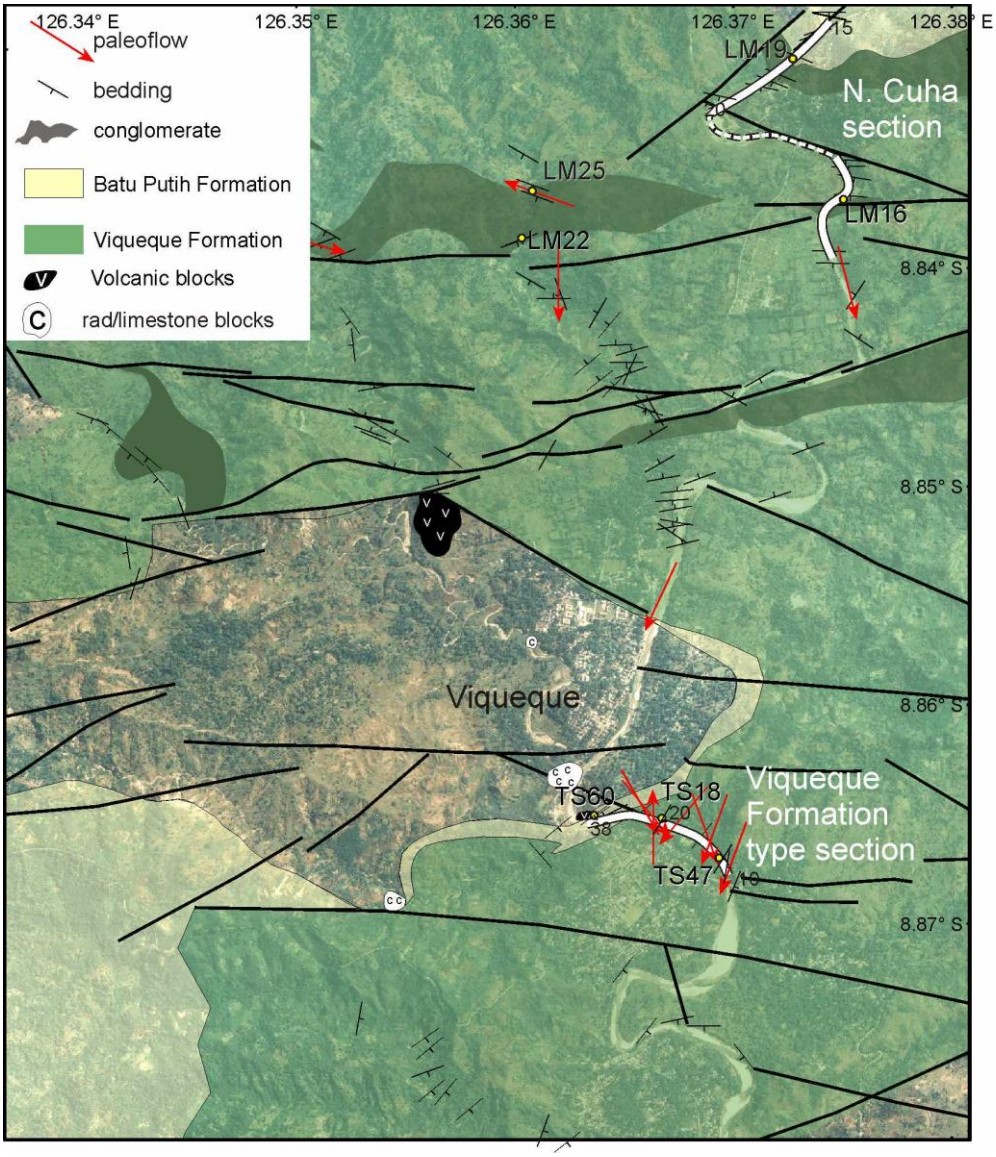

Figure 2.11: Map showing logged sections and conglomerate and sandstone distribution within the Viqueque area. Not all sample locations are indicated within the sections.

Lithologies

The lithofacies observed in the Viqueque area are summarized in Table 2.4 and illustrated in Figure 2.12. The Viqueque Formation of the Northern Cuha and type sections consists of a rhythmic succession of interbedded, normally graded sandstones (facies Vs3) and massive mudstones (facies Vm1), punctuated by thick, poorly sorted conglomerates and sandstones (facies Vc1 and Vs1) and laminated sandstones (facies Vs2) (Figure 2.12).

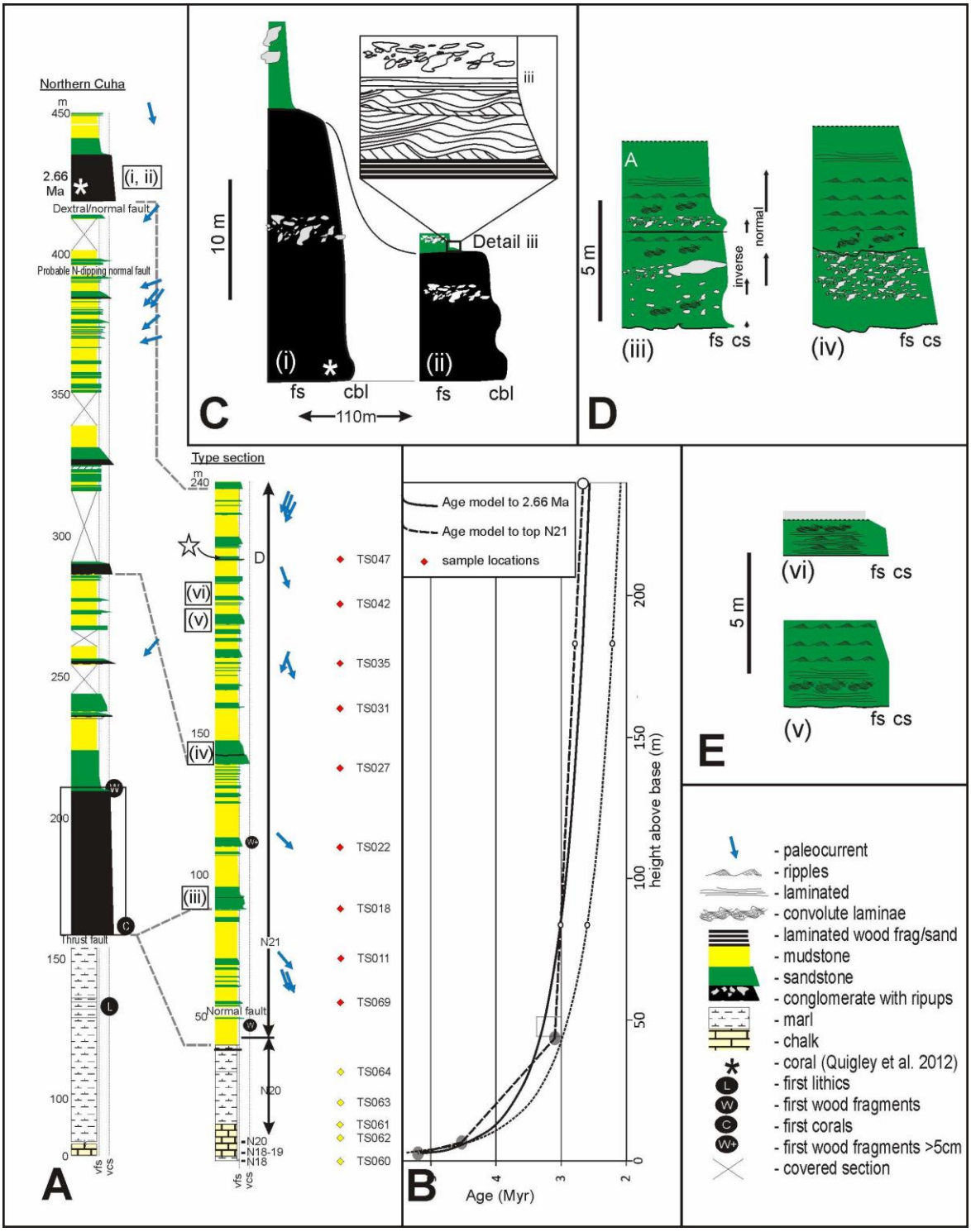

Figure 2.12: A) stratigraphy of the Northern Cuha and Type Sections of the Viqueque Megasequence in the Cuha River, Viqueque. Star shows location of Figure 2.15C&D. B) Age model with linear and best fits to biostratigraphy and combined bio and chronostratigraphy. C) Vertical and lateral grainsize and thickness variation of a VC1 conglomerate from the top of the Northern Cuha section [see Figure 2.14 A-D]. Note rapid transition from conglomerate into sandy turbidite with laminated woody fragments at its base. D) Detail of Vs1 sandy debris flows in type section. Note amalgamation surfaces and similar grading behavior to Vc1 conglomerates in C. See also Figure 2.14E and Figure 2.15A. E) Vs2 facies in type section showing repeated alternation of planar, convolute and ripple cross lamination, and grading confined to the top of the bed. Convolutions commonly associated with dish and pillar structure (see Figure 2.15B).

Table 2.4: Lithofacies of the Viqueque Basin

Facies	Lithology	Grain size	Textural features	Thickness	Sedimentary structures	Interpretation
Vc1	Coarse conglomerate (Figure 2.13A)	Boulder to pebble	Poorly sorted and crudely rounded to angular. Locally clast supported at base but becomes matrix supported upwards. Commonly contain aragonitic detrital corals (Quigley et al. 2012a).	<70m	Thickest, coarsest conglomerates are channelized at base, normally graded (Figure 2.13A & B) and contain armored mudballs of Batu Putih marls. Others have flat erosional base and are inversely graded over basal 10 cm (Figure 2.14B). Overall generally normally graded (compare Figure 2.14 B & C) but repeated inverse and normal grading of cobble size component (Figure 2.12C). Common floating intrabasinal clasts (Figure 2.14A), particularly at abrupt interface with overlying sandstone (Figure 2.13C). Thicker conglomerates abruptly capped by convolute, planar and ripple cross laminated siltstones and fine sandstones (Figure 2.13C). Thinner conglomerates commonly capped by laminated coaly debris and climbing rippled sandstone (Figure 2.14D)	R2 & R3 gravel (Lowe 1982) deposited by channelized debris flow in poorly confined slope channels. Coarsest debris in central channel (Figure 2.13) transitioning progressively to plastic laminar debris flow and/or Vs1 on the channel margins (Figure 2.14A)
Vs1	Thick bedded sandstone	Fine sand to granule	Poorly sorted angular to subrounded, matrix rich	3 to 8 m	Bases typically flame structured. Commonly stacked, with erosional or concretionary partings (Figure 2.14E). Local and sometimes repeated reverse grading (similar to Vc1 – see Figure 2.12C). Floating intrabasinal clasts common (Figure 2.14E).	Overspill thick bedded sandstones beyond the channel margins (Figure 2.14E) (Fig. 35b in Posamentier & Walker 2006; Fig. 7.9 in Shanmugam 2006).
Vs2	Thick, tabular, laminated sandstone	Fine to medium sand	Moderately to well sorted, interlaminated woody material	Up to 4 m	Ungraded repeated alternations of ripple and planar laminations and convolutions, dish and pillar structures, no clear internal contacts. Graded over last 20% of bed thickness. Examples at 165, 180, 190 and 200 m.	Sand deposited rapidly from suspension by quasi-steady turbidity current (e.g. Mulder & Alexander 2001), possibly fed directly by fluvial sediment (e.g. Dixon et al. 2012). Continuous deposition. Grading at top records final waning flow. Similar to Oemenu sandstone facies of the Noele Marls in West Timor (Kenyon 1974).
Vs3	Medium bedded sandstone	Fine to coarse sand	Moderately sorted		Normally graded, planar or planar/rippled sandstone	Tb, Tbc, rare Tbcd sandy turbidites (Bouma 1962)
Vm1	Massive mudstone	Silty mud with occasional very fine sand and silt interbeds	Upper levels contain abundant foraminifera	Up to 12 m, thickest overlying Vc1 or Vs1	Massive to faintly bedded, grading difficult to observe but can commonly be discerned between the top and bottom of the thickest beds	Turbiditic (Te) and hemipelagic mud (Kneller 1995; Shanmugam 1997,2000; Posamentier & Walker 2006)

The poorly sorted conglomerates (Vc1) are generally supported by a coarse sandy matrix but they thicken and become clast supported towards the NW part of the basin, where they locally attain thicknesses in excess of 70 m. The thickest conglomerates in the centre of the basin are clearly channelized (Figure 2.13) but the bases become progressively more planar as the beds extend laterally. Some beds extend laterally for >1 km but in other outcrops they can be seen to pinch out laterally over 100 m (Figure 2.12 C). Matrix supported conglomerates commonly contain aragonitic detrital coral heads such as those dated by Quigley et al. (2012a) from the top conglomerate of the Northern Cuha section (* in Figure 2.12). Most of the paleoflow directions in the Northern Cuha section, and in the northern side of the basin generally, are toward the SW (Figure 2.11).

The south side of the basin, where the type section is located, has relatively few conglomerate outcrops (Figure 2.11) and is dominated by normally graded sandstones (facies Vs3) and massive mudstones (facies Vm1) with paleoflow generally toward the SE (Figure 2.11). Conglomerate facies (Vc1) is absent in the type section but the poorly sorted sandstone facies (Vs1) is similar in many respects to the Vc1 conglomerates. For instance, facies Vc1 and Vs1 both exhibit a combination of inverse to normal grading and commonly contain ripped up and brecciated, finer-grained intraclasts that float some distance above the base of the bed (Figure 2.12 C&D; Figure 2.14 A&E). In two instances, the Vs1 sandstones were seen to be amalgamated (Figure 2.12D).

The rafted intraclasts that occur in both the poorly sorted conglomerate (Vc1) and sandstone (Vs1) facies are generally confined to well-defined horizons. Intact rafts up to 10 m long occur in the conglomerates (Figure 2.14A) and up to 3 m in the sandstones (Figure 2.14E). The rafted intraclast orientations are generally planar and, rarely, imbricated. Vs1 sandstone intraclasts commonly have discrete tails of disaggregated material (Figure 2.14E). Intraclast compositions include mudstone, sandstone and conglomerate lithologies. Mudstone balls also occur in the conglomerates and consist of Batu Putih type sediment, armored with conglomerate clasts. The Vc1 and Vs1 units both transition abruptly into normally graded sandstones (Vs3). Clasts floating at the top of the conglomerate or sandstone commonly protrude into the overlying Vs3 sandstone/siltstone bed (Figure 2.13C; Figure 2.15A).

Figure 2.13: Conglomerate in the centre of the Viqueque Basin. Note the flat base in A.

Amalgamated sandstone beds of facies Vs2 (Figure 2.15B) are mainly found at the top of the section (e.g. 165, 180, 190, 200m; Figure 2.12E). The tops of the beds are normally graded but most of the thickness is amalgamated sandstones with repeated alternations of planar, convolute and ripple cross laminae. The convolute laminae are commonly interspersed with dish and pillar structures that indicate rapid deposition and dewatering of saturated sand.

Woody detritus is common throughout both sections, usually incorporated within or overlying thick sandstone units of Vs1 or Vs2. The grainsize of woody detritus ranges from thin laminae through carbonaceous horizons to entire trees (Figure 2.15B-D).

Massive to subtly graded mudstones are found interbedded throughout the succession. They are generally silty at the base and become more plastic upwards. Foraminifera are typically concentrated in the uppermost few centimeters. The thickness of the mudstones is commonly greatest where they overlie poorly sorted conglomerates and sandstones (Vc1 or Vs1).

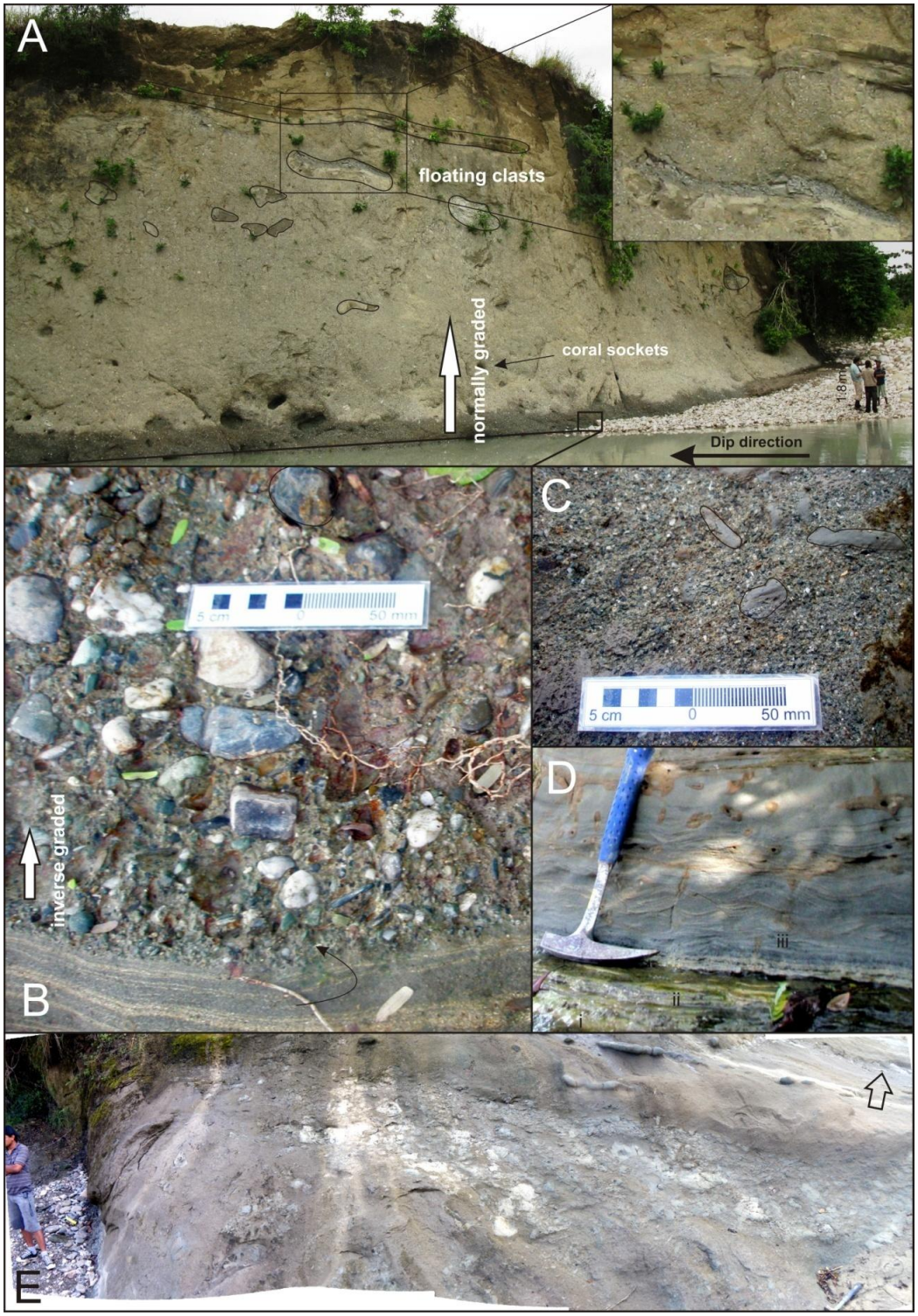

Figure 2.14: Debris flow deposits in the Viqueque sections. A) Sandy matrix supported conglomerate LM16 at the top of the Northern Cuha section [see Figure 2.12C]. The base of the conglomerate is rich in corals, which are quickly eroded out leaving empty sockets. Floating clasts >12 m long can clearly be seen beginning about 4-6 m above the base. B) the basal 10 cm of the conglomerate is inversely graded, after which the conglomerate is approximately normally graded [Compare B and C]. C) Coarse sand to granule conglomerate at top of Vc1 outcrop shown in A). D) Abrupt change from granule conglomerate (i) to organic laminae (ii) and climbing ripples (iii) at top of conglomerate [see detail C on Figure 2.3C]. E) Vs1 sandstone [Figure 2.12D(iv)], showing partially disaggregated floating clast.

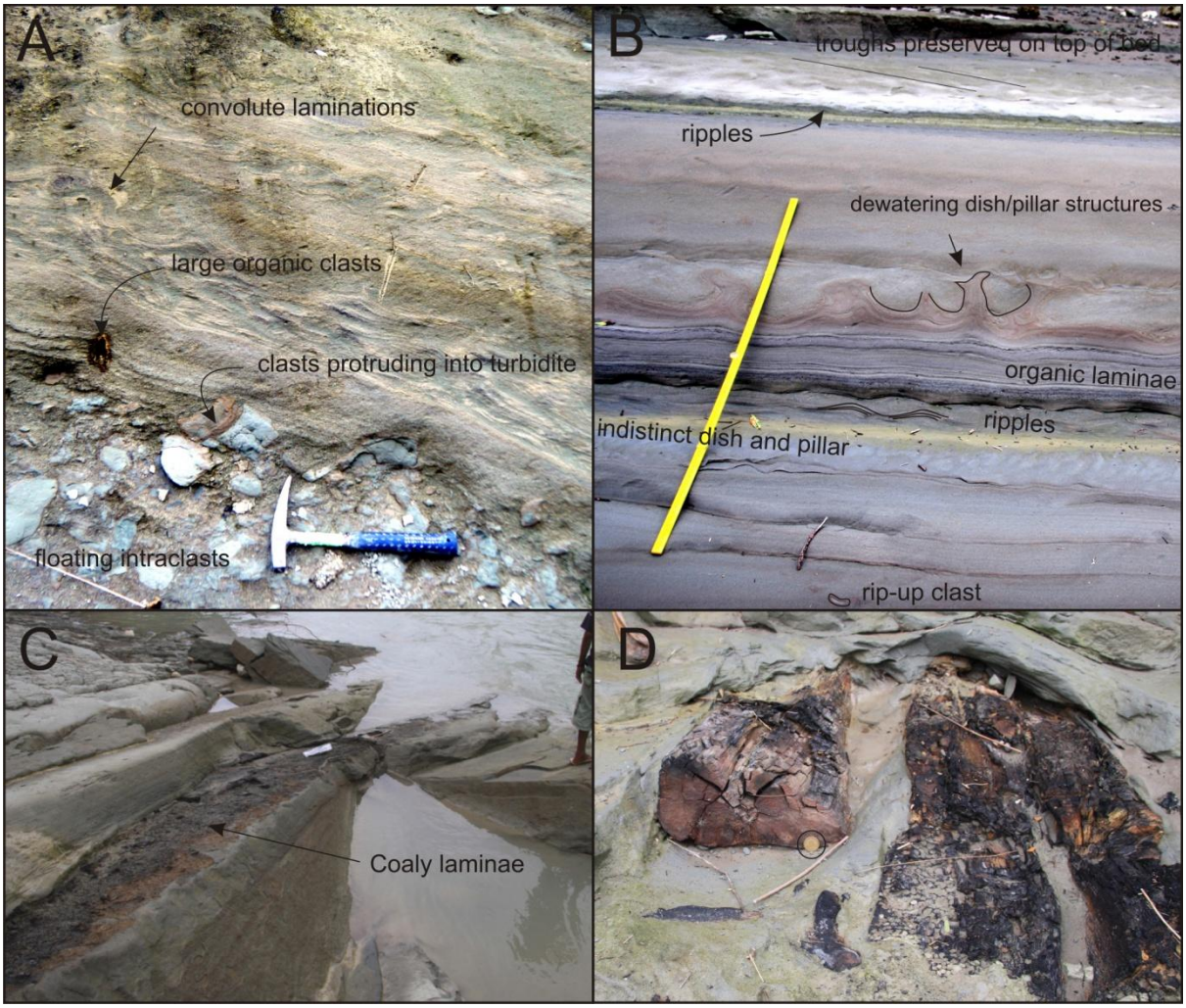

Figure 2.15: A) Boundary between sandy debris flow (facies Vs1) and overlying turbidite (Vs3) (see Figure 2.12D[iv]). B) amalgamated sandstone of VS2. C) Coaly horizons overlying a Vs3 sandstone overlain by a Vm1 mudstone. D) Tree trunk encased in graded sandstone that is exposed just out of sight in photograph C. US25c coin for scale [circled] – for location see star on Figure 2.12.

Interpretation of depositional setting

The characteristics of the poorly sorted conglomerates (facies Vc1) and sandstones (Vs1) within the Viqueque Formation in the Northern Cuha and type sections are similar to deposits in the Annot Sandstone, which were interpreted by Shanmugan (2006, p.307) as indicative of laminar flow within plastic debris flows. The changes from inverse to normal grading are interpreted as reflecting deposition from a density-stratified flow. The rafting of intraclasts within the Viqueque conglomerates and thick sandstones suggests that the sediment gravity flow had matrix strength and the planar clast orientations suggest that it was laminar (e.g. Sohn 2000; Shanmugam 2006). These facies therefore represent the frozen product of laminar plastic debris flows.

The width, extent (Figure 2.11) and lobe shape of the Vc1 conglomerates as seen in outcrop scale thickness variations (Figure 2.12C), suggest that the debris flow was poorly confined (Figure

2.27), although paleoflow directions suggest that they were emplaced toward the southwest. The poorly sorted Vs1 sandstones of the type section, that were emplaced towards the southeast, are interpreted as poorly confined channel overspill equivalents of the Vc1 conglomerates (Fig. 35b in Posamentier & Walker 2006; Fig. 7.9 in Shanmugam 2006).

The Vs2 facies of thick amalgamated sandstones are similar to the Oemenu sandstone facies of Kenyon (1974). The Vs2 facies sandstones are interpreted as having been deposited from a quasi-steady turbidity current (Mulder & Alexander 2001), possibly fed directly by fluvial sediment in a hyperpycnal setting (Mulder et al. 2003; Dixon et al. 2012) (Figure 2.27). Hyperpycnites are commonly earthquake related (Normark et al. 1998; St.-Onge et al. 2004) but are also related to climate through flood frequency and magnitude (Mulder et al. 2003). This suggests that the up-section increase in these deposits may reflect the climatic effects of the increasing topography of Timor documented by Nguyen et al. (2013).

The normally graded sandstones (facies Vs3), which occur either interbedded with massive mudstones of Vm1 or overlying the poorly sorted conglomerates (Vc1) and sandstones (Vs1), represent the deposition of sediment from turbid suspension. They are deposited either above or downslope of the debris flow. Thinner, normally graded fine sandstones and siltstones that are not connected to a debrite may represent downslope or leveé deposits (e.g. Kane et al. 2009).

The Vm1 facies massive to subtly graded mudstones represent rapidly deposited turbiditic (Te) mudstone, while the plastic foraminiferal mudstone that is commonly found at the tops of thick mudstones represents the background deposition of hemipelagic mud (Kneller 1995; Shanmugam 1997,2000; Posamentier & Walker 2006).

Overall, these characteristics, together with the presence of rounded conglomerates (Figure 2.13; Figure 2.14B), encased tree material (Figure 2.15D) and pristine coral detritus (Moody 2012; Quigley et al. 2012a) suggest a depositional setting at the base of a debris flow dominated slope, fed by the collapse of gravelly, mangrove covered deltas such as are exhumed in the Laleia Basin. The collapse would have released the large intraclastic blocks that are entrained within the deposit. The blocks were then probably transported at the interface between turbid and plastic flows. The collapse would also have removed lateral support for coral reefs that had developed adjacent to the delta, such as occurs on the north coast of Timor (Mills 2011), and caused entrainment of living reef material within the debris flow. The coral heads were rapidly entombed in the frozen plastic debris flow and largely protected from diagenesis, thus maintaining their aragonitic structure (Moody et al. 2011; Quigley et al. 2012a). The two examples of amalgamation of Vs1 sandstones

may represent repeated pulses of sediment that are released as the slope collapses back to a new stable angle.

Debrites elsewhere of a similar scale to those reported here have been linked to basin-scale turbidite deposition over distances <200 km (e.g. Soh 1989; Georgiopoulou et al. 2009). A growing base of literature is linking such basin-wide turbidites with earthquake chronologies on continental margins (Kastens 1984; Mutti et al. 1984; Adams 1990; Goldfinger et al. 2003b,a; Noda et al. 2008; Pouderoux et al. 2012). The delta front collapses may have been seismically-triggered.

Viqueque Basin age model

Haig and McCartain (2007) biostratigraphically dated the Synorogenic Megasequence in Audley-Charles' (1968) Viqueque Formation type section. The section comprises three distinct units (Figure 2.12). The basal Batu Putih Formation chalk was deposited within foraminiferal zone N18-19. The Batu Putih marl ranges through N20. Deposition of the remainder of the section, which comprises the Viqueque Formation, began at the start of N21 and is only biostratigraphically constrained to range within N21 (the Late Pliocene). However, Quigley et al. (2012a) obtained a coral U/Pb age of 2.66 Ma for the top of the Northern Cuha section. This age was duplicated on a second coral from the same site by Moody (2012). The Northern Cuha section is located ~3.3 km from the type section and, as discussed above, the two sections are of similar thickness and related character. The existing age data for the two sections therefore constrain an age model for their deposition (Figure 2.12B). Based on the age model, the first lithics arrive in the basin at ~ 3.25 to 3.4 Ma, and turbidite sedimentation begins in earnest at ~3.1 to 3.25 Ma. The age model records an exponential increase in sedimentation rates at the type section, from ~3.3 m/Ma in N18-19 (basal chalk) to ~27 m/Ma in N20 (Batu Putih marl), and increasing to <490 m/Ma in N21.

2.3.3.3 DSDP 262

A Deep Sea Drilling Project hole was drilled in 1978 on the axis of the Timor Trough south of West Timor. Micropaleontology of this drill core was subsequently used to determine the timing and rates of tectonic events and the bathymetric development of the Timor Trough (Veevers et al. 1978; Johnston & Bowin 1981). DSDP descriptions are summarized here, followed by a revision of the age model.

Lithology

The basal 28 m of sediments in the DSDP 262 core (Level A, Figure 2.16) are shallow marine calcarenites and foraminiferal mudstones that are dolomitized and phosphatized (Cook 1974a,b; Cooks et al. 1974; Heirtzler et al. 1974). Veevers et al. (1978) interpreted these sediments as having accumulated on the Australian shelf before the DSDP basement was bent down into the Timor Trough. They grade into a bathyal ooze that accumulated in the Timor Trough (Level B, Figure 2.16). This ooze is variably rich in foraminifera and radiolarians and extends until around 300 m above the base of the hole, where the first, ungraded, detrital foraminiferal sand layer is found that is taken as the start of Level C (Figure 2.16). Even within Level C, sand is of secondary importance to radiolarians and foraminifera, except for a 4.5 m thick graded sand that, based on the age model, has an age of ~90ka. Foraminiferal and radiolarian ooze sediments within Level C are designated as marls on the stratigraphic column, based on their geochemistry, which is discussed later. Apart from the basal 28 m of the core, the remainder of the DSDP 262 core seems to be lithologically equivalent to the Batu Putih Formation.

Age model

A revised age model is presented below for DSDP 262, so as to facilitate comparisons of synorogenic sections along strike (Figure 2.16), particularly in terms of their geochemistry. The revised DSDP 262 age model is based on the original biostratigraphy by Heirtzler et al. (1974), supplemented by revised biostratigraphy and new $\delta^{18}O$ stratigraphy for the upper part of the core (Rosenthal and Kalansky personal communication) (Figure 2.16). $\delta^{18}O$ stratigraphy is not useful below ~250 m core depth because of dolomitization of the sediments and commensurate increasingly heavy isotopic values down the core. However, Rosenthal's identification of OIS6 (135ka) at 160 m is of particular importance, and *P. lacunosa* decreases in abundance at ~270 m depth, corresponding to ~460ka (Rosenthal and Kalansky personal communication). Heirtzler et al. (1974) reported the first occurence at 337 m of *Globorotalia truncatulinoides*, which is now dated at 1.93 Ma (Lourens et al. 2004; Wade et al. 2011). The improved age model shows that sedimentation rates have reached around 120 cm/year since OIS6.

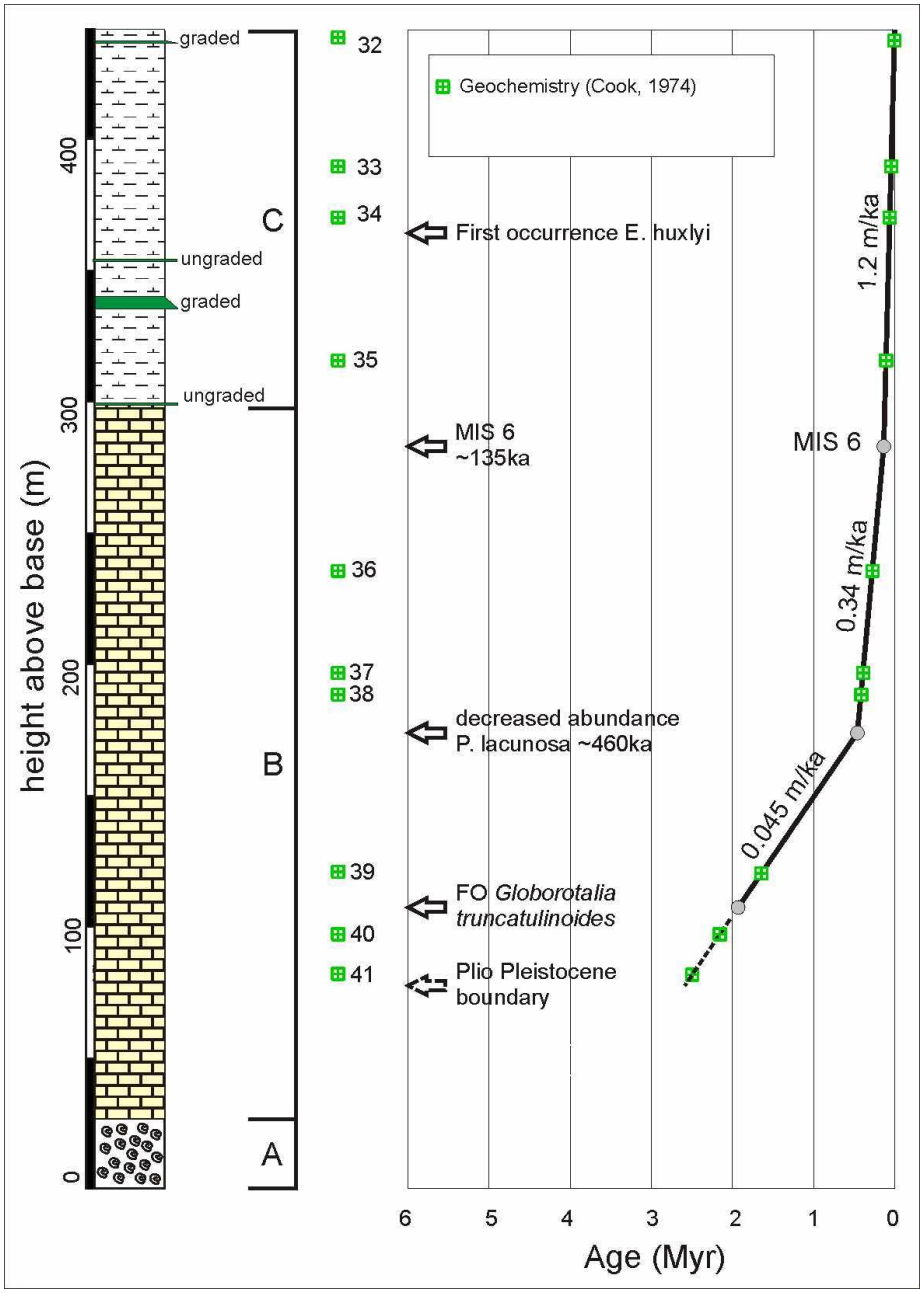

Figure 2.16: DSDP age model, based on Heirtzler et al. (1974) and supplemented with additional biostratigraphy and oxygen isotope stratigraphy (Yair Rosenthal personal communication). The elevations of geochemical sampling by Cook (Cook 1974a) are shown projected onto the age model. Stratigraphic column redrawn simplified from Heirtzler et al. (1974).

2.4 Provenance analysis

2.4.1 Introduction

Obduction of forearc basement such as is interpreted for the Banda Arc collision with Australia in Timor is a common feature of early orogenesis that is recorded in sedimentary basins (Hiscott 1984; Linthout et al. 1997; Dewey & Mange 2000; Dewey 2005). Combined petrography and geochemistry can be used to unravel provenance, exhumation histories and paleogeography (e.g. Najman & Garzanti 2000; Getaneh 2002; Armendáriz et al. 2008). Basin sediments retain a geochemical signature of bulk source lithology (Hiscott 1984; Roser & Korsch 1988; McLennan et al. 1993), tectonic setting (Bhatia & Crook 1986) and source area weathering and diagenesis (Nesbitt & Young 1989; Fedo et al. 1995; Nesbitt et al. 1996). Nd isotopic data provide information on the averaged mantle extraction age and crustal history of the precursor material (McCulloch & Wasserburg 1978) and have been used in conjunction with detrital zircon U-Pb geochronology to identify terrane boundaries and the presence of juvenile arc material (DeCelles et al. 2004; Tobgay et al. 2010).

Many of these studies have focused on tectonic reconstructions for deformed basins in evolved orogens such as the Himalaya, basins that contain far-travelled sediments and are commonly no longer contiguous with their source area (DeCelles et al. 1998; Najman & Garzanti 2000; Cina et al. 2009; Tobgay et al. 2010; Zhang et al. 2012). When basins are well dated and still connected to their source, such as in Timor, a higher resolution evaluation of the source characteristics and tectonic history becomes feasible, especially if the basin contains conglomerates that have only undergone short transport (Cutten 1979; Wandres et al. 2004). This section investigates the timing and provenance of terrestrial sedimentation in the synorogenic basins of Timor Leste, and thereby provides insights into the timing and effects of the collision of Australia with the Banda Arc.

2.4.2 Previous work and relevant datasets

The provenance of the synorogenic basins of Timor have been qualitatively evaluated and the sediments are generally considered to be derived largely from the Banda Terrane forearc basement (Audley-Charles 1967,1968; Kenyon 1974). A wealth of potentially useful geochemical datasets are emerging that allow this hypothesis to be tested by using discriminant diagrams. The igneous geochemistry of the Banda volcanic islands was reported by Ely et al. (2011 - Atauro), Elburg et al. (2005 – Wetar, including Nd isotopes) and Herrington et al. (2011 – also Wetar). Ultramafic rocks of Timor were characterized by Harris and Long (2000) and Falloon et al. (2006). Igneous and metamorphic rocks of Banda affinity exhumed on Timor have been studied by

Standley and Harris (2009) and lithologically similar Gondwanan affinity rocks were characterized by Berry and Jenner (1982). Major and trace element geochemistry and XRD mineralogy were reported for sediments from the DSDP 262 site in the Timor Trough (Cook 1974a; Cooks et al. 1974), which is a well dated site (Figure 2.16). Vroon et al. (1993; 1995) reported the trace element and Nd isotope geochemistry of modern sea floor sediments along a transect across the orogenic wedge east of Timor Leste. Their data included the NW shelf of Australia and further data from five DSDP 262 core samples. Honthaas et al. (1998) and Vroon et al. (1996) reported similar data for rocks dredged from the Banda Ridges including a 46 Ma basalt. Taylor and McLennan (1985) published detailed geochemical analyses and Allègre et al. (1984) published Nd isotope characteristics for Australian shales. Ron Harris provided εNd data for rock samples from the Maubisse and Aileu complex onshore Timor. This study compares these geochemical datasets, and published descriptions of the lithologies encountered in the various terranes, with conglomerate clasts and mudstones derived from the synorogenic basins of Timor Leste.

2.4.3 Methods

2.4.3.1 Conglomerate clast composition – point counting

Thin sections of samples from the Marobo, Laleia and Viqueque Basins were analyzed by point counting. The tectonic setting of the sediments is not in question so, rather than using traditional point counting techniques, preference was given to conglomerate samples and point counting took the place of clast counts, for which there was no time in the field. The poorly lithified conglomerate samples were broken apart and sieved to retain the 1 mm to 4 mm fraction, so as to preferentially observe identifiable lithics. Several sandstones from the Viqueque Formation type section were also thin sectioned and counted for comparison. The results are presented in Table 2.5 and summarized at the end of the table. Table 2.5 can be found at the end of this chapter.

2.4.3.2 Geochemistry

Carbonate, mudstone and conglomerate clast samples were selected from the Viqueque Type section and the Marobo section and analyzed to determine their major and trace element geochemistry, and weight loss on ignition. Geochemical characterization was carried out at the commercial ALS Minerals laboratory at Winnemucca, Nevada. Major elements were determined using Inductively Coupled Plasma – Atomic Emmission Spectroscopy (ICP-AES) following methods outlined in ALS (2006). Trace element geochemistry using ICP Mass Spectrometry (ICP-MS) followed procedures outlined in ALS (2009). Tabulated results can be found in Table 2.6 (Marobo section), Table 2.7 (Viqueque section) and Table 2.8 (conglomerate clasts). The tables can all be found at the end of this chapter.

Major, trace and rare earth element geochemistry were used to provide constraints on sedimentary provenance based on a variety of tectonic discrimination diagrams that are available (Hiscott 1984; Taylor & McLennan 1985; Bhatia & Crook 1986; Roser & Korsch 1988; McLennan 1989; McLennan et al. 1993) and on source area weathering based on the chemical index of alteration (Nesbitt & Young 1989; Fedo et al. 1995; Nesbitt et al. 1996).

Loss on ignition (LOI) refers to the weight loss of a sample following combustion in a furnace and is dependent on temperature and duration of combustion. Different temperatures of combustion affect different changes in the composition of the sediment. For instance, loss on ignition at 105°C mainly causes sediment water loss and is not considered further here. Loss on ignition at 550°C (LOI_{550}) is generally considered to be proportional to the total organic carbon content of the sediment (Dean 1974) but may also be contributed to by the loss of structural water in clay, which may account for <20% weight loss in clay rich samples (Mook & Hoskin 1982; Santisteban et al. 2004). XRD results indicate that the rocks analyzed here had minimal clay content, so LOI_{550} is taken to reflect organic carbon content. At higher temperatures the dominant factor that creates weight loss in carbonates between 550-1,000°C (reported as LOI_{1000}) is the loss of carbonate CO_2, such that carbonate content can be estimated from LOI_{1000} if LOI_{550} has previously been determined. When this relationship is applied, carbonate estimation error is proportional to clay content and inversely proportional to carbonate content (Santisteban et al. 2004). As noted above, the rocks analyzed here had minimal clay content. The samples for these analyses were selected so as to obtain a reasonable spread of ages. The base of the section, where age models show low sedimentation rates, was therefore sampled at closer intervals. Methodological details are appended.

Nd isotope analyses were carried out to determine the bulk provenance age of the sediments. Analyses were performed at the University of Alberta following procedures outlined in Creaser et al (1997) and Unterschutz et al. (2002).

2.4.4 Conglomerate clast composition

2.4.4.1 Marobo Basin

The Marobo section (Figure 2.5) is the least compositionally diverse section. The conglomerates are dominantly composed of dark grey sericite schist (30-63%), quartz (0.5 to 10%) and feldspar (4 to 22%), supplemented by small but regular amounts of intraformational sandstone (0 to 10%), quartzite (0 to 6%), calcareous schist (0 to 6%) and epidote schist (0 to 3%). Rare chlorotoid schist clasts are present at the base of the section, along with a single occurrence of four igneous clasts in a sample from the base of the clastic part of the section (65 m - CR24a). The sericite schist clasts are commonly mylonitized such that the quartz grains have a lattice preferred

orientation and are elongate at around a 10° angle to the mica schistosity. Even unmylonitized sericite schist clasts have elongate quartz grains that suggest high strain, and up to 20% of polycrystalline quartz lithics exhibit mylonitic fabrics. Several clasts from the top of the section (Cr62a - Figure 2.5) contained rounded zircon and relict feldspar grains in a matrix of fibrous quartz and sericite.

Calcite cemented samples, such as CR24a, were thin sectioned intact and contain up to 10% of intraformational sandstone clasts eroded from pre-existing synorogenic sandstone beds. This is in keeping with the common occurrence of floating layers of sandstone and mudstone clasts, even from the base of the section, and suggests significant reworking of older synorogenic sediments, either uplifted or sourced from channel wall collapse. The importance of extraformational, indurated, quartzofeldspathic sandstone clasts increases up section from ~250 m above base (a.b. – CR41a) and an influx of indurated mudstone clasts occurs above ~350 m a.b. (CR49a) in the upper half of the section. Limestone clasts only occur above ~480 m a.b. (CR56a), near the top of the section.

The clast composition of the Marobo Basin conglomerates suggests erosion of an evolved (continental?) source with a strong metamorphic signature. Sandstone intraclasts occur throughout but a source for indurated sandstones and limestones is progressively unroofed.

2.4.4.2 Laleia Basin

Three samples were examined from the Laleia Basin (La 587, 557 and 592). Their locations are indicated on Figure 2.9. The conglomerates of the Laleia Basin are more compositionally diverse than those of the Marobo Basin. A wide variety of limestones contribute 6 to 8% of the clast content. Sandstones contributed 9 to 20% of the conglomerate clasts but no clear trends were observed. Quartz clast content increases upsection from 8 to 21%. Amphibolite clasts declined in importance upsection, from 24 to 1.3%. A diverse assemblage of schists maintained a 30 to 40% contribution to clasts throughout all three samples. Igneous rocks contribute 3 to 12% of the clasts.

Limestone clasts are common throughout the studied Laleia conglomerates. The middle conglomerate (La557) contained a particularly diverse assemblage of limestone clasts. Distinctive lithologies included hornblende and serpentinite-bearing limestones (serpentinite also occurred separately), as well as calcilutites containing silicified fusulinids and unsilicified fusulinids and crinoids. The association of silicified fusulinids and crinoids is characteristic of the Permian Maubisse Formation of the Gondwanan Megasequence (Barkham 1993; Charlton et al. 2002). Silicification is characteristic of Paleozoic fossil assemblages in general (Schubert et al. 1997).

The metamorphic clasts of the Laleia Basin are completely distinct from those of the Marobo Basin. The basal conglomerate contains abundant clasts of epidote and chlorite rich amphibolites, amphibole schists, and epidote and chlorite schists. Many of the amphibolite clasts have a strong mylonitic fabric with preferred orientation of quartz grains. There is also abundant evidence of hydrothermal activity in the source area for the metamorphic clasts. An epidote amphibolite clast in the middle conglomerate (La557) was cut by a quartz vein that was in turn cross cut by a calcite vein, whereas another vein contained hydrothermal chlorotoid. Though uncommon, hydrothermal chlorotoid has been reported from metasomatized mafic igneous complexes in India and Australia (Gustafson 1946; Prider 1947; Venkatesh & Malhotra 1960; Halferdahl 1961).

Dacite, granophyre and peridotite clasts were identified in the basal sample (La587). These included several fresh I-type trachy-dacite clasts. One of these clasts (La587a – see geochemistry in Table **2.8**) initially contained a peridotite xenolith that fell out during thin sectioning, and also a dacite xenolith of comparable mineralogy to the host rock. The La587a dacite clast is composed of <85% low-albite, together with abundant magnetite, minor amphibole, interstitial chlorite and quartz, and up to 5% granophyre. Granophyre was also present as a discrete clast in the same sample, and was probably sourced from a dacitic rock. Another dacite clast contained titanite, suggesting that these were derived from oxidised magmas. No further dacite clasts were observed upsection, and the volcanic clasts higher in the section were mainly spherulitc and porphyritic basalts, dolerites and altered igneous rocks, suggesting an unroofing sequence of dacites capping basalts and dolerites.

2.4.4.3 Viqueque Basin

The basal conglomerate of the Northern Cuha section (LM19) has eroded deeply, entraining large amounts of pre-existing strata and is not considered as representative of the basal stratigraphy as the thinner turbidites at the base of the type section (Table 2.5; see also Figure 2.12). Therefore, point counts were made of seven type section sandstones and four conglomerate samples from the Viqueque area. The locations of the samples are indicated on Figure 2.11. Limestones increase their contributions from 1.5-1.9% of the lithics in the sandstones at the base of the type section, to 15-22% of the clasts in the conglomerates at the top of the section. Quartz content ranges up to 58% in the finer grained sandstones at the base of the section but is otherwise typically 5 to 15% of clasts in the conglomerates. In contrast, the fine grained type section sandstones (TS070 to TS017) contain almost 0% igneous material, which provides 5 to 12% of the conglomerate clasts. LM19 contains abundant peridotite clasts. Amphibolites contribute 5 to 26% of the conglomerate clasts, whereas the sandstones typically contain 6 to 20% amphibole crystals. Upwards of 5% of the

amphibolite clasts in the Viqueque conglomerates are mylonitized and they mostly contain albite with bent deformation twin lamellae. Several amphibolite clasts contained stout crystals of clear to pale green amphibole with a preferred orientation that were surrounded and intruded by tremolitic amphibole with a different preferred orientation. Three clasts of schist in LM19 contained chlorite and serpentine with rotated clinopyroxene porphyroclasts. Chlorite schist clasts or grains decline in importance upsection from 16% at the base of the Viqueque Formation to between 2 and 4.7% at the top of the Viqueque Formation. Total schist remains constant, however, as clasts of chlorite schist are replaced by clasts of chlorite/sericite and sericite schist. Quartz mylonite clasts appear at the top of the Northern Cuha section in association with the influx of sericite schists.

The first igneous material in the type section appears at about 86 m a.b. (TS018). Clasts consist of a mixture of diorite, dolerite, peridotite and spherulitic basalt. The composition is petrographically similar to the igneous material in the conglomerate at the base of the Viqueque Formation in the Northern Cuha section (LM19), apart from the peridotite-rich nature of the coarser LM19. In addition, both contain partly silicified and chloritized limestone clasts, which are not seen lower in the type section. These are characteristic of the Permian Maubisse Formation of the Gondwana Megasequence. TS018a and LM19 also contain similar percentages of sheared/mylonitized amphibolite clasts and do not contain the chlorite and chloritoid species of amphibolite that appear higher in the section. TS018a contains the greatest concentrations of amphibolite in the sandstones, and LM19 contains the greatest concentrations in the conglomerates. These characteristics suggest that TS018 and LM19 are correlative.

The clastic sediments contain variable amounts of carbonate material. The conglomerates typically contain ~2% of shallow water carbonate detritus such as *Platygyra* and *Goniastrea* corals, and gastropod shells. The coral heads are generally well preserved and aragonitic (Quigley et al. 2012a). Most carbonate detritus is concentrated within the sandstone lithologies, which contain 5% to 50% of comminuted shelly detritus and foraminifera. The concentration and preservation of carbonate detritus correlates negatively with grainsize within the sandstone lithologies. Intact foraminifera are generally found only in the plastic mudstones that form the top of individual fining-up packages and are erosionally truncated by the sandstone beds.

The common occurrence of peridotite, together with the association of chlorite and serpentine schist with rotated clinopyroxene porphyroclasts, is suggestive of a source terrane that includes metalherzolites such as those reported from the Jandaq ophiolite in Iran (Torabi et al. 2011). The mylonitization of amphibolites is a common feature of the Banda Terrane of West Timor (de Roever 1940). Deformation twinning of albite such as occurs in the amphibolites is not considered to occur below 500°C (Voll 1976; Tullis 1983; Gapais 1989) and is consistent with

high temperature metamorphism of the protolith. The widespread occurrence of tremolitic amphibole indicates that the source rocks underwent retrograde metamorphism following a high temperature metamorphic event.

2.4.5 Geochemical constraints on provenance

Source lithology exercises a dominant control on sedimentary geochemistry, which therefore provides a useful provenance indicator (Bhatia & Crook 1986; Wronkiewicz & Condie 1987; Roser & Korsch 1988; McLennan et al. 1990; McLennan et al. 1993). This study therefore used major and trace element geochemistry to investigate the provenance of carbonates, hemipelagic mudstones and conglomerate clasts from the Marobo and Viqueque Basins. Tabulated results are provided in Table 2.6 (Marobo section) and Table 2.7 (Viqueque section). This section presents evidence for changing rates of terrigenous sediment supply and the changing relative contributions to sedimentation from carbonate, Australian shale, Banda Terrane forearc, Gondwanan and volcanic arc sources.

2.4.5.1 Increasing terrigenous detritus

The fine grained sediments of the Synorogenic Megasequence of Timor can be split into three distinct groups based on their major (Figure 2.17 and Figure 2.18) and trace element geochemistry (Figure 2.17; Figure 2.19): i) the carbonate and marl rocks of the Batu Putih Formation; ii) the mudstones of the Viqueque section; iii) the mudstones of the Marobo section. The major and trace element compositions of all groups of fine grained synorogenic sediments, including the DSDP 262 data of Cook (1974a), are mainly controlled by dilution of carbonate with terrigenous sediment. The dilution effect is illustrated by the strong negative covariance of concentrations of major oxides (except P_2O_5), trace elements (except Sr) and organic content (based on LOI_{550} – see Figure 2.18b) with CaO (as a proxy for carbonate). Al_2O_3, a proxy for terrigenous sediment, shows the most linear negative correlation (Figure 2.17A). The sandstone samples have high SiO_2/Al_2O_3 ratios compared with the mudstones, which indicates quartz dilution of the sandstones. In contrast, the mudstones have relatively constant SiO_2/Al_2O_3 ratios, indicating that quartz dilution of mudstones by silt is insignificant.

The DSDP 262 core samples are similar in many respects to the rocks of the Batu Putih Formation. Most of the geochemical variability between DSDP 262 and Batu Putih rocks is consistent with differences in the relative importance of biogenic and diagenetic influences. For instance, the positive correlation of Sr with CaO is probably biologically controlled in both Batu Putih and DSDP 262 samples. However, high SiO_2/Al_2O_3 ratios in the DSDP 262 samples probably reflect the more radiolarian rich sediments in the DSDP core (Heirtzler et al. 1974) compared with foraminiferal sediments on Timor. Diagenetic dolomitization of the DSDP samples

leads to enrichment in Mg (Cooks et al. 1974). The dolomitized calcarenites from the base of DSDP 262 also have elevated P_2O_5/Al_2O_3 ratios, which Cook (1974b) interpreted as diagenetic phosphatization that occurred in association with dolomitization. The more calcareous Viqueque mudstones have higher phosphate concentrations than do the Marobo mudstones.

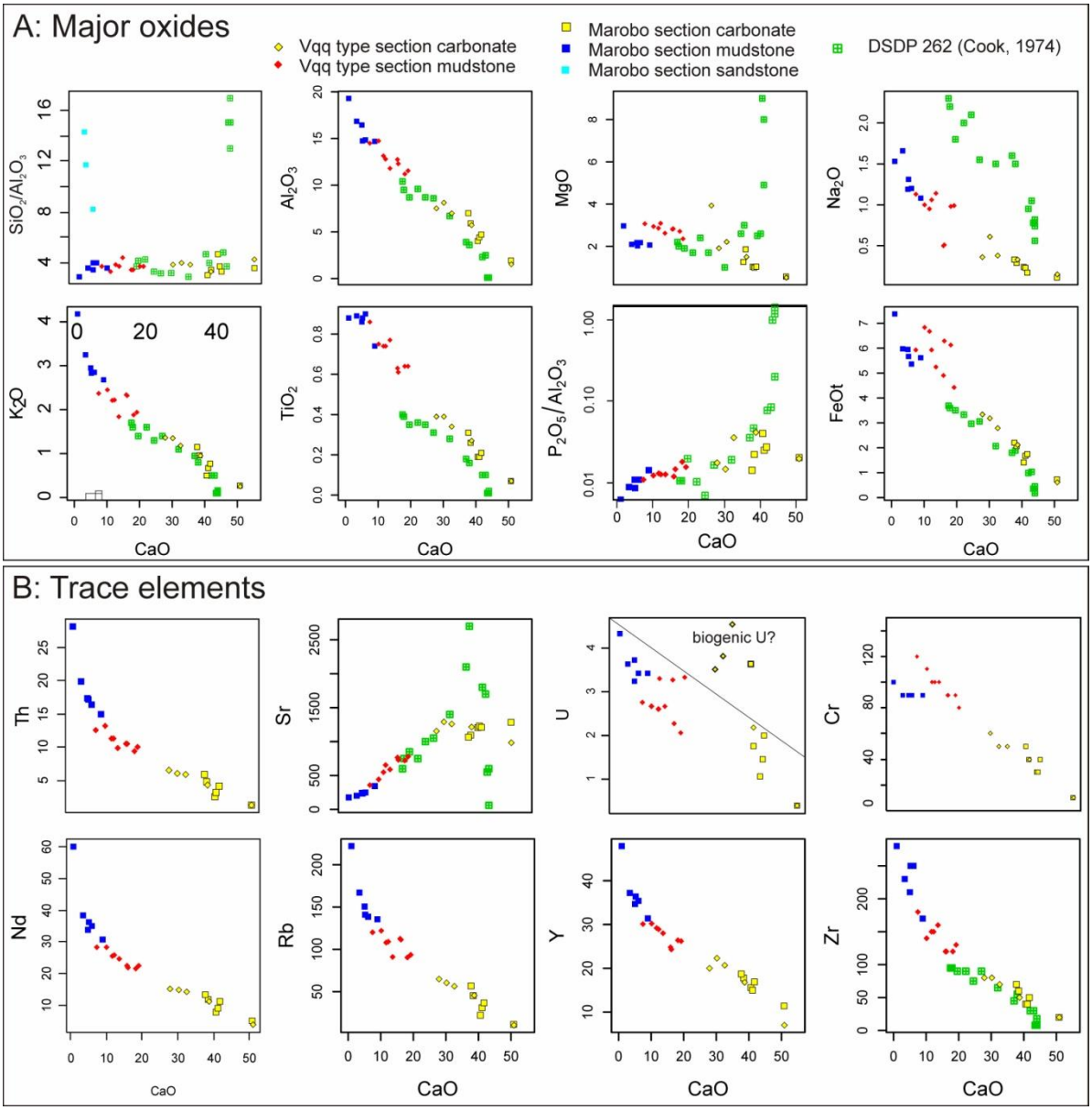

Figure 2.17: CaO vs. a) major oxides and b) trace elements, illustrating the effect of carbonate dilution and/or biogenic control on the geochemistry of synorogenic carbonates, marls and mudstones of the Viqueque and Marobo sections and DSDP 262 (Cook 1974a).

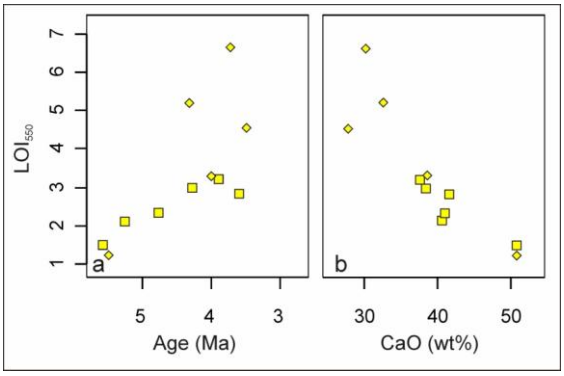

Figure 2.18: Correlations of LOI550 with age and CaO content for the Batu Putih Formation. Diamonds are Viqueque section, squares are Marobo section. A) The organic content increases throughout the Early Pliocene in both sections, and is matched B) by a decline in CaO due to increasing marliness.

The strong negative correlation between CaO and Al_2O_3, and between CaO and LOI_{550}, in the synorogenic carbonates and mudstones, including the Batu Putih and Viqueque Formations and the DSDP 262 core, is caused by variations in terrigenous sediment input. The LOI_{550} increase in the carbonates is correlated with increasing pollen concentrations (Nguyen et al. 2013). A plot of Al_2O_3 concentrations against biostratigraphic ages for all fine grained synorogenic rocks shows that Al_2O_3 concentrations increase upwards through all the sections (Figure 2.20). The LOI_{550} and Al_2O_3 trends in the Batu Putih Formation of the Viqueque and Marobo sections are both indistinguishable in terms of rate or timing. Both show a slow but steady increase in terrigenous sedimentation within the carbonate sediments, followed by a distinct jump associated with the onset of clastic sedimentation. The Al_2O_3 concentrations in the DSDP 262 core exhibit the same patterns and rates of but start increasing ~ 3 Myr later. Although the Al_2O_3 concentrations in the DSDP 262 samples remains low, the change in the rate of terrigenous sedimentation coincides approximately with the first sandy layer that marks the start of Level C of the DSDP 262 core (Figure 2.16).

2.4.5.2 Volcanic arc source

The volcanic arc north of Timor would have been active during deposition of the synorogenic sediments and only became extinct by around 2.4 Ma (Ely et al. 2011; Herrington et al. 2011). It could therefore reasonably be expected to contribute to terrigenous sedimentation. Major elements have proven useful for evaluating the provenance of mudstone suites by using discriminant function analysis to determine the bulk lithology of the source (Roser & Korsch 1988). A Roser and Korsch (1988) biogenically-influenced discriminant plot of mudstones and carbonates from the Viqueque, Marobo and DSDP 262 sections is compared with published whole rock geochemistry of volcanic and metamorphic rocks from Timor and the volcanic arc, and with Post Archaean Australian Shale (PAAS, Taylor & McLennan 1985; Pourmand et al. 2012) (Figure 2.19A). The major element geochemistry of the Batu Putih carbonates from the Viqueque and

Marobo sections has elevated values of discriminant function F2 that evolve from an apparently mature recycled field towards a more intermediate to mafic composition up the section (Figure 2.19B). The carbonate geochemistry ultimately converges on an intermediate to mafic area of the plot, which is occupied by the Viqueque section mudstones (Figure 2.19A). The major element geochemistry of the synorogenic samples, particularly those from the Batu Putih Formation, does not overlap significantly in composition with volcanic arc rocks from Atauro and Wetar (Elburg et al. 2005; Ely et al. 2011; Herrington et al. 2011), which have higher F1 values (Figure 2.19A).

A useful and simple distinction can be made between felsic, mafic and, particularly, ophiolitic provenance using Cr and Ni (e.g. Hiscott 1984). For example, Ni (in Olivine) and Cr (in Spinel, diopside and augite) are taken up by early crystallized mafic phases and thus provide useful indicators of mafic provenance. Felsic provenance is therefore generally associated with high Y/Ni ratios and low Cr/V ratios due to the lower concentrations of ferromagnesian minerals and higher concentrations of HREE. The Y/Ni ratios of the Batu Putih rocks from both the Viqueque and Marobo sections decline through time to values of 0.5-0.75 (Figure 2.19F). In the Viqueque section the mudstones fluctuate around the youngest values of the Batu Putih Formation. In the Marobo section, the Y/Ni ratios jump abruptly with the onset of clastic sedimentation and remain at relatively felsic values of 0.75 to 1.2. However, all synorogenic rocks have Y/Ni ratios that are an order of magnitude lower than the arc rocks from Atauro and Wetar. (Figure 2.19E).

The major and trace element characteristics of the synorogenic carbonates and mudstones suggest that the volcanic arc did not contribute significantly to background terrigenous sedimentation in the synorogenic basins and the sediment must have a different local source.

2.4.5.3 Banda Terrane (forearc) source

The relatively homogeneous discriminant function values of the Viqueque section mudstones plot on a mixing line between the average values of Banda Terrane metabasites on one hand and Banda Terrane metapelites on the other (Standley & Harris 2009) (Figure 2.19A). The discriminant function values for the Marobo section and DSDP 262 samples are within the range of Banda Terrane metapelites but more felsic than the average Banda Terrane metapelite (Standley & Harris 2009).

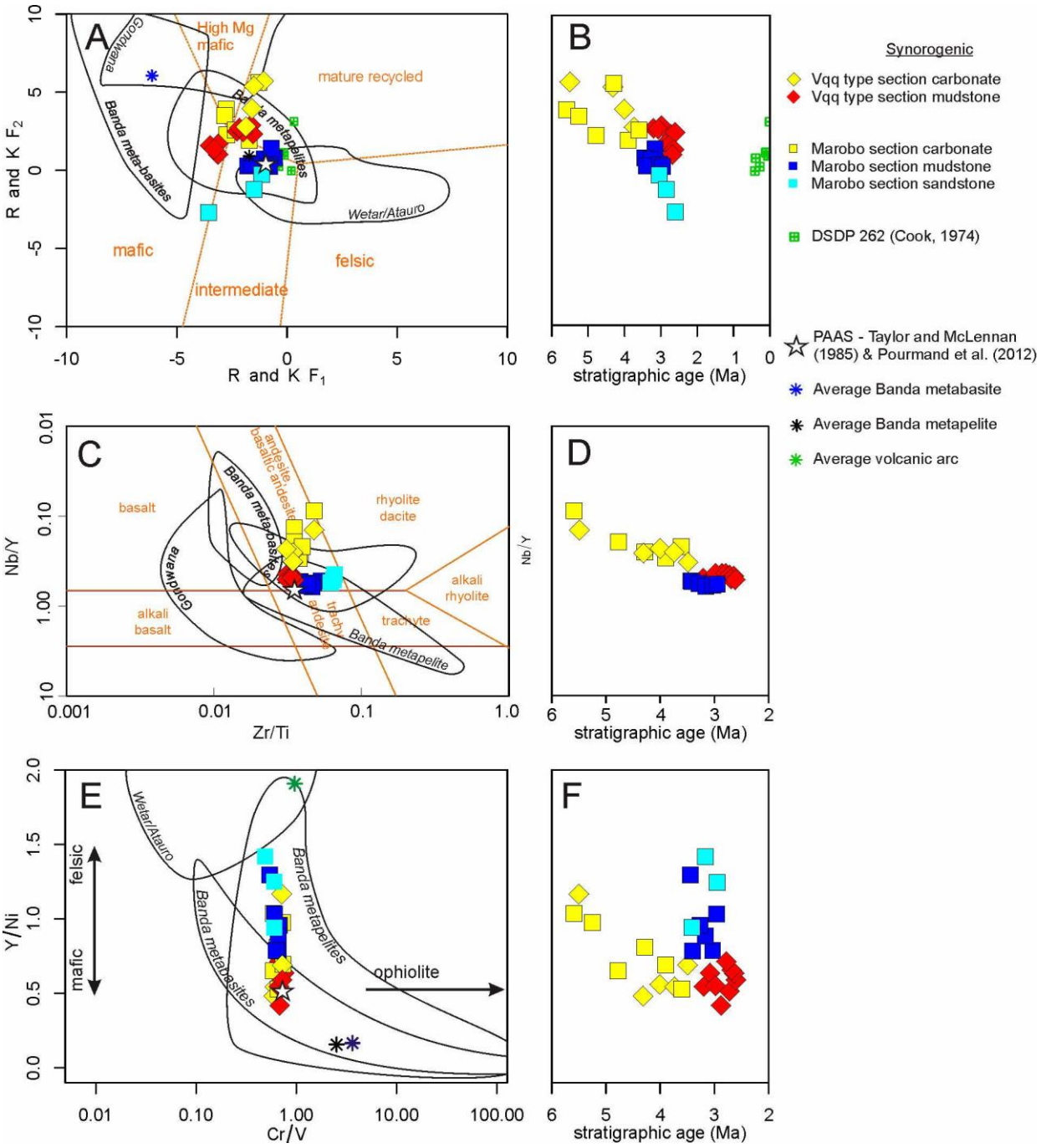

Figure 2.19: Sedimentary provenance discrimination diagrams for the synorogenic sediments. A) Sediment provenance discriminant function plot of Roser and Korsch (1988 - Al2O3 ratio functions for biogenically diluted geochemistry). The Viqueque Type Section mudstones plot on a mixing line between the average values of Banda Terrane metabasites and metapelites. The Marobo mudstones overlap with the DSDP 262 samples of Cook (Cook 1974a), and with PAAS (Taylor & McLennan 1985; Pourmand et al. 2012) but are slightly more felsic than the Banda metapelites. All synorogenic sediments have a more mafic composition than most local volcanic arc rocks. B) The carbonates of both sections show a trend toward lower F2 values and converge on the type section mudstone field. C) Ti/Zr v Nb/Y classification plot showing the intermediate trace element compositions of the mudstones. D) Trace element compositions evolve towards increasing Y during deposition of the Batu Putih carbonates. E) Plot of Y/Ni versus Cr/V for synorogenic sediments and potential source rocks. The synorogenic rocks have homogeneous and relatively low Cr/V ratios that are consistent with PAAS (Taylor & McLennan 1985; Pourmand et al. 2012), indicating that

ultramafic input into the basins is insignificant. G) Y/Ni trends downwards during deposition of the Batu Putih, indicating an increasing mafic source input.

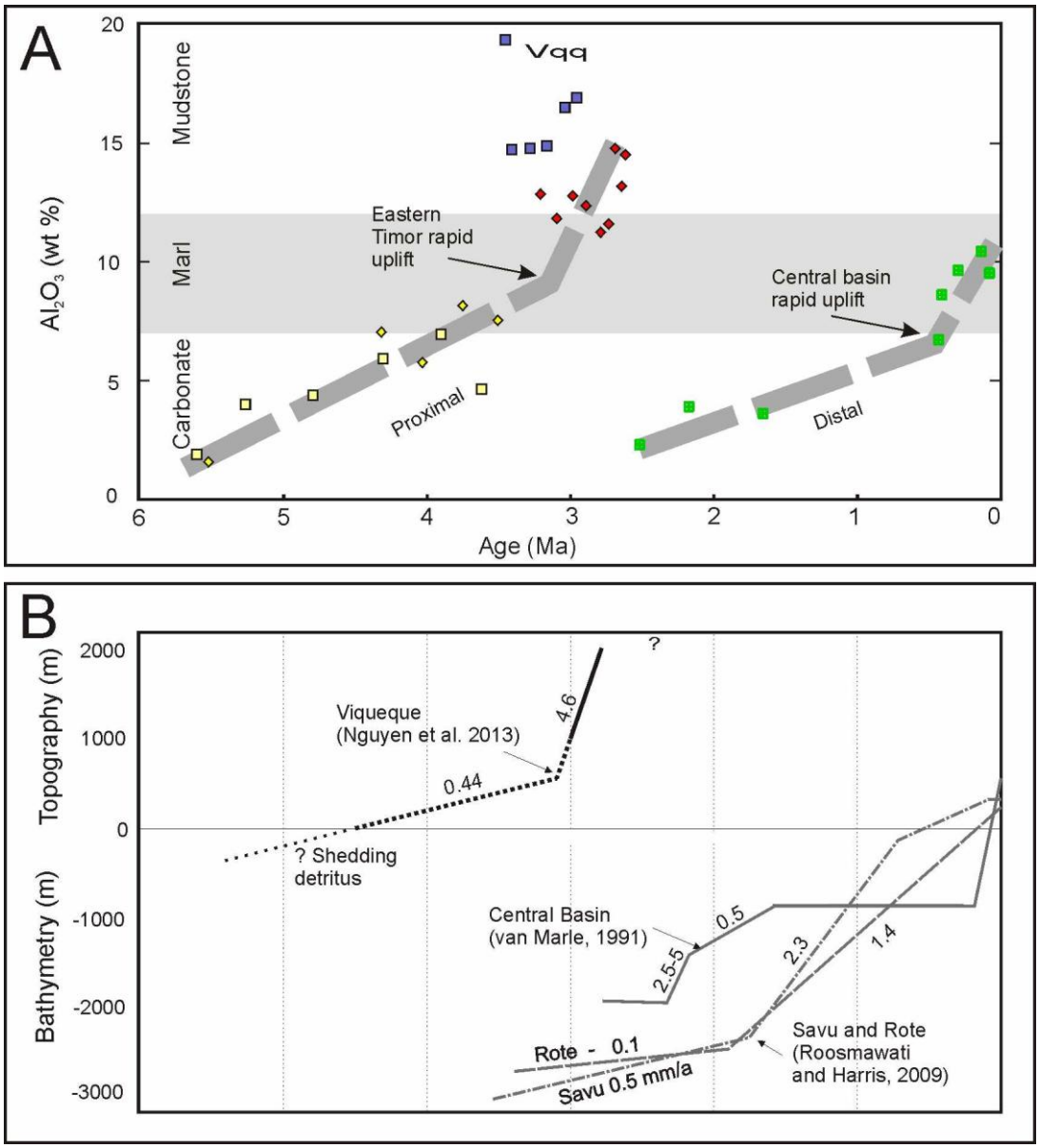

Figure 2.20: A) Plot of Al2O3 concentrations against sample age for the Timor Leste sections and the DSDP core. Both sections follow the same general trend but concentrations in the DSDP core begin increasing ~2.5 Ma later than in Timor Leste. B) Diagram showing uplift rates for the Viqueque type section (interpreted by present author based on age model and on Nguyen 2011. Note that Nguyen interpreted a single average uplift rate of 2.27mm/year), the Central basin of West Timor (van Marle 1991) and Rote and Savu (Roosmawati & Harris 2009). Carbonate, marl and mudstone fields are based on the relationship between CaO and Al_2O_3 shown in Figure 2.17A, with marl corresponding to approximate CaO percentages of 24% to 37%. Note the close correlation between the onset of rapid uplift in eastern Timor with a geochemical (and lithological) change in the type section, and the similar relationship between marl sedimentation in the DSDP core and uplift of West Timor. (Diagram B is published as Fig. 4 in Nguyen et al. 2013).

The Roser and Korsch (1988) plot is based on elements that may be mobile during diagenesis, but the discrimination scheme of Winchester and Floyd (1977) is based on the immobile trace element ratios Zr/TiO2 and Nb/Y (Figure 2.19C). Over time, the carbonate samples on this plot evolve from a dacite/rhyolite precursor composition to basaltic andesite composition and ultimately converge on the field occupied by the Viqueque section mudstones (Figure 2.19 C&D). The Marobo mudstones behave similarly on this plot to the Roser and Korsch plot, in that they occupy a more felsic field than the Viqueque mudstones but still have an intermediate composition.

The Cr/V versus Y/Ni diagram (Figure 2.19E) distinguishes ophiolite type source rocks, which have a high Cr/V signature (Figure 2.19E). The Banda Terrane rocks show great variability parallel to the Cr/V axis. However, neither synorogenic section shows any Cr enrichment trend, which would be expected if unroofing of the Banda Terrane forearc had been important in the source area.

Petrography of the conglomerates indicates that the Viqueque and Laleia Basins contained a large proportion of amphibolite and volcanic clasts. The geochemistry of similar lithologies has been reported from both the Gondwana Megasequence and Banda forearc Terranes (Berry & Jenner 1982; Standley & Harris 2009), so the geochemistry of several clasts was analyzed (Figure 2.21). The basic rocks of the Gondwana and Banda Terranes are generally geochemically distinctive from each other and most clasts fell well outside the range of compositions reported for Gondwanan rocks. This is consistent with their derivation from the Banda Terrane. However, the Banda and Gondwanan basic rocks do have an area of overlap on most geochemical plots including both Roser and Korsch and Winchester and Floyd plots (Figure 2.21 A&B). A basaltic clast from Viqueque (LM22-a-3) and an amphibolite clast from Laleia (La591-1) plotted in this area of overlap on the Ti/Zr v Nb/Y plot (Figure 2.21C). The Laleia amphibolite clast (La591-1) fell well inside the Banda Terrane field on the Roser and Korsch plot (Figure 2.19A) but the Viqueque basalt clast again occupied the overlapping field.

The REE profiles of these and other clasts taken from the three basins are shown in Figure 2.21C. Both clasts from the overlapping field had N-MORB-affinity chondrite-normalized REE profiles. The profiles were similar to the REE profiles of a presumably Gondwanan basaltic block that I sampled in the Synorogenic Mélange near Bobonaro, south of the Marobo Basin, and similar to a Cribas (Gondwanan) basalt. Both the Bobonaro and Cribas basalts co-plotted with the Viqueque and Laleia clasts in the Gondwana/Banda overlap zone on the Ti/Zr v Nb/Y plot (Figure 2.21C). Complete REE profiles are not available for the Banda Terrane rocks but the limited available data suggests that the Banda Terrane and Gondwana rocks and conglomerate clasts all

have MORB affinity REE profiles and cannot be discriminated without geochronologic data. The remainder of the clasts exhibited typical calc-alkaline REE profiles. All were LREE enriched and had negative Europium anomalies. These characteristics are consistent with a Banda Terrane forearc source area.

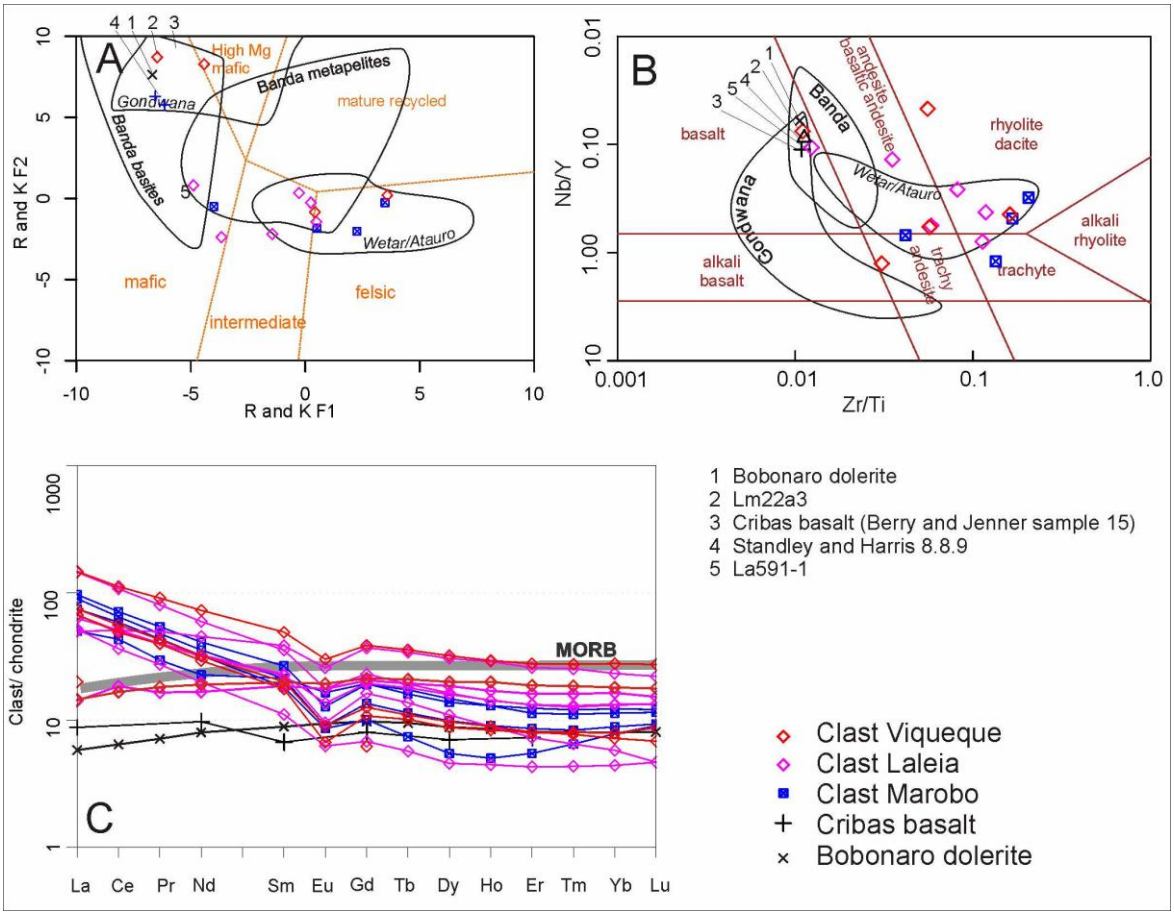

Figure 2.21: Provenance discrimination diagrams for the synorogenic conglomerate clasts, a basalt from Cribas reported by Berry and Jenner (1982), and a basalt collected from a mélange block near Bobonaro. A) Provenance discriminant function plot of Roser and Korsch (1988). Most clasts fall within the reported range of Banda Terrane lithologies but several fall in an area of overlap with the Gondwana basites, along with the Bobonaro and Cribas basalts. B) Ti/Zr v Nb/Y classification plot showing the trace element compositions of the conglomerate clasts. Note the narrow zone of overlap between Gondwanan basalts/alkali basalts and rocks from the Banda Terrane. C) Chondrite normalized (data of Boynton 1983) REE concentrations of conglomerate clasts compared with a Cribas basalt (Berry & Jenner 1982) and a gabbro from the Synorogenic Mélange (this study).

2.4.5.4 Australian continental source

The most noticeable similarity on all mudstone provenance diagrams (Figure 2.19) is the similarity between the mudstones and PAAS, which has a bulk intermediate composition (Taylor & McLennan 1985). This is explored further using a multi-element plot of trace elements normalized to PAAS (Figure 2.22A). Trace element concentrations are generally flat relative to PAAS. The ferromagnesian trace elements are slightly depleted in the Marobo section (Figure 2.22A). With the exception of biologically enriched Sr, the Large Ion Lithophile Elements (LILE)

are depleted in both sections but more so in the Viqueque section. The High Field Strength Elements (HFSE) are enriched in the Marobo section and slightly depleted in the Viqueque section. The strength of the relationship between the carbonates and mudstones is emphasized by the correlation plots in Figure 2.22B The ratio of the ferromagnesian and HFSE trace elements shows a continuous trend between the Batu Putih Formation and the Viqueque mudstones that is controlled by the carbonate concentration. However, the Marobo mudstones show a trend of HFSE enrichment with little variation in Cr and a slight decline in Ni.

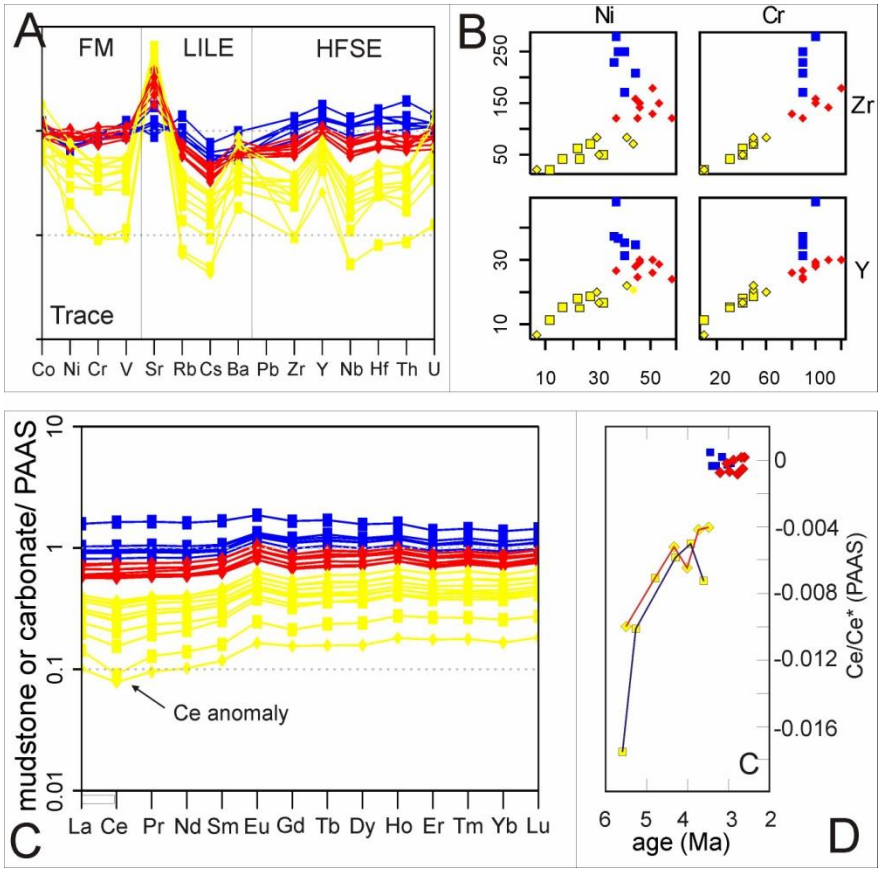

Figure 2.22: (A) PAAS normalized (Taylor and McLennan (1985), as modified by Pourmand et al. (2012)) multi-element diagram. B) Covariance plots for Ni and Cr (ferromagnesian – L and R) against Zr and Y (HFSE – top and bottom). Note the continuous trend for Batu Putih and Viqueque mudstones and divergent trend for Marobo mudstones. C) PAAS normalized (Taylor & McLennan 1985; Pourmand et al. 2012) REE concentrations for mudstone and carbonate samples. D) Temporal trend in the Ce anomaly.

The REE are well suited to studying sedimentary provenance because of their relatively short residence time in ocean water and their immobility during weathering, transport, diagenesis and metamorphism (McLennan 1989). REE and trace element multi-element plots of elemental concentrations normalized to PAAS are shown in Figure 2.22C. Overall the samples show flat REE profiles relative to PAAS. The fields for Batu Putih carbonates, Viqueque mudstones and Marobo mudstones are well defined and not overlapping. The PAAS-normalized REE concentrations are all <1 for the Batu Putih carbonates and for the Viqueque section mudstones.

Concentrations of REE increase upwards as carbonates become marlier, because the REE are bound in the clay structure (McLennan 1989). Marobo mudstones are slightly REE enriched relative to PAAS.

A slight enrichment can be seen in heavy relative to light REE in the carbonates, but is less obvious in the type and Marobo sections. The carbonates show a negative Ce anomaly relative to PAAS. The Cerium anomaly Ce/Ce* on a REE diagram (normalized Ce values that lie below or above a straight line interpolation between La and Pr) has been shown to be affected by seafloor redox conditions, diagenesis and proximity to terrigenous sources (Liu et al. 1988; Murray et al. 1991; Shields & Stille 2001). The Cerium anomaly relative to PAAS was calculated as

$$Ce/Ce^* = \log[2Ce^*/(La^* + Pr^*)]$$

where * is the sample value normalized to PAAS. All the carbonate samples reported here show a small negative Ce anomaly relative to PAAS (Figure 2.21). The anomaly becomes less negative upwards through the section and is positively correlated with Al_2O_3 (and negatively with CaO). This suggests that in this instance the anomaly becomes less negative due to an encroaching sediment source rather than a change in seafloor redox conditions. Nevertheless, the low U concentrations (0.38-0.39ppm) and the low U/Th ratios (0.3 to 0.31) at the base of the Batu Putih Formation are consistent with an oxic sedimentary environment at that time (e.g. Liu et al. 1988). Both sections show a noticeable negative excursion in the Ce anomaly at ~4 to 3.5 Ma.

Overall, the major, trace and REE geochemistry of the Batu Putih Formation and the Viqueque Formation mudstones is extremely similar to reported values for PAAS.

2.4.5.5 Neodymium isotope evidence for a mixed Banda forearc and PAAS source

In addition to standard geochemistry, mudstone samples from the base, middle and top of the Viqueque Formation in the Marobo and Viqueque Basins (a total of six samples) were analyzed to determine their Neodymium isotope characteristics. Samarium fractionates from neodymium during the melting of mantle and formation of continental crust, producing significant isotopic variations through time. The Nd model age of sediments therefore generally reflects the mean age of mantle extraction of the sediment source (McCulloch & Wasserburg 1978). However, Epsilon neodymium (εNd) of sediments may be affected by the chemistry of seawater that foraminifera use to grow their shells. εNd in seawater has been shown to vary independently of hemipelagic sediment inputs to seawater (Jones et al. 1994). The εNd of foraminifera seems to be similarly independent of detrital inputs and instead reflects the εNd of the water mass (Vance et al. 2004), which ranged between -4 and -6.6 in the Plio-Quaternary Indonesian Throughflow (Martin

& Scher 2006; Gourlan et al. 2008). For this reason, the carbonate rocks were excluded from Sm/Nd isotope analysis. The results are summarized in Table 2.9 and Figure 2.23.

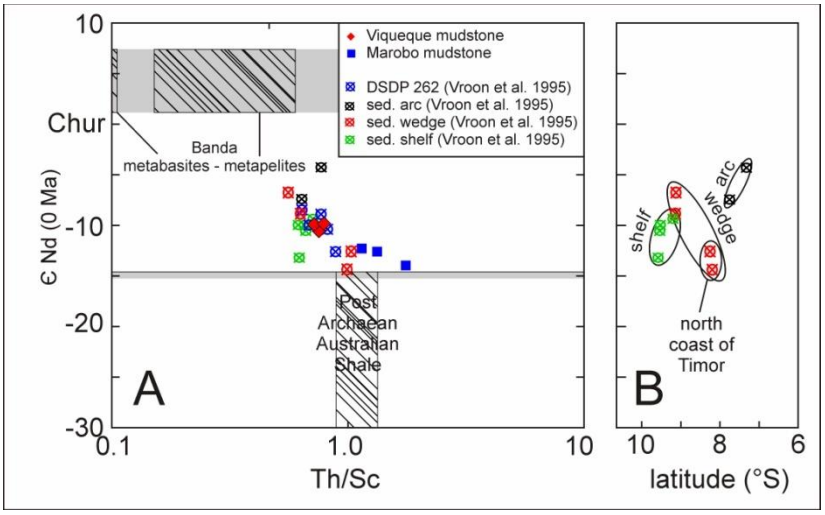

Figure 2.23: A) εNd versus Th/Sc ratio for modern seafloor sediments (Vroon et al. 1995) and the mudstones of the Viqueque and Marobo Basins. B) Latitudinal trend to most negative εNd on the north side of the orogenic wedge, where sediment is largely derived from erosion of the Gondwanan lithologies exposed on the north side of the drainage divide in Timor.

All mudstone samples had bulk provenance depleted mantle model ages (TDM) in excess of 1.6 Ga, and εNd values of -9.8 to -14. A plot of εNd (as an indicator of provenance age) against Th/Sc ratios (indicative of bulk composition) (Figure 2.23A) differentiates between old evolved crust and young arc sources (McLennan et al. 1993). The Viqueque section mudstones had less negative εNd values and lower Th/Sc ratios than the Marobo mudstones, which is consistent with a less evolved bulk provenance for the Viqueque mudstones, compared with the more evolved Marobo section mudstones.

The Proterozoic Nd model ages and εNd values of the synorogenic mudstones of Timor are not compatible with the age, tectonic setting or εNd values of the Banda Terrane and related rocks (Morris et al. 1984; Vroon et al. 1993; Honthaas et al. 1998; Harris 2006; Standley & Harris 2009) (Figure 2.23). Negative εNd values were obtained from Gondwanan Maubisse Formation samples on Timor by Ron Harris (unpublished data pers. comm). However, the Gondwanan volcanics are Permian in age, which is substantially younger than the Proterozoic bulk provenance model age calculated for the mudstones of the Viqueque Formation (Table 2.9).

The synorogenic mudstones have similar provenance ages and Th/Sc ratios to modern sediments accumulating in the Timor region (Vroon et al. 1995). Vroon et al.'s (1995) seafloor sediment data shows a latitudinal trend across the arc (Figure 2.23B), with the most negative εNd and oldest model ages found on the orogenic wedge north of Timor. The Marobo samples plot

close to these values (Figure 2.23A). The northern half of Timor, which sheds sediment to the northern side of the island, is dominated by outcrop of the shales, sandstones and metamorphic rocks of the Gondwana Megasequence (Figure 2.1). The Viqueque mudstones plot in the less-evolved field occupied by seafloor sediments presently accumulating on the southern part of the orogenic wedge, where most of the Banda Terrane sediments are shed.

Both the modern sediments and the Viqueque mudstones have similar model ages and εNd values to Australian shales (Allègre & Rousseau 1984) (Figure 2.23), which is consistent with the PAAS-type major and trace element geochemistry of the mudstones. Two sources may have contributed a PAAS type signature to Timor mudstones. Firstly, abyssal shales derived from Australia make up the base of the Australian Margin Megasequence in the Kolbano region (Charlton 1989; Sawyer et al. 1993) and would have provided the bulk of sediments incorporated in the Timor accretionary wedge. These would probably have a Nd isotope signature similar to that on the modern NW shelf of Australia (Vroon et al. 1995). Secondly, the synorogenic Mélange is formed of remobilized Triassic Australian shales (Harris et al. 1998). Overall, the Viqueque section samples appear to lie on a mixing line between a PAAS-type source and a Banda Terrane forearc source. The Marobo samples are very close to PAAS.

2.4.5.6 Chemical weathering evidence for rapid uplift

If the volcanic arc was not contributing to sedimentation and the terrigenous sediment was sourced from a newly emergent island, the new landmass might be expected to be a focus for chemical weathering. Source area weathering, diagenesis and potassium metasomatism can alter the geochemical characteristics of sediments in a quantifiable way (Nesbitt & Young 1989; McLennan et al. 1993; Fedo et al. 1995). Weathering of rocks results in enrichment of Al_2O_3 at the expense of alkalis. The effect, along with the effects of diagenetic K metasomatism, can be evaluated using the Chemical Index of Alteration (CIA, Nesbitt & Young 1982; Fedo et al. 1995) (Figure 2.24A). The CIA was calculated from molar proportions of oxides in mudstone samples only using the formula

$$CIA=Al_2O_3/(Al_2O_3+CaO^*+Na_2O+K_2O) \times 100,$$

where CaO* is silicate CaO. Dolomite was not detected by XRD so the molar proportions of major elements were used to calculate CaO* using the formula

$$\text{mol } CaO^* = \text{mol } CaO - \text{mol } CO_2 - 10/3 \text{ mol } P_2O_5$$

This calculation corrects for carbonate content (through CO_2) and apatite (through P_2O_5) and thus removes the influence of non-silicate CaO. CIA is meaningless (hence not calculated) for carbonate rocks, so phosphate enrichment is not problematic.

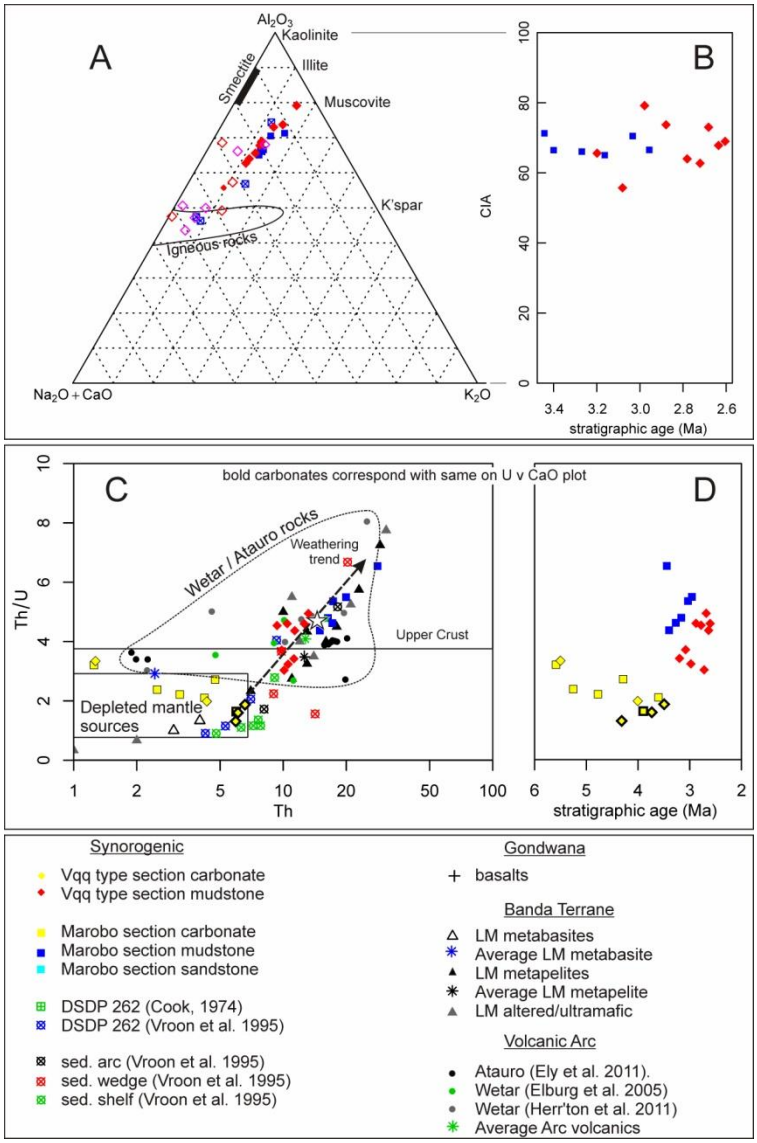

Figure 2.24: A) Chemical Index of Alteration plot C) Plot of Th/U versus U for mudstones, carbonates including DSDP 262, and sea floor sediments (Vroon et al. 1995). B & D) Temporal variations in CIA and Th/U.

The mudstone sediments of both basins plot along a trend approximately parallel to the 0% K_2O line, and show little evidence of diagenetic K_2O addition (Figure 2.24A) (e.g. Fedo et al. 1995). The low Al_2O_3 values indicate that the weathering in the source area was only moderate and average CIA value did not vary between sections. The average CIA value of the Viqueque section is 67.8±7 and of the Marobo section was 67.7±2.6. No temporal trends are observed (Figure 2.24B). Individual conglomerate clasts have lower CIA values in general than the mudstones.

Their CIA values are close to the primary CIA values of unweathered rocks, suggesting that they are only minimally weathered.

Th concentrations and Th/U ratios are lowest in depleted mantle and increase during weathering and sedimentary recycling as the U is mobilized. Figure 2.24C is a plot of Th/U vs. Th (McLennan et al. 1993). The Th/U ratios of the Batu Putih rocks in both the Marobo and Type sections lie within the range of depleted mantle sources typical of volcanic arc rocks (Figure 2.24C). However, the local volcanic arc rocks from Wetar and Atauro are Th-enriched by comparison with the terrigenous source for the Batu Putih marls. The Th/U ratio of the Batu Putih Formation rocks remains generally stable as Th concentrations increase (Figure 2.24D), with the exception of several of the youngest samples (bold on Figure 2.24A), mostly from the type section. These samples are enriched in U relative to the carbonate dilution trend in Figure 2.17B. The U-enriched characteristics of these particular samples, which are probably biogenic, are similar to those of sea floor sediments sampled across the Timor orogenic wedge immediately east of Timor, and in DSDP 262 by Vroon et al (1995). The Th/U ratios of the mudstone sections show a poorly-defined trend of increased weathering upwards through the section that is clearer in the Marobo mudstones (Figure 2.24B).

Together, the CIA and Th/U data indicate only moderate weathering intensity, with a minor increase in weathering upsection (Figure 2.24D). This suggests that erosion was keeping pace with chemical weathering and fresh rock was being quickly exhumed at the surface. Erosion is primarily driven by tectonic activity (e.g. Quigley et al. 2007), so the low intensity of weathering throughout the deposition of the Viqueque Formation (Figure 2.24) is consistent with rapid tectonic uplift. The greater degree of weathering in the source area for the Viqueque section is probably related to its more mafic and variable composition as seen in the petrography (Table 2.5) and major and trace element geochemistry (Figure 2.19).

2.5 Sedimentary response to collision and extrusion

Several stratigraphic sections have been biostratigraphically dated and logs published that document the transition from open marine carbonate to marl and thence to clastic sedimentation at various points along the strike of the Banda orogen (Heirtzler et al. 1974; De Smet et al. 1990; van Marle 1991; Haig & McCartain 2007; Harris et al. 2009; Roosmawati & Harris 2009; Haig 2012). Age models and geochemical analyses presented (Figure 2.5; Figure 2.12) and reviewed in this study (in the case of the DSDP 262 section, Figure 2.16) allow a quantitative estimation of the timing of onset of geochemically-defined-marl sedimentation and clastic sedimentation for the Marobo, Viqueque and DSDP 262 sections (Figure 2.20). Qualitative estimates for marl sedimentation and quantitative estimates of clastic sedimentation can also be derived from

published biostratigraphy for other locations in Timor Leste (Haig 2012), West Timor (De Smet et al. 1990; van Marle 1991) and the island of Rote immediately west of Timor (Roosmawati & Harris 2009). These can then be related to the established timing of uplift events (Figure 2.20 and Figure 2.25). The combination of these data provide new insights into the timing, rates and style of sedimentary response to uplift and exhumation associated with collision of Australia with the Banda Arc (Figure 2.25).

2.5.1 Batu Putih terrigenous sedimentation

2.5.1.1 Timing

The first indication of tectonic activity affecting the synorogenic sections described above is the influx of terrigenous sediment into the pelagic carbonate basins of the Batu Putih Formation, which gives rise to marl rather than carbonate sedimentation. Terrigenous sedimentation recorded by the geochemistry of the Viqueque and Marobo sections begins synchronously within the resolution of the data (Figure 2.20), and increases from close to the base of the section.

A similar trend is evident in the DSDP 262 core, which follows the same geochemical trend but begins about 3 Myr later. The DSDP 262 site is not yet exhumed and therefore not strictly equivalent to the exhumed Marobo and Viqueque Basins. However, the bio and lithostratigraphy of exhumed synorogenic sections in the Central basin of West Timor record open marine limestone deposition until 2.4 Ma when the Sabau area of West Timor first began to shallow (De Smet et al. 1990; van Marle 1991) (Figure 2.25). It is not possible without further work to say that no marl was accumulating in the central basin prior to 2.4 Ma but a) van Marle (1991) does distinguish between open marine limestones and marls, and b) Haig's (2012) section logs from Timor Leste indicate that marlyness in limestones is detectable in hand sample well before the geochemical limestone-marl threshold (black dotted line on Figure 2.25). On this basis, it seems clear that, having begun synchronously at >4 Ma across at least 130 km, the onset of terrigenous sedimentation took at least 1.6 Myr to propagate a further ~90 km to reach the Sabau section of the Central basin.

Haig's (2012) paleobathymetric analysis of foraminifera in several sections, including Marobo (he sampled a poor section in a more southern part of the basin) and Viqueque, also incorporated van Marle's (1991) data. Haig's results similarly indicated an early and relatively synchronous uplift of most of Timor Leste. The modern onshore and offshore slopes of Timor are not greatly different from each other and are compatible with the geometry of the orogen suggested by Haig's (2012) paleobathymetric contours. However, Haig's (2012) closure of the contours on the northern side of Timor seems without basis. Nevertheless, Haig's (2012) contours support the idea developed here that Timor emerged above sea level prior to 4.3 Ma.

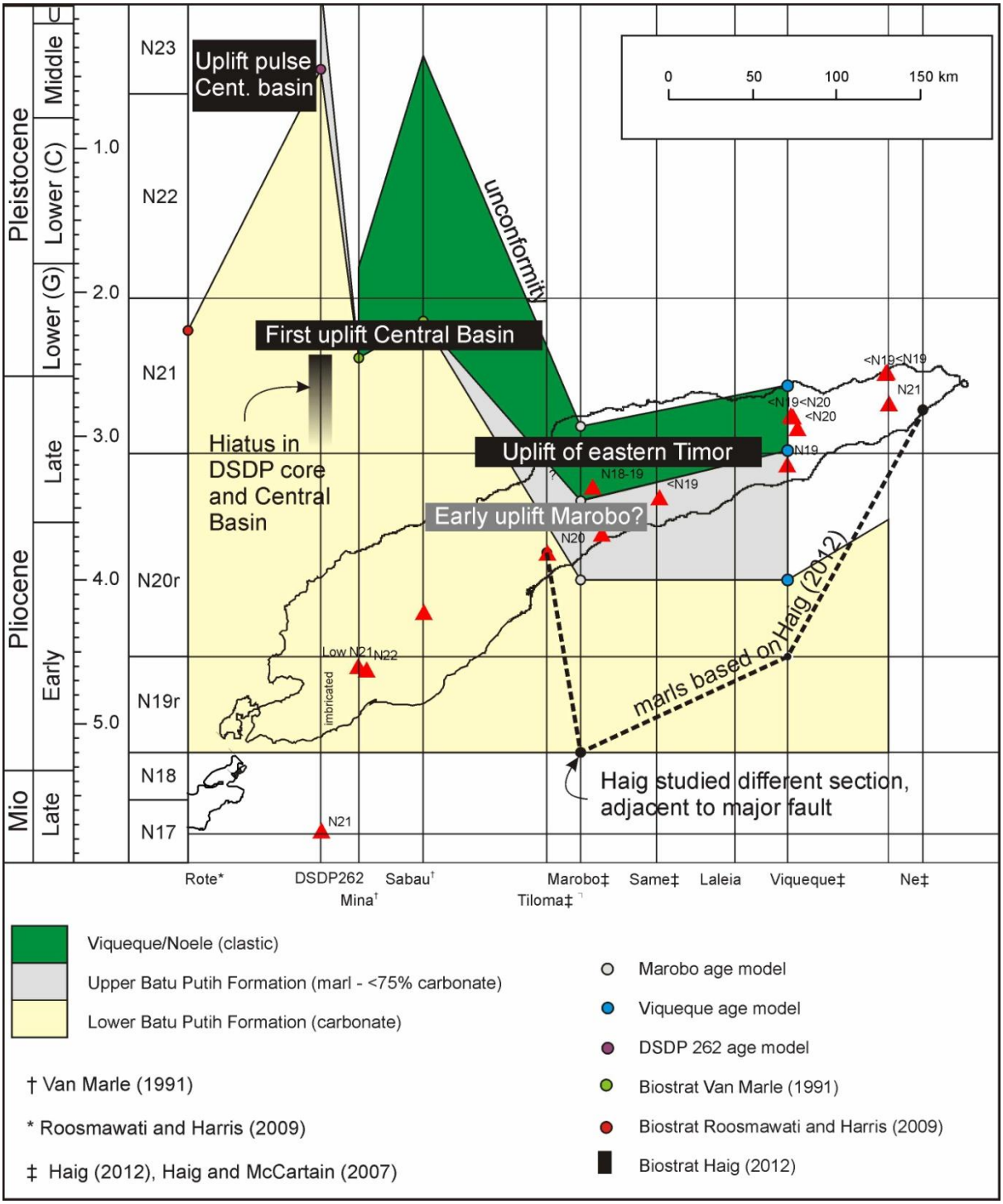

Figure 2.25: Generalized time (vertical axis) versus distance (horizontal axis) plot of synorogenic lithostratigraphy of Timor. Changes in the character of sediments correspond closely with uplift events.

2.5.1.2 Provenance

The tectonic interpretation of geochemical changes in the synorogenic sections requires an underlying assumption that the terrigenous sediment that contaminates the Batu Putih Formation is derived from a proximal and uplifting landmass, rather than from a distal mud source such as Australia or another island in the Indonesian region, possibly in the volcanic arc. A volcanic arc

source is almost excluded by comparison of the marl geochemistry with rocks on Wetar and Atauro (Figure 2.19; Figure 2.24). A volcanic arc source is also unlikely because the Banda Arc had been active since 12 Ma (Abbott & Chamalaun 1981; Honthaas et al. 1998) and yet the base of all measured sections is characterized by high carbonate content, low levels of terrigenous minerals and elements, and low LOI values (indicative of low organic carbon content - Dean 1974).

The DSDP 262 site was still accumulating clean carbonates, while the Marobo and Viqueque Basins were accumulating coarse clastic sediment (Figure 2.25). This suggests that mud dispersion was poor. The Timor region's modern rainfall is typically concentrated in a four month monsoon period over the austral summer, when the Indonesian Throughflow (ITF) is at its weakest (Cecil et al. 2003). Long range dispersal of mud from regional landmasses is therefore weak in the modern ITF setting. Poor mud dispersion presently gives rise to an Eastern Indonesian clay province around Timor that is characterized by high chlorite and kaolinite. Gingele et al. (2001) suggest that this is derived from the erosion and weathering of the mica-rich crystalline basement and the lack of volcanic effusives on Timor. Differences in clay mineral composition across the Timor Trough suggest that mud deposited north of the Timor Trough is presently unlikely to be of Australian provenance (Gingele et al. 2001).

In a setting characterized by poor mud dispersal, the clean carbonates at the base of the section suggest that no proximal land mass was shedding vegetation and clastic detritus into the Timor basin. That is to say, mud from the Banda Arc and Australia was being poorly dispersed, as it is at present, and not carried the <200 km distance to the synorogenic basins now exhumed on Timor. Therefore, the gradational change from clean pelagic carbonates to marls is interpreted to record an emerging proximal landmass. The increasing terrigenous sedimentation recorded in the Batu Putih marls is accompanied by an increase in total pollen and charcoal that Nguyen interpreted to record the emergence of a proximal landmass since at least 4.5 Ma (Nguyen 2011; Nguyen et al. 2013). The emergence of a proximal landmass at that time is also consistent with Haig's (2012) paleobathymetry.

The emergence of the Timor landmass was probably due to underplating of a Timor Plateau (Chapter 1 and Duffy et al. (accepted manuscript)). Underplating and duplexing of continental material would have resulted in doming of the forearc (e.g. Harris et al. 2000), leading in turn to exhumation of the outer arc high/accretionary wedge. Most of this wedge would have been formed of abyssal shales and cherts such as those that make up the base of the Australian Margin Megasequence in the Kolbano region (Charlton 1989; Sawyer et al. 1993). The terrigenous sediment in the upper part of the Batu Putih Formation in both the Viqueque and Marobo sections

is geochemically indistinguishable from the mudstones of the Viqueque section (Figure 2.19 and Figure 2.22B). Major and trace element concentrations and ratios (Figure 2.19) of the synorogenic carbonates and marls suggest that the terrigenous sediments in the marls are derived from a relatively mature source that compares well with PAAS. It therefore seems likely that erosion of Australian passive margin shales incorporated in the accretionary wedge provided the mature, early trace element signature in the Batu Putih Formation. The shale clasts in the basal carbonates of the Batu Putih Formation of the Marobo and Viqueque sections may therefore be derived from the accretionary wedge rather than the Synorogenic Mélange. If so, the diapirism that intrudes the Batu Putih and the Viqueque Formation (Chapter 1) may entirely post-date deposition of the Batu Putih Formation, and be a dubious indicator at best of the timing of collisional orogenesis (c.f. Haig & McCartain 2007, p.894).

The temporal evolution toward increasingly mafic geochemistry in the Batu Putih Formation (Figure 1.18) suggests that the mature shale source is increasingly diluted by a mafic source. This probably records the erosional removal of the accretionary wedge and initial exhumation of the Banda forearc in the hinterland.

The accretionary wedge has now been completely eroded away. The Proterozoic Nd model ages of Viqueque Formation mudstones (Table 2.9), and similar ages recorded in modern sediments accumulating on the modern orogenic wedge (Vroon et al. 1995), indicate that since the exhumation of the Banda Terrane, the Synorogenic Mélange, rather than the much younger arc or forearc, has been the primary source of muds incorporated in synorogenic sediments. A significant difference in the Nd model ages of sandstone mudstone pairs is commonly reported in other similar studies (McLennan et al. 1989; Augustsson & Bahlburg 2003; Evans et al. 2009; Tobgay et al. 2010). These differences are usually attributed to sedimentary sorting of different sources (McLennan et al. 1989). Shale diapirism and mélange formation is a common component of arc-continent collisions (Williams et al. 1984; Barber et al. 1986; Rangin et al. 1990; Yu & Jiunn Chenn 1995; Harris et al. 1998; Hall & Wilson 2000; Chang et al. 2001; Duerto & McClay 2011) and this study indicates a great potential for the recycled products of shale tectonics to control the Nd provenance signature in synorogenic mudstones derived from arc-continent collision zones. If exhumed basins are mudstone or carbonate dominated, and tectonically isolated from the source area, reconstruction of their tectonic setting may be problematic. For instance, Miller and O'Nions (1984) found that shales, slates and clay sediments in Britain did not tend to record the accretion of young mantle derived material during the Caledonian, Hercynian and Grenville orogenies. Results such as this may reflect the importance of remobilization and reworking of continental shales during arc-continent collision.

2.5.2 Viqueque Formation clastic sedimentation

2.5.2.1 Timing

Coarse clastic sedimentation in the Central basin of West Timor began at ~2.2 Ma and coincided closely with the onset of rapid uplift as determined by paleobathymetry in the Central basin (Figure 2.25) (De Smet et al. 1990; van Marle 1991). East of the Central basin, clastic sedimentation begins first in the Marobo Basin of central Timor at ~3.5 Ma, and later at ~3.1 Ma in the Viqueque Basin further east (Figure 2.25). Haig's (2012) paleobathymetry for Timor does not provide detailed insight into temporal patterns of uplift, but Nguyen (2011) used the palynological evolution of the type section to assign source paleoelevations to horizons within the type section. Nguyen's (2011) data indicated source paleoelevations of 1000 m at 84 m above the base of the section and 2000 m at 173 m above the base of the section. Based on these points, Nguyen (2011) estimated a bulk uplift rate of 2.27 mm/yr for the combined Batu Putih and Viqueque Formations of the type section.

Nguyen's (2011) uplift rates can be refined using age model constraints. Therefore, by assigning a conservative 0 m elevation to my geochemical sample TS061, which records an increase in terrigenous sedimentation, and assigning ages from the type section age model to Nguyen's (2011) paleoelevations, I derived a revised topographic uplift rate of 0.44 mm/yr during deposition of the Batu Putih marl (Figure 2.20B). This uplift rate increases to between 2.6 mm/yr and 4.6 mm/yr (depending on the age used for the top of the section) during deposition of the Viqueque Formation (Figure 2.20B) (For full details see Nguyen et al. 2013). These rates of uplift are higher than rates of up to 1.6 mm/yr determined for Timor's north coast during the last 150 kyr (Cox 2009). However, the pattern and rates are consistent with, but 0.7 Myr earlier than, the first phase of bathymetric uplift of the Central basin of West Timor (De Smet et al. 1990; van Marle 1991). They are also 1.2 Myr earlier than a similar uplift event on Savu and Rote (Harris et al. 2009; Roosmawati & Harris 2009), and 2.7 Myr earlier than final uplift of the Central basin into the terrestrial realm.

The revised surface uplift rates for Timor based on Nguyen's (2011) palynology suggest that, like the Central basin, rapid uplift of the Viqueque Basin hinterland triggered the onset of coarse clastic sedimentation. The close association between the onset of rapid uplift and the onset of turbidite sedimentation is in keeping with observations by Klein (1985) who suggested that turbidite stratigraphy, particularly frequency and periodicity, provides an event stratigraphy that is related to tectonic uplift in the hinterland, and that deep sea fan turbidites begin to be generated at a threshold uplift rate of 0.4 mm/yr. It is also notable that the onset of rare clastic sedimentation at the DSDP 262 site is marked by a distinct change in the marlyness (Al_2O_3 concentrations) of the

background sedimentation, and that these lithological changes appear to record the most recent rapid uplift and subaerial exposure of the Central basin (Figure 2.20; Figure 2.25). This is probably because the uplift and emergence of the Central basin diverted sediment that would previously have been deposited in the Central basin, into the Timor Trough. In contrast, the DSDP 262 core does not lithologically record the earlier uplift of Rote (Figure 2.20), probably because the core site is upstream of Rote in the Indonesian Throughflow. The DSDP 262 core geochemistry suggests that rates of change of geochemical stratigraphy may provide a useful means of determining the timing of pulses of tectonic activity in the hinterland, even for successions that do not include a clastic sediment component.

2.5.2.2 Paleogeography and basin tectonic setting

The influx of clastic sediments records the rapid increase in source area uplift rates, but the basin style and clast provenance provide insights into the relationship between structural development and unroofing sequences in the hinterland.

Marobo Basin

Structural mapping (Chapter 1) has shown that the Marobo Basin is a narrow graben that subsided within and perpendicular to the orogen, at an early stage of subduction of an continental plateau that lay on the northern margin of Australia, and that the basin is bounded to the south by a shear zone that may have >10 km of slip (Figure 2.26). Although the basin floor is buried, the age of the basal carbonates, which are up to 5.7 Myr old, suggest that the floor of the basin is forearc basement, overlain by Australian margin shales that were accreted in the accretionary wedge. If the present topography is reflective of the original basin setting, the sediments accumulated in a roughly rectangular basin that had an east-west width of no more than 7 km and a north-south extent of up to 20 km. The long edges of the basin run approximately N-S and the basin was filled by conglomeratic debris flows and high density turbidites that were emplaced towards the southwest and southeast, i.e. by southerly flow. These sediments have a proximal character that is unlike any reported from elsewhere in Timor.

The lack of erosion of the uppermost conglomerate of Level C by the pebbly sandstones of Level D (Figure 2.8), and the overall tectonic setting of the section in a major orogen-perpendicular graben, suggests that the onlap of D onto C represents growth strata following an interval of faulting (Figure 2.26). This indicates that the sediments in this basin were sourced from rapidly uplifting land to the north and northeast, and were filling a half graben that was subsiding asymmetrically about a hinge to the north (Figure 2.26).

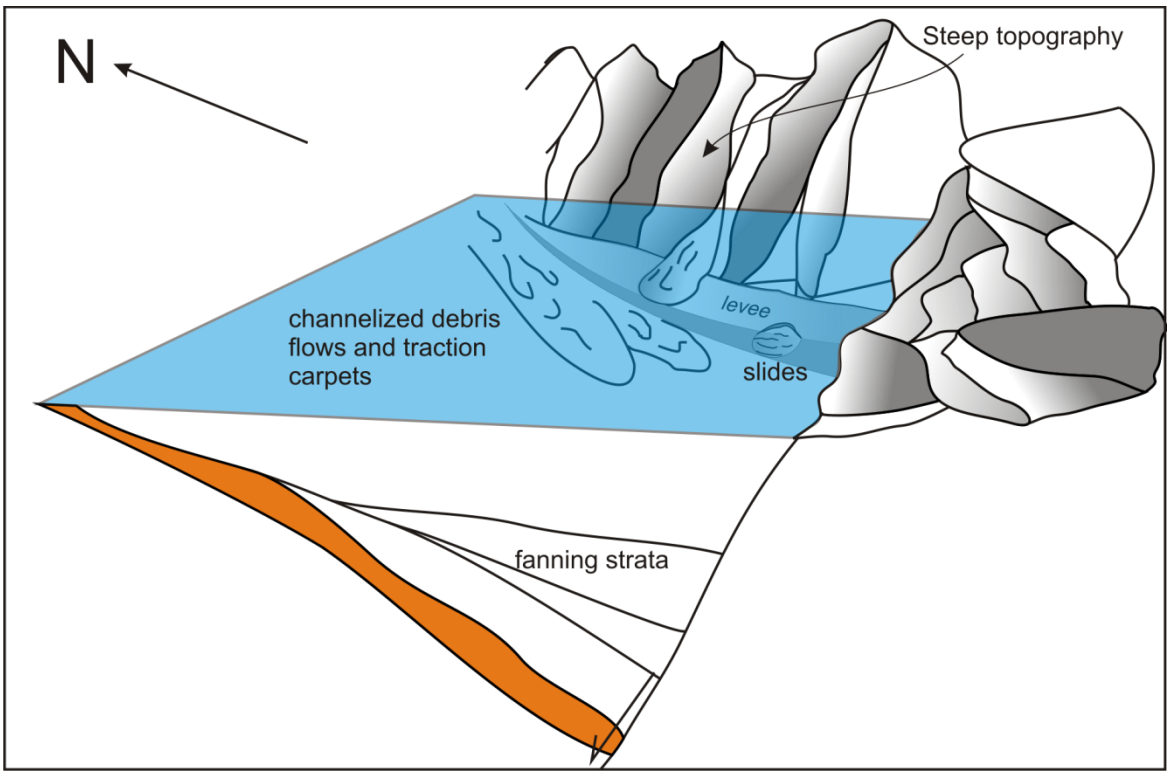

Figure 2.26: Cartoon showing interpreted depositional setting of the Marobo Basin. Fill is a mixture of debris flows and slides sourced from the north and east. Slip on the basin bounding fault causes fanning of growth strata.

The general lack of terrestrial plant detritus below Level D suggests that the topography was steep enough to deter plant colonization. Similarly, the lack of shelly detritus in the lower two thirds of the section suggests that the coastline had extreme topography and beaches were poorly developed. A similar situation presently exists on the north coast of Timor Leste both east and west of Dili, where the topography is steep and bathymetry even steeper. Steep mountain catchments there deposit their sediment almost directly into Wetar Strait across a narrow to non-existent shelf (Figure 2.28).

The rocks of the Marobo Basin have a provenance that is both petrographically and geochemically distinct from that of the more eastern Laleia and Viqueque Basins. The source area for the Marobo Basin was one of highly strained metapelites that are more geochemically evolved compared with the underlying Batu Putih Formation and the Viqueque mudstones (Figure 2.19). This is reflected in the higher concentrations of REE and HFSE (Figure 2.21) in the mudstones, and in their high Th/Sc ratios (Figure 2.23). The evolved source of the Marobo Basin sediments is consistent with erosion of continental affinity schists. The Aileu metamorphic complex has a reported exhumation age from apatite fission track data of <2 Ma (Harris et al. 2000), so is unlikely to have contributed to the synorogenic sedimentation at 3.5 Ma. This suggests that the schist clasts are derived from the lower levels of the Banda Terrane, where they may represent a

continental block encased in the Banda Terrane basement (e.g. Harris 2006). The base of the Banda Terrane Mutis Complex of West Timor is reported to have sericite schists, similar to those that form the bulk of the conglomerate clasts in the Marobo basin fill (de Roever 1940).

The change to a more evolved source is abrupt, and the only hint of a transition is in the presence of four weathered volcanic clasts in sample CR24A from the base of the clastic succession (Table 2.8). The Marobo section area is dissected by normal faults, and the abrupt change occurs across a zone of no exposure between the top of the exposed Batu Putih Formation and the base of the overlying Viqueque Formation clastic sedimentary succession. It is therefore possible that a transitional part of the section is faulted out. However, the sudden change in provenance suggested by geochemistry and discussed above can be interpreted as suggesting that the pelitic rocks emerged rapidly in the footwall of the basin bounding normal fault and shed material south and west, while overlying material became diverted to the north and east.

Laleia and Viqueque Basins

The Viqueque Basin is part of the E-W elongate Southern Basin, and the Laleia Basin is part of the NE Basin (Figure 2.1). Structural mapping (Chapter 1) has shown that the Viqueque and Laleia Basins lie either side of the Lacluta fault (oblique normal-dextral) (Figure 2.1B), which formed during extrusion of a shortened outlying continental terrace that had been thrust under the forearc (Chapter 1). The floors of both basins are therefore almost certainly forearc crust and are overlain by several kilometers of Australian Margin Megasequence shales that formed part of the accretionary wedge (Figure 2.1B).

The Laleia and Viqueque Basins were clearly originally deposited in separate basins, with paleoflow in the opposite directions relative to the Lacluta fault. However, it is useful to interpret them as proximal and distal facies in a cartoon depositional model as shown in Figure 2.27. The cartoon is simplified as the true picture would be a complex interplay between shortening and deformation of the forearc and accretionary wedge, and normal faulting as the deformation led to extrusion.

In the Viqueque area, the marl-dominated Batu Putih basin thickens northwards towards the hinterland, indicating that the marls were accumulating in a half graben that was subsiding asymmetrically about a hinge to the south (Figure 2.27). Similar basin styles have been documented in seismic sections on the north side of the Timor Trough (e.g. Veevers 1971; Crostella & Powell 1975). In the Suai sub-basin offshore south of the Marobo Basin, the Mola-1 well (Figure 2.1B&C) encountered 3065 m of Lower Pleistocene and Upper Pliocene turbidites (Althorpe 1975). This is an accumulation some 500 m thicker than the maximum depth of the

present Timor Trough. Seismic reflection studies show that the basin sediments accumulated in a normal-fault-bounded basin above a sub-basinal thrust (Fig. 10 in Crostella & Powell 1975; see also Charlton 2002).

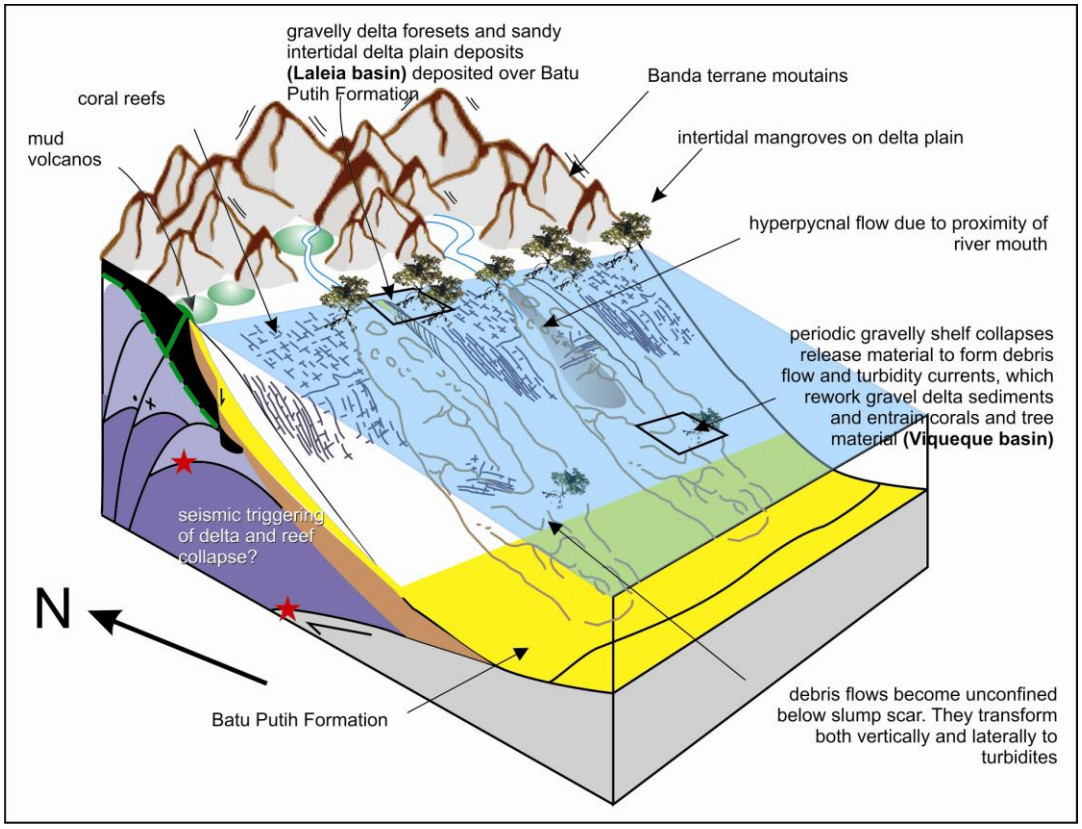

Figure 2.27: Cartoon showing depositional setting of the Laleia Basin (gravelly delta) and Viqueque Basin (debris flow dominated slope).

Deltaic deposits such as are found in the Laleia Basin accumulated in shallow water on a narrow shelf, which was probably bounded on its landward side by a normal fault. The delta overlay poorly consolidated Batu Putih Marls that had accumulated at progressively shallower depths as uplift got under way (Haig 2012) and were exhumed in the *hanging wall* of major normal faults (Figure 2.27). Rocks exhumed in the footwall would have been rapidly eroded into younger sedimentary basins as was seen in the Mola-1 well of the Suai basin, where the upper Pliocene section contained abundant reworked Lower Pliocene sediments (Althorpe 1975). This configuration and the seismicity of the active orogen destabilized the shelf and provided a staging post for the transfer of gravelly sediment to the deep basin. The gravelly deltas would have interfingered with fringing coral reefs, and mangrove swamps would have been developed on the delta plain. Analogous settings presently exist all along the north coast of modern Timor, where a narrow shelf gives way to a steep slope, and large braided rivers discharge gravelly sediment into deltas fringed by coral reefs and mangrove swamps (Figure 2.28). Collapse of the gravelly deltas would have ripped coral reef communities and mangrove swamps from their growth positions,

entraining them in poorly confined debris flows that originated close to the shelf slope break and flowed down the slope. The paleoflow directions indicate that the clastic sediments were being transported approximately perpendicular to the apparently extensional faults.

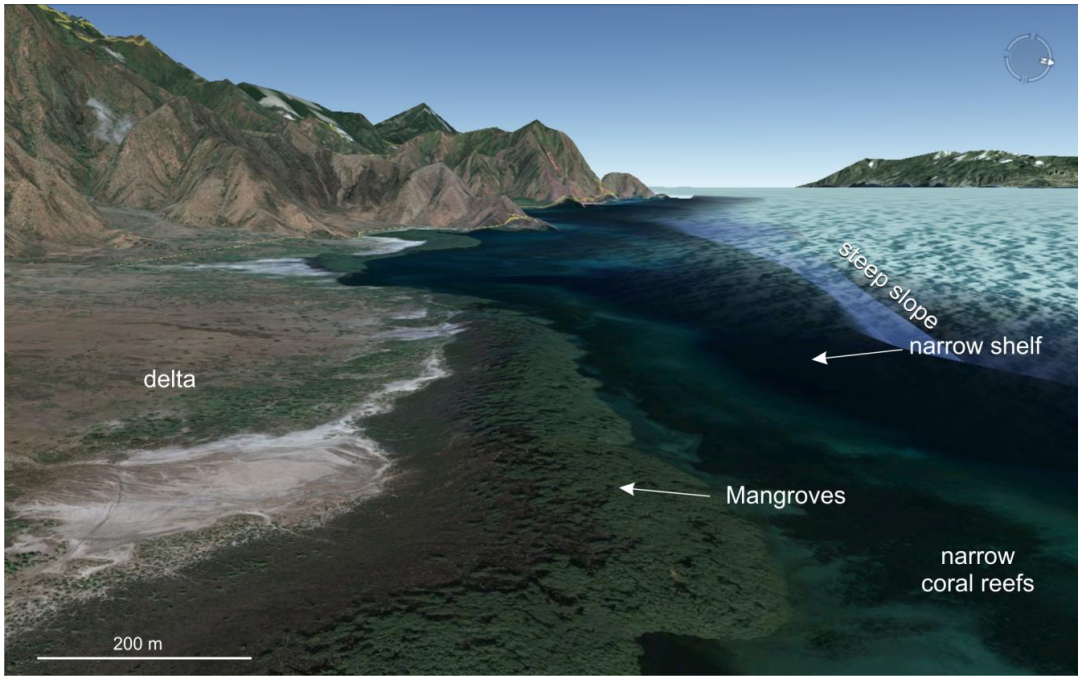

Figure 2.28: Google earth perspective image looking west and showing a typical small gravelly delta on the north coast of Timor Leste, with fringing mangrove swamps and coral reefs. Note the narrow shelf (less than 1.5 km wide) and the steep slope beyond into the Wetar Strait.

Although the Laleia and Viqueque Basins are interpreted in a single depositional model, they lie on opposite sides of the normal fault-bounded Lacluta Massif (Chapter 1), and have differing clast provenance. The Laleia Basin contains lithologies such as volcaniclastic limestones and dacites that indicate a source similar to the Banda Terrane Palelo Group, a forearc cover sequence that overlies the forearc basement of the Lolotoi Metamorphic Complex (Harris 2006). Dacites in particular are reported to overlie the Banda Terrane Mosu massif of West Timor (Standley & Harris 2009). They are also found as Paleocene to Miocene intrusive and extrusive rocks in the forearc basement of Sumba (Chamalaun et al. 1982; Wensink 1994; Rutherford et al. 2001), where they are associated with metasomatized basalts and are commonly slightly altered to secondary assemblages that include chlorite, albite and carbonate (Wensink & van Bergen 1995). These same associations and mineral assemblages are characteristic of the dacite clasts in the Laleia conglomerates and suggest that the Laleia Basin fill was derived from erosion of Banda Terrane cover rocks of the Palelo Group.

In contrast, the conglomerate clasts of the Viqueque Basin have crystalline lithologies that are consistent with a dominantly metamorphic source similar to the Banda Terrane Lolotoi

metamorphic complex that lies below the Palelo Group. Epidote amphibolite facies schist is reported from the Lolotoi-equivalent massifs of West Timor (van West 1941; Earle 1981), along with amphibolites, metagabbros and peridotite (Earle 1981; Sopaheluwakan et al. 1989). Both the Banda Terrane and the Gondwana Megasequence contain basalts and amphibolites (de Roever 1940; de Roever 1942; Berry & Jenner 1982; Standley & Harris 2009). However, the albite deformation seen in the Viqueque conglomerate clasts suggests high temperature metamorphism, which is overprinted by stretching, mylonitzation and retrogression, leading to the growth of tremolitic amphibole into the feldspars and amphiboles. This history is consistent with the tectonic history inferred for the Banda Terrane (Harris 2006; Standley & Harris 2009). Small percentages of the clasts, particularly silicified limestones seen in the Viqueque and Laleia areas point to a source in the Gondwanan Maubisse Formation (e.g. Barkham 1993). However, these lithologies are common in the Synorogenic Mélange, which was the dominant source for mudstone and therefore widespread in the source area.

The contrasting clast provenance in the Laleia and Viqueque Basins may be interpreted in a similar way to the sudden change in the provenance of the Marobo Basin. The preferential shedding of Banda Terrane cover sediments into the Laleia Basin and crystalline basement into the Viqueque Basin may reflect Northwards tilting of the Lacluta Massif during exhumation of the Banda Terrane along south dipping normal faults such as the southern boundary of the Lacluta Massif (Duffy et al. (accepted manuscript)). This tilting may have diverted cover rocks northwards whilst preferentially supplying deeper lithologies to the southern basin.

2.6 Summary and conclusions

The Synorogenic Megasequence is a coarsening up succession that records the exhumation and erosion of the Timor landmass. I have presented new data for the Synorogenic Megasequence from several basins including well-dated measured sections in central and eastern Timor (the Marobo and Viqueque basins respectively). The Batu Putih Formation is generally poorly exposed but is only gently deformed. In the Viqueque Basin it thickens considerably northwards which I interpret as reflecting deposition in a normal fault- bounded half graben. In both the Marobo and Viqueque Basins, the Batu Putih Formation becomes progressively marlier upwards due to an influx of terrigenous sediment.

Terrigenous sedimentation began prior to 4.5 Ma. Temporal geochemical trends in the Batu Putih Formation are indistinguishable between the Marobo and Viqueque sections and indicate a progression from a mature, probably accretionary wedge source, to a more mafic to intermediate terrigenous source. These results suggest that much of the eastern half of the island of Timor was emergent and shedding terrigenous sediment into carbonate basins by no later than 4.5 Ma.

Meanwhile the Central Basin of West Timor remained relatively free of terrigenous sediment until 2.5 Ma. The stepwise westward younging of terrigenous sedimentation is consistent with early arrival of a Timor Plateau in the area of Timor Leste.

Uplift was rapid and created an extreme relief that resulted in an abundant supply of coarse detritus to synorogenic basins. Coarse clastic sedimentation began earliest at 3.5 Ma in the Marobo Basin of central Timor and propagated both eastward, beginning at ~3.1 Ma in Viqueque, and westward, beginning at 2.5 Ma in the Central basin of West Timor according to Van Marle (1991). Again, the relative timing of this event is consistent with early collision of an outlying Timor Plateau in the eastern half of the island (Timor Leste).

Each basin has clastic sediments of different depositional characters that overlie Batu Putih Formation carbonates and marls. The Marobo Basin is a deep, orogen-perpendicular graben and was filled from the north and east by a coarse grained submarine fan fed by debris flows and slides. Growth strata are clearly evident at the top of the section. The regressive facies in the Laleia Basin is a coarse, cross-bedded gravelly delta conglomerate that is overlain by thin, normally-graded sandstones containing root casts and plant detritus. I interpret the sandstones as delta plain mangrove deposits. The Viqueque conglomerates and sandstones are dominated by debris flow processes, probably derived from collapse of gravelly delta complexes similar to those seen in the Laleia section.

All three basins contain a fill that I interpreted to be derived from the Banda Terrane. Differences between sandstone/conglomerate clast provenance in the three basins is interpreted to reflect eastward (Marobo) and northward tilting of Banda Terrane blocks (Viqueque and Laleia), and differential exhumation of cover and underlying basement rocks. This tilting is consistent with the large scale tilting of massifs suggested in Chapter 1.

The sandstone/conglomerate and mudstone provenance are different for the same location. Mudstones in the Marobo and Viqueque Basins have old Neodymium model ages and negative epsilon Nd, which are indicative of a source dominated by Australian shales, such as provide the matrix of the synorogenic Mélange, rather than by Banda Terrane sediments. This is interpreted as the result of turbiditic sedimentary sorting of the coarse grained, Banda Terrane detritus, from the fine grained, Synorogenic Mélange detritus. Australian affinity rocks present in the sandstones are probably sourced from the Synorogenic Mélange. Overprinted on the mélange geochemistry of the mudstones are a mafic (Viqueque) and felsic geochemistry (Marobo) that are consistent with sandstone petrography and with different elements of the Banda Terrane.

Table 2.5: Point count data. Samples are arranged from base of the section (left) to top of the section (right) for each section to highlight trends.

		Sample	Marobo						Laleia			Viqueque									
			24a	27a	41a	49a	56a	62a	587	557	592	TS070	TS006	TS013	TS017	TS018a	TS018b	LM19	TS030	LM16	Lm25	LM22
		marble/twinned calcite							1.9	2.7			1.0		0.4	3.7	6.7		1.1		6.3	2.7
		Acaranina (Eocene)																			0.7	
		alviolina(Eocene)							1.3													
		calcarenite											0.3				0.7	1.3		1.3		
		calcilutite with chloritized forams and pyrite														6.9			6.7			
		calcilutite with silica infilled chloritized forams																0.3				1.0
		chlorite calcilutite								0.7												
		crinoid/fusulinid																				2.0
		crystalline								0.7		3.6	3.5	4.9	0.9	0.6	3.4		0.4	0.7		
		dolomitic calcarenite								1.7												
		dolomitic calcilutite																2.0				
		dolomitized radiolarian(?)																				0.3
		foraminiferal						1.6								0.9		3.0				
		fossil fragment								1.0						3.5			11.9		0.3	
		limestone with serpentinite clasts																				2.0
		micritic tuffaceous							2.2	0.7	1.0											
		micritic/calcilutite						4.0	0.9	0.3		6.0	2.9	5.6	6.1		7.1	1.3		1.3		
		ooid																		1.0		1.7
		qz felds sandy calcilutite with echinoid spine																				2.0
		qz felds sandy foraminiferal calcarenite																				2.7
		qz felds sandy foraminiferal marl																5.7				
		red radiolarian																2.3				
		sandy									1.3											
		sheared qz veined cherty calcarenite																		0.7		
		shelly unidentified						1.2	2.8		5.3	0.9	2.2		6.5		1.5					1.0
		silicified crinoidal																			0.3	
		silicified fusulinid								0.3												
Carbonate	Limestone	silicifying/cherty						0.8	0.6							0.4		1.0	1.1	3.0		
		stylolitic/breccia								0.3										3.7	0.7	2.7
		undifferentiated					10.0		0.6		0.3					0.4			2.2			0.3

Sample			Marobo						Laleia			Viqueque										
			24a	27a	41a	49a	56a	62a	587	557	592	TS070	TS006	TS013	TS017	TS018a	TS018b	LM19	TS030	LM16	Lm25	LM22
	total		0	0	0	0	10	7.5	8.5	5.7	8	10.5	8.9	10.4	13.5	12.8	12.8	17	22.4	11.6	2	15.7
Chert									0.9			1.2	0.3	7.6	4.3		4.4	1.7	2.2			0.3
Clastic	Mudstone	calcareous mudstone								0.3								0.3			3.3	
		epidote chlorite mudstone																				0.7
		mudstone					6.7	0.4	1.3	3.0		0.9	0.6	5.6	1.7	3.2	16.3	0.7	5.2	0.7		3.3
	Sandstone	calc veined qz ab biotite chlorite																		3.3		
		calcareous					2.0			1.7	5.0											
		calcite cement angular qz feldspar sand																1.7				1.7
		chlorite biotite sericite																			2.6	
		chlorite cemented angular feldspathic sand																				3.0
		chlorite qz							2.5				0.3		0.4					1.0	0.7	
		chlorite sandstone w forams																			0.7	
		chlorite sericite qz								0.7	3.0										9.6	0.7
		epidote qz							2.8		0.7										0.3	
		epidote sericite qz feldspar arenite																4.7				
		fossiliferous muddy arenite																				2.3
		Intraclast (typically uncemented matrix rich calc qz felds amph)	10.3		0.8	2.2	0.3	0.8	1.6									9.7		1.0	1.7	1.7
		qz			1.3							0.6		0.7			1.7					
		qz + pericline albite									2.0											
		qz/ab/±chl			0.4	3.7		7.5														
		sericite qz felds							0.6	3.0	9.0							2.7		3.3	1.7	
		undifferentiated					6.4									1.5			3.0		1.7	2.3
		siltstone											1.0	1.4		5.4			0.7			
	total		10.3	0	2.5	5.9	15.4	8.7	8.9	8.7	19.6	1.5	1.9	7.6	2.2	10.2	18	19.7	9	9.3	22.2	15.7
Mineral grains		andalusite										0.3										
		chlorite								0.3		0.3	0.3	0.7		3.5	0.5		7.5			
		chlorotoid										2.4	0.6	0.7	0.9							

		Sample	Marobo						Laleia			Viqueque										
			24a	27a	41a	49a	56a	62a	587	557	592	TS070	TS006	TS013	TS017	TS018a	TS018b	LM19	TS030	LM16	Lm25	LM22
		epidote													1.3							
		feldspar	14.0		22.9	11.8	9.0	4.0	0.3	3.3		5.1	4.1	4.5	3.9	8.0	0.5	1.3	12.7		0.3	0.7
		feldspar altering to sericite									2.0									2.7		
		hornblende										13.8	20.0	16.0	14.8	6.1	0.2		6.0		0.3	
		kspar														3.2			0.4			
		muscovite											0.3		0.4	0.4	2.5					
		myrmekite									1.3											
		olivine																				
		opx										0.3	0.3			0.2			0.4			
		perthite																	0.4			
		sphene							0.3													
		spinel											0.3									
		straight qz														2.4			2.6			
		undulose poly qz	4.7	8.3	4.8	9.7	4.8	0.5	7.6	10.3	21.3	47.3	58.4	39.6	50.4	18.6	12.6	5.0	14.2	11.0	13.9	5.3
		zircon												0.3								
	total		18.7	8.3	27.7	21.6	13.8	4.4	8.2	14	24.6	69.5	84.4	61.8	71.7	42.4	16.3	6.3	44	13.6	14.6	6
Igneous	Altered	trachytic texture								0.7											0.7	
		Unidentifiable (igneous texture)								5.0	1.0							0.6			6.0	
		Unidentifiable (no clear texture)																0.7		2.3		1.3
		serpentinite								0.7								1.7	1.1	0.3		
	Intrusive	dacite titaniferous							0.6													
		dacite/diorite							1.3							2.2	0.7	0.3		1.7		0.3
		dolerite/gabbro							0.6	1.3	0.7					0.4	3.7	1.0		4.0	1.0	
		granophyre							0.6													
		peridotite							0.3					0.3		0.6		5.7				3.0
	Volcanic	spherulitic (basalt)								4.0	1.0					1.3	0.5	1.0	1.1	4.0	0.7	3.0
		undifferentiated volcanic	1.3							0.3												0.7

Sample			Marobo						Laleia			Viqueque										
			24a	27a	41a	49a	56a	62a	587	557	592	TS070	TS006	TS013	TS017	TS018a	TS018b	LM19	TS030	LM16	Lm25	LM22
	total		1.3	0	0	0	0	0	3.5	12	2.7	0	0	0.3	0	4.5	4.9	11	2.2	12.3	8.3	8.3
Metamorphic	Amphibolite	chlorite							1.8													
		chlorite tremolite																		1.0		
		chlorite tremolite epidote hornblende																		0.7		
		chlorotoid							0.3												0.3	1.0
		epidote							3.5									1.0			0.7	
		epidote tremolite magnetite								3.0											3.0	
		magnetite																			0.3	
		sheared							0.6	6.7	0.7					9.5		6.7	2.2	7.3	5.6	
		tremolitic							3.2	1.3								1.0		4.7	4.3	
		undifferentiated			1.3		1.0		14.2	4.3	0.7					8.0		17.7	8.2	9.6	2.0	3.7
		total	0	0	1.3	0	1	0	23.7	15.3	1.3	0	0	0	0	17.5	0	26.3	10.5	23.3	16.2	4.7
	Quartzite	0	2.0	5.9	2.1	0.7	0.3		0.6		7.0			1.7	0.9	1.9	3.9	1.0	1.1	1.0	5.0	8.3
	Schist	amphibole qz feldspar							2.2													
		andalusite calcite sericite									2.7											
		biotite chlorite																			1.3	
		biotite sericite								2.0	4.0									0.3		
		Calcareous qz	0.7	3.7			6.0	2.0	0.9	3.3	1.0									0.7	2.3	2.3
		chlorite						0.4	5.7	3.3	1.7	16.8	2.9	9.4	5.7			1.3	0.7	2.0	2.0	4.7
		chlorite amphibole							3.8													
		chlorite cpx serp																1.0				
		chlorite epidote ± calcite							7.9	2.3	1.0							0.3				1.7
		chlorite epidote amphibole																				0.7
		Chlorotoid	0.3	0.5													0.5			2.0	1.0	
		chlorotoid ±tremolite, hornblende																1.7		2.0		
		Chlorotoid tremolite epidote amphibole																		1.3		
		epidote	3.0	1.1	0.8	0.7	1.3															

		Sample	Marobo						Laleia			Viqueque										
			24a	27a	41a	49a	56a	62a	587	557	592	TS070	TS006	TS013	TS017	TS018a	TS018b	LM19	TS030	LM16	Lm25	LM22
		epidote calcite																		0.7		
		epidote sericite								2.3												
		epidote tremolite ± calcite								1.0										4.0		1.3
		magnetite amphibole							2.2													
		qz epidote tremolite magnetite																		2.3		
		qz feldspar									2.7									2.7		
		sericite	44.7	47.3	35.6	30.6	31.1	63.2			8.6		0.6		1.3	5.6	29.6	3.3	6.7	6.0	10.3	15.0
		sericite ± calcite								6.3	0.3							0.3		2.3	0.7	
		sericite ± chlorite							3.8	20.3	10.0					1.3		2.7		0.3	2.6	6.3
		sericite ± chlorite mylonitized			10.6																	
		sericite chlorite calcite																		1.3		
		sericite epidote chlorite							5.1									0.3				
		stilpnomelane chl qz calc									0.7											
		tremolite																4.3				4.3
		undifferentiated										0.6		1.0			3.0					
		total	48.7	52.6	47	31.4	38.5	65.6	31.6	41	32.6	17.4	3.5	10.4	7	6.9	33	15.3	7.5	27.9	20.2	36.3
	Slate	chlorite ± epidote							0.9									0.7				1.3
	Slate	undifferentiated				1.5	1.7	11.9	11.1		3.0										2.6	
	Slate	total	0	0	0	1.5	1.7	11.9	12	0	3	0	0	0	0	0	0	0.7	0	0	2.7	1.3
Mylonite		calcareous quartz mylonite								0.3								1.0				
Mylonite		Quartz mylonite	3.3	5.8	3.4	6.8	3.4	0.3		0.3	1.3									1.0	2.6	0.7
		Summary																				
Met'c	total		50.7	58.5	50.4	33.6	41.4	77.5	68	56.3	43.9	17.4	3.5	12.2	7.8	26.4	36.9	43.3	19	52.2	44	50.7
Igneous	total		1.3						3.5	12	2.7			0.3		4.5	4.9	11	2.2	12.3	8.3	8.3
Sed.	total		10.3		2.5	5.9	25.4	16.2	17.4	14.3	27.5	12	10.8	18	15.7	22.9	30.8	36.7	31.3	20.9	24.1	31.3
Diversity		No of different lithologies	10	7	11	9	14	14	39	37	30					27	20	41	26	41	38	40

Table 2.6: Major (wt%) and trace element (ppm) geochemistry of the Marobo section

Sample	CR 01	CR 08	CR 13	CR 18	CR 21	CR 22	CR 24	CR 27	CR 41	CR 49	CR 56	CR 62	CR25A	CR49A	CR63A
Lithology	Carb	Carb	Carb	Carb	Carb	Carb	mud	mud	mud	mud	mud	mud	sand	sand	sand
Height (m)	0.13	5	12	18.7	24.3	28.4	68.5	111	242	348	478	554	101	348	564
Age (Ma)	5.58	5.25	4.77	4.29	3.9	3.6	3.44	3.4	3.27	3.16	3.03	2.96	3.4	3.16	2.95
SiO_2	7.06	18.8	16.55	20.7	21.7	15.6	56.3	52.6	59.2	58.7	58	60.3	81.7	80.5	69.2
Al2O3	1.94	4.02	4.41	5.91	7.01	4.71	19.3	14.7	14.75	14.85	16.45	16.85	5.65	6.81	8.38
Fe2O3	0.81	1.57	1.87	2.3	2.45	1.94	8.2	6.24	6.3	5.96	6.61	6.64	3.47	3.1	3.56
CaO	50.8	40.6	41.1	38.4	37.7	41.7	0.97	8.98	5.23	6.1	5.04	3.45	3.04	3.48	5.63
MgO	0.57	1.03	0.99	1.86	1.26	1.04	2.97	2.06	2.02	2.18	2.18	2.09	0.81	0.9	1.17
Na2O	0.11	0.24	0.23	0.29	0.33	0.17	1.53	1.08	1.31	1.2	1.19	1.66	1.08	1.31	1.39
K2O	0.27	0.5	0.67	0.96	1.15	0.77	4.18	2.68	2.83	2.85	2.95	3.25	0.91	1.12	1.4
Cr2O3	<0.01	<0.01	<0.01	<0.01	0.01	<0.01	0.01	0.01	0.01	0.01	0.01	0.01	<0.01	<0.01	0.01
TiO2	0.07	0.19	0.19	0.26	0.31	0.21	0.88	0.74	0.88	0.9	0.86	0.89	0.27	0.33	0.44
MnO	0.12	0.09	0.09	0.1	0.1	0.12	0.08	0.09	0.09	0.09	0.1	0.08	0.08	0.1	0.1
P2O5	0.04	0.16	0.11	0.13	0.1	0.13	0.12	0.21	0.16	0.16	0.14	0.15	0.08	0.07	0.11
SrO	0.16	0.15	0.14	0.14	0.13	0.14	0.02	0.04	0.03	0.03	0.03	0.02	0.01	0.02	0.02
BaO	0.01	0.02	0.03	0.02	0.02	0.02	0.07	0.04	0.05	0.04	0.04	0.05	0.02	0.02	0.03
LOI550	1.52	2.13	2.34	2.98	3.22	2.84	2.26	1.84	-	3.03	4.02	3.9	1.15	0.92	1.57
LOI	39.2	32.5	33.1	30.6	29.5	33.5	3.49	8.82	6.09	6.53	6.23	4.76	3.48	4.06	6.06
Total	101.16	99.87	99.48	101.67	101.77	100.05	98.12	98.29	98.95	99.6	99.83	100.2	100.6	101.82	97.5
Ag	0.6	0.6	0.7	0.6	0.8	0.7	<0.5	0.8	0.6	0.5	0.7	<0.5	<0.5	<0.5	<0.5
As	<5	6	<5	<5	<5	5	7	6	8	7	8	9	5	8	8
Ba	118.5	175.5	278	210	203	214	636	370	442	351	368	449	178	195.5	225
Cd	<0.5	<0.5	<0.5	<0.5	<0.5	<0.5	<0.5	<0.5	<0.5	<0.5	<0.5	<0.5	<0.5	<0.5	<0.5
Ce	8	13.6	17.8	24	28.1	21.8	144	72.1	84.7	82.5	80.2	91.3	27.7	34.8	46
Co	12	13	14	22	18	13	28	23	24	24	26	24	55	74	83
Cr	10	30	30	40	50	40	100	90	90	90	90	90	30	30	50
Cs	0.73	1.39	1.93	2.77	3.66	2.35	11.35	8.78	7.74	7.86	8.65	9.34	2.18	2.57	3.02
Cu	13	19	26	28	31	31	37	33	33	33	38	34	9	10	14
Dy	1.28	1.99	1.91	2.31	2.57	2.19	8.33	5.28	6.25	5.95	5.89	6.4	2.08	3.09	3.86
Er	0.82	1.2	1.15	1.4	1.49	1.27	4.29	2.91	3.29	3.23	3.24	3.52	1.12	1.61	1.95
Eu	0.3	0.46	0.49	0.59	0.64	0.58	2.26	1.39	1.58	1.55	1.49	1.62	0.5	0.77	0.97
Ga	2.5	5.1	5.8	8	9.6	6.7	30.5	20.4	20.9	21.3	24	24.5	7.3	8.9	11.3
Gd	1.28	1.95	2.08	2.51	2.73	2.45	10.05	5.96	7.04	6.74	6.62	7.25	2.29	3.49	4.6
Hf	0.4	1.2	1.2	1.5	1.9	1.2	7.9	4.9	7	7	5.9	6.7	2.8	3.5	4.7
Ho	0.29	0.44	0.43	0.51	0.55	0.48	1.68	1.11	1.28	1.24	1.24	1.33	0.43	0.63	0.79
La	6.4	8.8	10.8	14	16.2	13.2	70.4	36.2	42.3	40.8	40.4	45.7	13.7	16.9	22.5
Lu	0.12	0.19	0.18	0.21	0.23	0.19	0.63	0.43	0.49	0.48	0.48	0.52	0.17	0.23	0.28
Mo	<1	<1	<1	<1	<1	<1	<1	<1	<1	<1	<1	<1	<1	<1	<1
Nb	1	2.1	2.9	4.5	5.5	3.7	25.2	16.8	20.3	21.6	20.7	21.4	6.7	8.2	11.5
Nd	5.2	7.8	9.1	11.9	13.4	11.2	60.1	30.8	36.1	34.9	33.9	38.4	11.6	14.9	20.1
Ni	11	16	23	22	27	32	37	40	38	40	44	36	13	13	18
Pb	4	5	5	8	12	9	35	16	22	18	21	21	11	10	11
Pr	1.3	1.95	2.36	3.14	3.56	2.92	16.7	8.45	9.98	9.58	9.36	10.65	3.2	4.03	5.44
Rb	11.3	22	31.1	45.2	56.7	36.7	222	135.5	141	138.5	150.5	167	45.8	54.3	67.1
Sc	3	5	5	6	7	5	16	14	15	14	15	15	4	6	7
Sm	1.1	1.74	1.88	2.47	2.62	2.31	11.5	6.05	7.15	6.73	6.48	7.32	2.31	3.1	4.19
Sn	<1	1	1	1	1	1	6	3	4	4	4	4	1	2	2
Sr	1285	1205	1230	1095	1065	1210	177.5	344	233	250	244	202	122	138	185
Ta	0.2	0.3	0.4	0.5	0.6	0.4	2	1.4	1.9	1.9	1.8	1.9	2.1	2.4	2.9
Tb	0.21	0.32	0.32	0.38	0.42	0.37	1.51	0.93	1.09	1.04	1.02	1.15	0.37	0.54	0.7
Th	1.25	2.5	3.21	4.73	5.97	4.21	28.2	14.95	17.15	16.35	17.3	19.95	6.09	7.23	9.14
Tl	<0.5	<0.5	<0.5	<0.5	<0.5	<0.5	0.8	0.5	0.6	0.5	0.6	<0.5	<0.5	<0.5	<0.5
Tm	0.12	0.18	0.17	0.2	0.22	0.19	0.65	0.44	0.51	0.49	0.5	0.54	0.17	0.24	0.3
U	0.39	1.05	1.45	1.74	3.64	2	4.31	3.42	3.71	3.41	3.23	3.63	1.13	1.36	1.78
V	17	41	51	62	68	61	184	136	133	137	144	149	39	49	64
W	29	28	33	39	38	30	78	68	142	92	87	93	809	823	926
Y	11.4	15.6	15	17.8	18.7	16.9	47.9	31.4	36.4	35.4	34.7	37.2	12.2	18.4	22.5
Yb	0.77	1.17	1.13	1.35	1.47	1.22	4.13	2.82	3.12	3.12	3.17	3.39	1.08	1.52	1.81
Zn	20	33	41	49	56	55	118	102	104	100	110	107	35	43	59
Zr	20	40	40	60	70	50	280	170	250	250	210	230	100	130	170

Table 2.7: Major (wt%) and trace element (ppm) geochemistry of the Viqueque section

Sample	TS 060	TS 061	TS 062	TS 063	TS 064	TS 069	TS 011	TS 018	TS 022	TS 027	TS 031	TS 035	TS 042	TS 047
Lithology	carb	carb	carb	carb	carb	mud	mud	mud	mud	mud	mud	mud	mud	mud
Height (m)	0.1	8	13	20.5	31.5	56	71.5	89	111	139	160	176	197	212.5
Age (Ma)	5.5	4.32	4.0	3.73	3.49	3.2	3.08	2.98	2.88	2.78	2.72	2.68	2.63	2.6
SiO2	6.59	27.2	19.4	32.3	29.6	48.1	51.8	44.8	43.3	42.7	43	50.1	50.7	55.2
Al2O3	1.52	6.99	5.72	8.12	7.52	12.8	11.8	12.75	12.3	11.2	11.55	14.75	13.15	14.5
Fe2O3	0.68	3.1	2.35	3.54	3.71	6.59	5.83	5.45	6.99	6.81	4.92	7.6	7.42	6.59
CaO	50.9	32.6	38.7	30.2	27.9	12.3	13.65	15.95	16.2	18.2	19.2	10.15	11.65	7.48
MgO	0.52	2.21	1.5	1.91	3.93	3.09	2.62	2.81	2.83	2.71	2.36	2.94	2.86	3.07
Na2O	0.15	0.38	0.33	0.61	0.36	1.06	1.14	0.5	0.51	0.98	0.99	1	0.95	1.13
K2O	0.25	1.18	0.95	1.35	1.36	2.22	1.84	2.34	2.32	1.88	1.94	2.45	2.21	2.37
Cr2O3	<0.01	0.01	<0.01	0.01	0.01	0.01	0.01	0.01	0.01	0.01	0.01	0.01	0.01	0.01
TiO2	0.07	0.34	0.27	0.39	0.39	0.74	0.77	0.63	0.61	0.64	0.64	0.75	0.74	0.86
MnO	0.08	0.07	0.12	0.09	0.1	0.17	0.13	0.18	0.46	0.38	0.15	0.21	0.4	0.16
P2O5	0.03	0.25	0.24	0.12	0.13	0.16	0.15	0.15	0.18	0.2	0.18	0.18	0.17	0.16
SrO	0.12	0.16	0.14	0.16	0.14	0.08	0.07	0.09	0.09	0.09	0.1	0.06	0.07	0.04
BaO	0.07	0.03	0.04	0.05	0.06	0.05	0.04	0.06	0.04	0.05	0.04	0.05	0.05	0.05
LOI550	1.24	5.2	3.3	6.63	4.54	6.18	4.58	6.48	6.86	4.85	4.47	6.08	7.22	6.15
LOI	40.1	26.4	31.1	22.7	24.9	11.55	11.35	15.65	15.25	16.1	16.7	10.45	11.15	7.97
Total	101.08	100.92	100.86	101.55	100.11	98.92	101.2	101.37	101.09	101.95	101.78	100.7	101.53	99.59
Ag	0.5	1.1	0.8	1	0.8	0.9	0.8	1	0.7	0.7	0.7	0.5	0.6	0.7
As	5	<5	<5	8	6	<5	6	<5	6	8	<5	8	<5	5
Ba	572	239	323	441	493	388	390	523	360	406	379	404	437	399
Cd	<0.5	1.1	<0.5	0.6	0.6	0.5	<0.5	0.6	<0.5	<0.5	0.7	<0.5	0.5	<0.5
Ce	6.9	29.8	22.4	30.8	32.3	58.9	54.6	52.4	51.6	49.5	51.7	65.8	58.6	64.8
Co	40	42	20	22	18	21	28	19	22	20	22	22	23	26
Cr	10	50	40	50	60	100	100	90	90	90	80	110	100	120
Cs	0.64	3.45	2.72	3.55	3.84	6	4.86	6.58	6.49	5.07	5.39	7.13	6.27	6.86
Cu	11	57	36	47	42	51	39	52	51	48	51	47	45	43
Dy	0.84	2.8	2.16	3.2	2.79	4.56	4.57	3.83	3.76	4.1	4.08	4.98	4.68	4.92
Er	0.54	1.63	1.28	1.88	1.63	2.52	2.53	2.2	2.12	2.29	2.32	2.79	2.61	2.79
Eu	0.2	0.7	0.55	0.77	0.69	1.15	1.18	0.97	0.97	1.04	1.07	1.27	1.16	1.29
Ga	2	9.7	7.8	11.1	10.4	17.9	16.3	17.4	17.1	15.5	15.9	20.4	18.2	20
Gd	0.94	2.98	2.36	3.3	2.98	4.84	4.86	4.15	4.05	4.44	4.38	5.34	5.02	5.35
Hf	0.4	1.9	1.4	2.4	2.3	4.4	4.6	3.5	3.4	3.5	3.6	4.2	4.2	5
Ho	0.19	0.62	0.48	0.7	0.61	0.95	0.97	0.82	0.82	0.88	0.89	1.05	1	1.06
La	4.5	17.1	13.3	17	18.1	29.8	26.9	26.7	25.9	25.2	26.1	32.8	29.6	31.7
Lu	0.08	0.25	0.2	0.29	0.25	0.39	0.38	0.34	0.33	0.35	0.36	0.42	0.39	0.42
Mo	<1	<1	<1	<1	<1	<1	<1	<1	<1	<1	<1	<1	<1	<1
Nb	1	5.4	3.9	5.7	6.5	14	14.2	10.7	10.7	11.6	11.9	15.3	13.6	15.5
Nd	3.8	14.3	11.3	15	15.1	25.8	24.5	22.6	21.8	21.7	22.5	28.3	25.4	28.2
Ni	6	43	30	41	29	53	44	45	58	37	51	46	46	51
Pb	3	8	7	10	9	15	13	14	14	13	14	17	12	12
Pr	0.97	3.83	2.94	3.91	4.04	6.98	6.47	6.15	5.96	5.86	6.12	7.59	6.88	7.61
Rb	10.3	56.4	45.6	60.4	64.9	109	91	112.5	111.5	90.4	93.5	122	108	120
Sc	2	9	7	10	9	15	14	15	15	13	13	15	14	16
Sm	0.81	2.91	2.3	3.2	3.1	5.1	5.06	4.43	4.27	4.38	4.56	5.58	5.06	5.64
Sn	<1	1	1	2	2	3	2	3	3	2	2	3	3	3
Sr	983	1260	1215	1290	1155	654	589	765	732	721	779	443	548	358
Ta	0.4	0.7	0.5	0.7	0.7	1.2	1.3	0.9	0.9	1	1	1.3	1.3	1.4
Tb	0.14	0.47	0.36	0.53	0.46	0.76	0.75	0.64	0.62	0.69	0.69	0.85	0.79	0.84
Th	1.27	5.93	4.32	6.08	6.57	11.25	9.84	10.55	10.45	9.35	10.1	13.2	11.35	12.6
Tl	<0.5	<0.5	<0.5	<0.5	<0.5	<0.5	<0.5	0.5	<0.5	<0.5	<0.5	0.5	0.5	<0.5
Tm	0.08	0.25	0.2	0.29	0.25	0.39	0.38	0.34	0.33	0.36	0.35	0.42	0.4	0.42
U	0.38	4.53	2.18	3.8	3.51	3.29	2.65	3.26	2.27	2.06	3.33	2.67	2.6	2.74
V	14	84	65	82	83	149	132	135	132	131	125	164	154	166
W	83	63	34	59	37	33	82	20	27	30	35	50	54	61
Y	7	20.7	16.8	22.3	20	28.9	28	24.8	24.3	26.4	26.2	30.2	29.2	30.1
Yb	0.5	1.65	1.26	1.81	1.6	2.45	2.44	2.15	2.09	2.23	2.24	2.67	2.54	2.71
Zn	16	74	55	75	68	100	90	107	99	94	96	98	96	107
Zr	20	70	50	80	80	150	160	120	120	120	130	140	150	180

Table 2.8: Major (wt%) and trace element (ppm) geochemistry of the conglomerate clasts

Sample	CR54 1	CR56 1	CR56 2	CR62 1	La557 1	La557 2	La587 A	La591 1	La591 2	La592 1	LM22 1	LM 22 2	LM 22 4	LM 25	LM22 3
Basin	Mar	Mar	Mar	Mar	Lal	Lal	Lal	Lal	Lal	Lal	Vqq	Vqq	Vqq	Vqq	Vqq
Lith	Qz sericite phyllite		Qz sericite phyllite	Qz sericite phyllite	s/stone		dacite	Chlorite amphibole schist	Chlorite schist		biotite schist	Chlorite schist	Amphibole shcist	Calc schist	basalt
SiO2	63.1	75.3	77.6	84.5	60.1	85.4	63.8	40.8	80.1	69.8	77.5	81.8	49.2	3.87	47.7
Al2O3	8.27	11.15	7.46	8.45	9.31	6.44	13.05	13.95	7.94	13.2	10.85	8.31	17.05	0.58	13.4
Fe2O3	4.83	1.92	1.88	1.61	4.55	1.92	9.16	9.81	2.02	5.12	3.39	1.5	12	0.5	12.7
CaO	8.55	0.14	2.14	0.34	8.77	0.12	1.92	13.25	0.17	0.33	0.2	0.54	1.22	52.5	7.93
MgO	1.38	0.78	0.63	0.48	1.06	1.01	1.56	3.23	0.85	1.96	1.23	0.64	6.91	0.98	7.48
Na2O	0.92	2.16	2.17	2.54	1.91	1.88	5.24	4.48	2.09	2.12	2.28	1.62	3.19	0.12	3.77
K2O	1.22	2.58	0.99	1.42	1	0.82	1.69	0.47	1.16	2.42	1.9	1.91	0.61	0.09	0.19
Cr2O3	<0.01	<0.01	<0.01	<0.01	0.01	<0.01	<0.01	0.03	<0.01	0.01	<0.01	<0.01	0.01	<0.01	0.02
TiO2	0.52	0.36	0.3	0.29	0.53	0.25	1.47	1.62	0.24	0.63	0.41	0.32	2.39	0.03	1.67
MnO	0.47	0.04	0.11	0.02	0.39	0.01	0.14	0.17	0.03	0.03	0.03	0.01	0.16	0.42	0.18
P2O5	0.06	0.09	0.04	0.07	0.07	0.06	0.48	0.14	0.07	0.11	0.1	0.1	0.12	0.08	0.15
SrO	0.04	0.01	0.02	0.01	0.02	<0.01	0.03	0.01	0.01	0.01	0.01	0.01	0.01	0.04	0.01
BaO	0.02	0.06	0.02	0.02	0.02	0.02	0.03	<0.01	0.02	0.05	0.03	0.07	0.01	<0.01	<0.01
LOI	9.83	2.27	3.24	1.6	10.45	1.32	2.38	10.95	1.82	3.27	2.24	1.83	5.65	42.2	5.62
Total	99.21	96.86	96.6	101.35	98.19	99.25	100.95	98.91	96.52	99.06	100.17	98.66	98.53	101.41	100.82
Ag	0.6	<0.5	0.5	<0.5	<0.5	<0.5	<0.5	0.6	<0.5	<0.5	<0.5	<0.5	<0.5	0.6	0.6
As	17	<5	<5	<5	5	<5	5	<5	<5	10	<5	<5	<5	<5	<5
Ba	163.5	539	184.5	227	136	154.5	287	24.2	216	418	291	566	107	22.4	41.2
Cd	0.5	<0.5	<0.5	<0.5	<0.5	<0.5	<0.5	<0.5	<0.5	<0.5	<0.5	<0.5	<0.5	<0.5	0.5
Ce	34.9	47.5	57.5	52.3	40.6	29.4	40.8	14.9	41.4	86.9	39.4	45.2	90.4	7.2	13.4
Co	64	63	74	46	32	82	61	73	88	33	46	99	60	23	58
Cr	40	20	20	20	60	20	<10	270	20	80	40	20	50	<10	160
Cs	2.73	5.48	1.89	2.57	2.35	0.97	0.32	0.3	2.58	5.78	3.39	1.38	0.79	0.24	0.1
Cu	25	2	2	1	13	2	54	70	5	15	8	7	36	1	100
Dy	4.44	1.76	4.74	3.17	5.12	1.47	9.81	5.96	3.53	5.24	2.81	3.12	10.3	1.45	6.44
Er	2.6	1.15	2.38	1.8	2.76	0.9	5.42	3.38	1.53	2.78	1.67	1.69	5.82	0.8	3.93
Eu	1.21	0.63	0.94	0.66	1	0.46	1.89	1.29	0.7	1.3	0.49	0.66	2.21	0.35	1.42
Ga	13.4	14.6	9.6	10.8	12	7.1	20.7	15.8	9.5	20.4	13.8	9.1	23.5	0.9	18.7
Gd	5	2.61	4.94	3.5	5.03	1.76	9.57	5.3	4.2	5.96	2.79	3.26	10	1.61	5.51
Hf	3.8	7.9	9.5	7.5	7	4.6	8.5	3.2	4.8	6.2	4.3	8.8	11	0.2	3.2
Ho	0.93	0.36	0.93	0.65	1.03	0.32	2.07	1.22	0.64	1.02	0.6	0.64	2.11	0.31	1.43
La	15.5	23.1	30	27.9	20.7	16	15.5	4.4	19.5	45	20.9	23.2	45.7	6.2	4.5
Lu	0.39	0.29	0.37	0.3	0.43	0.15	0.71	0.49	0.15	0.43	0.28	0.22	0.88	0.1	0.57
Mo	<1	<1	<1	<1	<1	<1	<1	<1	<1	<1	<1	<1	<1	<1	<1
Nb	18.5	11.7	8.2	8.8	7.8	6.9	7.7	3.4	7.8	15.9	9.4	8	68.9	0.6	3
Nd	13.6	19.3	24.6	21.3	19	11.9	27.2	10	19.5	35.7	17.6	19.2	43.7	5.9	11.4
Ni	23	6	6	5	28	7	2	107	9	20	9	7	36	2	48
Pb	24	3	9	7	11	5	2	<2	10	29	16	8	9	4	127
Pr	3.61	5.3	6.61	5.84	4.87	3.34	6.05	2.01	4.9	9.81	4.84	5.24	11.1	1.35	2.22
Rb	56.5	119.5	53.1	68.1	56.2	38.3	37.3	13.5	61.7	135	93.7	73	23.9	5	2.8
Sc	8	6	4	4	12	3	16	31	4	12	7	5	18	1	39
Sm	4.16	3.55	5.2	4.13	4.37	2.16	7.51	3.61	4.46	6.92	3.43	3.9	9.58	1.38	3.86
Sn	3	3	2	2	2	1	2	1	2	4	3	2	3	<1	1
Sr	377	56.9	189.5	49.8	165.5	30.8	285	130	65.5	73.1	85.5	79.5	90.5	307	102
Ta	2.6	2.6	2.4	2.1	1.1	2.3	1.6	1.5	3.8	1.9	2	2.9	5.3	0.5	1
Tb	0.76	0.35	0.82	0.54	0.85	0.27	1.62	0.92	0.65	0.91	0.48	0.52	1.69	0.25	0.99
Th	10.9	13.15	10.75	10.55	9.26	5.28	4.23	0.42	9.21	19.85	11.2	9.47	10.65	0.62	0.33
Tl	<0.5	0.5	<0.5	<0.5	<0.5	<0.5	<0.5	<0.5	<0.5	0.5	<0.5	<0.5	<0.5	<0.5	<0.5
Tm	0.39	0.21	0.36	0.27	0.41	0.14	0.82	0.52	0.21	0.42	0.26	0.25	0.89	0.11	0.6
U	2.03	3.22	2.35	2.34	2.42	1.02	1.1	0.22	1.78	2.36	1.8	2.02	2.93	0.63	0.23
V	96	31	26	23	69	25	109	305	27	120	61	29	259	<5	382
W	641	826	1110	790	243	1100	513	561	1570	300	606	1050	409	227	295
Y	26.7	9.7	26.4	18.2	29.9	8.7	55.9	31.8	18.4	28.3	16.2	18	54.6	12.8	39.7
Yb	2.56	1.63	2.37	1.85	2.74	0.92	4.86	3.42	1.21	2.78	1.65	1.5	5.81	0.67	3.77
Zn	110	39	26	24	63	35	99	85	43	83	51	26	165	12	158
Zr	130	290	370	290	260	170	310	120	170	220	140	310	440	<20	110

Table 2.9: Summarized results of Nd isotope analyses for the Viqueque and Marobo sections.

Sample	Position	Sm (ppm)	Nd (ppm)	$^{147}Sm/^{144}Nd$	$^{143}Nd/^{144}Nd$	$^{143}Nd/^{144}Nd$ Uncertainty	T_{DM} (Ma)	ε Nd (0Ma)
TS069	base	5.118	25.72	0.1203	0.512098	0.000007	1730	-10.5
TS027	middle	4.37	21.73	0.1216	0.512131	0.00001	1700	-9.9
TS047	top	5.549	27.84	0.1205	0.512138	0.00001	1670	-9.8
CR24	base	11.2	58.78	0.1152	0.511923	0.000008	1910	-14
CR41	middle	7.185	36.53	0.1189	0.51201	0.000008	1850	-12.3
CR62	top	7.431	38.94	0.1154	0.511991	0.000008	1810	-12.6

T_{DM} is the depleted mantle model age calculated using the linear model of Goldstein et al. (1984)
Uncertainty in Nd isotopic composition is 2 Standard Errors.

CHAPTER 3. IMPLICATIONS FOR TIMOR'S ROLE IN THE INDONESIAN THROUGHFLOW

3.1 Abstract

The tectonic closure of the Indonesian Gateway and accompanying volcanic activity has exerted a first-order control on bathymetric sill depths over geologic timescales. This in turn has influenced the source and dynamics of shallow and deep ocean currents that transport water between the Pacific and Indian Oceans, with potential implications for Indian Ocean cooling, aridification in Africa, hominid evolution, ENSO evolution and global climate. Bathymetric shallowing in the Halmahera region has been proposed as a key regulator of this system. Here I show that the rapid uplift of Timor between the Latest Miocene and Early Pleistocene is also likely to have influenced ITF dynamics by influencing the temperature and volume of deep water passing into the Indian Ocean.

3.2 Introduction

Atmospheric and oceanic heat transport exert a first order control on global climate (Covey & Barron 1988; Vranes et al. 2002) but are themselves largely determined by tectonic influences (e.g. Hay 1996). In particular, the tectonic closure of ocean gateways causes major oceanographic reorganizations, which perturb the global transfer of heat from one ocean to another and from equatorial to polar regions (Keigwin 1982; Mikolajewicz et al. 1993; Haug & Tiedemann 1998; Cane & Molnar 2001; Schneider & Schmittner 2006).

The Indonesian Seaway (Figure 3.1A) is the remains of a large oceanic gateway known as the Indonesian Gateway that used to exist between the northern margin of Gondwana (Australia) and Eurasia (Crostella 1977; Audley-Charles et al. 1988; Metcalfe 1996; Charlton 2001; Li & Powell 2001; Hall 2002,2011,2012). Beginning in the Permian, several crustal blocks were rifted off the northern margin of Gondwana and crossed the Tethys Ocean to accrete to Eurasia (e.g. Audley-Charles & Harris 1991; Acharyya 1998; Hall 2012). Their passages resulted in the consumption of ocean basins and the opening of others. The latest Ceno-Tethys ocean basin closed as Australia became the latest rift block and moved north since 45 Ma, progressively colliding with various elements of the Eurasian margin in the Indonesian region (Figure 3.2). The closure of the Indonesian Gateway caused causing rapid vertical movements and the opening and closing of small seas in Indonesia, culminating in the topographic and bathymetric development of the modern Indonesian archipelago (Hall 2002; Spakman & Hall 2010; Hall 2011,2012).

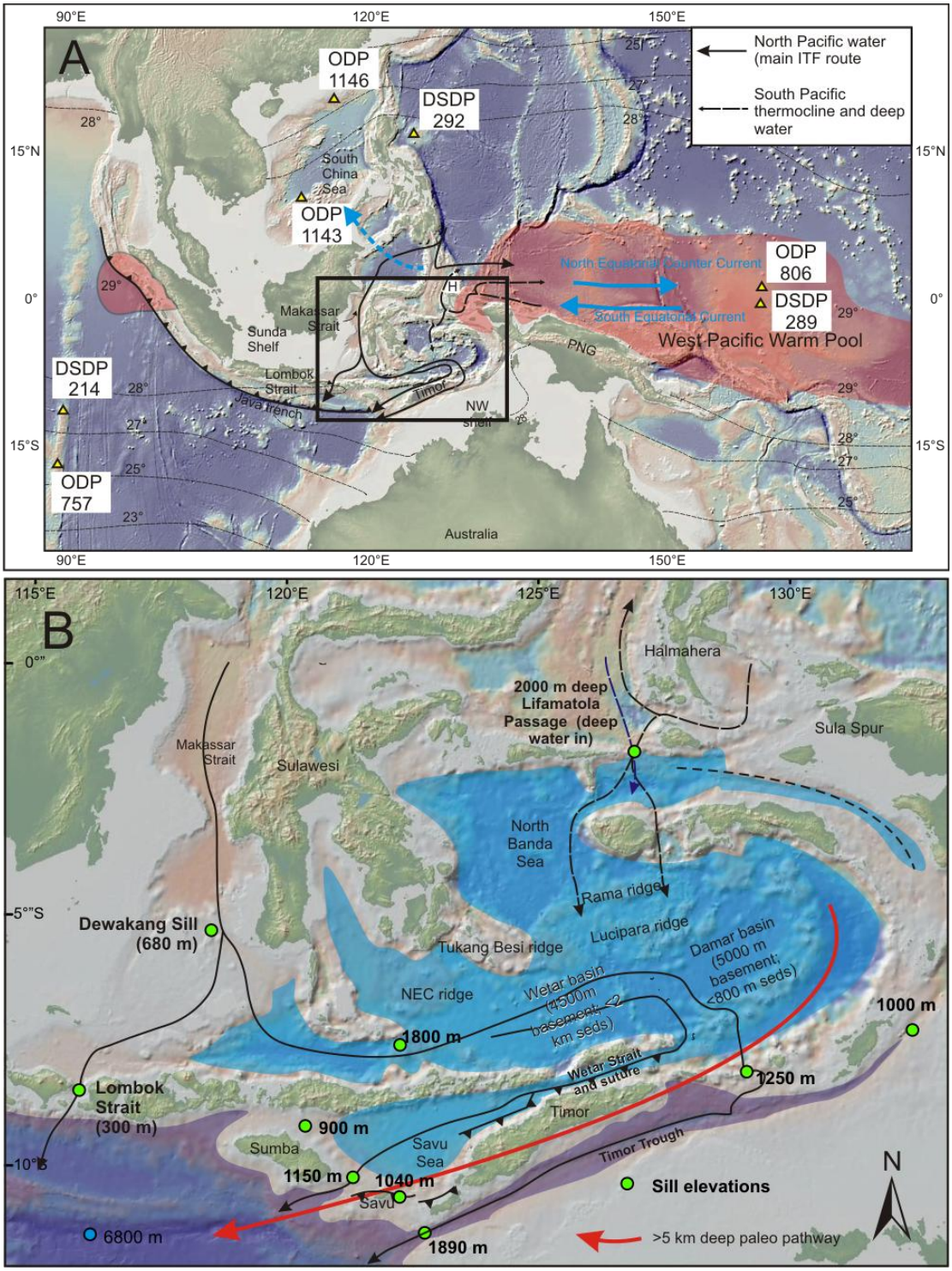

Figure 3.1: (Previous page) Timor's oceanographic setting. A) Map of the West Pacific Warm Pool illustrating the ponding of the West Pacific Warm Pool (WPWP) east of the Indonesian Seas. PNG – Papua New Guinea; H – Halmahera. Annual sea surface isotherms are after Gallagher et al. (2009). Area within the 29° isotherm shaded red. Arrows indicate the modern route of the Indonesian Throughflow are after Gordon and Fine (1996). IODP sites shown were used by various authors to define the evolution of the WPWP and the Indonesian Throughflow (see text). B) detail of area indicated by rectangle in A, showing the separation of waters deeper than 1300 m in the Banda Sea area (pale blue) from the Indian Ocean and Timor Trough (dark blue) by a Timor-Savu-Sumba deep-water dam. Global multiresolution topography basemaps (Ryan et al. 2009) via GeoMapApp. Sill depths based on Smith and Sandwell (1997).

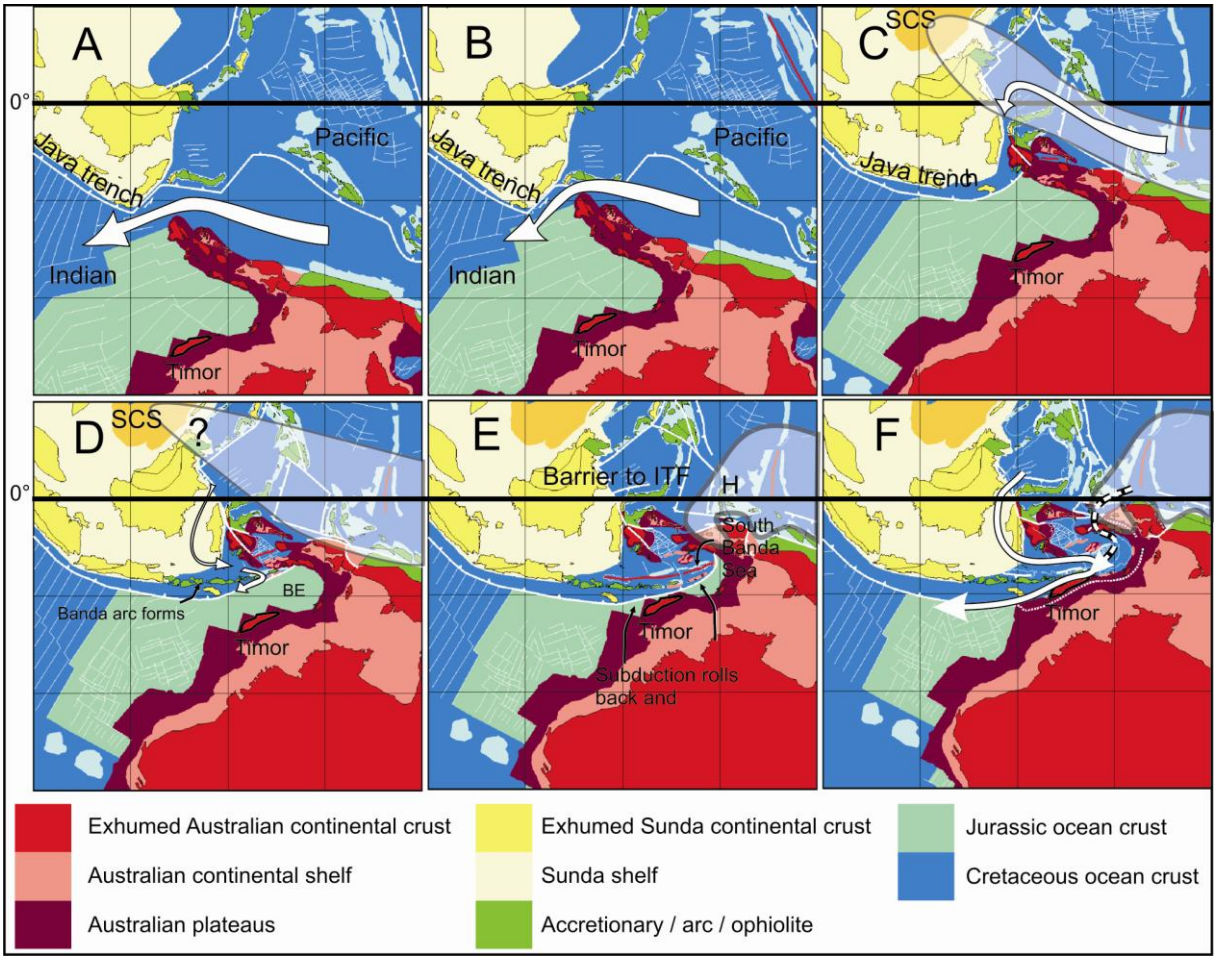

Figure 3.2: Tectonic evolution of the Indonesian Throughflow. Figures adapted from Spakman and Hall (2010). MS – Makassar Strait; SCS – South China Sea; BE – Banda embayment; ITF – Indonesian Throughflow; H – Halmahera; For discussion see text.

The modern Indonesian Seaway is the only tropical pathway between the world's oceans and provides a passage for surface and intermediate water of the Indonesian Throughflow (ITF - Gordon & Fine 1996; Gordon & McClean 1999; Gordon et al. 2003a)(Figure 3.1A). The ITF is a group of currents that transfers water from the thermocline in the northwest Pacific Ocean to the Eastern Indian Ocean via the Indonesian Archipelago (Gordon & Fine 1996) (Figure 3.1A}, and are the constricted remnant of the Indonesian Gateway current.

The modern ITF is volumetrically small at only 11 sverdrups1 (Gordon & Fine 1996; Gordon et al. 2003a), but its immediate influence and that of the WPWP extends beyond the

1 Sverdrup (Sv) is a volume transport unit equivalent to one million cubic metres per second. 1 Sv approximates all the water flowing in all the worlds rivers, whilst the Gulf Stream transports ~150 Sv (http://oceancurrents.rsmas.miami.edu/glossary.html).

eastern Indian Ocean, where ITF waters discharge from the Indonesian Passage, right across to the East African coast, toward which ITF waters flow with the South Equatorial Current (Schott & McCreary Jr 2001). The far-reaching influence of even the attenuated ITF makes it a critical global circulation component, with the potential to impact climate on interannual and longer time scales (Schott & McCreary Jr 2001).

Cane and Molnar (2001) proposed a major role for the tectonic evolution of the Indonesian archipelago in influencing the Late Cenozoic oceanography of the ITF and thereby global climate. They noted the synchronicity of final closure of the Indonesian Gateway, particularly Pliocene uplift of Halmahera, with the onset of northern hemisphere glaciations, and through their circulation modeling they suggested a cause and effect relationship. Their hypothesis suggests that, late in the closure history of the Indonesian Gateway, New Guinea's northward movements culminated in the uplift of Halmahera, which switched the source of the ITF from warmer South Pacific waters to cooler North Pacific waters. The probable effects of a sudden cooling would have included a contribution to global shoaling of the thermocline at the Mid Pliocene climate transition, and thus to a reduction in poleward atmospheric heat transport. These would have led to cooling of global climate and to the intensification of the Northern Hemisphere Glaciation, with consequences for hominid evolution in the last 3-4 million years (Cane & Molnar 2001).

The critical geographical aspects of Cane and Molnar's (2001) hypothesis are (i) the position of the Java trench, which lies 10° south of the equator, and (ii) the northern extent of the Halmahera/New Guinea/Australia barrier. The Java trench is relatively stable over 20 Myr (Besse & Courtillot 1991; Hall 2002; Schettino & Scotese 2005; Spakman & Hall 2010). Australia, however, moved rapidly NW toward the equator during the Cenozoic, culminating in the collision of Australia with the Banda Arc (Hall 2002; Spakman & Hall 2010). The island of Timor lies in an area of extreme and complex topography and bathymetry that lies east of the Java trench (Figure 3.1). This topography and bathymetry developed due to the collision of Australia with the Banda Arc and presently controls the exit of the ITF from the Indonesian Seaway (Gordon et al. 2003a; Kuhnt et al. 2004). The remainder of this introduction will outline the relationships between tectonics and oceanography in the Indonesian Seaway and propose a hypothetical role for Timor in the evolution of the ITF and thereby global climate.

3.3 Neogene tectonic and oceanographic evolution of the Indonesian Throughflow

The tectonic and paleogeographic evolution from Indonesian Gateway to Indonesian Seaway has been reconstructed in several publications by Hall and co-authors (Hall 2002,2009;

Spakman & Hall 2010; Hall 2012). It is summarized below (Figure 3.2) in the context of the development of the ITF.

Australia had begun to move northwards in the Eocene (Hall 2012), subducting under Sunda and leading to the extensional opening of the Makassar Strait (Hall et al. 2009). The Makassar Strait is the major route for shallow waters (<680 m) of the modern ITF (Figure 3.1B). In the Early Oligocene the remains of a deep ocean seaway still connected the Pacific and Indian Oceans (Figure 3.2A). By the late Oligocene (Figure 3.2B) the northward passage of Australia began to constrict the seaway as the northernmost outlying elements of Australia passed the eastern end of the Java trench, but the Makassar Strait was already mostly more than 1 km deep (Hall 2009). In the late Middle Miocene (Figure 3.2C), the ocean gateway had virtually closed as the leading edge Australian continent collided with the subduction zone to its north. Gallagher (2009) suggested that the Indonesian Seaway became a biogeographic barrier to benthic foraminifera by ~10 Ma, but Indian Ocean Nd isotope evidence from fossil seawater and from fish teeth both suggest that the surface to intermediate strength of the throughflow actually increased when it was constricted (Martin & Scher 2006; Gourlan et al. 2008). Planktic biogeography over this period is uncertain, but a pool of warm water known as the West Pacific Warm Pool (WPWP - Wyrtki 1989) (see Figure 3.1A) began to form on Australia's eastern margin.

The WPWP is a pool of warm water that ponds on Australia's eastern margin and is fed by the South Equatorial Current (Figure 3.1A). The WPWP is marked by a deep thermocline that impacts on the presence and isotopic compositions of depth-stratified foraminifera (e.g. Li et al. 2004). The foraminiferal record at ODP 806 and DSDP 289 in the Western Pacific indicates that the WPWP became established by 9.9 Ma (Gasperi & Kennett 1993; Sato et al. 2008), as the northern limits of the Australian continent passed the eastern end of the Java trench and approached the equator (Hall 2002; Spakman & Hall 2010). Biostratigraphic dating of the depth evolution of the thermocline in the South China Sea at ODP 1143 and 1146 (Figure 3.1) indicates the thermocline there also warmed and deepened between 11-9 Ma(e.g. Li et al. 2004). The warming of the South China Sea did not initially affect DSDP 292 (e.g. blue dotted arrow Figure 3.1).

As the seaway became tectonically impeded, the northern edge of the Jurassic ocean crust of the Banda embayment drew level with the eastern end of the Java trench (Figure 3.2C). The subduction zone propagated eastwards across the northern edge of the embayment and subducted its dense Jurassic ocean crust. This subduction gave rise to the Banda volcanic arc, which began erupting around 12 Ma and was well established by the latest Miocene (Abbott & Chamalaun 1981; Honthaas et al. 1998) (Figure 3.2D), maintaining the barrier to deep water flow through the

ITF. As Australia advanced northeastwards, the Banda subduction zone rolled back across the Banda embayment, leading to Latest Miocene and Early-Pliocene (6.6-3.5Ma) seafloor spreading and subsidence in the South Banda Sea (Honthaas et al. 1998), which is recorded by magnetic lineations in the Damar basin of the South Banda Sea (Hinschberger et al. 2001) (Figure 3.1B; Figure 3.2E). During this period of subduction of the Banda embayment a trench of similar proportions to the Java trench would have lain south of the Banda Arc and provided a narrow deep passage between the South Banda Sea and the Indian Ocean (red arrow, Figure 3.1B).

According to Hall and Wilson (2000), Halmahera was uplifted in the Pliocene due to closure of the doubly-subducting Molucca Sea. The unconformity between older Neogene and Pliocene clastic sedimentary rocks on Halmahera has an age of 3 Ma (Hall & Wilson 2000), similar to the age of the unconformity on Timor (Audley-Charles 1986a; Haig & McCartain 2007). The uplift of Halmahera probably caused the WPWP to expand northwards across the equator, where it was established at DSDP292 by ~4.4 Ma (Figure 3.1) (Cane & Molnar 2001; Sato et al. 2008). Halmahera presently plays a major role in restricting the volume of WPWP water that enters the throughflow from the South Pacific thermocline (Morey et al. 1999).

Cane and Molnar attributed the cooling of the eastern Indian Ocean to a change in the source of the ITF caused by the uplift of Halmahera (Cane & Molnar 2001). Foraminiferal biogeography shows that the ITF became a barrier to planktic foraminifera around 5.2 Ma (Srinivasan & Sinha 1998) and Nd isotope data from the eastern Indian Ocean has been interpreted to suggest closure of the Indonesian seaway around 5.5 - 4 Ma (Martin & Scher 2006; Gourlan et al. 2008). Martin and Scher additionally found evidence for a reopening of either an invigorated or North Pacific sourced seaway around 3.5 Ma (Martin & Scher 2006). Surface water temperature and salinity appears to have changed little over this time (Karas et al. 2009), but foraminiferal $\delta^{18}O$ from DSDP 214 (Figure 3.1A) suggests that the reopening of the seaway introduced cooler fresher subsurface water into the eastern Indian Ocean between 3.5 to 2.95 Ma, either due to the introduction of cool subsurface water or to the exclusion of West Pacific Warm Pool water (Karas et al. 2009).

3.4 Timor's role in the modern Indonesian Throughflow

The water of the modern ITF is composed of water from the North Pacific thermocline, which passes through the Makassar Straits, and deep, cool water that is sourced from the South Pacific (Gordon & Fine 1996; Ilahude & Gordon 1996). The evolution of the ITF on its transit through the Indonesian Seaway is controlled by the bathymetry of the seaway, particularly the elevation and location of sills (Figure 3.1B), which control the temperature and salinity of Indonesian waters that enters the eastern Indian Ocean (Gordon et al. 2003b; Sprintall et al. 2009; van Aken et al. 2009).

Although surface waters west of Halmahera flow north, at depths of 2000 m the Lifamatola Passage provides the only route for southward-flowing, deep, cold water (>2 Sv, with a mean temperature of 3.2°C) to join the ITF (Figure 3.1B) (van Aken et al. 2009). The southern exits of the Banda Sea are all presently shallower than the Lifamatola Passage (Gordon et al. 2003a; van Aken et al. 2009) (see sill depths on Figure 3.1B). The modern pathway has a maximum sill depth of only 1280 m east of Timor where a narrow pathway accesses the Timor Trough (Figure 3.1B). The Banda arc-continent collision effectively forms a Timor-Savu-Sumba tectonic dam that separates the Indonesian Seaway from the Indian ocean at depths >1280 m (Figure 3.1B).

Recent transport estimates suggest that exit flow above 700 m is dominated by surface waters from the Makassar strait, and that Lifamatola deep inflow contributes the bulk of Indonesian Intermediate Water component of the throughflow that exits the Timor Trough and Wetar Straits at depths between 700 and 1200 m (Sprintall et al. 2009). In order for this water to leave the Banda Sea via the Timor Trough, it must upwell to depths less than 1300 m where it is significantly warmer than the 2000 m deep inflowing water (Gordon et al. 2003a; van Aken et al. 2009). van Aken (2009) suggested that the temperature gain is achieved by turbulent mixing and a downward flux of heat from the overlying 500 m of water, which implies that upwelling Indonesian Intermediate Water may cool the overlying water column between 200-700 m depth. By contrast, the surface waters of the ITF are warmed by >3°C as they pass through the Flores and Banda Seas (Sprintall et al. 2009).

3.5 A proposed role for Timor in the development of the Indonesian Throughflow

As indicated in the Prologue to this thesis, and previously by Kuhnt (2004), the timing and rates of arc-continent collision in Timor are potentially relevant to global climate through the impact on the bathymetric development of the ITF. The common factor of the oceanographic regime since the Miocene development of the Banda Arc (Figure 3.2D) is the exit of the ITF from the Indonesian seaway, south of the Sunda shelf and along the Java trench, via the present location of Timor. Prior to collision in Timor, a 5 km deep pathway is likely to have linked the South Banda Sea to the Java Trench and provided a discharge channel for deep water from the Indonesian Seaway. Both Martin and Scher (2006) and Gourlan et al. (2008) documented an apparent shutdown of the ITF inflow to the Indian Ocean between 5.5 and 4 Ma, during which time this study has indicated that the Banda subduction trench was shallowing dramatically due to the uplift of Timor.

At first glance this would suggest that oceanographic changes due to Timor's emergence should have resulted in a warming of water entering the ITF due to damming of the deep cold water flow. However, Karas et al. (2009)documented no surface temperature change since 5.2 Ma but a temperature decrease at depths of 300 m to 450 m between 3.5Ma and 2.95 Ma. However, the paleoceanographic results of Martin and Scher (2006), Gourlan et al. (2008) and Karas et al. (2009), and the temperature and transport characteristics of the ITF (Gordon et al. 2003a; Sprintall et al. 2009; van Aken et al. 2009), suggest a hypothetical scenario in which Timor may have played an important role in controlling the depth of the thermocline in the eastern Indian Ocean, and thereby global climate.

Collision in Timor may have shallowed the subduction trench to depths less than the contemporaneous depth of the Dewakang Sill, reducing the cross-sectional area of the ITF exit flow and effectively isolating the flow of deep water through the ITF. This may have ultimately resulting in virtual shutdown of the ITF or its immediate precursor around 5Ma (e.g. Martin and Scher, 2006; the MioJet of Gourlan et al., 2008). Haig's (2012) paleobathymetry shows the Timor orogen surrounded by deep water throughout the Pliocene but his northern contours are without evidence and his western boundary is based on the Marobo Basin, which I have shown to be a deep orogen perpendicular graben that was bounded to the east by an emergent landmass by 4.5 Ma at the latest. A modern analogue to this proto-Timor barrier might be the island of Sumba, which has a sill depth of only 900 m on its northern side (Figure 3.1B).

Overthrusting of the forearc along the Wetar Suture initiated at 3.5 Ma (Price & Audley-Charles 1983,1987) and would have provided a progressively deepening bypass that increased the cross sectional area of the ITF, re-invigorating it and causing upwelling of IIW, resulting in cooling of subsurface waters and shoaling of the thermocline in the eastern Indian Ocean (Karas et al. 2009). During this time, Timor was being uplifted to elevations that were, at least locally, greater than the modern elevations, resulting in the development of orographic precipitation and a dry lee side (Nguyen et al. 2013). This may have caused a resultant freshening of the surface waters of the ITF in the Timor Trough.

This initial hypothesis is based on correlation of the shallowing of the Timor Sea and emergence of Timor, with the ~5 Ma shutdown of the ITF. Further work would obviously be required to test this hypothesis. Some testable implications are that the Banda sea waters would have been poorly ventilated and poorly mixed below the controlling sill depth between 5 and 3.5Ma. This situation may be recorded by a geochemical signature, possibly including a Ce anomaly due to paleo-redox conditions, a steeper temperature gradient in intermediate water temperatures, and a change in the isotopic composition and biogeography of depth-stratified

foraminifera, particularly benthic foraminifera. Although the Banda Sea is deep and has not been cored by any IODP drill holes, ridges such as the Tukang Besi ridge south of Sulawesi may be in the right position and range of water depths to yield useful results.

PART TWO: THE WEST SEGMENT OF THE GREENDALE FAULT

CHAPTER 4. KINEMATICS OF THE WATERFORD RELEASING BEND ON THE GREENDALE FAULT

4.1 Abstract

Dextral slip at the western end of the east-west-striking Greendale fault during the 2010 M_W 7.1 Darfield earthquake transferred onto a northwest-trending segment, across an apparent transtensional zone, here named the Waterford releasing bend. This study used detailed surface mapping, differential analysis of pre- and post-earthquake LiDAR, and property boundary (cadastral) re-surveying to produce high-resolution (cm-scale) estimates of co-seismic ground-surface displacements across the Waterford releasing bend. The results indicate that the change in orientation on the Greendale fault incorporates elements of a large-scale releasing bend (from the viewpoint of westward motion on the south side of the fault) as well as a smaller-scale restraining stepover (from the viewpoint of southeastward motion on the north side of the fault). This results in the Waterford releasing bend exhibiting a decrease in displacement to near zero at the change in strike, and the presence within the overall releasing bend of a nested, localized restraining stepover with contractional bulging. The exceptional detail of surface deformation and kinematics obtained from this contemporary surface-rupture event illustrates the value of multi-method investigations. The data provide insights into strike-slip fault bend kinematics, and into the potentially subtle but important structures that may be present at bends on historic and prehistoric rupture traces.

4.2 Introduction

Over the past 10 years or so, documentation of earthquake fault surface rupture by well-established field methods, including geological/geomorphological mapping and geodetic surveying, has increasingly been supplemented by technologies such as interferometric synthetic aperture radar (InSAR) (e.g. Reigber et al. 1997; Price & Burgmann 2002; Beavan et al. 2010a) and LiDAR (e.g. Hudnut et al. 2002; Quigley et al. 2012b). In combination, these methods provide an opportunity for examining fault deformation and kinematics in unrivalled detail and precision. Contemporary surface rupture events, in favorable land surface settings, provide primary evidence for the style and kinematics of fault deformation, and documenting their character provides an invaluable interpretive analogue for structural and kinematic studies of prehistoric fault deformation.

The 2010 Darfield earthquake in Canterbury, New Zealand (Figure 4.1) caused surface rupture of the Greendale fault across a low-relief alluvial plain. The plain is an intensively-farmed agricultural region and contains a multitude of straight lines in the form of roads, fences and ditches that provided ideal piercing points for quantifying fault rupture (Barrell et al. 2011; Quigley et al. 2012b; Villamor et al. 2012). Quigley et al. (2012b) took advantage of these piercing points to undertake detailed field mapping, and in combination with evaluation of LiDAR flown after the earthquake, were able to quantify fault offsets to high precision.

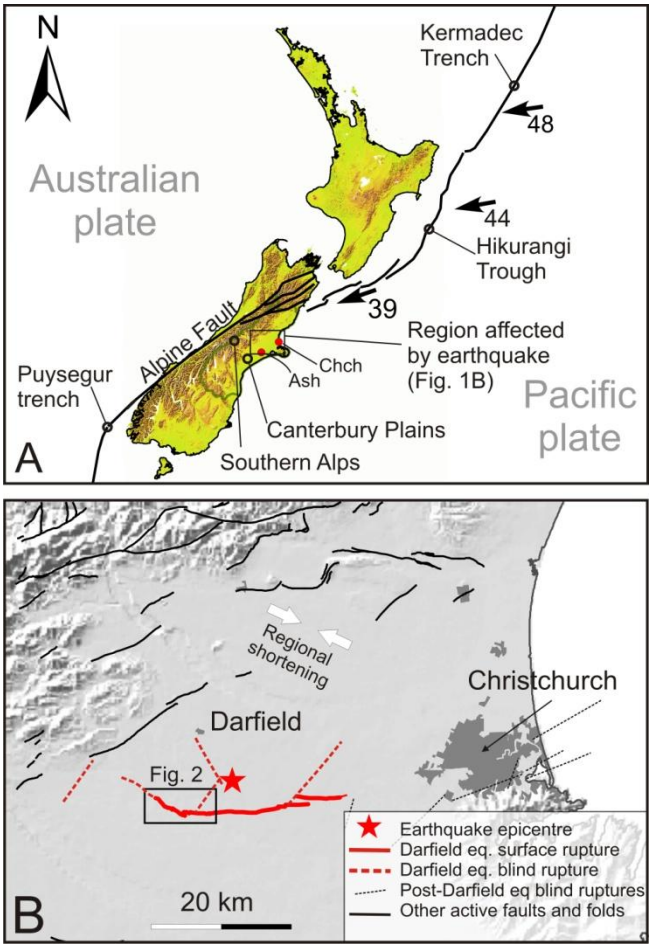

Figure 4.1: Regional setting. A) New Zealand plate boundary and relative motion vectors (mm/yr) between the Australian and Pacific Plates (DeMets et al., 2010). Canterbury Plains form the low relief (green) east of the Southern Alps in the central South Island. Ash – Ashburton; Chch – Christchurch. B) Location of the Greendale fault west of Christchurch in mid-Canterbury. The extent of surface rupture is from Quigley et al. (2012), and extents of blind ruptures are from Beavan et al. (2012). Known active (i.e. late Quaternary) faults and folds are based on GNS Science QMAP datasets (Cox & Barrell 2007; Forsyth et al. 2008). Regional shortening direction from Sibson et al. (2011a).

Serendipitously, two high-quality geodetic datasets had been acquired prior to the earthquake, in the vicinity of the western end of the Greendale fault. A LiDAR survey flown 5 months before the earthquake was partly overlapped by LiDAR flown a few days after the earthquake. Also, a cadastral survey was conducted one month before the earthquake on a property through which the Greendale fault subsequently ruptured for ~2 km. Rupture of the Greendale fault also temporarily diverted the course of the Hororata River. This study included mapping of the earthquake-induced flood, analyses of pre- and post-earthquake LiDAR surveys and post-earthquake cadastral re-surveying of property boundaries, to further aid understanding of the surface deformation and displacement across the Greendale fault. These datasets span a zone where the fault strike changed by ~40°, and have allowed us to characterize this fault bend in remarkable detail. Documentation of this detail is the focus of this paper.

4.3 The Darfield earthquake

New Zealand lies astride the boundary between the Pacific and Australian plates, at a location where they converge obliquely at rates of 30–50 mm yr (DeMets et al. 2010) (Figure 1A). Continental collision across the South Island drives uplift of the Southern Alps (Norris & Cooper 2001) and is expressed by varying rates and styles of active deformation across Canterbury (Pettinga et al. 2001; Campbell et al. 2012). The rupture of a fault network beneath the Canterbury Plains, eastern South Island, on 4 September 2010 generated the M_W 7.1 Darfield earthquake (Beavan et al. 2010b; Gledhill et al. 2010; Gledhill et al. 2011; Beavan et al. 2012), which caused widespread ground-shaking and damage (Cubrinovski et al. 2010; Gledhill et al. 2010; Quigley et al. 2010a; Quigley et al. 2010b; Van Dissen et al. 2011; Quigley et al. in press). Geodetic modeling has revealed that this single earthquake event comprised an interlinked succession of ruptures on several fault structures (Figure 4.1B; Figure 4.2) (Beavan et al. 2012). All remained blind, apart from the Greendale fault, which produced a c. 30 km long surface rupture, predominantly strike-slip with dextral sense (Quigley et al. 2010a; Quigley et al. 2010b; Barrell et al. 2011; Quigley et al. 2012b). The Greendale fault lies in a large sedimentary basin. Fault rupture was initiated c. 10 km deep, within indurated, slightly metamorphosed, Mesozoic greywacke rock, and propagated to the surface through a surficial 1-1.5 km thick cover of post-mid Cretaceous sedimentary strata, including as much as 500 m of Quaternary fluvial gravels (Browne et al. 2012; Jongens et al. 2012).

The Greendale fault comprises three geometric segments, each named for their relative locations (Quigley et al. 2012b). The East and Central segments strike east-west, whereas the West segment strikes northwest (Figure 4.2). In the context of dextral rupture exhibited by the fault trace, the strike change between the West and Central segments is transtensional in nature (Quigley et al. 2012b), so the zone across which the strike change occurs is referred to here as the Waterford releasing bend, taking its name from a nearby farm. Dextral displacement of up to ~5.3 m on the Central segment decreases to ~ 1.2 m on the West segment (Quigley et al. 2012b). The West segment displayed a notably south-side-up vertical component of offset (c. 1.5 m), which caused temporary partial avulsion of the Hororata River (Quigley et al. 2010b; Barrell et al. 2011) (Figure 4.2). Seismic source models indicate that the Greendale fault rupture proceeded bilaterally from the vicinity of the Waterford releasing bend, which itself lies close to the intersection of the Greendale fault with the northeast-southwest-striking Charing Cross reverse fault, on which the Darfield earthquake was initiated (Figure 4.2) (Holden et al. 2011; Beavan et al. 2012).

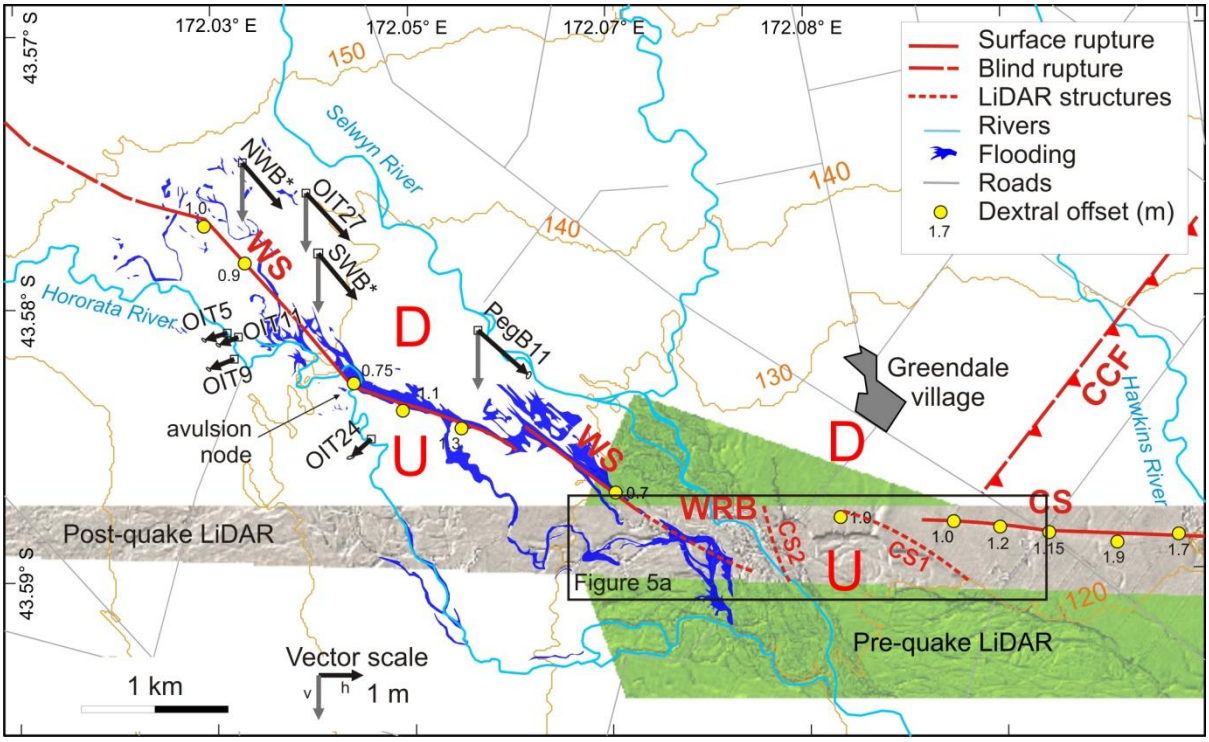

Figure 4.2: Fault map of the West segment (WS) and westernmost part of the Central segment (CS) of the Greendale fault. U and D denote relative upthrow and downthrow across the scarp. The immediate area of the change in strike between the segments is here named the Waterford releasing bend (WRB). CCF is the location of the subsurface tip of the blind Charing Cross Fault (Beavan et al. 2012), teeth towards hanging wall. The extent of co-seismic avulsion and resulting flooding is shown as well as the location of pre- and post-earthquake LiDAR. Arrows indicate displacement vectors for re-surveyed cadastral witness marks (Table 2). Dotted red lines denote structures defined from LiDAR analysis in this study (Figure 4.5). Dextral offset measurements are from Quigley et al. (2012). The Waterford releasing bend includes an approximately 1.5 km wide zone where no surface deformation was able to be detected from field mapping. Topographic contours (brown) are in meters above sea level. Contours, roads and streams are from Land Information NZ digital data, Crown Copyright reserved.

4.4 Methods

4.4.1 Flood mapping

The extent of avulsion-induced post-earthquake flooding (Figure 4.2) was mapped by digitizing flooded areas seen in a set of overlapping oblique aerial photographs taken about 12 hours after the earthquake. The photographs were georeferenced using ArcGIS software with reference to digital topographic maps and pre-earthquake digital orthophotos.

4.4.2 Cadastral surveys

Cadastral surveys have been used to document surface displacements resulting from the Chi Chi earthquake in Taiwan (Lee et al. 2006; Lee et al. 2010; Lee et al. 2011). A cadastral property survey done about one month before the earthquake spanned the northern half of the West

segment. Baseline surveying employed a Trimble R8 Global Navigation Satellite System (GNSS) RTK, and the survey was adjusted in '12d Model' software using simple loops and the Bowditch adjustment method (Bowditch 1808). The survey was fixed relative to local benchmarks by locating the RTK base station on a buried iron tube witness mark that was established relative to three local benchmarks in 2004. The flat, unforested farmland provided a favorable GPS environment, so the baseline survey over the survey extent of 2 km is likely to be internally accurate to within 2 centimeters, with exact accuracy depending on the detail of satellite geometry during the survey (Table 4.1).

Table 4.1. ESTIMATED Accuracy of data used in determination of surface displacements

Survey	Horizontal (m)		Vertical (m)	
	IGS05	Relative	Lyttelton 1937 Via NZGeoid05	Relative
Pre-quake cadastral	±0.05	±0.02	NA	±0.02
Post-quake GPS	±0.05	0		
Post-quake cadastral	*	0<0.16	NA	±0.15
Pre-quake LiDAR		<0.1 †	0.07	
Post-quake LiDAR		<0.1 †	0	

* sum of post-quake GPS and error ellipse dimensions from Table 4.2

† based on COSI-Corr results

After the Darfield earthquake, thirteen of the cadastral survey marks lying within 200 to 700 m of the West segment rupture trace were re-occupied (Table 4.2). The ground surface positions of two boundary pegs (NWB and SWB - Figure 4.2) were established in the IGS05 reference frame by a 24-hour-mode GPS survey on 14-15 April 2011, 7 months after the Darfield earthquake. Both marks lie northeast of the surface rupture, so a correction was applied to remove the effects of post-seismic deformation, based on trends observed during repeat observations of nearby first-order bench marks a few kilometers north of the fault (Beavan et al. 2012). The corrected observations were converted to NZGD2000, and then to the NZGD2000 Mount Pleasant Circuit coordinate system, then finally to NZMG, replicating transformations applied to the pre-earthquake cadastral survey. Taking account of the various error sources, the accuracy of ground surface displacements of these marks is likely to be $\pm$5 cm (John Beavan, GNS Science, pers. comm., Table 4.1).

The cadastral marks were resurveyed using a Trimble 5600 semi-robotic total station and reduced the data using Trimble's Terramodel 10.41 survey software. The total station survey was georeferenced by assigning the GPS survey coordinates to pegs NWB and SWB. Pre and post-earthquake surveys were combined in a single AutoCAD drawing and point displacements were measured in terms of azimuth and horizontal (Table 4.2) and vertical components (Table 4.3).

Table 4.2: Waterford Farm trilateration network locations and shifts. Coordinates in New Zealand Map Grid coordinate system. All values in meters, except azimuths in degrees. Data are grouped to show marks on the hanging wall (direction E) ordered from north to south, followed by marks on the footwall (direction NW), also ordered north to south.

	Error Ellipses			Pre-earthquake		Post-earthquake		Shifts			
Point ID	Major axis (m)	Minor axis (m)	Azimuth	Easting	Northing	Easting	Northing	Easting	Northing	Magnitude	Azimuth
Hanging wall											
OIT 28	0.074	0.030	308°57'18"	2432259.755	5736862.809	2432260.741	5736861.735	0.986	-1.074	1.458	137.433
NWB	Fixed with GPS survey	0.000	0.000	2432144.186	5736738.788	2432145.117	5736737.705	0.931	-1.083	1.428	139.308
OIT 27	0.074	0.030	308°57'18"	2432579.007	5736523.240	2432580.008	5736522.193	1.000	-1.047	1.448	136.307
OPEG 48	0.022	0.019	310°07'45"	2432779.314	5736217.303	2432780.285	5736216.250	0.971	-1.053	1.433	137.337
SWB	Fixed with GPS survey	0.000	0.000	2432664.006	5736120.018	2432664.882	5736118.971	0.875	-1.047	1.365	140.112
PEG B11	0.144	0.024	64°42'50"	2433753.819	5735597.614	2433755.013	5735596.558	1.194	-1.056	1.594	131.499
Footwall											
OPEG 47	0.108	0.016	311°26'44"	2432054.014	5735579.074	2432053.522	5735578.894	-0.493	-0.180	0.525	249.980
OIT 5	0.115	0.021	310°49'56"	2432020.894	5735552.382	2432020.370	5735552.204	-0.524	-0.178	0.554	251.225
OIT 11	0.105	0.016	316°33'07"	2432121.319	5735543.383	2432120.900	5735543.212	-0.418	-0.171	0.452	247.822
OIT 9	0.119	0.025	320°49'52"	2432116.744	5735410.867	2432116.185	5735410.675	-0.560	-0.192	0.591	251.099
OPEG 41	0.121	0.026	319°58'16"	2432097.694	5735401.008	2432097.075	5735400.764	-0.619	-0.245	0.665	248.416
OIT 24	0.160	0.045	14°01'38"	2433027.352	5734858.853	2433026.901	5734858.433	-0.451	-0.421	0.616	226.973
OLD POST	0.163	0.045	14°29'41"	2433036.960	5734832.804	2433036.502	5734832.378	-0.457	-0.426	0.625	227.037
Average hanging wall								0.993	-1.060	1.454	136.999
1σ deviation hanging wall								0.108	0.015	0.076	3.035
Average footwall								-0.505	-0.272	0.584	242.095
1σ deviation footwall								0.076	0.120	0.074	11.770

OIT – Old iron tube; NWB – NW boundary peg; OPEG – Old peg; SWB – SW boundary peg

Table 4.3: Relative elevation change matrix for cadastral marks. Negative values indicate that the mark listed in the row has subsided relative to the mark listed in the column.

	Height adjustments	OIT28	OIT27	OPEG 48	PEG B11	OPEG 47	OIT 5	OIT 11	OIT 9	OPEG 41	OIT 24
OIT28	open	0	0.2156	0.1065	0.0819	-1.131	-0.9837	-1.3831	-1.2316	-1.0466	-1.1746
OIT27	0.173		0	-0.1091	-0.1337	-1.3466	-1.1993	-1.5987	-1.4472	-1.2622	-1.3902
OPEG 48	0			0	-0.0246	-1.2375	-1.0902	-1.4896	-1.3381	-1.1531	-1.2811
PEG B11	0.119		Hanging wall		0	-1.2129	-1.0656	-1.465	-1.3135	-1.1285	-1.2565
OPEG 47	0.071					0	0.1473	-0.2521	-0.1006	0.0844	-0.0436
OIT 5	0.113						0	-0.3994	-0.2479	-0.0629	-0.1909
OIT 11	0.102							0	0.1515	0.3365	0.2085
OIT 9	0.113								0	0.185	0.057
OPEG 41	0.113									0	-0.128
OIT 24	0.173						Footwall				0

4.4.3 LiDAR

Aerial LiDAR surveys provide high-resolution topographic data using the two-way travel time of laser pulses. Such datasets are used to image fault scarps in a variety of environments (Hudnut et al. 2002; Muller & Harding 2007). This study documents the vertical motions associated with uplift and subsidence in the Waterford releasing bend area by differencing pre- and post-earthquake LiDAR data where they overlapped (see Figure 4.2). This technique is widely applied in a diverse range of earth science disciplines, including volcanology (Marsella et al. 2009) and glaciology, and has recently been applied to fault surface rupture (Oskin et al. 2012).

Two LiDAR datasets were collected in 2010 using NZ Aerial Mapping's (NZAM) Optech ALTM 3100EA LiDAR system with system PRF set to 70KHz. Pre-earthquake LiDAR was flown in late March 2010 at 1,300 meters above ground with a 40° field of view. The pre-earthquake survey was controlled using a geodetic reference mark established by NZAM at Ashburton (Figure 4.1A) and positional and vertical accuracy was verified by an independent commercial survey. Vertical accuracy for ground returns in the Selwyn area was 0.07 m (1σ) across 5 sites (Table 4.1). NZAM checked the positional accuracy using surveyed positions of vertical discontinuities such as bridges and walls, and found it to be a good fit. The LiDAR data was supplied for this project as a 1m pixel raster.

Post-earthquake LiDAR was flown along the general line of the Greendale fault on 10 September 2010 at 600 meters above ground, with a field of view of 38°, but did not encompass the West segment as it had not, at that time, been delineated by mapping. This LiDAR survey was brought into terms of the post-earthquake geodetic reference system using a control site established

by GNS Science. Vertical accuracy of ground returns was determined using the GNS control site and adjusted to improve it from an average height difference of +/-0.03 m to 0.00 m (Table 4.1). Positional accuracy was checked by overlaying GNS Science survey data over LiDAR data and a good fit was observed. Post-earthquake LiDAR data was supplied for this project as a 0.5 m pixel raster.

Overlapping pre-earthquake LiDAR was subtracted from the post-earthquake LiDAR and the difference mapped at 1 m cell size, the resolution of the pre-earthquake LiDAR raster (Figure 4.5). Sub-pixel correlation of the pre-and post-earthquake LiDAR rasters was carried out using COSI-Corr to determine horizontal offsets (Leprince et al. 2007a; Leprince et al. 2007b; Konca et al. 2010).

4.5 Deformation and kinematics of surface rupture

4.5.1 Co-seismic scarp development and avulsion

As a result of the earthquake, the West segment of the Greendale fault formed a co-seismic scarp across a meander bend in the Hororata River (Figure 4.2, Figure 4.3A). The scarp impeded downstream flow and partly avulsed the Hororata River onto an older, higher surface. The river flow was high and relatively turbid, resulting from the expulsion of large volumes of groundwater as a result of the earthquake. Within 2 km of the fault trace, the unconfined groundwater table rose by several tens of meters (Cox et al. 2012a), producing widespread uncontrolled artesian flows from bores and from earthquake-induced ground fissures. Numerous examples of fissures were observed during field mapping, surrounded by localized deposits of sand and fine-gravel ejecta which attest to the force of the groundwater expulsion.

The newly formed scarp directed part of the Hororata River flow to the southeast (Figure 4.2), parallel to and generally within 100 m of the scarp (Figure 4.3). Fortunately, the avulsion flooding was identified from the air and recorded photographically within 12 hours of the rupture, because the landowners moved rapidly to remediate the flooding by deepening the bed of the Hororata River across the scarp. Documentation of the onlap of avulsion floodwater along the scarp was instrumental in defining the location of the West segment, and guiding the field mapping of displacements (Figure 4.3D). Mapping of the distribution of floodwaters from georeferenced oblique aerial photographs revealed subtle features such as slight strike changes and the presence of a small left stepover (Figure 4.2).

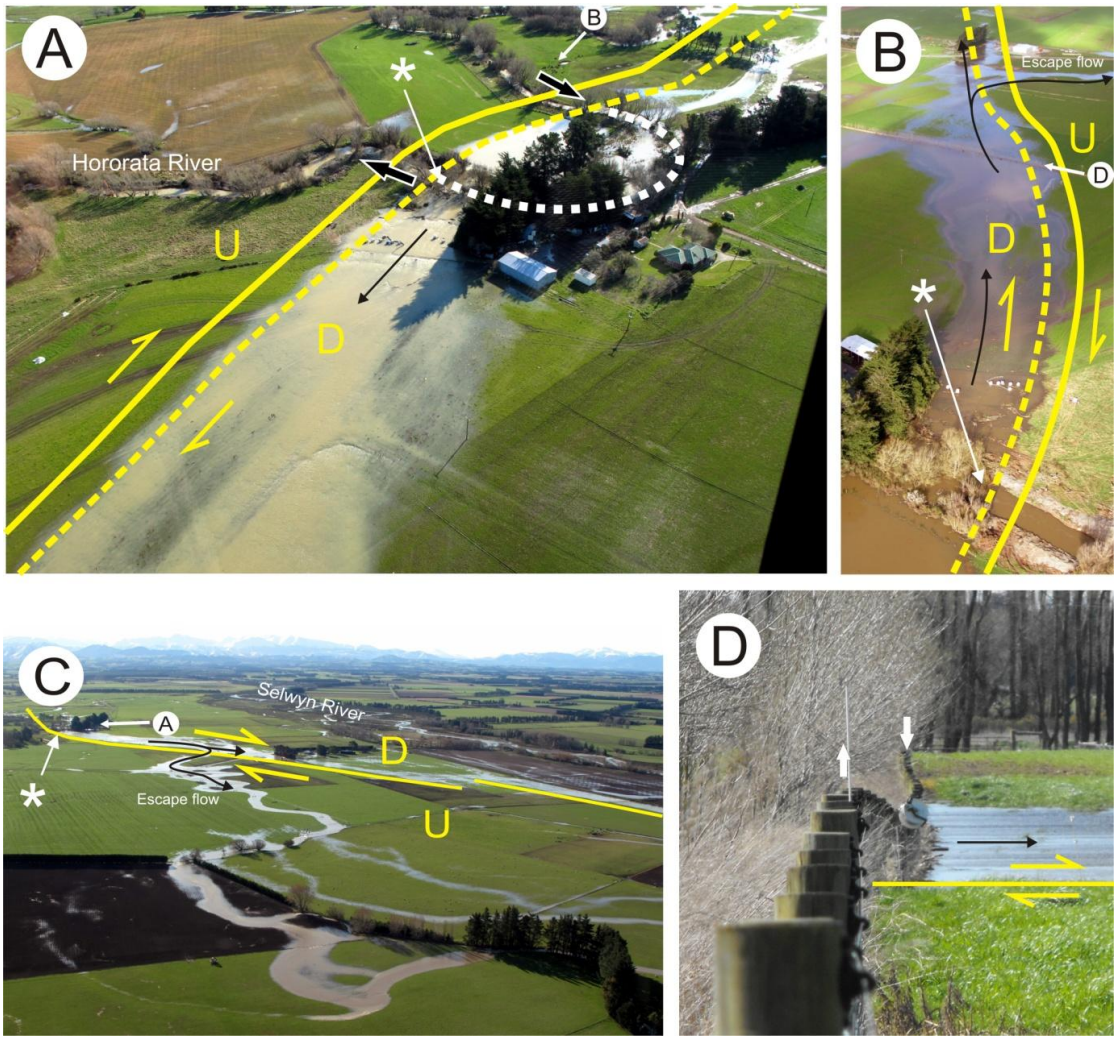

Figure 4.3: Deformation and flooding resulting from rupture of the West segment of the Greendale fault. Solid line/dashed line respectively mark the crest and base of the surface trace, while U and D denote relative upthrow and downthrow. Thin black arrows show the direction of avulsion flow. A) View to the northwest of the avulsion node (*) (Barrell et al. 2011). Here, ~1.5 m of oblique dextral southwest-side up displacement impeded the Hororata River channel (dashed white), leading to partial avulsion and widespread flooding. Block arrows show original flow direction. Large shed is 20 m long. B) View to the southeast from the avulsion node showing scarp-parallel flooding and escape flow across the scarp via a pre-existing channel on the alluvial plain. Location/orientation of photo indicated on A. C) Long view north showing the split of the flooding due to southward escape from the scarp-directed flow. D) View northeast across the scarp, showing relationship of flooding to dextral and vertical deformation of previously straight fenceline (location indicated by white arrows). Location/orientation of photo indicated on photo B.

4.5.2 Kinematics of the West segment of the Greendale fault

Barrell et al. (2011) and Quigley et al. (2012b) reported that much of the dextral displacement, especially on the East segment, was accommodated by horizontal flexure that was mappable only with reference to previously linear features. The West segment scarp was rounded rather than sharp, and involved displacement of the order of 1 m, distributed over a zone typically about 20 m wide (Figure 4.3D). No free-faces were observed on the West segment, which suggests that ground-surface deformation was an oblique-dextral monoclinal flexure of near-surface gravelly sediments above the fault plane (Figure 4.4).

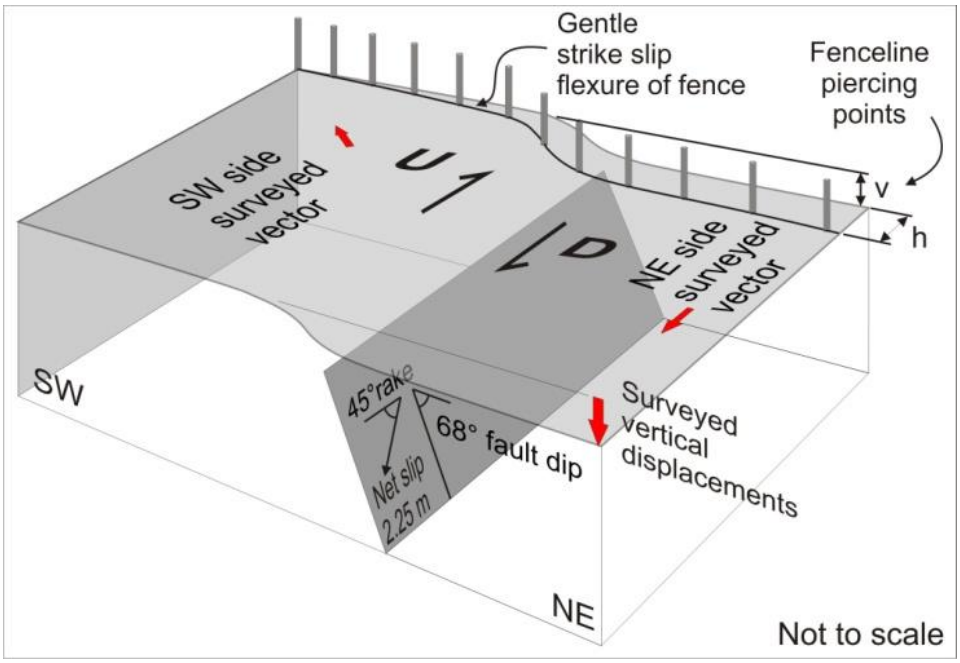

Figure 4.4: Diagrammatic sketch showing the results of cadastral re-surveying and the derivation of net slip across the West segment scarp from the survey data. U and D denote relative upthrow and downthrow across the scarp. The surface 'scarp' is a monoclinal flexure of the gravel above the fault plane and is typically at least 20 m wide (see Figure 4.3, Figure 4.5B). The total width of the strike-slip deformation zone may range up to several hundred meters (see for example Villamor et al. 2012). The cadastral survey provides a broader perspective on total displacement and does not depend on long straight linear features (e.g. fencelines) spanning the full width of the deformation zone.

Cadastral survey marks show a distinct pattern of displacement relative to the West segment of the fault. On each side of the fault, the marks showed only small amounts of vertical movement relative to one another (average of ~0.12 m), but the marks on one side of the fault shifted substantially and consistently relative to those on the other side (Table 3). On the northeast side of the fault, marks were downthrown by an average of 1.48 m (maximum 1.6 m) relative to OIT11, the survey mark on the southwest side of the fault closest to the fault trace (Figure 4.2; Table 4.3). The northeast side of the fault moved horizontally an average of 1.45 m toward 137° (maximum 1.59 m toward 131.5°) (Figure 4.2; Table 2); these vectors are approximately parallel to the strike of the fault. The southwest side of the fault moved horizontally an average of 0.58 m toward 242° (maximum 0.67 m toward 248.5°); these vectors are approximately perpendicular to and away from the fault trace, and thus perpendicular to displacement on the downthrown side. These observations indicate that the West segment fault is extensional and may therefore be robustly inferred to dip towards the northeast.

The flexural nature of the scarp means that the West segment fault plane is not exposed, so the cadastral survey displacements were used to estimate the fault plane attitude and the orientation and magnitude of the net slip on the fault (Figure 4.4). The fault scarp through most of the cadastral survey area strikes 138°. The horizontal displacements of the upthrown and downthrown sides were applied in their displacement directions and yielded an average horizontal component of net

slip of 1.7 m towards 117.7° (maximum of 1.99 m towards 114°). Adding the vertical displacement between the southwest and northeast sides of the fault to the horizontal slip returns an average net slip of 2.25 m (maximum 2.55 m) (Figure 4.4) on a fault dipping approximately 68° to the northeast (63° using maximum slip values). For both average and maximum calculations, the net slip rakes 45° from the south, which yields a transtensional dip-slip to strike-slip ratio of 1:1.

4.5.3 Kinematics of the Waterford releasing bend

Differencing of the two 2010 LiDAR surveys reveals the displacement patterns across the Waterford releasing bend between the West and Central segments (Figure 4.5A). The difference map has negative elevation values for subsidence and positive values for uplift. Vertical differences can arise from horizontal as well as vertical displacement of topographic features (e.g. Mukoyama 2011; Oskin et al. 2012). Within Figure 4.5A, bright vertical anomalies denote horizontal displacement of the margins of streams and abandoned channels, as well as braid channels of the Selwyn River that have migrated during the interval between the surveys. However, due to the subdued topography within the study area, this latter effect is insignificant compared with tectonic displacements.

The differential elevation map (Figure 4.5A) shows that land to the south and west of the Waterford releasing bend was uplifted by amounts ranging from 0.4 m to 1.0 m. Land north and east of the Waterford releasing bend subsided by between ~0.4 and 0.8 m. Both subsidence and uplift contributed to the physical expression of scarps on either side of the Waterford releasing bend (Figure 4.5B). Maximum subsidence is recorded in a half-graben developed on the downthrown side of the West segment, which subsided by at least 0.8 m. However, profile 1 (Figure 4.5B), located 2 km east of the Waterford releasing bend, also records 0.4 m of net subsidence. The wide extent of subsidence northeast of the Waterford releasing bend is in keeping with east-west dilation on West segment due to the dextral slip on the Central segment. Maximum uplift (~1 m) occurred on the south side of the Central segment, east of the Waterford releasing bend (Figure 4.5A), while ~0.4 m of uplift occurred on the southwest side of the West segment (profile 3, Figure 4.5B).

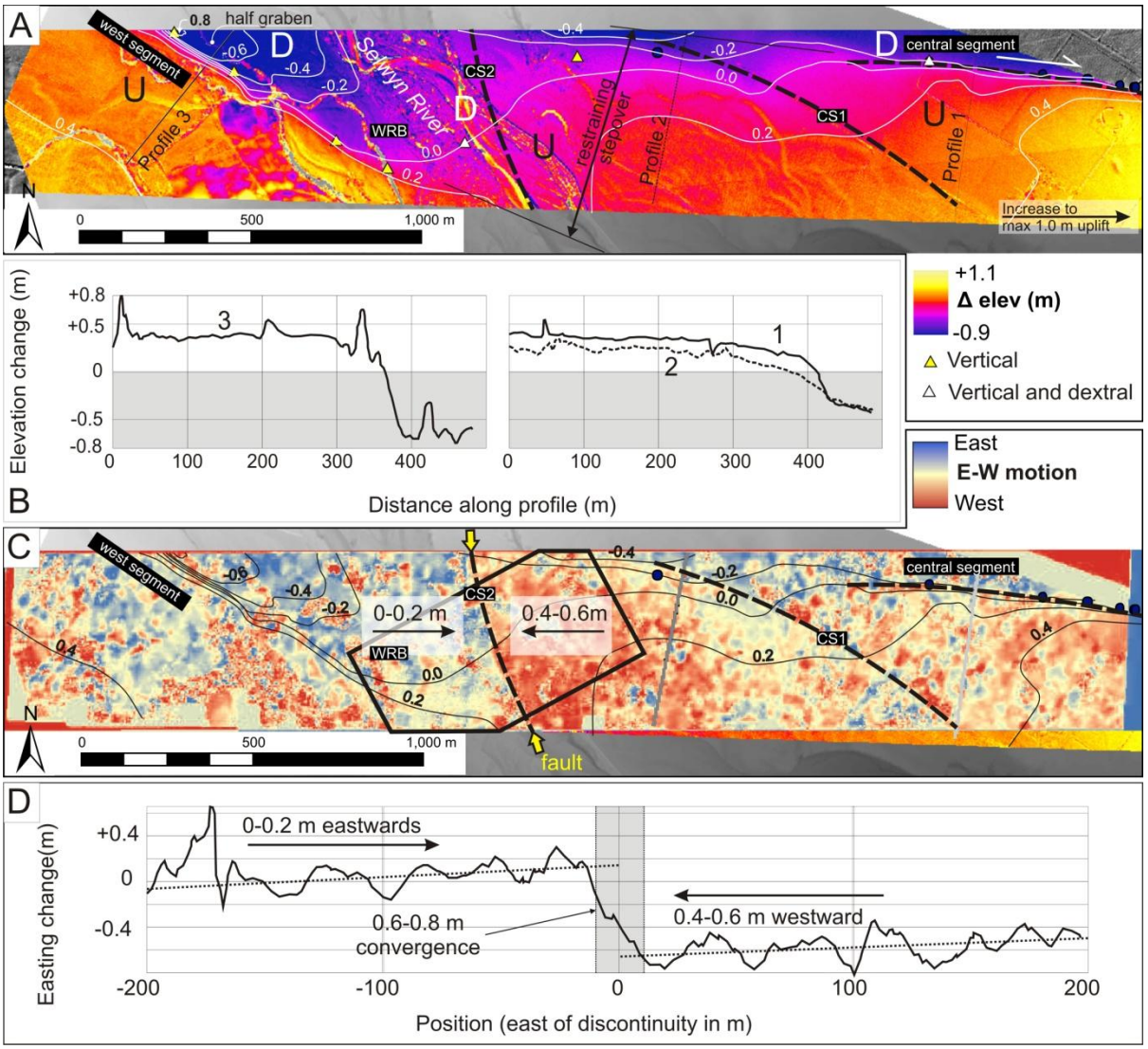

Figure 4.5: Results of LiDAR differencing. U and D denote relative upthrow and downthrow across the scarp. A) Post-minus-pre-quake LiDAR elevation difference map. White lines are simplified uplift contours (negative values for subsidence). Heavy dashed black lines are faults. Note half-graben development west of the Selwyn River. Selwyn River passes through the surface rupture at a local uplift minimum on the Waterford releasing bend. B) Same-scale topographic profiles of [1, 2] fault scarps of the Central segment and [3] fault scarp of the West segment. Grey background indicates net subsidence. For location see A. Central segment scarps (particularly profile 2) are smaller and more diffuse than the clear scarp on the West segment (profile 3). C) COSI-Corr sub-pixel correlation of LiDAR difference model, showing the CS2 structure, along with uplift contours from panel A. The rectangle area was sampled to produce a stacked plot of east-west horizontal displacement (D) that demonstrates 0.6 to 0.8 m of convergence across the CS2 structure. The grey band denotes the CS2 structure, and the dotted lines represent the mean displacement trends.

The vertical displacements revealed by LiDAR difference mapping of the Waterford releasing bend clearly define the strike of the fault and highlight subtle structures that are not otherwise discernible. Most strikingly, LiDAR-determined displacements highlight the overlapping nature of the West and Central segments of the Greendale fault across the Waterford releasing bend. The Greendale fault does not simply curve into a releasing bend, but rather transitions via at least two smaller-scale (<1km) restraining left steps that are nested within the overall releasing

bend. This nested stepover region, which spans ~800 m, is referred to as the 'restraining stepover' (Figure 4.5A).

The left-stepping minor structures making up the restraining stepover are identified here as CS1 and CS2 (Figure 4.5A). The western end of the Central segment strikes 098° and has a well-defined surface scarp about 50m wide (profile 1, Figure 4.5B). About 200 m beyond the western limit of surface deformation on the Central segment, across a restraining bulge defined by uplift contours, is the CS1 structure. The southeastern 300 to 400 m of the CS1 structure strikes 120° but westward, near the edge of the difference map area, it curves back to an east-west strike. The vertical expression of the CS1 structure comprises a broad (~200 m wide) warp that is about 0.7 m high (profile 2, Figure 4.5B). Dextral displacement on CS1 was recorded by Quigley et al. (2012b) but vertical displacement on CS1, and its left stepping relationship to the Central segment, was only determined from the LiDAR data, because the broad, subtle, warping was not visible in the field. About 500 m farther west is the north-northwest-striking CS2 structure, which lies approximately sub-parallel to the Selwyn River. CS2 was not detected in the field. Although the vertical anomaly associated with the CS2 structure is somewhat ambiguous (Figure 4.5A), it is clearly revealed by horizontal sub-pixel correlation of pre-and post-earthquake LiDAR rasters (Figure 4.5C). Stacked horizontal displacement profiles across CS2 reveal east-west shortening of approximately 0.8 m (Figure 4.5D), due to ~0.6 m of westward motion east of CS2 and ~0.2 m eastward motion between CS2 and the West segment. The 0.2 m of eastward motion occurred on the northeast side of the West segment.

Although fault slip planes were not exposed on the Central segment of the Greendale fault, the displacement of the northeast side of the West segment toward the Central segment of the Greendale fault (Figure 4.2), coupled with consistent, although slight, uplift to the south of the trace of the Central segment, implies that the Central segment has a southward dip and a minor component of reverse slip. This is in keeping with geodetic modeling by Beavan et al. (Beavan et al. 2010b; Beavan et al. 2012). Similarly, minor structure CS2 is compressional and uplifted to the east, suggesting a component of eastwards dip. Together CS1 and CS2 appear to define a positive flower structure.

Apart from the definition of CS2, pixel correlation in this study is generally noisy due to limited extent of the data and few suitable correlation points. Any north-south strike-slip on CS2 is lost within this noise and is thus negligible compared with the east-west dip-slip. The lack of COSI-Corr evidence for north-south displacements comparable with vertical displacements at the releasing bend suggests that the dip of the Central segment is very steep. CS2 is almost perpendicular to the Central segment, which means that horizontal convergence across CS2 must have been fed by strike slip on the Central segment, particularly on CS1. The east-west

convergence of 0.8 m across CS2 therefore provides a minimum measure of the strike-slip on CS1, which is compatible with the minimum 1.0 ±0.25 m measured in the field by Quigley et al. (2012b) using RTK. By adding a 0.8 to 1.0 m horizontal displacement to the 0.7 m vertical displacement of CS1 at profile 2, a minimum net slip of 1.1 to 1.2 m is calculated for CS1. Again, this is compatible with RTK measurements but includes considerably less uncertainty regarding the vertical component of displacement.

In the LiDAR overlap area the West segment strikes ~122°, slightly more westerly than the strike of the fault in the cadastral survey area. The scarp of the West segment, which is clearly defined in the northern part of the difference map (profile 3, Figure 4.5B), dies out towards the southeast, ~500 m south of the western end of the Central segment. The Waterford releasing bend between the West and Central segments is a transtensional right bend with respect to strike slip on the Central segment (Figure 4.6Ai), but a contractional left bend with respect to strike slip on the West segment (Figure 4.6Aii). The east-west shortening on segment CS2 effectively solves the space problem created by transtension on the West segment extending south into the contractional field of CS1 and the Central segment (Figure 4.6B).

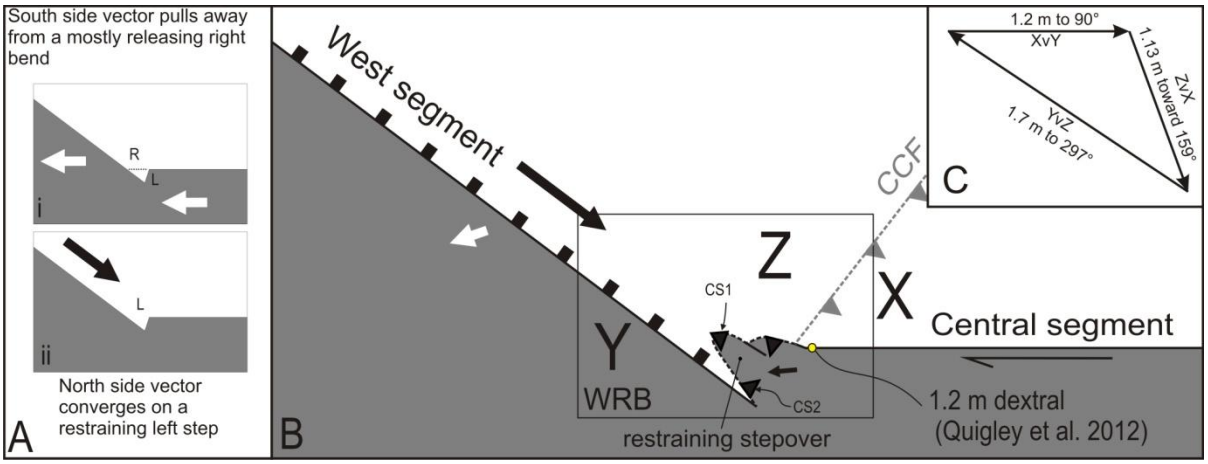

Figure 4.6: Structures contributing to the development of the Waterford releasing bend area. A) Sketch maps of the bend from the perspectives of surface displacement vectors on the south (i) and north sides of the fault (ii). L and R indicate left and right bends or steps. B) The net result of combining the two sets of structures. CCF = location of subsurface tip of blind Charing Cross fault. The westward-directed south side vector dilates the West segment. The minor left bend onto the overlapping southern tip of the West segment is accommodated by CS2. Convergence of the north-side vector with the Central segment is expressed by the nested restraining stepover onto CS1, and accommodated at a larger scale by underplating at the footwall of the CCF. C) Vector calculation for relative horizontal displacement across the Charing Cross fault based on Equation 1, assuming a triple junction between the West and Central segments and the Charing Cross fault.

4.5.4 Displacement trends

The combination of cadastral and LiDAR mapping techniques clarifies fault displacement trends (Figure 4.7). Strike-slip displacements on the West segment increased slightly for 2.5 km southwards from the northwestern end of the surface scarp (Figure 4.7A) and were generally

consistent with, although as much as 25% larger than, the field-survey displacement measurements (Quigley et al. 2012b). The discrepancy is probably due in part to the lack of suitably long, originally straight markers crossing this sector of the fault zone, and in part to the survey marks reflecting the overall effects of larger displacements at depth (e.g. Beavan et al. 2010b).

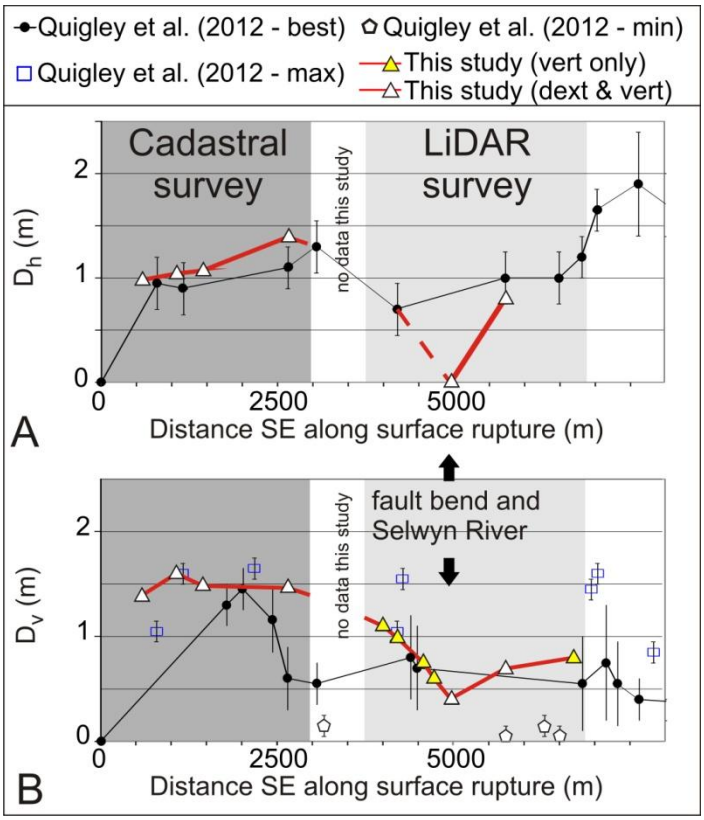

Figure 4.7: Displacement trends on the West and Central segments in the vicinity of the Waterford releasing bend. A) dextral and B) vertical displacement plots for the bend area comparing data of Quigley et al. (2012 – field mapping) and this study. Note the displacement minimum at the Waterford releasing bend at distance 5000 m.

Southeast of the cadastral survey area, strike-slip displacements determined by LiDAR differencing decline over a distance of 2.5 km from 1.5 m to approximately zero at the Waterford releasing bend, where only 0.2 m of eastwards horizontal motion of the hanging wall is calculated from pixel correlation at the restraining stepover to the Central segment (Figure 4.5D). Strike-slip displacements increase east of Waterford releasing bend. A single estimate of 0.8 m of dextral displacement at the location of profile 2 (Figure 4.5) is consistent with previously obtained at-fault displacement measurements (Quigley et al. 2012b).

The net vertical displacement also declines in the area of the restraining stepover (Figure 4.7B). Relative vertical displacements in the cadastral survey area range from 1.4 to 1.6 m. Within the LiDAR map area, the vertical displacements on the West segment immediately northwest of the restraining stepover totaled ~1.2 m, about 25% less than the 1.4 to 1.6 m vertical displacements across the cadastral survey network. These data show a consistent reduction in vertical

displacement south towards the Waterford releasing bend and its restraining stepover (Figure 4.7B). This pattern of decreasing displacement is associated with dying-out of a half graben that is highlighted by vertical displacement contours northwest of the Waterford releasing bend (Figure 4.5A).

The 2.25 m of net slip calculated using the cadastral-based vertical and strike-slip determinations on the West segment is more than double the 1 m of net slip estimated close to the Waterford releasing bend at profile 2 (Figure 4.5A). The reduced displacement towards the Waterford releasing bend coincides with increasingly diffuse and subtle scarp expression. Away from the Waterford releasing bend, within the study area, the scarp on both segments is well-defined (≤50 m wide, Figure 4.5B, profile 1, 3). Closer to the Waterford releasing bend, the scarp becomes diffuse and elevation change is distributed across 200 to 300 m (e.g. profile 2, Figure 4.5A, B). Between CS2 and the West segment, the uplift gradient declines to only around 0.2% and no scarp is definable. The Selwyn River, either fortuitously or due to structural control (as inferred for the nearby Hawkins River by Campbell et al. 2012), crosses the fault trace at this local minimum in vertical displacement (Figure 4.5A, Figure 4.7), and exhibits a reduction of its bed gradient of only <0.1% over 600 m. The slight reduction in bed gradient, coupled with a 0.2% tilt toward the fault imposed by the half graben, may increase the flood hazard in the vicinity of the fault.

4.6 Discussion

The processes governing fault rupture behavior at releasing bends are not well understood (Cunningham & Mann 2007; Mann 2007), in part because surface rupture at a fault bend is commonly subtle and/or distributed (King & Nábělek 1985; King 1986; Devès et al. 2011). Accurate, high-resolution documentation of surface displacement provides an important piece of information on fault characteristics in these zones. This study has illuminated the displacement interrelationships that arose across a releasing bend between the West and Central segments of the Greendale fault during a single, surface-rupturing, multi-fault earthquake. The deformation at the Waterford releasing bend is particularly subtle. Field-based fault mapping was only able to identify the main scarps of the West and Central segments, but no deformation was detected in the releasing bend area. Furthermore, this area lay in a ~1.5 km-wide low-coherence zone in the differential InSAR data (Beavan et al. 2010b; Elliott et al. 2012), and therefore the InSAR could not quantify the nature of deformation across the Waterford releasing bend. Because the post-earthquake LiDAR was flown prior to mapping of the West segment, and thus did not cover that segment, the mapping of fault-induced avulsion flooding provided a useful asset that was instrumental in helping define the location and geometry of the West segment and Waterford releasing bend.

The vertical displacements shown by LiDAR on the West segment near the Waterford releasing bend are greater than Beavan et al.'s (2010b), in terms of both maximum uplift (0.4 compared to 0.1 m) and maximum subsidence (0.8 compared to 0.6 m). The total vertical displacements in the cadastral survey area along the West segment of the Greendale fault are even greater but cannot be stated in terms of absolute uplift and subsidence. The greater uplift and subsidence at the West segment, compared with the far-field, suggest that the footwall of the West segment is a southwest-tilted uplifted block and that the hanging wall is downwarped into a half graben close to fault. This is consistent with elastic rebound on a normal fault (Koseluk & Bischke 1981) or with a near-surface steepening of fault dip (Bray et al. 1994).

Surface displacement on the Greendale fault reaches a minimum at the Waterford releasing bend, and increases either side of the bend. This is consistent with predictions of slip distribution at the intersection of two separate, differently oriented, same-sense fault zones (King & Nábělek 1985). The clear changes in slip distribution attributable to this earthquake indicate that the fault wall rocks are behaving non-rigidly, and are locally lengthening and shortening in the slip direction. Given that one wall locally shortens, while the other locally lengthens, the faults can be regarded as local, mixed stretching faults in the sense of Means (1989). Similar patterns of coseismic displacements occurred during the Denali Earthquake, at the intersection of the Denali and Totschunda faults (Fig. 3B in Eberhart-Phillips et al. 2003); the Landers earthquake between the Emerson and Homestead Valley faults (Fig. 3 D&E in Sieh et al. 1993); and at the transition into the Lake Eften releasing bend during the Duzce earthquake (Fig. 3C in Konca et al. 2010). The latter slip distribution reactivated and smoothed the overall slip distribution on the terminal segment that ruptured during the Izmit earthquake.

Changes in the orientation of strike-slip faults that cause local extension or contraction on continuously curved bounding faults are typically referred to as releasing and restraining bends respectively. On the other hand, stepovers commonly transfer slip between separate, sub-parallel, overlapping faults (e.g. Christie-Blick & Biddle 1985). The combination of investigation techniques shows that the Waterford releasing bend, which appeared at first glance to be a simple curve in a single strike-slip fault (e.g. Sibson et al. 2011a) marks a complicated transition from a steeply south-dipping strike-slip fault (Central segment) to an overlapping, northwest-dipping, dextral transtensional fault (West segment) (Figure 4.5). The transition incorporates elements of bend as well as stepover geometry.

Compared with regional geodetic surveys (Beavan et al. 2010b; Beavan et al. 2012; Elliott et al. 2012), the data provide improved constraints on the displacements that occurred within an area where the InSAR decorrelated and where there were few high-order trigonometric points for GPS surveys. The horizontal displacements and the net slip estimates from the cadastral survey detailed

here are consistent with those of Beavan et al. (2010b) in azimuth and magnitude, and the GPS horizontal displacements measured by Beavan for the cadastral part of this study are incorporated in the model of Beavan et al. (2012). My determination of net slip of 2.25 m is greater than the near surface value of 1.5 m calculated by Elliott et al. (2012) from InSAR but consistent with their modeled slip at 1 to 2 km depth.

My calculated movement vectors show that the south and southwest side of the Greendale fault shifted westward as a coherent block. Therefore, seen from the south side of the fault, the Waterford releasing bend is indeed a transtensional right bend (Figure 4.6Ai). However, the southeastern 500 m of the West segment is in a contractional quadrant for the Central segment. In this context, the east-west contraction across the CS2 component of the restraining stepover (Figure 4.5D) accommodates this convergence (Figure 4.6Ai and B).

Movement vectors on the north and northeast side of the Greendale fault are towards the east-southeast, parallel to the West segment, and thus movement of the north side of the West segment converged towards a restraining left step onto the Central segment (Figure 4.6Aii). The restraining step is nested in the overall releasing bend (Figure 4.6B) and is at least 800 m wide, similar to the width of the restraining stepover that separates the Central and east Greendale fault segments (Quigley et al. 2012b).

Restraint of strike-slip on the West segment is one way of kinematically reconciling the restraining stepover nested within the Waterford releasing bend. However, the blind Charing Cross fault, on which the rupture sequence initiated, forms a triple junction with the Central and West segments and therefore may have had a role to play in the co-seismic geometric relationships expressed in and around the Waterford releasing bend. For a triple junction to remain stable, the relative motion vectors at the triple junction should sum to zero such that

$${}_{X}V_{Y} + {}_{Y}V_{Z} + {}_{Z}V_{X} = 0 \qquad \text{(Eqn. 1)}$$

where ${}_{X}V_{Y}$ is the motion of block Y relative to block X (Figure 4.6C). The Charing Cross fault is blind, so the exact location of its intersection with the Central and West segments is unclear. However, the best available estimate is provided by the surface projection shown by Beavan et al. (2012), lying just outside the differential LiDAR (see Figure 4.2). Based on that location, block Y, which lies south of the Central segment and southwest of the West segment (Figure 4.6), moved 1.2 m west relative to the southeastern side (hanging wall) of the Charing Cross fault (block X on Figure 4.6) (Quigley et al. 2012b), and ~1.7 m northwest, relative to block Z, which is the footwall of the Charing Cross fault (and also the hanging wall of the West segment). By equation 1, horizontal convergence across the Charing Cross fault was therefore ~1.13 m toward 159° (Figure 4.6C). A northwest-striking sinistral strike slip fault of this

orientation is inferred to form the northern termination of the Charing Cross fault (Beavan et al. 2012; Elliott et al. 2012) (Figure 4.1B). It is suggested by both Beavan et al. (2012) and Elliott et al. (2012) that the northwest-striking, opposite sense strike-slip faults at either end of the Charing Cross fault acted as transfer structures, between which rock was fed towards the Charing Cross fault. Therefore, slip on the Charing Cross fault comprised underplating of what, moments later, was to become the hanging wall block of the West segment. Contraction on the Charing Cross fault may have contributed to ground surface deformation in the area of the Waterford releasing bend.

Fault complexities such as bends and stepovers are widely recognized to be important factors in rupture arrest (Wesnousky 2006). Studies such as Elliott et al. (2009) and Ben-Zion et al. (2012) suggest that bend complexities may influence and even control dynamic rupture behaviour, and those authors set out to develop geomorphic and structural parameters to aid prediction of rupture arrest at smaller bends and stepovers. Much larger pop-up structures, the collective expression of numerous rupture events, have been identified nested in equivalent positions at releasing transfer zones on several Californian faults, including the stepover between the San Andreas and Imperial faults (Ben-Zion et al. 2012). Ben Zion et al. postulated that such structures are likely locations of rupture segmentation. Similar subtle structures developed in bedrock during the Duzce earthquake at the Lake Eften releasing double bend (Duman et al. 2005, their Figure 3), which formed an overlap segment that ruptured during both the Izmit and Duzce earthquakes (Akyüz et al. 2002; Hartleb et al. 2002; Konca et al. 2010). Dextral slip on the Totschunda fault during the Denali earthquake (Eberhart-Phillips et al. 2003) would almost certainly have created similar structures at the intersection with the Denali fault. However, the types of structures that are detected at the Waterford releasing bend, which are subtle but fundamental surface expressions of fault kinematics, are commonly indiscernible at single rupture displacement scales and particularly in alluvial settings. At the Waterford releasing bend on the Greendale fault, the combination of subtle deformation and the location of the nested restraining stepover in an active alluvial setting suggest that the preservation of these specific structures will be short-lived in the local geologic-geomorphic record. Nevertheless, this study has extracted a very valuable single-event deformation record that is unencumbered by topographic features related to previous events. Similar datasets are likely to emerge from initiatives such as GeoEarthScope LiDAR acquisition in California (Prentice et al. 2009). Such datasets are expected to provide detailed insights into fault complexity and kinematic interactions and should contribute greatly to modeling and field testing of hypotheses regarding the influences of fault bends and stepovers on the terminations of earthquake ruptures (Elliott et al. 2009; Ben-Zion et al. 2012).

4.7 Conclusions

Spatial and temporal overlap of a number of high quality datasets, including pre- and post-earthquake LiDAR, cadastral survey data, fault rupture mapping, and displaced piercing points (e.g. straight fences and the like), have allowed remarkably high resolution documentation of the kinematics and fault interactions at a releasing fault bend. The measurements confirm that the West segment of the Greendale fault is a separate, northwest-striking dextral oblique normal fault that released dextral motion on the Central segment of the Greendale fault, across what is broadly speaking a releasing bend. In detail a ~800 m-wide zone of left-stepping restraining stepovers lies nested within the overall releasing bend. Cadastral survey data allowed determination of net slip on the West segment, which at 2.25 m is substantially higher than previously estimated from piercing point measurements. This displacement decreases to near-zero at the restraining stepover. The clear documentation and characterization of deformation and structure at this releasing bend provides insight into subtle, but potentially important, structures and issues that may be present at bends on strike-slip faults elsewhere.

CHAPTER 5. GEOMORPHIC AND HYDROGEOLOGICAL PERSPECTIVES ON DEFORMATION ALONG THE WEST SEGMENT OF THE GREENDALE FAULT

5.1 Abstract

An integrated analysis of fluvial geomorphology and hydrogeology in the area surrounding the West segment of the Greendale fault provides evidence for slip history and tectonic influences on landscape development. The Hororata River that flows on the West segment footwall migrated northeastwards over the Holocene towards the eventual Darfield earthquake surface rupture trace of the fault. The Selwyn River, which lies on the hanging wall of the West Segment and the footwall of the Charing Cross fault, moved in the same direction. However, a 100 year record of the Selwyn River bank locations show that it had latterly narrowed its course, changed its planform from braided to meandering, and begun to incise its bed as it approached the Greendale and Charing Cross faults. These characteristics exhibited by the Hororata and Selwyn Rivers are consistent with subtle precursory warping on the structures involved in the September 2010 Darfield earthquake. Comparison of the pre and post-earthquake geomorphology of the fault trace also suggests that a subtle scarp or groove was present along much of the trace. Geometric characteristics and slip distribution along the central section of the West segment is consistent with an advanced stage of breaching of a ramp that links en-echelon segments. A review of hydrogeology and well logs supports a hypothesis of extended slip history and suggests that that the Selwyn River fan may be infilling a graben that has accumulated late Quaternary vertical slip of <30 m. This has resulted in partitioning of the aquifer across the fault. The landscape associated with the West segment can thus be considered as an integrated system comprised of interacting components, including the river channels, their flood plains and the alluvial aquifer system, which record the accumulation and release of elastic strain on the fault.

5.2 Introduction

The channel morphology and depositional character of an alluvial river are influenced by the averaged topography and lithology of upstream reaches, which together control the discharge and sediment type within a given reach (e.g. Leopold et al. 1964; Schumm 1985). Discharge and sediment-type in turn control the permeability and flow characteristics within the alluvial aquifer (e.g. Larkin & Sharp Jr 1992). Active tectonic deformation exerts a first order control on channel slope and accommodation space within a basin. The planforms of rivers respond to both longitudinal and lateral slope changes (Schumm 1986; Leeder & Alexander 1987; Alexander et al. 1994; Holbrook & Schumm 1999), with flow on influence on fluvial discharge and sediment erosion, deposition and grainsize (Schumm 1986; Holbrook & Schumm 1999) and hence alluvial aquifer characteristics. However, fault complexity, slow slip rates, high sedimentation or erosion rates, flood events or human activity can all obscure the records of tectonic activity.

Scientists increasingly favor multi-disciplinary approaches to studying fluvial dynamics that integrate landscape components such as channels, floodplains, alluvial aquifers and faults (Dutcher

& Garrett 1963; Poole et al. 2002; Jain & Sinha 2004,2005; Larned et al. 2008). It thus seems reasonable to suggest that an integrated assessment of alluvial plain geomorphology and alluvial aquifer characteristics should reveal useful information regarding underlying faults, even in extremely active alluvial settings.

The 4 September 2010 Darfield earthquake in Canterbury, New Zealand provides an example of a previously undetected fault that ruptured through an alluvial basin (Figure 5.1). Coseismic ground surface displacements resulted from complex rupture on as many as seven fault segments (Beavan et al. 2012; Elliott et al. 2012). Surface rupture occurred on two E-W-striking segments (Quigley et al. 2012b), and discrete warping occurred at the western end of the fault on a NW-striking segment (Quigley et al. 2012b; Duffy et al. 2013). At the junction between the Central and West segments, the Hororata and Selwyn Rivers flow southeastwards, approximately parallel to the surface trace of the West segment. River bank locations in this area have been repeatedly surveyed as property boundaries since the 1860s. Repeated aerial photography has been carried out since 1940. In the 2000s, the area was subjected to intense conversion to dairy farming, with associated hydrogeological investigations and allocation of water rights (Vincent 2005). The Hororata River partially avulsed during the Darfield earthquake (Duffy et al. 2013). This area therefore provides a useful opportunity for retrospective consideration of its geomorphology and hydrogeology, in the light of events during the Darfield earthquake, as a tool to understand the signals of tectonic deformation in an active alluvial setting.

This study presents the results of investigations in the vicinity of the West segment of the Greendale fault. Using data from the 1860s to present, it summarizes the pre-rupture and post-rupture geomorphological and hydrogeological characteristics of this fault. The presence of active streams that relate differently to the major structures provides the opportunity to examine responses to both lateral and longitudinal river gradient perturbations. A compilation of geomorphic and hydrogeological data from close to the fault is presented and interpreted on the basis of the recent earthquake. The results of this study suggest that the rivers in this region have responded to slow tectonic movements, and that the West segment slipped in the late Holocene. The study concludes with a discussion of implications for fault slip history.

5.3 Regional geology

Canterbury is located in the South Island of New Zealand and as such is part of the New Zealand plate boundary between the Pacific and Australian Plates (Figure 5.1A). The relative motion of the Pacific and Australian plates causes oblique convergence of ~38 mm/yr in the central South Island (DeMets et al. 2010). Partitioning of plate convergence drives uplift of the Southern Alps (e.g. Norris & Cooper 2001) and is further expressed by varying rates and styles of faulting

across Canterbury (Cowan 1992; Pettinga et al. 2001; Campbell et al. 2003), including reactivation and inversion of many of the inherited E-W-striking basement normal faults (Nicol 1992,1993; Campbell et al. 2012; Ghisetti & Sibson 2012).

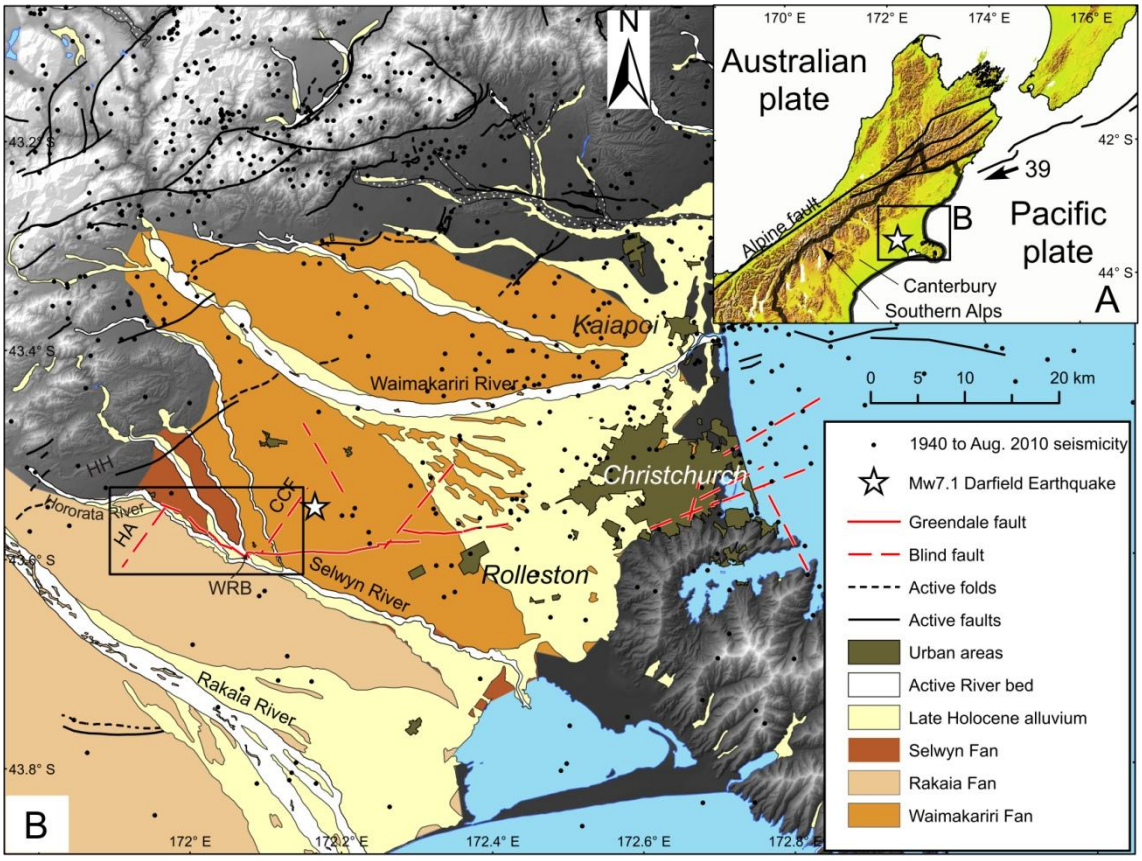

Figure 5.1: A) The Greendale fault ruptured through the low relief (green) Canterbury plains east of the Southern Alps and west of Christchurch in the central South Island of New Zealand. B) The Canterbury Plains consist of several large fans that issue from the rangefront. The larger fans are associated with major rivers including the Waimakariri and Rakaia Rivers, whilst the smaller Selwyn Fan deposits sediment between the Rakaia and Waimakariri fans, close to the rangefront. Rectangle indicates location of Figure 5.2. Seismicity is shown for the period from 1940 to 31 August 2010. Red faults ruptured during the Canterbury earthquake sequence (Beavan et al. 2012). CCF – Charing Cross fault; HA – Hororata anticline blind thrust fault; HH – Harper Hills; WRB – Waterford releasing bend. Surficial geology modified from Forsyth et al. (2008).

The pre-Quaternary geology of Canterbury consists mainly of <2 km of Late Cretaceous to Pliocene sediments and minor volcanics that overlie Mesozoic basement composed primarily of greywacke and argillite rocks (Browne et al. 2012). The Cenozoic sediments fill E-W-striking half grabens that can be identified using the trend of gravity lineaments that include the West and Central segments of the Greendale fault (Davy et al. 2012).

Erosion of the uplifting Southern Alps sheds large volumes of gravel to the east coast plains, particularly during glacial periods (Suggate 1963). Much of the surface of the Canterbury Plains consists of the large Waimakariri and Rakaia outwash gravel fans (Figure 5.1B) that built out during several glacial aggradation phases, the last of which occurred from 30ka to 6ka (Forsyth et

al. 2008). The thickness of these Late Pleistocene to Holocene gravels varies across Canterbury, ranging from 10 to >260 m in the foothills areas of western Canterbury (Brown & Weeber 1992; Finnemore 2004) and to more than 400 m in the Christchurch area (Bexley M35/w6038 groundwater bore in Brown & Weeber 1992). Close to the rangefront, the Waimakariri and Rakaia braided rivers presently incise into these old fans and redistribute the gravel further east where younger fans are actively building out into the Pacific Ocean (Figure 5.1B). Close to the rangefront, the Selwyn River has built a smaller fan in the interfan low between the Waimakariri and Rakaia fans (Wilson 1989) (Figure 5.1B and Figure 5.2). The Hororata River presently occupies the interfan low between the Rakaia and Selwyn River fans (Wilson 1989) (Figure 5.2).

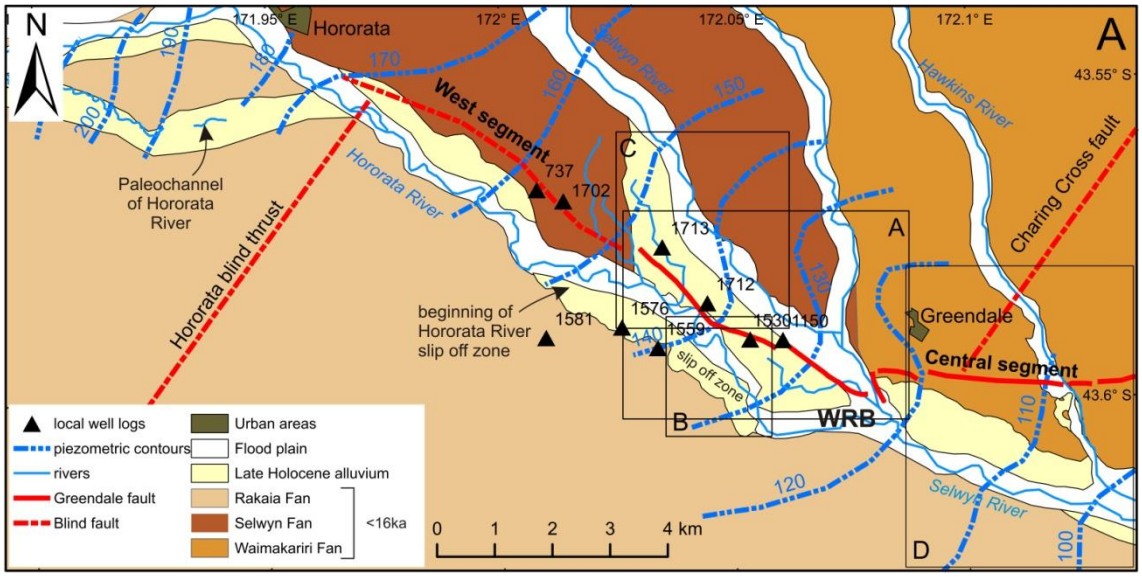

Figure 5.2: Detail of the Hororata and Selwyn interfluve east of the rangefront. For extent see Figure 5.1B. WRB – Waterford releasing bend. The trace of the fault closely follows the interfan low between the Selwyn and Rakaia fans, and the area of surface trace is associated with an inflexion in the potentiometric contours of the shallowest aquifer (Vincent 2005). Surficial geology modified from Forsyth et al. (2008). The extent rectangles show A - Figure 5.6; B - Figure 5.4; C - Figure 5.5; D - the location of planform changes in the Hawkins River (Campbell et al. 2012).

Prior to the Mw 7.1 Darfield earthquake, much of the Canterbury plains had displayed low levels of background seismicity and no previous historical earthquakes had ruptured the plains remarkably flat topography (Figure 5.1B). Two earthquakes >Mw5 shook Christchurch in 1869 and 1870 (Pettinga et al. 2001 ; Downes & Yetton 2012) but no earthquakes >Mw4.5 were recorded within the area of Figure 5.1 between 1940 and the September 2010 earthquake. Nevertheless, large parts of the Canterbury Plains were known to be deforming above active faults (Dorn et al. 2010; Campbell et al. 2012; Jongens et al. 2012).

5.4 Greendale fault rupture

The September 2010 Mw 7.1 earthquake on the dextral Greendale fault (Quigley et al. 2010b; Quigley et al. 2012b) caused widespread ground-shaking across Canterbury and associated

damage as far away as Christchurch and Kaiapoi (e.g. Cubrinovski et al. 2010; Quigley et al. 2010b; Wood et al. 2010). Coseismic surface displacements occurred on three segments of the fault. The Central and East segments strike E-W across the Canterbury Plains from the Selwyn River in the west, to Rolleston in the east. The West segment strikes NW along the interfluve of the Selwyn and Hororata Rivers. The earthquake initiated north of the Greendale fault, on the Charing Cross fault (Beavan et al. 2010b; Holden et al. 2011), which is a SE dipping blind thrust that forms a triple junction with the Central and West segments at the Waterford releasing bend (Figure 5.1B & Figure 5.2) (Beavan et al. 2010b; Beavan et al. 2012; Duffy et al. 2013). Net slip at the surface of up to 5.3 ±0.5 m on the Central segment of the surface rupture (Quigley et al. 2012b) dwindles westwards to ~1.0 m at the Waterford releasing bend before climbing back to ~2.5 m on the West segment (Duffy et al. 2013). The vertical motion on the Central and West segments was south side up and the greatest vertical slip occurred on the West segment (Quigley et al. 2012b; Duffy et al. 2013). Kinematic analysis of the West segment (Duffy et al. 2013) shows that it performs a dual role. The NE hanging wall side of the fault feeds material southeastwards towards the Charing Cross fault, whilst the SW footwall block pulls away from a releasing bend associated with dextral slip on the Central segment of the Greendale fault.

During the Darfield earthquake, the E-W-striking Central and East segments of the Greendale fault ruptured across the surface of the ≥16 ka Waimakariri fan (Suggate 1963; Forsyth et al. 2008) which is widely considered to have been unmodified through the Holocene (e.g. Barrell et al. 2011; Villamor et al. 2011). The West segment, however, deformed a Holocene alluvial surface that occupies the interfluves between the Hororata and Selwyn Rivers. Blind rupture of the West segment extended beyond the zone of field-mapped surface deformation and its InSAR-derived surface projection closely followed the course of the Hororata River (Beavan et al. 2010b; Beavan et al. 2012).

5.5 Hydrologic and meteorological setting

Large rainfall events in the Selwyn and Hororata catchments during August 2010 caused ground saturation and contributed to a rapid, nearly 1 m increase in stage height in the Selwyn River system following a moderate, 3 day rainfall event from ~28 August (Figure 5.3). The flood stage reached on 01 September 2010, SE of the study area, was the third highest during the 12 months to 09 December 2010. It was at least 1m higher than background summer stage height and was increasing again due to further rainfall on 3 September when the instrument malfunctioned during the earthquake on 4 September (P. Durney, ECAN personal communication). Both the Hororata and Selwyn Rivers would, therefore, have been at a relatively high stage when the earthquake occurred.

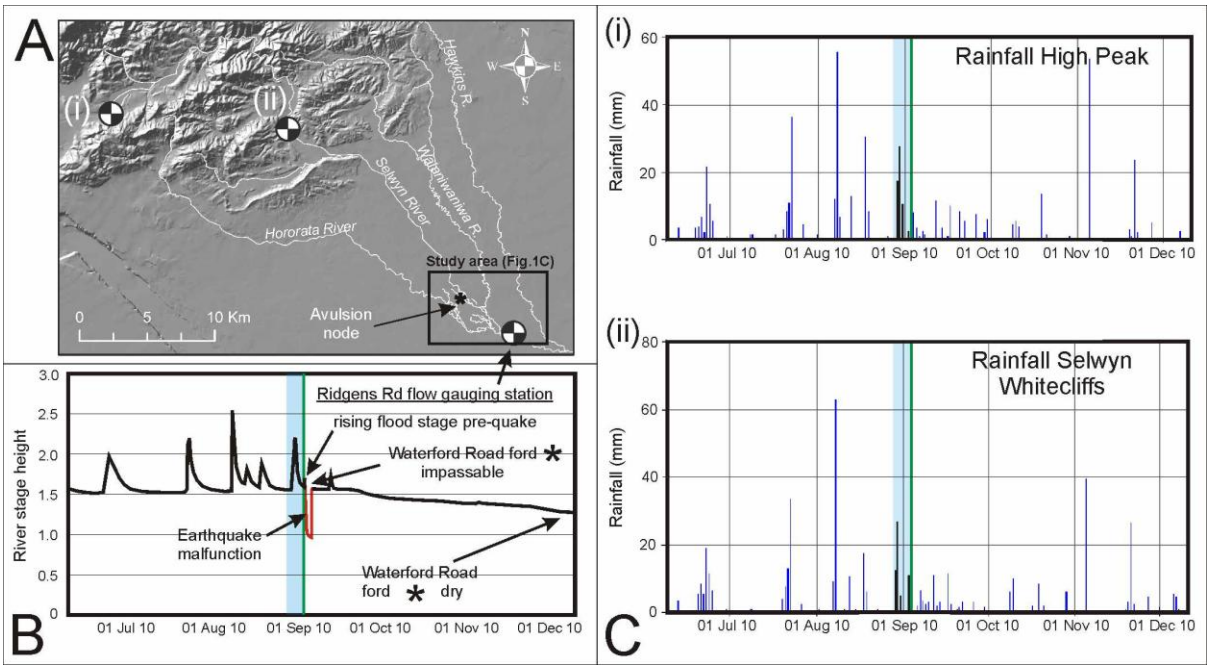

Figure 5.3: A) Locations of rainfall gauging stations [(i) High Peak and (ii) Selwyn Whitecliffs], the Ridgens Road hydrograph, and the Waterford Road vehicle ford (*) in the Selwyn River catchment. B) Flood stage graph for the 6 months to 10 Dec 2010 (ECAN - http://www.ecan.govt.nz/services/online-services/monitoring/pages/default.aspx). The earthquake timing is recorded by a malfunction in the Ridgens Road hydrograph. The shaded area indicates the sustained period of moderate rainfall in the Selwyn River catchment prior to the earthquake. C) Rainfall records for the High Peak and Selwyn Whitecliffs rain gauges.

5.6 Methods

Data compiled since September 2010 to characterize the impacts of fault rupture on the western segment has included displacement mapping at the fault scarp (Quigley et al. 2012b), flood mapping, and geodetic constraints using cadastral-type surveying and LiDAR differencing (Duffy et al. 2013). This study presents additional field, air photo and DEM geomorphic mapping, fault scarp measurements and a review of hydrogeology and irrigation well logs.

A 5m inverse distance weighted DEM of limited extent was constructed from an RTK point cloud collected in the vicinity of the surface rupture tip. A raster grid was created using *GEON Points2Grid* (Kim et al. 2006) and holes in the raster were filled using *Whitebox* LiDAR tools (Lindsay 2010).

Stratigraphy of the study area was investigated by reviewing drillers logs (Environment Canterbury 2011) from irrigation wells surrounding West segment. The locations and numbers of wells are provided in Table 5.1.

Table 5.1: Locations and numbers of well logs reviewed in this study (Environment Canterbury 2011).

Well No.	Longitude	Latitude	Drill date	Well depth (m)
L36 1702	172.013575	-43.567164	16/01/2006	113.25
L36 1712	172.044308	-43.583339	15/12/2008	96
L36 1713	172.03469	-43.574545	28/10/2004	95.7
L36 1530	172.053407	-43.58904	2/04/2002	84.4
L36 1559	172.033573	-43.590261	6/12/2002	90.44
L36 1576	172.02591	-43.586992	29/10/2002	89.97
L36 1581	172.009639	-43.588456	2/08/2002	98.96
L36 1150	172.060389	-43.589214	16/10/1996	27.5
L36 737	172.007922	-43.56536	30/11/1990	12

5.7 Results

5.7.1 Pre-earthquake geomorphology of the Hororata-Selwyn River system

5.7.1.1 Hororata River

The upstream reach of the Hororata River curves around the rangefront, staying close to the base of the Harper Hills as it follows the northern edge of the Rakaia fan (Figure 5.1B). This reach, which lies on the northern flank of the uplift created by blind thrusting below the Hororata anticline, relocated northwards during the Holocene. The Hororata paleo-channel (Figure 5.2) is now seasonal but while it was occupied it incised deeply (>5 m) into the surface of the Rakaia fan before abandoning its bed for a more northerly course.

At the town of Hororata the Hororata River deflects to the southeast as it encounters the Selwyn fan. From there the river flows along the interfan low between the Selwyn and Rakaia fans, towards its confluence with the Selwyn River (Figure 5.2). As it flows SE, it trims the northern margin of the Rakaia fan until it reaches as far south as the northern tip of the mappable surface deformation on the West segment. South from there, the Hororata River has slipped northeast across the footwall and towards the fault, leaving a largely abandoned meander belt that has meander loops that open to the northeast (Figure 5.4). Modern photos hide this migration because the Hororata River appears to have returned westwards and presently follows a course that lies within its 'abandoned' meander belt. However, this is a cultural modification that was achieved post-1940 by the digging of artificial meander cutoffs. Airphotos from 1940 clearly show the unilateral migration, and show the Hororata River occupying the NE side of its meander belt.

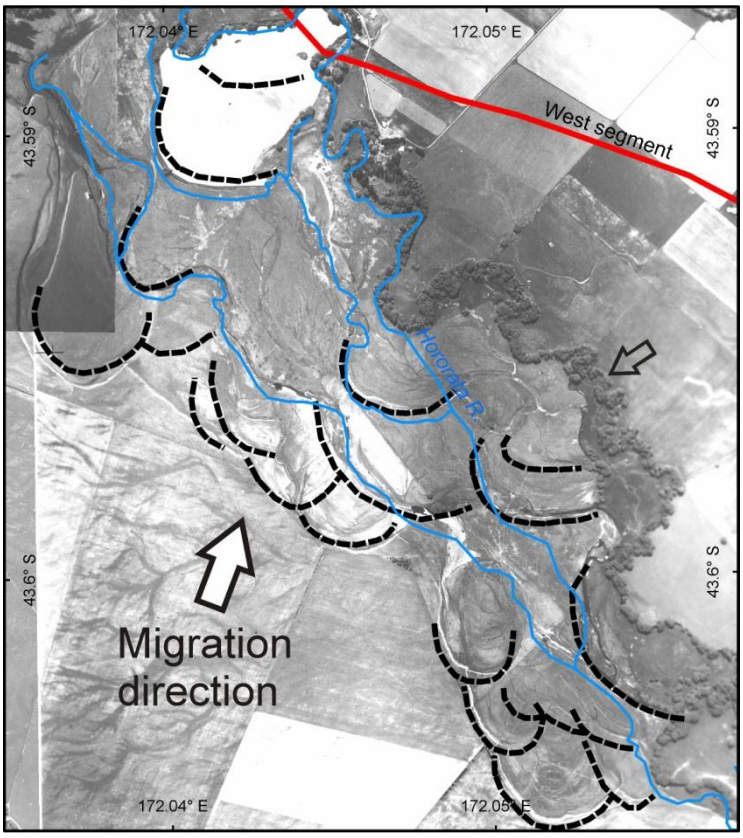

Figure 5.4: Abandoned meander loops of the Hororata River (heavy black dashed lines) are all concave toward the northeast, indicating northeast migration of the Hororata River toward the West segment fault trace (large white arrow) prior to 1940. The small open arrow shows the tree-lined course of the Hororata River in 1940. The blue lines show the present location of the river, which was relocated westwards by landowners soon after the photograph was taken in 1940.

5.7.1.2 Selwyn River

The surface trace of the West segment cuts across Late Holocene alluvium on the interfluve between the Selwyn and Hororata Rivers. The Selwyn River presently flows on the hanging wall of the West segment, sub-parallel to the Hororata River (Figure 5.2). Aerial photographs taken in 1940 clearly show that paleochannels of the Selwyn River, such as the Waterford Channel, have previously flowed across the projection of the modern fault trace at its northern tip (Figure 5.5A). The Hororata River is presently trimming the braided surface as it migrates to the northeast. East of the modern fault trace a series of slip off terraces (Figure 5.5) step down to the east and record eastwards migration of the Selwyn River over the late Holocene.

The terraces are presently undated but property survey plans from circa 1860 record the position of the terrace risers that formed the active river banks at that time (marked 1860 on Figure 5.5). These banks were indicated at ~1 m high and bounded a 600 m wide river. Since 1860, and even since 1940, the Selwyn River has decreased in width and localized into a meandering thalweg that is now incised <2 m into its old bed.

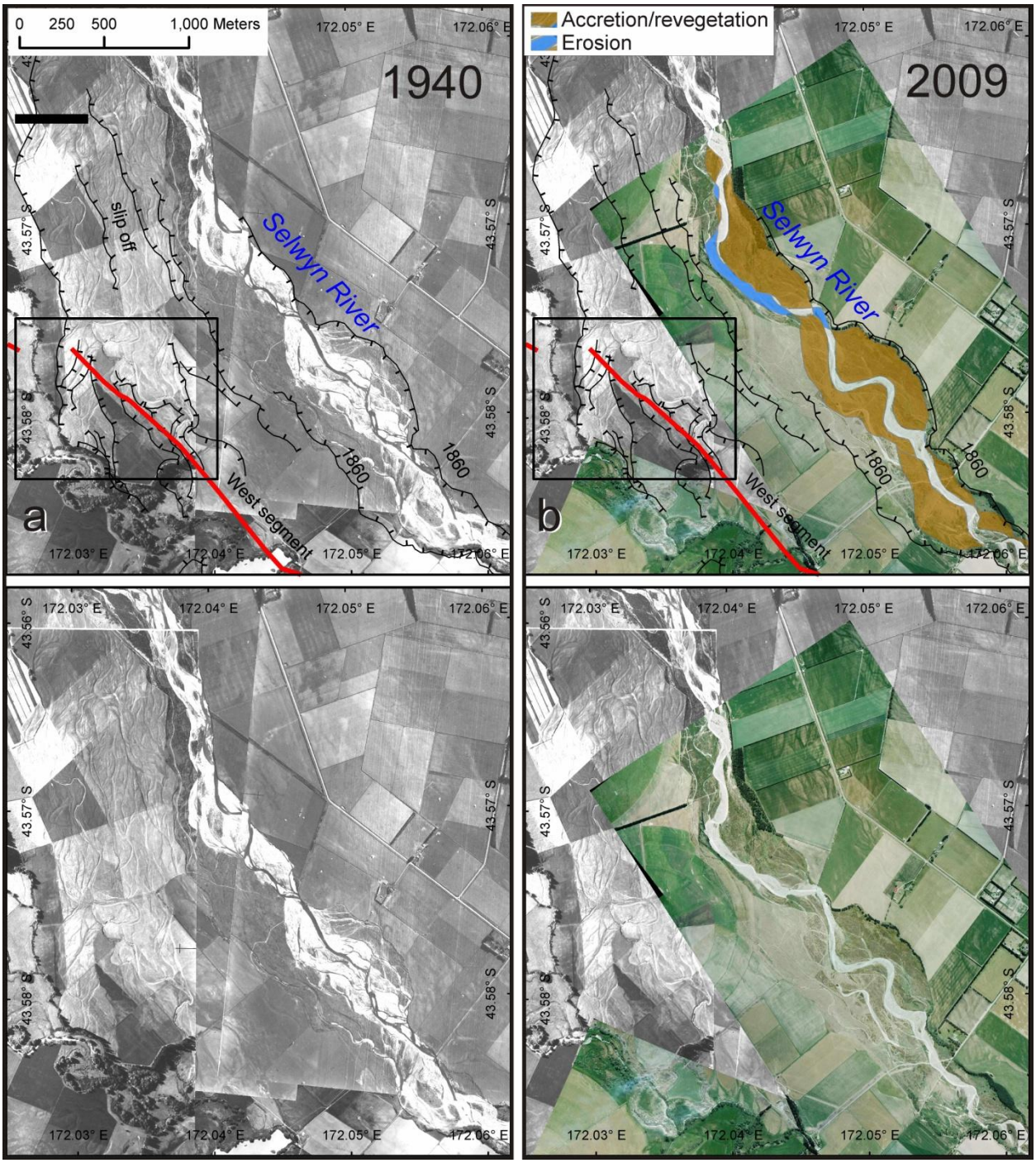

Figure 5.5: Marked up aerial photographs of the Hororata and Selwyn Rivers at the NW end of the fault trace from A) 1940 and B) 2009 (colour area only). Uninterpreted photos shown below. Comparison of the two photos shows that the width of the Selwyn River bed has decreased since 1940, resulting in revegetation of much of the river bed (brown shaded area in B). Only a small amount of net erosion (blue shaded area in B) has occurred since 1940. Rectangle shows extent of Figure 5.9A. Faint paleochannels can be seen on the surface of the Selwyn fan, east of the Selwyn River.

The Selwyn River passes across the fault at the Waterford releasing bend, where the scarp height is at its minimum (Duffy et al. 2013). Limited geomorphic data does not allow a comprehensive evaluation as to whether this position is structurally controlled.

5.7.2 Geomorphology of the fault scarp

The surface rupture on the West segment deformed a late Holocene alluvial surface (Figure 5.6). Although the fault dips steeply at ~70° (Duffy et al. 2013), the width of the deformation zone varies between 20 and 200 m (Figure 5.7; Figure 5.8). No discrete surface ruptures were observed, which suggests that the fault trace is formed by a monoclinal flexure (Duffy et al. 2013).

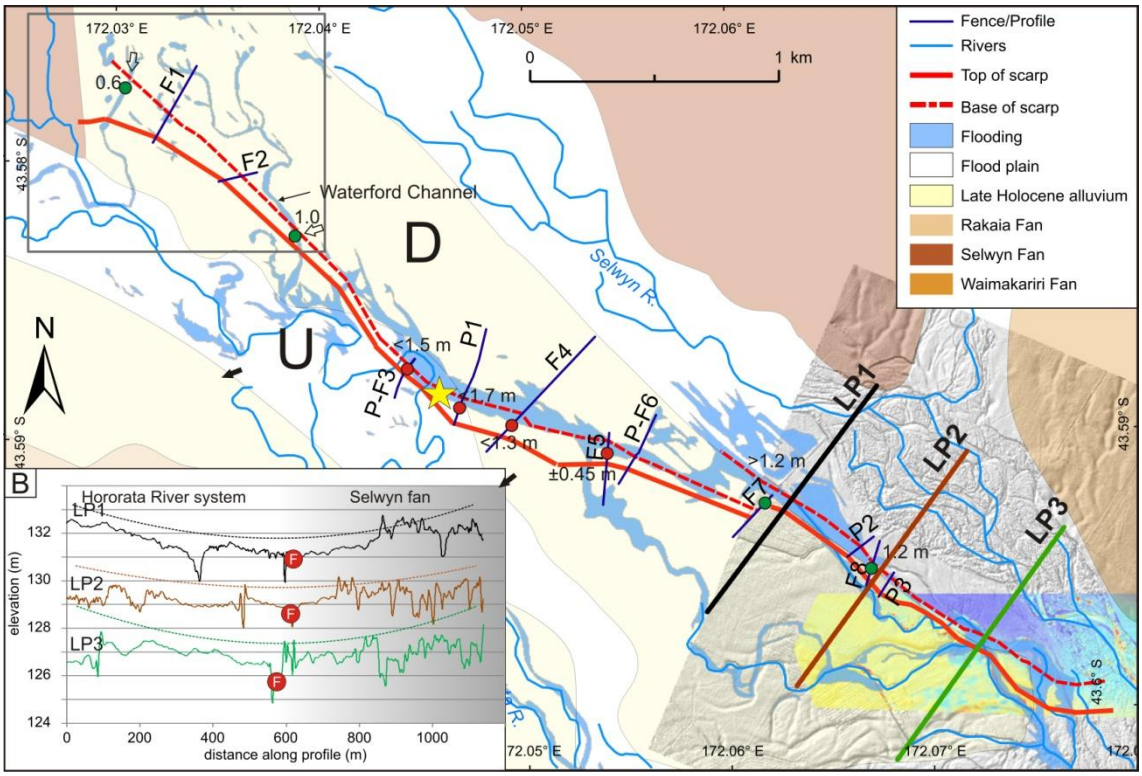

Figure 5.6: A) Coseismic scarp formation and flooding caused by the earthquake. U and D refer to relative up and down sides of surface rupture. Yellow star shows Hororata River avulsion node. Rectangle indicates the extent of Figure 5.7A, open arrows in rectangle show points at which water in the dammed Waterford Channel passed westwards across the scarp. Colored dots show scarp heights. Green dots indicate that the pre-existing topography is well constrained from a deformed active channel bed (the Waterford Channel) or from differencing post-quake RTK and pre-quake LiDAR. Red dots are constrained from RTK only. Grey shaded relief 2008 LiDAR coverage of the Selwyn River is shown, along with the elevation difference map over the Waterford releasing bend (Duffy et al. 2013). Yellow areas were uplifted, blue subsided. Note overlap of southern RTK fences/topographic profiles with 2008 LiDAR. Heavy black, brown and green lines indicate locations of LiDAR profiles in B. B) Profiles run perpendicular to the fault trace indicate that the southern section of the fault (F) emerged along a pre-existing linear low point in the topography. This appears to coincide with the change from the Selwyn fan to the Hororata River system.

In plan view the fault trace is gently corrugated, with two sections that strike NW at ~320°, separated by a section that strikes WNW at ~290°. Quigley et al. (2012b) acquired multiple RTK profiles across the West segment fault trace after the earthquake to constrain surface displacements. The RTK profiles on the southern NW-striking section overlap with 2008 pre-earthquake LiDAR (Figure 5.6). This LiDAR dataset has practically the same overlap with earthquake LiDAR as the 2010 pre-earthquake LiDAR used in the kinematic study by Duffy et al. (2013) but is horizontally

mis-registered by ~50 cm (Sebastien Le Prince, personal communication). Nevertheless, it extends further northwards and, in an area of low topography, the LiDAR still provides valuable geomorphic information.

Repeated 1.2 km long topographic profiles oriented perpendicular to the fault scarp (Figure 5.6B) show no evidence for a pre-existing scarp. However, the modern fault scarp coincides with a subtle flexure in the pre-existing topography. The Selwyn River gravel bed lies northeast of this low point, and faint meander traces picked out by the flooding (Figure 5.6A) suggest that the Hororata River has occupied the area southwest of this low point in the past.

Previously-obtained RTK profiles (Quigley et al. 2012b) that overlap with the 2008 Selwyn River LiDAR were differenced to refine the vertical displacements and to allow comparison of pre-earthquake topography with the fault scarp (Figure 5.7). Fence 7 lies close to an apparent stepover in the fault trace that was interpreted by Duffy (2013) as a lateral ramp. The difference between LiDAR and RTK elevations along Fence 7 (Figure 5.7C) shows two scarps and supports this interpretation. More importantly, the 2008 LiDAR profile clearly shows a pre-existing topography that mimics the geometry of the modern scarp. The remaining profiles showed that the scarp height remains consistently at ~1.2 m along this section of the fault. The pre-existing topography results in overestimation of the scarp height by <0.4 m based on RTK alone. Pre-earthquake LiDAR along these profiles shows evidence only of a pre-existing furrow/channel, rather than a scarp. The presence of a linear topographic low that coincides approximately with the fault and is not presently occupied by drainage is confirmed by flow accumulation analysis of the 2008 LiDAR DEM, but is not visible on the shaded relief map.

In the central WNW-striking section of the West segment, RTK surveys at fences and profiles provide the only recourse for estimating surface displacements. Within this sector dextral displacements decrease northwards and topographic profile height (the best available measure of scarp height) increases northwards (Figure 5.6; Figure 5.8). It remains unclear how much scarp height in the WNW-striking section is due to pre-existing topography.

On the northern NW-striking section, a flight of four terraces (numbered 1 to 4 with decreasing elevation and age) were identified above the level of the modern Waterford channel (Figure 5.9A). Apart from the highest terrace (terrace 1), the terraces merge northwards with the floodplain of the Waterford Channel. The Waterford channel changes from a braided to a meandering planform immediately NE of the fault trace, where the terraces emerge from the floodplain, and deflects left to meander along the fault trace. The terrace edges (particularly the edges of levels 3 and 4) lie parallel to the fault trace and at a high angle to the flow direction of the

paleochannels preserved on the higher terraces (Figure 5.9A). A DEM was constructed from an RTK point cloud to investigate the nature of these terraces and the displacements of their surfaces.

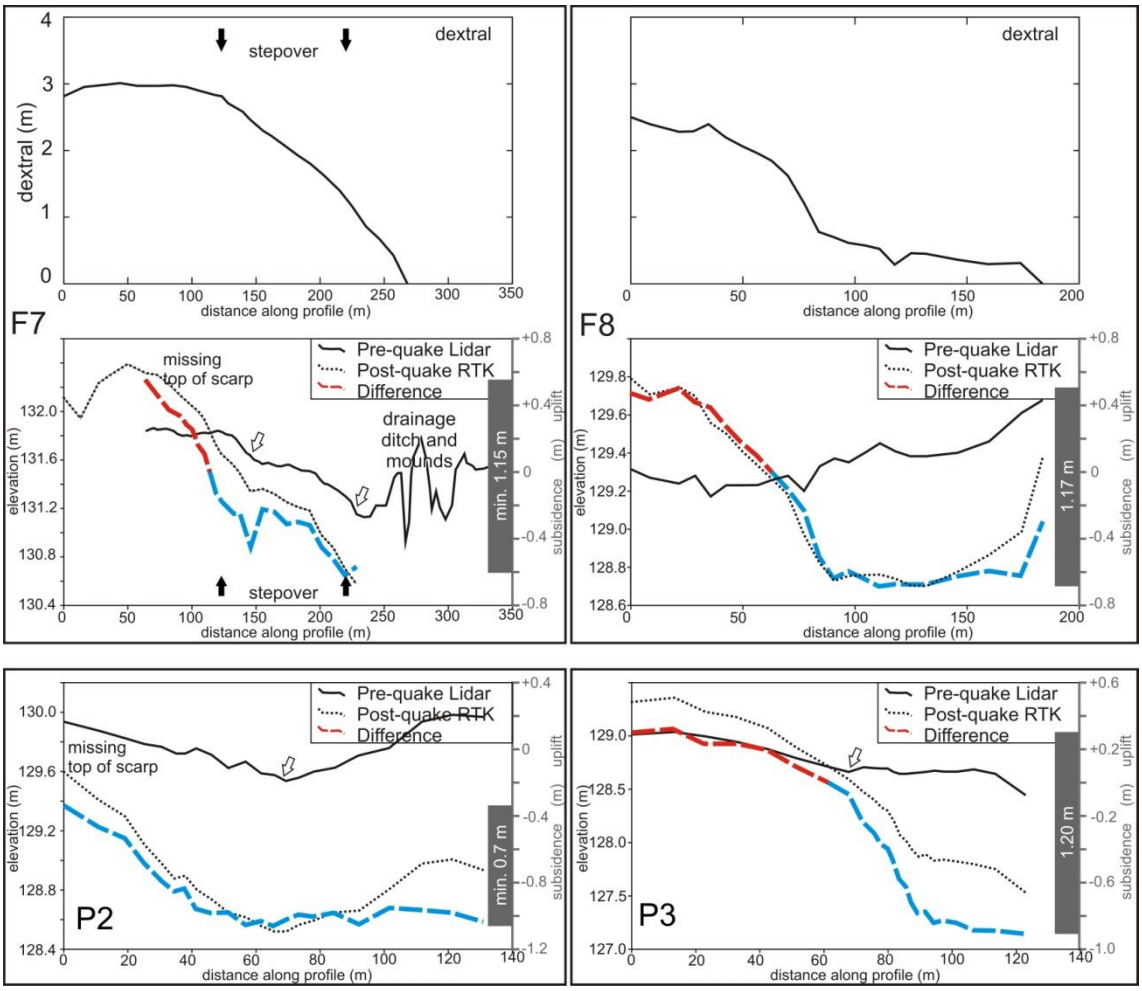

Figure 5.7: Multi-temporal topographic differencing constraints on pre-rupture geomorphology. F7 and F8 are fences, and P2 and P3 are topographic profiles, all shown on Figure 5.6A. Top two graphs show dextral displacements for the fences. Lower four graphs show RTK and LiDAR profile elevations (left axes) and differences (right axes).

Figure 5.9B shows profiles run along the terrace surfaces, obliquely across the fault trace. Although the DEM is at coarse resolution, the terrace profiles are warped as expected due to coseismic deformation. The height of the scarp crossing terrace 4 is ~0.6 m (Figure 5.9B). A scarp of the same height crosses 2 paleochannels of the Selwyn River that merge just south of the fault trace (Figure 5.9D). This suggests that 0.6 m is the approximate elevation of the scarp along the last few hundred meters of the surface trace. A 0.6 m scarp is in keeping with declining height of a 1.0 m scarp measured in the bed of the Waterford Channel further south (Figure 5.9E).

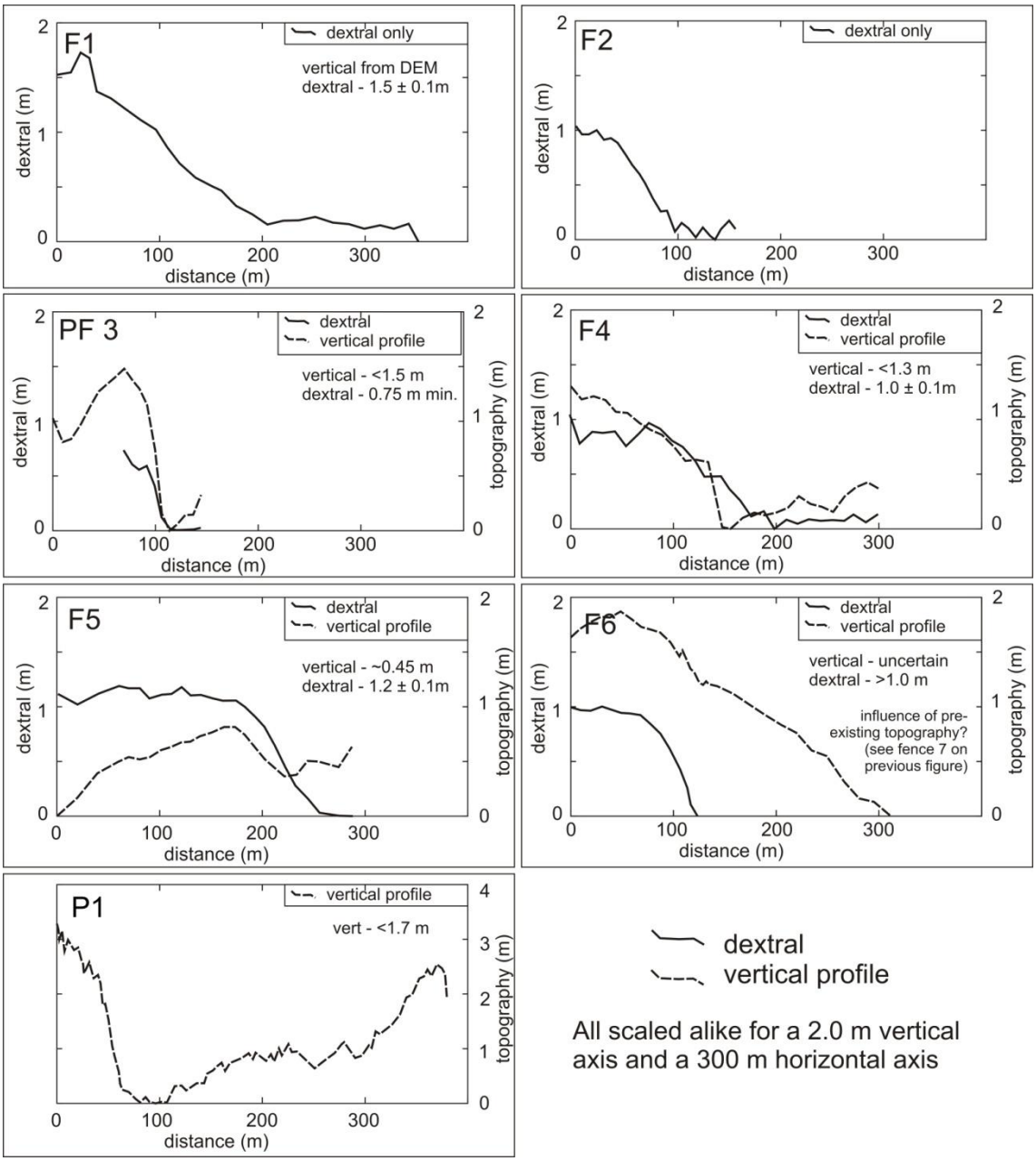

Figure 5.8: RTK profiles across the fault scarp, showing dextral displacements and topography. For locations see Figure 5.6.

The apparent warping of the terrace surfaces increases northwards in proportion to the height/age of the terraces, although scarp elevation should decline northwards. Higher terraces are warped by <1.2 m within the limits of the DEM, which is approximately double the 0.6 m scarp height on the lowest terrace and channel. Topographic cross sections perpendicular to the Waterford Channel show that the increased warping of higher surfaces is reflected by an increase in the height of the terrace surfaces relative to the Waterford channel (Figure 5.9C).

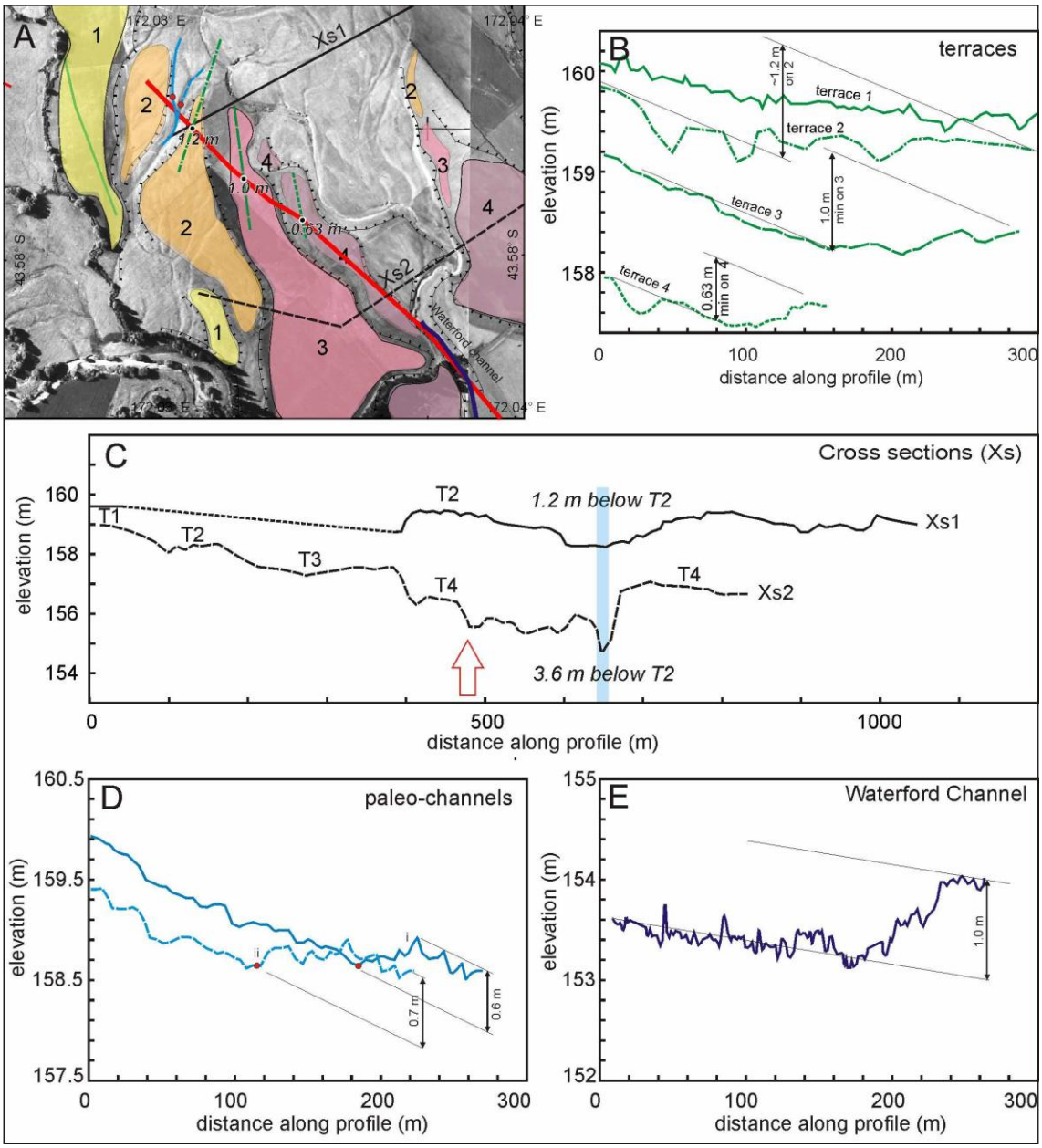

Figure 5.9: Terraces at the NW end of the fault surface trace. A) 1940 air photo showing the extent of degradation terraces (numbered 1 – 4 with decreasing age). Measurements shown are the magnitude of terrace warping determined from B. B) Topographic profiles run along terrace surfaces. For location see green lines on A. C) Cross valley profiles showing the southward increase in depth of the Waterford Channel. D) Topographic profiles run along Selwyn River paleochannels. For locations see blue lines on A. Red dots on the profiles correspond with dots on the map. E) topographic profile of the bed of the Waterford Channel.

5.7.3 Local hydrological response to the earthquake

Part of the fault scarp emerged across a meander of the Hororata River and partially diverted the Hororata River onto an older, higher surface (Figure 5.6). The channel diversion did not exhibit a dextral offset. Instead, the avulsion floodwaters flowed south along the scarp, in an *apparently* sinistral sense, causing widespread flooding and highlighting the geometry of the scarp (Barrell et

al. 2011; Duffy et al. 2013). Where the floodwaters passed across the scarp they generally occupied meandering paleochannels, presumably of the Hororata River.

North of the Hororata River avulsion node (yellow star, Figure 5.6), the fault scarp dammed the Waterford channel and caused backflooding of its incised valley (Figure 5.9E). The Waterford Channel responded in a similar way to the Hororata River. Part of the flood passed downstream across the scarp. Water also built up in the dam and drained westwards across the NW tip of the fault scarp into an adjacent reach of the Hororata River.

Flood mapping from oblique aerial photographs taken in the 12 hours following the earthquake showed no obvious surface connection between floodwaters in the Waterford Channel and the Selwyn River (Figure 5.6). The paleo-channel that connects the Waterford Channel with the Hororata River has a westward gradient, and the main stem of the Hororata River is incised ~1 m below the mouth of the connecting channel, so the Hororata River is not a plausible source for the Waterford channel flooding. The Selwyn River was at a high stage at the time of the earthquake (Figure 5.3B), and is known to recharge an unconfined gravel aquifer, whereas the Hororata River flows across an aquitard (Vincent 2005) (see section 5.7.4 of this study). A combination of underflow from the flooded Selwyn River, together with the rapid rise in groundwater levels reported by Cox et al. (2012a), probably caused the hanging wall flooding north of the avulsion node.

5.7.4 Hydrogeology

Vincent (2005) mapped potentiometric contours for three levels of aquifer in the Hororata and Selwyn catchments. The contours for the shallowest aquifer are shown on Figure 5.2 and bend across the fault, particularly in the area of modern scarp. Drill logs for nine wells in this vicinity, although not of high quality, record the subsurface lithologies and water bearing horizons (Figure 5.10). The logs for wells on the downthrown side of the fault record the presence of a thick shallow aquifer in the near surface. Conversely, the wells on the upthrown side of the fault encounter a thick near surface aquitard. At depth, a seemingly distinctive unit of stained gravels (see arrows Figure 5.10) is recorded from ~85 m on the downthrown side (wells 1712 and 1713) that is also present at ~54 m on the upthrown side (well 1559). The fundamental lithological difference between the aquifer and aquitard either side of the fault causes the gaining and losing reaches of the Hororata and Selwyn Rivers to be out of phase in the area of the surface rupture, which is highlighted by the potentiometric contours.

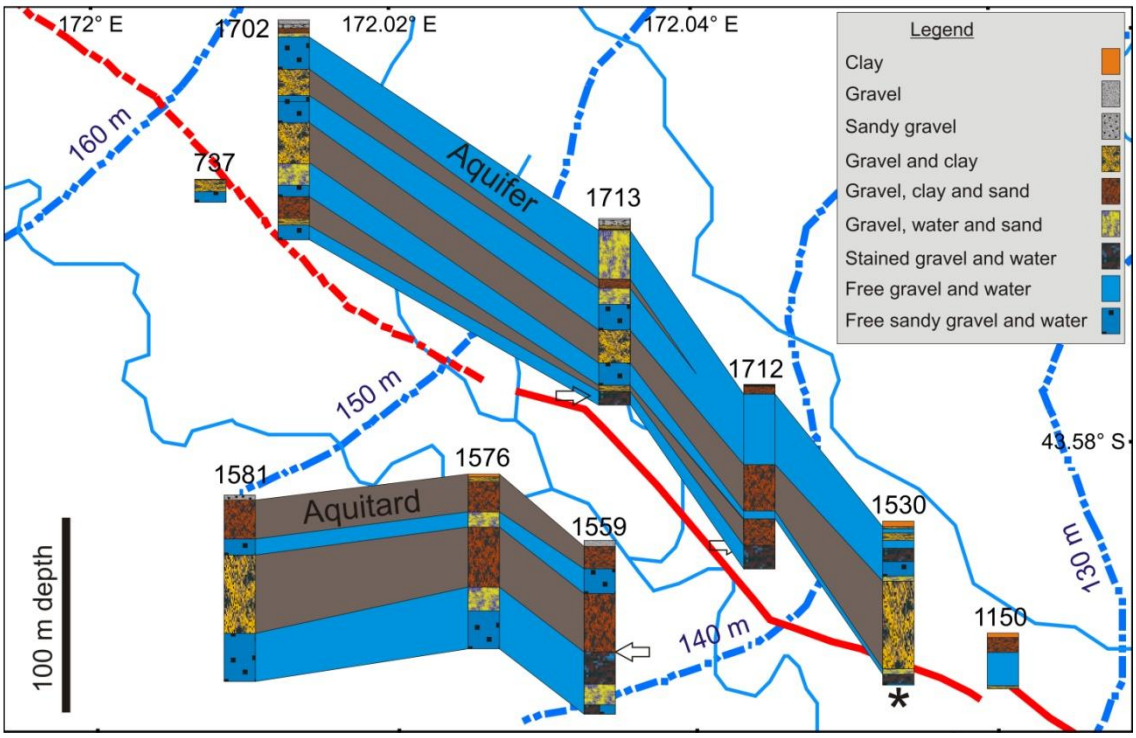

Figure 5.10: Fence diagram showing borehole stratigraphy either side of the West segment. The differences may be the result of faulting or of the fault's position at the junction of two fans. Well 1530 (*)is located almost on the mapped fault trace.

5.8 Discussion

5.8.1 Geomorphic evidence for fault history

The West segment of the Greendale fault performs a dual role as a releasing bend for the Central segment of the Greendale fault and as a transfer fault feeding rock toward the Charing Cross blind thrust (Duffy et al. 2013). An important question therefore arises regarding the slip history and earthquake recurrence interval of the West segment.

Geomorphic factors outlined above, including A) the apparent presence of a double scarp at the stepover location (Figure 5.7); B) the consistency of terrace edges with the orientation of the fault trace (Figure 5.9); C) the discordance of terrace edges with older paleochannels; D) the increase of warping of the alluvial surface with elevation; E) the continuity of terrace paleochannels across the fault trace, all provide circumstantial evidence to suggest the occurrence of at least one surface rupture on the West segment of the Greendale fault. That surface rupture displaced a surface that is presently tentatively considered to be of Late Holocene age (Forsyth et al. 2008).

In addition to evidence suggestive of a previous rupture, the geomorphic evolution of the Hororata and Selwyn Rivers seems to suggest that the rivers were responding to inter-seismic tilting to the NE. Unilateral meander migration, such as the NE migration of the Hororata River meander belt, is widely recognised as an indicator of tectonic tilting (Leeder & Alexander 1987; Alexander et al. 1994; Jackson & Leeder 1994; Holbrook & Schumm 1999)(Figure 5.4) and the development of slip off terraces west of the Selwyn River (Figure 5.5) resembles terraces that were interpreted as indicators of pre-Darfield earthquake southward tilt on the south side of the Central segment of the Greendale fault, and adjacent to the Selwyn River (Campbell et al. 2012, their figure 7).

5.8.2 Implications of scarp geometry for fault history

The morphology of the scarp may also provide insight into the stage of development of the fault. The post-Darfield fault scarp has a corrugated morphology with two well-defined, en-echelon NW-striking traces, linked by a WNW trace on which topography declines southward (Figure 5.6). The WNW trace is ramp-linked at its southernmost tip with the southern NW-striking segment.

Ramp-linkage of en-echelon segments is typical of normal fault scarp morphology and typically evolves into hard-linked corrugated faults by breaching of the ramp (Peacock & Sanderson 1991; Trudgill & Cartwright 1994). In isotropic media such as alluvium, ramp breaching generally occurs by curved propagation that results in fault-parallel extension of the footwall at the apex of the curve. The extension accommodates the displacement gradients on the linking faults (Ferrill et al. 1999). Cadastral survey vectors in the footwall either side of the bend show fault parallel extension of ~ 0.2 m (Duffy et al. 2013). Curved propagation is also generally accompanied by a decline in scarp elevation as it curves toward the next segment, followed by a sudden increase in scarp height at the cusp of the two segments (Fig.1b in Ferrill et al. 1999). This is precisely the progression that is observed along WNW-striking section of the West segment (Figure 5.6).

The extent to which a particular ramp has been breached is a function of the total extension on the controlling faults (Peacock & Sanderson 1991; Trudgill & Cartwright 1994). The geomorphology of this scarp suggests that the WNW section has almost completely breached a ramp that separated the two NW-striking sections, which implies a prolonged period of normal faulting.

5.8.3 Implications of hydrogeology for fault history

The presence of a thick gravel aquifer on the hanging wall of the fault (Figure 5.10) that deflects potentiometric contours (Figure 5.2) is in keeping with the apparent advanced evolution of the faults segmentation. The gravel aquifer on the downthrown side of the fault is suggestive of a fill of gravel from the Selwyn River accumulating on the hanging wall of the fault. Repeated vertical slip on the fault and filling of the graben with Selwyn River gravels could be expected to result in tectonic partitioning of aquifers. The same effect has been well documented in gravel-river basins in North Canterbury (Armstrong 2000; Finnemore 2004; Dodson 2009) and elsewhere (Dutcher & Garrett 1963) due to fault and fold-related sub-basin development. Structural growth in gravel basins controls basement and surficial topography, which in turn controls and localizes the distribution of permeable gravels.

5.8.4 Implications for interpreting slow-slip rate tectonic structures in alluvial geomorphic settings

This study highlights the difficulties that arise when attempting to recognize and/or quantify fault activity in an alluvial setting, where a slow slip-rate fault late in its inter-seismic cycle is likely to be considerably degraded or buried by young sediments (e.g. Hart & Bryant 1997; Similox-Tohon et al. 2006; Cox et al. 2012b). The observations presented here provide insight into the likely geomorphic and stratigraphic consequences of this event over the next 1000 years in the absence of human intervention.

Cross- and along-channel gradients are extremely sensitive to local tectonic influence and in turn control the geomorphic and depositional character of rivers(Schumm 1985,1986; Holbrook & Schumm 1999). Therefore, the drainage system can be expected to respond on multiple time scales. Had the Hororata River not been reinstated, the immediate post-seismic landscape response would probably have focused on the reach-scale (10^1 to 10^2 m) development of the avulsed river. In this instance, the avulsion was not complete, because the scarp height in the channel (probably around 1.5 m) was at or below the lip height of the avulsion node. Such an event can progress in one of three ways (Slingerland & Smith 2004). A) The avulsion node (analogous to the crevasse of Slingerland & Smith 1998) could incise and eventually capture the entire flow. B) The avulsion node could alluviate and heal and flow could return to the main channel, or C) An equilibrium condition could arise where both channels are permanently occupied.

Option C above would give the river an anastomosing character in the short term (e.g. Makaske 2001) but ultimately, the location of the Hororata River will be controlled by basin scale slope changes. Subsidence of the hanging wall of the West segment at the fault scarp both increased the gradient of the Selwyn fan and provided accommodation space at its toe. Uplift of the footwall of the fault reduced the gradient of the Hororata River. The bedload-rich Selwyn River

will therefore probably fill the accommodation space on the downthrown side. Overtopping of the scarp by periodic Selwyn River floods, together with deposition of overbank material by the small, reduced-gradient Hororata River will add fine material to the upthrown side of the fault. This scenario would create both sedimentological and tectonic partitioning of the alluvial aquifer and is in keeping with well logs adjacent to the West segment.

Gradient changes caused by uplift of the footwall of the fault, together with impingement of Selwyn fan sediments on the Hororata River's course, may tilt the Hororata River to the SW, potentially allowing it to trim the Rakaia fan. However, as stress begins to accumulate on the fault, pre-seismic warping may occur (Koseluk & Bischke 1981) and tilt the rivers back to the NE. Complications may arise from folding due to elastic strain on the linked Charing Cross and Hororata blind thrust faults. For instance, the Charing Cross blind thrust may contribute a transverse uplift component to the development of the Selwyn River, in the same way that the Hawkins River seems to have developed prior to this latest event (Campbell et al. 2012).

It is notable that the apparent sense of the coseismic deflection of the Hororata River is sinistral rather than dextral. The same appears to have happened previously to the Waterford Channel in the northern part of the field area. The 'sinistral' displacement occurs because the scarp height is equal to or greater than the channel depth, causing the river to preferentially avulse down gradient rather than be dextrally displaced. A similar response was observed where the dextral Beichuan Fault cut obliquely across a braid channel of the Baisha River during the Wenchuan earthquake and diverted the channel downstream in a sinistral sense (Liu-Zeng et al. 2010, p. 2624). Classic fault sense displacement of streams generally occurs at mountain fronts where the displaced rivers are deeply incised and avulsion is not feasible (e.g. Howard et al. 2005). This has implications for studies on the paleoseismicity of the Central segment of the Greendale fault. For instance Villamor et al. (2011) observed no evidence for previous dextral displacement of channels across the Central segment but several of their figures including 3.3 and 3.4 show channels with apparent sinistral deflections. This feature, combined with Villamor et al.'s (2011) observations of channels in the same figures losing expression where they encounter pop-ups, suggests that these sites would be fruitful targets for paleoseismic investigations.

5.8.5 Implications for displacements estimation

After the Denali earthquake, Haeussler et al. (2004) compared measurements of the Trans-Alaska Pipeline distortion with fault trace offset measurements. They concluded that single near field offset measurements do not provide a suitable basis for evaluating the reliability of surface slip estimations. In that instance only 84% (4.9 m) of the true maximum displacement of 5.8 m occurred within a 100 m zone straddling the fault trace, with the remainder spread over some 1000

m. The data presented here and by Duffy (2013) provides a similar opportunity to assess the reliability of traditional on-fault displacement measurements as indicators of total slip.

Far-field displacements that were determined by cadastral surveying range up to 1.6 m but the best constrained fenceline offsets range from 1 to 1.5 m with an average of ~1.1m (Figure 5.8). Values along shorter fences are smaller and more variable. For instance dextral offsets apparently decline southwards from fence 1 to fence 3 (Figure 5.8). However, fence 3 is short and probably does not cross the entire deformation zone so its 0.7 m dextral displacement is only a minimum estimate and true displacement may not be smaller than at fence 2. These comparisons seem to suggest that in this instance the on-fault measurements of dextral offset underestimate the total dextral value, even though some fencelines extend for many tens to hundreds of meters. As previously concluded by Van Dissen et al. (2010) for the Greendale fault, and by Haeussler et al. (2004) for the Denali fault, this study indicates that on-fault slip measurements only record 60-90% of total displacement.

In a similar way, the profiles in Figure 5.7 show that vertical profiles may systematically overestimate scarp height, especially where channels, terrace edges or unrecognised scarps occur within the deformation zone. Without detailed pre-earthquake topographic mapping, the estimates of vertical offsets provided by topographic profiling can only be considered generally indicative of co-seismic displacement because of uncertainty about pre-scarp topography. This problem is, however, entirely resolved by differencing of pre and post earthquake topographic datasets (Oskin et al. 2012; Duffy et al. 2013).

5.8.6 Implications for seismic hazard assessment

Considerable disagreement exists in estimates of the surface rupture length on the Greendale fault, especially on the western end. Quigley et al. (Quigley et al. 2012b) mapped surface displacements and feature offsets for only ~5 km northwards along the West Segment. In contrast, Elliot et al. (2012) mapped a surface rupture along the full length of the western segment on the basis of InSAR. Offsets at the scarp apparently decline rapidly at the surface rupture tip (Figure 5.8; Figure 5.9) but cadastral measurements of far field displacements do not (Duffy et al. 2013). Therefore, northward extension of the fault trace is consistent with cadastral survey data (Duffy et al. 2013) but inconsistent with the field mapped surface rupture termination (Quigley et al. 2012b and this study). This difference in on-scarp and far-field displacement gradient suggests that the mapped end of the surface trace of the fault may actually reflect a transition from a scarp to more distributed deformation. What then constitutes a surface rupture for the purposes of hazard assessment? The word ‘rupture’ suggests breakage or dislocation of the ground surface along a scarp or trace (Stewart & Hancock 1990) but the ability to detect such a dislocation is scale dependent. A ‘rupture’ that is not observable at fieldwork scale (Quigley et al., 2012) may be

clearly defined at differential topographic mapping scale, whether by InSAR (Beavan et al. 2012; Elliott et al. 2012) or LiDAR (Duffy et al. 2013). Modern seismic hazard assessment is commonly reliant on field mapped paleoseismic scarps, rather than differential imagery, because such imagery is not available until the fault has already ruptured. Subtle surface displacements such as cracks will also disappear and result in paleoseismic fault length underestimation. It therefore seems unwise to clutter magnitude scaling relationships with surface rupture determinations that are based on differential mapping that is unavailable for paleoseismic faults.

5.8.7 Future response of the Selwyn and Hororata Rivers

River channels are the most sensitive part of a drainage basin to relative elevation changes (Burbank & Anderson 2001), a factor that has driven a great deal of research on their responses to active tectonics. Much of the research has focused on stream table (e.g. Ouchi 1985) and numerical experiments (e.g. Snow & Slingerland 1990), and field observations to document channel planform and gradient evolution in response to uplift and subsidence. Field studies of paleo-responses have refined our understanding of tectono-fluvial landforms and their development, with decadal to centennial river response recorded at sites such as the Tiptonville Dome in the New Madrid Seismic Zone (Guccione et al. 2002). However, to the author's knowledge it has never been possible to observe at first hand the response of an alluvial river to absolutely geodetically-constrained co-seismic perturbations. This is because high resolution determination of near fault co-seismic ground displacements across a surface rupture trace is rarely achieved, particularly where the fault crosses an alluvial river. The surface rupture of the NW-striking West segment crosses two rivers, including one at its transition into the east-striking Central segment. This provides a unique baseline dataset from which to predict and then monitor the response of the modern river system to co-seismic disturbance.

5.9 Conclusions

Terrace mapping suggests that the Selwyn and Hororata Rivers have migrated toward the NE in a manner suggestive of local tilting. The West segment fault trace emerged along a pre-existing topographic anomaly that in several instances mimics the geometry of the fault trace, even including a double scarp at the stepover location. The large scale, breached ramp morphology of the fault trace is typical of a fault that has an extended history of slip. The hydrogeological characteristics of the Selwyn and Hororata Rivers support a model in which the fault has slipped repeatedly and accumulated a gravel fill on its downthrown side. A displaced marker is tentatively identified in well logs that may record up to 30 m of vertical displacement across the fault. In summary, this study has provided a significant amount of circumstantial evidence for a penultimate rupture and prolonged previous deformation on the West segment of the Greendale fault. Geomorphic evidence suggests that ongoing investigations will reveal a history of slip with

episodes of activity concealed within the fluvial stratigraphy and channel architecture. However, the aquifer geometry also could relate to the interfingering of sediments in the Rakaia to Selwyn interfan area, so further rigorous investigations will be required. Dating of surfaces on the Hororata Selwyn interfluve will be critical to developing a robust earthquake chronology, Nevertheless, the dual role performed by this fault as a transfer fault for the Hororata Charing Cross system and as a releasing fault for the Central segment suggests that it will record the combined slip history of these faults, even where the whole system does not rupture together as it did in the recent earthquake. For this reason, the West segment should be a primary target for paleoseismic investigations.

CHAPTER 6. CONCLUSIONS

6.1 Timor synthesis

This thesis investigates aspects of the structural, geomorphic and sedimentary response to transpressional plate boundary deformation at two distinct margins of the Australian plate. In each case, the links between faulting and landscape evolution have been explored. My research uses the sedimentary record and the kinematics of brittle faulting to develop a model of how ductile and brittle processes, indenter collision, passive margin geometry and underthrusting of a plateau all contributed to the kinematics of faulting and the development of syn-collisional extension in Timor. A list of questions about the Timor orogen and about arc-continent collisions in general was put forward in the Prologue. This synthesis addresses some of these questions.

a) When was contact initiated between the Australian continental margin and the Banda Forearc in the Timor orogen?

Litho and chemostratigraphy indicate that the collision began earlier than the generally accepted Mid Pliocene. Geochemistry shows that an emergent island was almost certainly present by >4.5 Ma and shedding lithogenic sediment into a previously clean carbonate basin. This conclusion is supported by palynological studies (Nguyen 2011). The initial sediment source was probably derived from subaerial erosion of the accretionary wedge.. I applied an age model to Nguyen's (2011) palynological data and showed that initial slow uplift rates of 0.5-0.6 mm/year accelerated to 2 to 5 mm/year at 3.1 Ma (see Nguyen et al. 2013). The acceleration was probably due to arrival of the continental slope (Bowin et al. 1980), inception of the Wetar Suture (Price & Audley-Charles 1983,1987), possibly slab detachment (Sandiford 2008; Ely et al. 2011), or a combination of these factors. However, the first arrival of continental crust clearly preceded this event.

b) How can seemingly disparate depositional histories in Timor's orogenic basins be reconciled using a single orogenic model?

In Chapter 1 I showed that the Marobo Basin in central Timor, which I interpreted as a syn-collisional graben, remained at mid-bathyal depths at least until the onset of clastic sedimentation around 3.5 Ma. Meanwhile, Chapter 2 indicates that the Bath Putih Formation pelagic carbonates of both Marobo and Viqueque were progressively contaminated with lithogenic sediment since at least 4.5 Ma. The sediment was increasingly derived from the Banda Terrane, which was exhumed above duplexed Australian-affinity rocks.

The situation in West Timor is clearly quite different as shown by the stepwise change in timing of the onset of clastic sedimentation (Chapter 2). This stepwise change is consistent with early collision in the eastern half of the island. The structure of the Marobo Basin, the stepwise change in the onset of clastic sedimentation from Timor Leste to West Timor, and the characteristic geometry of

the faulting in Timor Leste when compared with indenter models (e.g. Boutelier et al. 2012) indicate that collision initiated due to the arrival of an outlying plateau at the trench in the region of Timor Leste. The Marobo Basin developed on the western margin of the plateau. This highlights the importance of combining depositional histories from multiple basins to understand the tectonic and topographic evolution of source areas.

c) How do the forearc and the passive margin respond to collision, specifically, which is subducted and which is obducted/accreted (Afonso & Zlotnik 2011; Boutelier et al. 2012).

Several publications have suggested that the Australian passive margin was subducted and duplexed below the forearc (Harris 1991; Harris et al. 2000), giving rise to a thick low gravity anomaly (e.g. Snyder et al. 1996a). Other authors disagree and suggest that no continental subduction occurred, and that the Banda Terrane nappe that occupies the highest structural position in Timor was emplaced as a tectonic flake (Price & Audley-Charles 1983,1987; Audley-Charles 2011). Chapter 1 of this study indicates that the syn-collisional extension seen in the Marobo Basin is a first-order response to collision and resulted from the subduction and duplexing of a bathymetric high associated with an outlying continental plateau. Duplexing of the continental material (e.g. Harris 1991) accentuated (thickened) the pre-existing topography of the lower plate and caused the forearc to dome above it, stretching the forearc. This was accentuated by the orientation of the lower plate convergence vector away from the transition to oceanic crust, which resulted in further stretching of the forearc due to differential coupling of the upper and lower plate. Rapid lateral changes in composition, density and subductability associated with the passive margin geometry caused an abrupt lateral transition from subduction to crustal thickening and possibly buoyant rebound at the margin of the subducting plateau. This locally oversteepened the slope and resulted in gravitational collapse of the domed and stretched upper plate at the edges of the buoyant duplexed plateau on the lower plate.

d) What drives extension in collisional orogens? (e.g. Dewey 2005)

Orogen-parallel extension has been widely documented from convergent orogens including the Himalaya and Tibet (England & Houseman 1989; England & Molnar 1993), the high plateau of the Andes (Dalmayrac & Molnar 1981), the Southern Appenine Belt of Italy (Ferranti et al. 1996) and many forearc complexes (McCaffrey 1996). Different mechanisms have been proposed for these extensional features. Forearc complexes are particularly sensitive to changes in the obliquity of subduction (Ave Lallemant & Guth 1990). Other mechanisms put forward to explain extension of other orogens have included variability in subduction parameters including rate, crustal thickness and

accretion mechanism (Platt 1986 – the Franciscan Complex in the European Alps), orogen arcuation (Ferranti et al. 1996), spreading and backarc extension towards a retreating slab (Schellart & Lister 2005), slab breakoff and subduction reversal (Teng et al. 2000) and increases in the elevation of the mountain belt (England & Houseman 1989 – Tibet). Subduction of asperities and bathymetric highs such as is described above has also been shown to cause extensional collapse within a forearc (Cloos 1993; Fleury et al. 2009; Pedley et al. 2010). Although these mechanisms for driving extension vary from one orogen to another, each is rooted in spatial and temporal changes in stress distributions that control the availability of the potential energy within the thickened crust to power extension (England & Molnar 1993).

Previously inferred possible causes for extension in Timor have focused on slab rupture and isostatic rebound (Grady & Berry 1977; Price & Audley-Charles 1983,1987; Charlton 1991; Sandiford 2008; Ely et al. 2011). Seismicity suggests that slab rupture processes are presently occurring (Sandiford 2008), but also indicates that the Timor orogen grows parallel to the arc (McCaffrey 1988; McCaffrey & Abers 1991) (see also Harris 1992). The slab rupture is not well developed as indicated by a lack of evidence for a slab window (Sandiford 2010; Spakman & Hall 2010). Tomography suggests a thinned slab, possibly delaminating and being overridden by the advancing Australian continent, but not ruptured. Masson et al (1991) suggested obliquity-driven arc-parallel extension, in the manner of Ave Lallemant and Guth (1990) based on seafloor geomorphology in the Wetar Strait north of Marobo Basin but McCaffrey (1996) subsequently discounted obliquity-driven arc parallel extension in Timor, having determined that a pole of rotation could be found to account for earthquake slip vectors.

My structural mapping indicates that extension occurred as a first order response to the subduction of a continental plateau, but I have also shown that duplexing and shortening of the plateau elicited a secondary extrusion response. Yin and Taylor (2011) recently proposed a mechanism to explain the wide angle conjugate normal faults that are commonly seen in orogens including Tibet (Styron et al. 2011) and the Eastern European Alps (Ratschbacher et al. 1991a; Frisch et al. 1998). They explained these features as the surface expression of Riedel shears associated with ductile extrusion at depth between opposite sense strike slip faults. My mapping of faults in Timor, and review of previously mapped faults is consistent with this mechanism in the context of continuing contraction across Timor and eastward extrusion of Timor Leste. However, in Timor the extrusion occurred below the forearc and dismembered the forearc. The extrusion was probably driven by shortening of the continental plateau, and facilitated by subduction of the oceanic embayments bounding the subducted plateau, which provided free space and allowed an influx of heat below the plateau.

The combination of differential coupling of the forearc, and extrusion of the underplated continental plateau, accounts for the tectonic setting and kinematic development of synorogenic basins in Timor more effectively than any previous model.

e) How is uplift generated and topography created and distributed (e.g. slab rupture and buoyant rebound or crustal thickening)?

The timing of the most rapid phase of uplift at ~3.1 Ma (Chapter 2, see Nguyen et al. 2013) is close to the previously inferred age of both collision of the continental slope and initiation of the Wetar Suture (Bowin et al. 1980; Price & Audley-Charles 1983,1987). This suggests that uplift was related to collision due to contraction on the plate boundary. During the uplift, differential topography appears to have been generated dominantly in the footwall of high angle, cross-cutting oblique normal faults that still dominate the topography of Timor Leste and are coupled with shortening and ductile extrusion at depth.

6.2 Future research in Timor

Despite the arduous and extensive fieldwork that underpins the Timor section of this thesis, mapping of the synorogenic basins is still only at a reconnaissance stage. Further work should focus on the major topographic scarps to establish their tectonic significance, if any. Similar faults have yet to be properly mapped in West Timor, where speculative fault mapping by Kenyon (1974) is quite at odds with equally speculative faults indicated on maps prepared by Charlton (1991). A useful starting point should be the area immediately west of the Marobo Basin, so as to understand the links between collision in the Marobo area and the fault kinematics and basin histories of the Maliana basin of Timor Leste and the Central basin of West Timor. A great deal of additional work will also be required to establish the rates and timing of activity on all of the faults mapped in this thesis.

6.3 Greendale fault synthesis

Fault junctions and discontinuities are important locations for the initiation and stopping of earthquake ruptures due to interaction of seismogenic structures (King & Nábělek 1985; Sibson 1985; King 1986; Sibson 1989; Elliott et al. 2009; Ben-Zion et al. 2012). One of the main ways in which we study active faults is by their preservation in the geomorphic record as fault scarps and traces. Identifying fault scarps and traces at junction zones can be problematic, however, due to the typically subdued geomorphic expression caused by distribution of deformation away from a clear trace (King & Nábělek 1985; Devès et al. 2011). The Darfield earthquake of 4 September 2010 provided an opportunity to study the geomorphic expression of a fault junction zone in full cognizance of its kinematic development.

In Chapter 4, I studied the junction of the Central and West segments of the Greendale fault, and the Charing Cross blind thrust. Using high resolution multi-temporal datasets, I showed that that the fault junction incorporates elements of a large-scale (5 km) releasing bend and a smaller-scale (1 km) restraining stepover. This situation is caused by the coseismic interactions of the faults at the junction. Westward motion on the south side of the Central and West segments pulled away from a right bend, while southeastward motion on the northeast side of the West segment converged on a left bend onto the Central segment and fed material towards the Charing Cross fault. The restraint at the fault junction created a pop-up structure that was nested within the overall releasing bend. Net slip declined to near zero at the fault junction. This single-event deformation record is unencumbered by topographic features related to previous events, and thus provides a valuable analogue for interpretation of pop up structures nested in releasing bends elsewhere (e.g. Duman et al. 2005) that have been interpreted as indicators of rupture segmentation (Ben-Zion et al. 2012).

The combination of subtle deformation and the location of these features in an active alluvial setting suggest that their preservation will be short-lived in the local geomorphic record. In Chapter 5 I looked for evidence of pre-Darfield earthquake elastic strain accumulation and displacements. I found that the Selwyn and Hororata Rivers have migrated toward the NE in a manner suggestive of local tilting driven by elastic strain on the West segment. The West segment fault trace emerged along a pre-existing topographic anomaly that in several instances mimics the geometry of the fault trace, even including a double scarp at the location of a small stepover and lateral ramp. However, apart from the path of the Selwyn River, which fortuitously crosses the fault trace at the slip minima associated with the triple junction, I found no evidence for a pre-existing pop-up similar to that documented in Chapter 4. Nevertheless, the large scale morphology of the modern fault trace suggests that the fault has an extended history of slip. The hydrogeological characteristics of the Selwyn and Hororata Rivers also support a model in which the fault has slipped repeatedly and accumulated a gravel fill on its downthrown side. Given that the modern graben was created by westward movement on the south side of the Central segment, its apparent influence on the aquifer suggests that the Central segment has also slipped repeatedly.

6.4 Future research on the West segment of the Greendale fault

The dual role performed by the West segment as a transfer fault for the Hororata Charing Cross system and as a releasing fault for the Central segment suggests that it will record the combined slip history of these faults, even where the whole system does not rupture together as it did in the recent earthquake. For this reason, the West segment should be a primary target for geophysical and paleoseismic investigations.

6.5 Conclusion

During this research I mapped arrays of strike-slip and normal faults that accommodate contraction at different scales on collisional plate boundaries. I show that in each case, the development of topography reflects the interaction of these fault arrays. The topography generated by a single earthquake in Canterbury reflects the complexities of the interaction of several faults, and future topographic and geological development will depend largely on which of the faults in the system is most active. In Timor, shortening occurs on décollements at depth but differential topography is created and controlled by normal faulting due to the influence of a subducted bathymetric high and large scale extrusion. The extrusion is coupled to contraction at depth. In neither instance do normal faults reflect a regional extensional strain field.

Ultimately, the development of syn-collisional normal faulting is a function of the nature of the colliding elements and the kinematics of their interaction. Special importance in Timor is attributed to passive margin geometry (e.g. Spakman & Hall 2010; Boutelier et al. 2012), indenter collision (e.g. Boutelier et al. 2012), pre-existing structure including the presence of underthrust plateaus (e.g. Jamieson & Beaumont 2011; Reyners et al. 2011), relative convergence vectors, differential coupling of the forearc (e.g. Nugroho et al. 2009) and coupling of brittle and ductile processes (e.g. Jamieson & Beaumont 2011; Yin & Taylor 2011) in determining the outcome and style of an arc-continent collisional event.

REFERENCES

Abbott, MJ & Chamalaun, FH 1981, 'Geochronology of some Banda Arc Volcanics', in AJ Barber & S Wiryosujono (eds), *The Geology and Tectonics of Eastern Indonesia*, vol. Special Publication 2, Geological Research and Development Centre, Bandung, pp. 253-68.

Acharyya, SK 1998, 'Break-up of the greater Indo-Australian continent and accretion of blocks framing south and east Asia', *Journal of Geodynamics,* vol. 26, no. 1, pp. 149-70.

Adams, J 1990, 'Paleoseismicity of the Cascadia subduction zone: evidence from turbidites off the Oregon-Washington margin', *Tectonics,* vol. 9, no. 4, pp. 569-83.

Afonso, JC & Zlotnik, S 2011, 'The Subductability of Continental Lithosphere: The Before and After Story', in D Brown & PD Ryan (eds), *Arc-Continent Collision*, vol. 1, Springer Berlin Heidelberg, pp. 53-86.

Akyüz, S, Hartleb, R, Barka, A, Altunel, E, Sunal, G, Meyer, B & Armijo, R 2002, 'Surface Rupture and Slip Distribution of the 12 November 1999 Düzce Earthquake (M7.1), North Anatolian Fault, Bolu, Turkey', *Bull. Seismol. Soc. Am,* vol. 92, no. 1, pp. 61-6.

Alexander, J, Bridge, JS, Leeder, MR, Collier, REL & Gawthorpe, RL 1994, 'Holocene meander-belt evolution in an active extensional basin, southwestern Montana', *Journal of Sedimentary Research B: Stratigraphy & Global Studies*, no. B64, p. 4. Retrieved 3 May 2011, from Scopus database.

Allègre, CJ & Rousseau, D 1984, 'The growth of the continent through geological time studied by Nd isotope analysis of shales', *Earth and Planetary Science Letters,* vol. 67, no. 1, pp. 19-34. DOI:10.1016/0012-821x(84)90035-9

Allison, MA, Khan, SR, Goodbred Jr, SL & Kuehl, SA 2003, 'Stratigraphic evolution of the late Holocene Ganges–Brahmaputra lower delta plain', *Sedimentary Geology,* vol. 155, no. 3–4, pp. 317-42. DOI:10.1016/s0037-0738(02)00185-9

Allmendinger, RW 2002, *StereoWin (Windows) Version 1.2 and user's manual*.

Allmendinger, RW, Marrett, RA & Cladouhos, T 2001, *FaultKinWin (Windows) Version 1.2.2 and user's manual*.

ALS 2006, 'Whole rock geochemistry - ME-ICP06 and OA- GRA05. Analysis of major oxides by ICP-AES '. ALS Minerals,, Winnemucca, Nevada

ALS 2009, 'Geochemical procedure ME-MS81, Ultra-Trace Level Methods'. ALS Global, Winnemuca, Nevada, 2009, pdf

Althorpe, M 1975, *Paleontological report on the Timor Oil/B.O.C.A.L. Mola No 1 well, Portuguese Timor*, BOC of Australia Pty Ltd, Perth.

Amos, CB & Burbank, DW 2007, 'Channel width response to differential uplift', *Journal of Geophysical Research-Earth Surface,* vol. 112, no. F2, p. 11. Article. DOI:F02010 10.1029/2006jf000672

Andresen, A, Hartz, EH & Vold, J 1998, 'A late orogenic extensional origin for the infracrustal gneiss domes of the East Greenland Caledonides (72-74°N)', *Tectonophysics,* vol. 285, no. 3-4, pp. 353-69. Retrieved 30 May 2012, from Scopus database.

Armendáriz, M, López-Guijarro, R, Quesada, C, Pin, C & Bellido, F 2008, 'Genesis and evolution of a syn-orogenic basin in transpression: Insights from petrography, geochemistry and Sm-Nd systematics in the Variscan Pedroches basin (Mississippian, SW Iberia)', *Tectonophysics,* vol. 461, no. 1-4, pp. 395-413. Retrieved 9 February 2011, from Scopus database.

Armstrong, MJ 2000, *Geomorphological and Geophysical Investigation of the Effects of Active Tectonic Deformation on the Hydrogeology of North Culverden Basin, North Canterbury*, PhD Thesis, University of Canterbury.

Audley-Charles, MG 1965, 'A Miocene Gravity Slide Deposit from Eastern Timor', *Geological Magazine,* vol. 102, no. 3, pp. 267-76.
Audley-Charles, MG 1967, 'Greywackes with a Primary Matrix from the Viqueque Formation (Upper Miocene-Pliocene), Timor', *Journal of Sedimentary Petrology,* vol. 37, no. 1, pp. 5-11.
Audley-Charles, MG 1968, *The Geology of Portugese Timor*, Geological Society of London, London.
Audley-Charles, MG 1985, 'The Sumba enigma: Is Sumba a diapiric fore-arc nappe in process of formation?', *Tectonophysics,* vol. 119, no. 1-4, pp. 435-49.
Audley-Charles, MG 1986a, 'Rates of Neogene and Quaternary tectonic movements in the southern Banda Arc based on micropalaeontology', *Journal of the Geological Society,* vol. 143, no. 1, pp. 161-75.
Audley-Charles, MG 1986b, 'Timor- Tanimbar Trough: the foreland basin of the evolving Banda orogen', *Foreland basins*, pp. 91-102.
Audley-Charles, MG 2004, 'Ocean trench blocked and obliterated by Banda forearc collision with Australian proximal continental slope', *Tectonophysics,* vol. 389, no. 1-2, pp. 65-79.
Audley-Charles, MG 2011, 'Tectonic post-collision processes in Timor', in R Hall, MA Cottam & MEJ Wilson (eds), *The SE Asian Gateway: History and Tectonics of the Australia-Asia Collision*, Geological Society Special Publication 355, London, pp. 241-66.
Audley-Charles, MG, Ballantyne, PD & Hall, R 1988, 'Mesozoic-Cenozoic rift-drift sequence of Asian fragments from Gondwanaland', *Tectonophysics,* vol. 155, no. 1-4, pp. 317-30.
Audley-Charles, MG & Carter, DJ 1972, 'Palaeogeographical significance of some aspects of Palaeogene and Early Neogene stratigraphy and tectonics of the Timor Sea region', *Palaeogeography, Palaeoclimatology, Palaeoecology,* vol. 11, no. 4, pp. 247-64.
Audley-Charles, MG, Carter, DJ, Barber, AJ, Norvick, MS & Tjokrosapoetro, S 1979, 'Reinterpretation of the geology of Seram: implications for the Banda Arcs and northern Australia', *Journal of the Geological Society,* vol. 136, no. 5, pp. 547-68.
Audley-Charles, MG & Harris, RA 1991, 'Allochthonous terranes of the southwest Pacific and Indonesia', *Allochthonous terranes*, pp. 115-31.
Augustsson, C & Bahlburg, H 2003, 'Active or passive continental margin? Geochemical and Nd isotope constraints of metasediments in the backstop of a pre-Andean accretionary wedge in southernmost Chile (46°30′-48°30′S)', vol. 208, pp. 253-68
Ave Lallemant, HG & Guth, LR 1990, 'Role of extensional tectonics in exhumation of eclogites and blueschists in an oblique subduction setting: northeastern Venezuela', *Geology,* vol. 18, no. 10, pp. 950-3.
Bakker, RR 2011, *Surface uplift in world's youngest orogen, can crustal thickening explain the uplift in Timor?*, MSc Thesis, Utrecht University.
Barber, AJ & Audley-Charles, MG 1976, 'The significance of the metamorphic rocks of Timor in the development of the Banda Arc, Eastern Indonesia', *Tectonophysics,* vol. 30, no. 1-2, pp. 119-28.
Barber, AJ, Tjokrosapoetro, S & Charlton, TR 1986, 'Mud Volcanoes, Shale Diapirs, Wrench Faults and Melanges in Accretionary Complexes, Eastern Indonesia', *American Association of Petroleum Geologists Bulletin,* vol. 70, no. 11, pp. 1729-41.
Barkham, ST 1993, *The structure and stratigraphy of the Permo-Triassic carbonate formations of West Timor, Indonesia*, PhD Thesis, Royal Holloway and Bedford New College, University of London.
Barrell, DJA, Litchfield, NJ, Townsend, DB, Quigley, MC, Van Dissen, RJ, Cox, SC, Cosgrove, R, Furlong, K, Villamor, P, Begg, JG, Hemmings-Sykes, S, Jongens, R, Mackenzie, H, Stahl, T, Bilderback, E, Duffy, B, Lang, EMW, Nicol, R, Noble, D & Pedley, K 2011, 'Strike-slip ground-surface rupture (Greendale Fault) associated with the 4 September 2010 Darfield earthquake, Canterbury, New Zealand', *Quarterly Journal of Engineering Geology and Hydrogeology,* vol. 44, pp. 283-91. DOI:10.1144/1470-9236/11-034

Bayona, G, Montes, C, Cardona, A, Jaramillo, C, Ojeda, G, Valencia, V & Ayala-Calvo, C 2011, 'Intraplate subsidence and basin filling adjacent to an oceanic arc–continent collision: a case from the southern Caribbean-South America plate margin', *Basin Research,* vol. 23, no. 4, pp. 403-22. DOI:10.1111/j.1365-2117.2010.00495.x

Beavan, J, Motagh, M, Fielding, E, Donnelly, N & Collett, D 2012, 'Fault slip models of the 2010- 2011 Canterbury, New Zealand, earthquakes from geodetic data, and observations of post-seismic ground deformation', *New Zealand Journal of Geology and Geophysics (Special issue: Canterbury, New Zealand, 2010-2011 earthquake sequence),* vol. 55, no. 3, pp. 207-21. DOI:10.1080/00288306.2012.697472

Beavan, J, Samsonov, S, Denys, P, Sutherland, R, Palmer, N & Denham, M 2010a, 'Oblique slip on the Puysegur subduction interface in the 2009 July M_W 7.8 Dusky Sound earthquake from GPS and InSAR observations: implications for the tectonics of southwestern New Zealand', *Geophysical Journal International,* vol. 183, no. 3, pp. 1265-86. DOI:10.1111/j.1365-246X.2010.04798.x

Beavan, J, Samsonov, S, Motagh, M, Wallace, LM, Ellis, SM & Palmer, N 2010b, 'The Darfield (Canterbury) Earthquake: Geodetic observations and preliminary source model', *Bulletin of the New Zealand Society for Earthquake Engineering,* vol. Vol. 43, no. 4, pp. 228-35.

Becker, A 1995, 'Conical drag folds as kinematic indicators for strike-slip fault motion', *Journal of Structural Geology,* vol. 17, no. 11, pp. 1497-506. DOI:10.1016/0191-8141(95)00057-k

Ben-Zion, Y, Rockwell, TK, Shi, Z & Xu, S 2012, 'Reversed-polarity secondary deformation structures near fault stepovers', *Journal of Applied Mechanics,* vol. 79, 031025, no. 3. DOI:10.1115/1.4006154

Benincasa, A, Keep, M & Haig, DW 2012, 'A restraining bend in a young collisional margin: Mount Mundo Perdido, East Timor', *Australian Journal of Earth Sciences,* vol. 59, no. 6, pp. 859-76. Retrieved 16 August 2012, from Scopus database.

Berggren, WA & Hollister, CD 1977, 'Plate tectonics and paleocirculation - Commotion in the ocean', *Tectonophysics,* vol. 38, no. 1-2, pp. 11-48.

Berry, RF 1981, 'Petrology of the Hili Manu Lherzolite, East Timor', *Journal of the Geological Society of Australia,* vol. 28, pp. 453-69.

Berry, RF & Grady, AE 1981, 'Deformation and metamorphism of the Aileu Formation, north coast, East Timor and its tectonic significance', *Journal of Structural Geology,* vol. 3, no. 2, pp. 143-67.

Berry, RF & Jenner, GA 1982, 'Basalt geochemistry as a test of the tectonic models of Timor', *Journal of the Geological Society of London,* vol. 139, pp. 593-604.

Berry, RF & McDougall, I 1986, 'Interpretation of $^{40}Ar/^{39}Ar$ and K/Ar dating evidence from the Aileu Formation, East Timor, Indonesia', *Chemical Geology (Isotope Geoscience Section),* vol. 59, pp. 43-58.

Besse, J & Courtillot, V 1991, 'Revised and synthetic apparent polar wander paths of the African, Eurasian, North American and Indian plates, and true polar wander since 200 Ma', *Journal of Geophysical Research,* vol. 96, no. B3, pp. 4029-50.

Bhatia, MR & Crook, KAW 1986, 'Trace element characteristics of graywackes and tectonic setting discrimination of sedimentary basins', *Contributions to Mineralogy and Petrology,* vol. 92, no. 2, pp. 181-93. Retrieved 16 September 2012, from Scopus database.

Bistacchi, A & Massironi, M 2000, 'Post-nappe brittle tectonics and kinematic evolution of the north-western Alps: an integrated approach', *Tectonophysics,* vol. 327, no. 3-4, pp. 267-92. DOI:10.1016/s0040-1951(00)00206-7

Blasco, F, Saenger, P & Janodet, E 1996, 'Mangroves as indicators of coastal change', *Catena* vol. 27, no. 3–4, pp. 167-78. DOI:10.1016/0341-8162(96)00013-6

Bock, Y, Prawirodirdjo, L, Genrich, JF, Stevens, CW, McCaffrey, R, Subarya, C, Puntodewo, SSO & Calais, E 2003, 'Crustal motion in Indonesia from Global Positioning System measurements', *Journal of Geophysical Research B: Solid Earth,* vol. 108, no. 8.

Bouma, AH 1962, *Sedimentology of some Flysch Deposits: A Graphic Approach to Facies Interpretation*, Elsevier, Amsterdam.

Boutelier, D, Oncken, O & Cruden, A 2012, 'Fore-arc deformation at the transition between collision and subduction: Insights from 3-D thermomechanical laboratory experiments', *Tectonics,* vol. 31, no. 2. Retrieved 11 July 2012, from Scopus database.

Bowditch, N 1808, 'The first method to adjust a traverse based on statistical considerations', *The Analyst or Mathematical Museum,* vol. 1, no. 2, p. 42.

Bowin, C, Purdy, GM, Johnston, C, Shor, G, Lawver, L, Hartono, MS & Jezek, P 1980, 'Arc-continent collision in the Banda Sea region', *American Association of Petroleum Geologists Bulletin,* vol. 64, pp. 868-918.

Boynton, WV 1983, 'Cosmochemistry of the rare earth elements: meteorite studies', *Rare Earth Element Geochemistry*, pp. 63-114. Retrieved 7 October 2012, from Scopus database.

Bray, J, Seed, R, Cluff, L & Seed, H 1994, 'Earthquake Fault Rupture Propagation through Soil', *Journal of Geotechnical Engineering,* vol. 120, no. 3, pp. 543-61. DOI:10.1061/(ASCE)0733-9410(1994)120:3(543)

Breen, NA, Silver, EA & Roof, S 1989, 'The Wetar back arc thrust belt, eastern Indonesia: the effect of accretion against an irregularly shaped arc', *Tectonics,* vol. 8, no. 1, pp. 85-98. Retrieved 27 November 2011, from Scopus database.

Brouwer, HA 1942, 'Summary of the geological results of the expeditions', *Geological Expeditions to the Lesser Sunda Islands,* vol. 4, pp. 345-402.

Brown, D & Huang, CY 2009, 'An introduction to the Tectonophysics special issue on arc-continent collision processes', *Tectonophysics,* vol. 479, no. 1-2, pp. 1-3. DOI:10.1016/j.tecto.2009.11.008

Brown, D, Ryan, PD, Afonso, JC, Boutelier, D, Burg, JP, Byrne, T, Calvert, A, Cook, F, DeBari, S, Dewey, JF, Gerya, TV, Harris, RA, Herrington, R, Konstantinovskaya, E, Reston, T & Zagorevski, A 2011, 'Arc–Continent Collision: The Making of an Orogen', in D Brown & PD Ryan (eds), *Arc-Continent Collision, Frontiers in Earth Sciences*, Springer-Verlag, Berlin, pp. 477-93.

Brown, LJ & Weeber, JH 1992, 'Geology of the Christchurch urban area'. Institute of Geological and Nuclear Sciences Ltd., Lower Hutt, New Zealand, p. 1 map sheet + 104p.

Brown, M & Earle, MM 1983, 'Cordierite-bearing schists and gneisses from Timor, eastern Indonesia: P-T conditions of metamorphism and tectonic implications', *Journal of Metamorphic Geology,* vol. 1, no. 2, pp. 183-203.

Browne, GH, Field, BD, Barrell, DJA, Jongens, R, Bassett, KN & Wood, RA 2012, 'The geological setting of the Darfield and Christchurch earthquakes', *New Zealand Journal of Geology and Geophysics (Special issue: Canterbury, New Zealand, 2010-2011 earthquake sequence),* vol. 55, no. 3, pp. 193-7. DOI:10.1080/00288306.2012.682654

Burbank, D, Meigs, A & Brozovic, N 1996, 'Interactions of growing folds and coeval depositional systems', *Basin Research,* vol. 8, no. 3, pp. 199-223.

Burbank, DW 1992, 'Causes of recent Himalayan uplift deduced from deposited patterns in the Ganges basin', *Nature,* vol. 357, no. 6380, pp. 680-3. DOI:10.1038/357680a0

Burbank, DW & Anderson, RS 2001, *Tectonic Geomorphology*, Blackwell Science.

Burnett, AW & Schumm, SA 1983, 'Alluvial-River response to neotectonic deformation in Louisiana and Mississippi', *Science,* vol. 222, no. 4619, pp. 49-50. Retrieved 30 April 2011, from Scopus database.

Campbell, J, Pettinga, J & Jongens, R 2012, 'The tectonic and structural setting of the 4th September 2010 Darfield (Canterbury) Earthquake sequence, New Zealand', *New Zealand Journal of*

Geology and Geophysics (Canterbury, New Zealand, 2010-2011 earthquake sequence), vol. 55, no. 3, pp. 155-68.

Campbell, JK, Nicol, A & Howard, ME 2003, 'Long-term changes to river regimes prior to late Holocene coseismic faulting, Canterbury, New Zealand', *Journal of Geodynamics,* vol. 36, no. 1-2, pp. 147-68.

Cane, MA & Molnar, P 2001, 'Closing of the Indonesian seaway as a precursor to east African aridification around 3-4 million years ago', *Nature,* vol. 411, no. 6834, pp. 157-62.

Carter, DJ, Audley-Charles, MG & Barber, AJ 1976, 'Stratigraphical analysis of island arc-continental margin collision in eastern Indonesia', *Journal of the Geological Society of London,* vol. 132, pp. 179-98.

Cecil, CB, Dulong, FT, Harris, RA, Cobb, JC, Gluskoter, HG & Nugroho, H 2003, 'Observations on climate and sediment discharge in selected tropical rivers, Indonesia', in CB Cecil & TE Edgar (eds), *Climate Controls on Stratigraphy*, vol. 77, Society for Sedimentary Geology Special Publication, Tulsa, Oklahoma, pp. 29-50.

Chamalaun, FH, Grady, AE, von der Borch, CC & Hartono, HMS 1982, 'Banda Arc tectonics: The significance of the Sumba Island', in JS Watkins & CL Drake (eds), *Studies in continental margin geology*, vol. 34, Amer. Assoc. Petrol. Geologists, pp. 361-75.

Chang, CP, Angelier, J, Huang, CY & Liu, CS 2001, 'Structural evolution and significance of a mélange in a collision belt: the Lichi Mélange and the Taiwan arc-continent collision', *Geological Magazine,* vol. 138, no. 6, pp. 633-51. DOI:10.1017/s0016756801005970

Chappell, J & Veeh, HH 1978, 'Late Quaternary tectonic movements and sea-level changes at Timor and Atauro Island', *Geological Society of America Bulletin,* vol. 89, no. 3, pp. 356-68. DOI:10.1130/0016-7606(1978)89<356:lqtmas>2.0.co;2

Charlton, TR 1987, *The tectonic evolution of the Kolbano-Timor trough accretionary complex, Timor, Indonesia.*, PhD Thesis, University of London.

Charlton, TR 1989, 'Stratigraphic correlation across an arc-continent collision zone: Timor and the Australian Northwest Shelf', *Australian Journal of Earth Sciences,* vol. 36, no. 2, pp. 263-74. Retrieved 7 September 2012, from Scopus database.

Charlton, TR 1991, 'Postcollision extension in arc-continent collision zones, eastern Indonesia', *Geology,* vol. 19, no. 1, pp. 28-31.

Charlton, TR 1997, 'Backthrusting on the BIRPS deep seismic reflection profiles, Banda Arc, Indonesia, a response to changing slab inclination?', *Journal of the Geological Society,* vol. 154, no. 2, pp. 169-72.

Charlton, TR 2001, 'Permo-triassic evolution of gondwanan Eastern Indonesia, and the final mesozoic separation of SE Asia from Australia', *Journal of Asian Earth Sciences,* vol. 19, no. 5, pp. 595-617.

Charlton, TR 2002, 'The Petroleum Potential of East Timor', *APPEA Journal,* vol. 42, pp. 351-69.

Charlton, TR, Barber, AJ & Barkham, ST 1991, 'The structural evolution of the Timor collision complex, eastern Indonesia', *Journal of Structural Geology,* vol. 13, no. 5, pp. 489-500.

Charlton, TR, Barber, AJ, Harris, RA, Barkham, ST, Bird, PR, Archbold, NW, Morris, NJ, Nicoll, RS, Owen, HG, Owens, RM, Sorauf, JE, Taylor, PD, Webster, GD & Whittaker, JE 2002, 'The Permian of Timor: Stratigraphy, palaeontology and palaeogeography', *Journal of Asian Earth Sciences,* vol. 20, no. 6, pp. 719-74.

Charlton, TR, Barber, AJ, McGowan, AJ, Nicoll, RS, Roniewicz, E, Cook, SE, Barkham, ST & Bird, PR 2009, 'The Triassic of Timor: Lithostratigraphy, chronostratigraphy and palaeogeography', *Journal of Asian Earth Sciences,* vol. 36, no. 4-5, pp. 341-63.

Charlton, TR & Suharsono 1990, 'Mesozoic-Tertiary stratigraphy of the Kolbano area, Southern West Timor', *Bulletin of the Geological Research Development Centre,* vol. 14, pp. 38-58.

Charlton, TR & Wall, D 1994, 'New biostratigraphic results from the Kolbano area, southern West Timor: Implications for the Mesozoic-Tertiary stratigraphy of Timor', *Journal of Southeast Asian Earth Sciences,* vol. 9, no. 1-2, pp. 113-22.

Christie-Blick, N & Biddle, KT 1985, 'Deformation and basin formation along strike slip faults', in KT Biddle & N Christie-Blick (eds), *Strike-slip deformation, basin formation, and sedimentation*, Sociey of Economic Paleontologists and Mineralogists, Tulsa, Okla., pp. 1-34.

Chung, S-L, Lee, T-Y, Lo, C-H, Wang, P-L, Chen, C-Y, Yem, NT, Hoa, TT & Genyao, W 1997, 'Intraplate extension prior to continental extrusion along the Ailao Shan-Red River shear zone', *Geology,* vol. 25, no. 4, pp. 311-4. DOI:10.1130/0091-7613(1997)025<0311:ieptce>2.3.co;2

Cina, SE, Yin, A, Grove, M, Dubey, CS, Shukla, DP, Lovera, OM, Kelty, TK, Gehrels, GE & Foster, DA 2009, 'Gangdese arc detritus within the eastern Himalayan Neogene foreland basin: Implications for the Neogene evolution of the Yalu–Brahmaputra River system', *Earth and Planetary Science Letters,* vol. 285, no. 1–2, pp. 150-62. DOI:10.1016/j.epsl.2009.06.005

Clift, P & Vannucchi, P 2004, 'Controls on tectonic accretion versus erosion in subduction zones: Implications for the origin and recycling of the continental crust', *Reviews of Geophysics,* vol. 42, no. 2, p. RG2001. DOI:10.1029/2003rg000127

Clift, PD, Dewey, JF, Draut, AE, Chew, DM, Mange, M & Ryan, PD 2004, 'Rapid tectonic exhumation, detachment faulting and orogenic collapse in the Caledonides of western Ireland', *Tectonophysics,* vol. 384, no. 1-4, pp. 91-113. DOI:10.1016/j.tecto.2004.03.009

Cloos, M 1993, 'Lithospheric buoyancy and collisional orogenesis: Subduction of oceanic plateaus, continental margins, island arcs, spreading ridges, and seamounts', *Geological Society of America Bulletin,* vol. 105, no. 6, pp. 715-37. DOI:10.1130/0016-7606(1993)105<0715:lbacos>2.3.co;2

Cohen, BE, Knesel, KM & Vasconcelos, PM 2011, 'Rapid changes in Australian plate velocity due to collisions in New Guinea and Ontong Java indicated by high resolution $^{40}Ar/^{39}Ar$ geochronology of Australian intraplate volcanoes', in *American Geophysical Union Fall Meeting*, San Francisco

Cook, PJ 1974a, 'Major and trace element geochemistry of sediments from Deep Sea Drilling Project, Leg 27, Sites 259-263, eastern Indian Ocean', *Init. Repts. DSDP,* vol. 27, pp. 481-97.

Cook, PJ 1974b, 'Phosphate content of sediments from Deep Sea Sites 259 to 263, Eastern Indian Ocean', *Init. Repts. DSDP,* vol. 27, pp. 455-61.

Cooks, HE, Zemmels, I & Matti, JC 1974, 'X-ray mineralogy data, eastern Indian Ocean - Leg 27 Deep Sea Drilling Project', *Init. Repts. DSDP,* vol. 27, pp. 535-48. Retrieved 2 February 2012, from Scopus database.

Covey, C & Barron, E 1988, 'The role of ocean heat transport in climatic change', *Earth-Science Reviews,* vol. 24, no. 6, pp. 429-45.

Cowan, HA 1992, *Structure, seismicity and tectonics of the Porters Pass-Amberley Fault Zone, North Canterbury, New Zealand.* , PhD Thesis, University of Canterbury.

Cox, NL 2009, *Variable uplift from Quaternary folding along the northern coast of East Timor, based on U-series age determinations of coral terraces*, MSc Thesis, Brigham Young University.

Cox, SC & Barrell, DJA 2007, 'Geology of the Aoraki area. Institute of Geological and Nuclear Sciences Geological Map 15'. GNS Science, Lower Hutt, New Zealand

Cox, SC, Rutter, HJ, Sims, A, Mangad, M, Weir, JJ, Ezzy, T, White, PA, Horton, TW & Scott, D 2012a, 'Hydrological effects of the M_W7.1 Darfield (Canterbury) earthquake, 4 September 2010, New Zealand', *New Zealand Journal of Geology and Geophysics (Special issue: Canterbury, New Zealand, 2010-2011 earthquake sequence),* vol. 55, no. 3, pp. 231-47.

Cox, SC, Stirling, MW, Herman, F, Gerstenberger, M & Ristau, J 2012b, 'Potentially active faults in the rapidly eroding landscape adjacent to the Alpine Fault, central Southern Alps, New Zealand', *Tectonics,* vol. 31, no. 2. Retrieved 21 May 2012, from Scopus database.

Creaser, R, Erdmer, P, Stevens, R & Grant, S 1997, 'Tectonic affinity of Nisutlin and Anvil assemblage strata from the Teslin tectonic zone, northern Canadian Cordillera: Constraints from neodymium isotope and geochemical evidence', *Tectonics,* vol. 16, pp. 107-21.

Crostella, A 1977, 'Geosynclines and plate tectonics in Banda arcs, eastern Indonesia', *AAPG Bulletin,* vol. 61, no. 12, pp. 2063-81.

Crostella, A & Powell, DE 1975, 'Geology and hydrocarbon prospects of the Timor area', *4th annual convention of the Indonesian Petroleum Association*, BOC of Australia Limited, Jakarta, Indonesia.

Cubrinovski, M, Green, RA, Allen, J, Ashford, S, Bowman, E, Bradley, B, Cox, B, Hutchinson, T, Kavazanjian, E, Orense, R, Pender, M, Quigley, MC & Wotherspoon, L 2010, 'Geotechnical reconnaissance of the 2010 Darfield (Canterbury) earthquake', *Bulletin of the New Zealand Society for Earthquake Engineering,* vol. 43, no. 4, pp. 243-320. Retrieved 19 May 2011, from Scopus database.

Cunningham, WD & Mann, P 2007, 'Tectonics of strike-slip restraining and releasing bends', in D Cunningham & P Mann (eds), *Tectonics of Strike-Slip Restraining and Releasing Bends*, Geological Society of London Special Publication 290, pp. 1-12.

Cutten, HNC 1979, 'Rappahannock Group: late Cenozoic sedimentation and tectonics contemporaneous with Alpine Fault movement (New Zealand)', *New Zealand Journal of Geology & Geophysics,* vol. 32, no. 5, pp. 535-53. Retrieved 29 September 2012, from Scopus database.

Dalmayrac, B & Molnar, P 1981, 'Parallel thrust and normal faulting in Peru and constraints on the state of stress', *Earth and Planetary Science Letters,* vol. 55, no. 3, pp. 473-81. DOI:10.1016/0012-821x(81)90174-6

Davis, D, Suppe, J & Dahlen, FA 1983, 'Mechanics of fold-and- thrust belts and accretionary wedges', *Journal of Geophysical Research,* vol. 88, no. B2, pp. 1153-72.

Davy, B, Stagpoole, V, Barker, D & Yu, J 2012, 'Subsurface structure of the Canterbury region interpreted from gravity and aeromagnetic data', *New Zealand Journal of Geology and Geophysics,* vol. 55, no. 3, pp. 185-91. DOI:10.1080/00288306.2012.690765

de Roever, WP 1940, 'Geological Investigations in the Southwestern Moetis Region (Netherlands Timor). ', in HA Brouwer (ed.), *Geological Expedition of the University of Amsterdam to the Lesser Sunda Islands in the South Eastern Part of the Netherlands East Indies 1937*, vol. 2, N.V. Noord-Hollandsche Uitgevers Maatschappij, Amsterdam, pp. 97-344.

de Roever, WP 1942, 'Olivine-basalts and their alkaline differentiates in the Permian of Timor', in HA Brouwer (ed.), *Geological Expedition of the University of Amsterdam to the Lesser Sunda Islands in the South Eastern Part of the Netherlands East Indies 1937*, vol. 4, N.V. Noord-Hollandsche Uitgevers Maatschappij, Amsterdam, pp. 211-89.

De Smet, MEM, Fortuin, AR, Troelstra, SR, Van Marle, LJ, Karmini, M, Tjokrosapoetro, S & Hadiwasastra, S 1990, 'Detection of collision-related vertical movements in the Outer Banda Arc (Timor, Indonesia), using micropaleontological data', *Journal of Southeast Asian Earth Sciences,* vol. 4, no. 4, pp. 337-56.

de Waard, D 1954, 'Contributions to the geology of Timor, V. Structural development of the crystalline schists in Timor, tectonics of the Lalan Asu Massif', *Indonesian Journal of Natural Sciences,* vol. 110, pp. 143-53.

de Waard, D 1956, 'Geology of a N-S section across western Timor', *Indonesian Journal of Natural Sciences,* vol. 112, pp. 101-14.

Dean, WE 1974, 'Determination of carbonate and organic matter in calcareous sediments and sedimentary rocks by loss on ignition: Comparison with other methods', *Journal of Sedimentary Petrology,* vol. 44, pp. 242-8. Retrieved 24 January 2012, from Scopus database.

DeCelles, PG, Gehrels, GE, Najman, Y, Martin, AJ, Carter, A & Garzanti, E 2004, 'Detrital geochronology and geochemistry of Cretaceous-Early Miocene strata of Nepal: implications

for timing and diachroneity of initial Himalayan orogenesis', *Earth and Planetary Science Letters,* vol. 227, pp. 313-30.

DeCelles, PG, Gehrels, GE, Quade, J, Ojha, TP, Kapp, PA & Upreti, BN 1998, 'Neogene foreland basin deposits, erosional unroofing, and the kinematic history of the Himalayan fold-thrust belt, western Nepal', *Geological Society of America Bulletin,* vol. 110, no. 1, pp. 2-21. DOI:10.1130/0016-7606(1998)110<0002:nfbdeu>2.3.co;2

DeMets, C, Gordon, RG & Argus, DF 2010, 'Geologically current plate motions', *Geophysical Journal International,* vol. 181, no. 1, pp. 1-80. Retrieved 8 June 2011, from Scopus database.

DeMets, C, Gordon, RG, Argus, DF & Stein, S 1994, 'Effect of recent revisions to the geomagnetic reversal time scale on estimates of current plate motions', *Geophysical Research Letters,* vol. 21, no. 20, pp. 2191-4.

Demirkesen, AC 2008, 'Digital terrain analysis using Landsat-7 ETM+ imagery and SRTM DEM: A case study of Nevsehir province (Cappadocia), Turkey', *International Journal of Remote Sensing,* vol. 29, no. 14, pp. 4173-88.

Devès, M, King, GCP, Klinger, Y & Agnon, A 2011, 'Localised and distributed deformation in the lithosphere: Modelling the Dead Sea region in 3 dimensions', *Earth and Planetary Science Letters,* vol. 308, no. 1-2, pp. 172-84. Retrieved 4 September 2011, from Scopus database.

Dewey, J & Mange, M 2000, 'Petrography of Ordovician and Silurian sediments in the western irish Caledonides: Tracers of a short-lived Ordovician continent-arc collision orogeny and the evolution of the Laurentian Appalachian-Caledonian margin', vol. 164, pp. 55-107

Dewey, JF 1988, 'Extensional collapse of orogens', *Tectonics,* vol. 7, no. 6, pp. 1123-39. DOI:10.1029/TC007i006p01123

Dewey, JF 2005, 'Orogeny can be very short', *Proceedings of the National Academy of Sciences of the United States of America,* vol. 102, no. 43, pp. 15286-93. DOI:10.1073/pnas.0505516102

Di Celma, C 2011, 'Sedimentology, architecture, and depositional evolution of a coarse-grained submarine canyonfill from the Gelasian (early Pleistocene) of the Peri-Adriatic basin, Offida, central Italy', *Sedimentary Geology,* vol. 238, pp. 233-53.

Dixon, JF, Steel, RJ & Olariu, C 2012, 'River-dominated, shelf-edge deltas: delivery of sand across the shelf break in the absence of slope incision', *Sedimentology,* vol. 59, no. 4, pp. 1133-57. DOI:10.1111/j.1365-3091.2011.01298.x

Dodson, M 2009, *Active tectonics, geomorphology and groundwater recharge to the Waipara-Kowai Zone, North Canterbury*, MSc Thesis, University of Canterbury.

Dominguez, S, Lallemand, SE & Malavieille, J 1998, 'Upper plate deformation associated with seamount subduction', *Tectonophysics,* vol. 293, pp. 207-24.

Dominguez, S, Malavieille, J & Lallemand, SE 2000, 'Deformation of accretionary wedges in response to seamount subduction: insights from sandbox experiments', *Tectonics,* vol. 19, no. 1, pp. 182-96.

Dorn, C, Green, AG, Jongens, R, Carpentier, S, Kaiser, AE, Campbell, F, Horstmeyer, H, Campbell, J, Finnemore, M & Pettinga, J 2010, 'High-resolution seismic images of potentially seismogenic structures beneath the northwest Canterbury Plains, New Zealand', *Journal of Geophysical Research B: Solid Earth,* vol. 115, no. 11. Retrieved 12 January 2011, from Scopus database. DOI:10.1029/2010JB007459

Downes, G & Yetton, M 2012, 'Pre-2010 historical seismicity near Christchurch, New Zealand: the 1869 M W 4.7–4.9 Christchurch and 1870 M W 5.6–5.8 Lake Ellesmere earthquakes', *New Zealand Journal of Geology and Geophysics,* vol. 55, no. 3, pp. 199-205. DOI:10.1080/00288306.2012.690767

Duerto, L & McClay, K 2011, 'Role of the shale tectonics on the evolution of the Eastern Venezuelan Cenozoic thrust and fold belt', *Marine and Petroleum Geology,* vol. 28, no. 1, pp. 81-108. DOI:10.1016/j.marpetgeo.2009.11.005

Duffy, B 2011, 'The Canterbury Earthquake Sequence: Implications for surveyors', in *Annual conference of the Institute of Cadastral Surveyors of New Zealand*. NZICS, Christchurch, New Zealand

Duffy, B 2012, 'Tectonics, earthquakes, geomorphology and surveyors', in *Annual conference of the Institute of Cadastral Surveyors of New Zealand*. NZICS, Christchurch, New Zealand

Duffy, B, McInnes, C, Van Dissen, R, Litchfield, N, Barrell, D, Quigley, MC, Bilderback, E & Stahl, T 2011a, 'Kinematics of the Greendale Fault releasing bend: Insights from cadastral and multi-temporal LiDAR surveys', in *IUGG General Assembly - Earth on the Edge: Science for a Sustainable Planet*, Melbourne, Australia

Duffy, B, McInnes, C, Van Dissen, R, Litchfield, N, Barrell, D, Quigley, MC, Bilderback, E, Stahl, T & Carson, N 2011b, 'Tectonic geomorphology, river avulsion and fault kinematics at the releasing termination of the strike slip Greendale Fault, Canterbury, New Zealand', *Australia New Zealand Geomorphology Group*, Oamaru, New Zealand.

Duffy, B & Quigley, MC 2010, 'Extension at a collision-subduction transition: New insights from Timor', *Geoscience Society of New Zealand Miscellaneous Publication 129A*, eds. JD Eccles, MR Grigor, PWO Hoskin & DCH Hikuroa, Auckland, New Zealand, p. 89.

Duffy, B, Quigley, MC, Barrell, D, Van Dissen, R, Stahl, T, Leprince, S, McInnes, C & Bilderback, E 2013, 'Fault kinematics and surface deformation across a releasing bend during the 2010 M_W 7.1 Darfield, New Zealand, earthquake revealed by differential LiDAR and cadastral surveying', *GSA Bulletin,* vol. 125, no. 3-4, pp. 420-31. DOI:10.1130/B30753.1

Duffy, B, Quigley, MC, Haig, DW & Bassett, K 2009, 'Indonesian Geodynamics and Paleoceanography revealed in an exhumed Pliocene Forearc Basin, Timor Leste', *Geosciences 09*, eds. DJA Barrell & AJ Tulloch, Geological Society of New Zealand Miscellaneous Publication 128A, Oamaru, New Zealand, p. 62.

Duffy, B, Quigley, MC, Nguyen, N & Shulmeister, J 2011c, 'The rise and fall of an arc-continent collisional orogen: insights from synorogenic sediments in Timor Leste', *AGU Fall Meeting*.

Duffy, B, Quigley, MC & Ring, U (accepted manuscript), 'Arc-parallel extrusion of the Timor sector of the Banda arc-continent collision', *Tectonics*.

Duffy, B, Van Dissen, R, Quigley, MC, Litchfield, N, McInnes, C, Leprince, S, Barrell, D, Stahl, T & Bilderback, E 2011d, 'Co-seismic displacements from differencing and sub-pixel correlation of multi-temporal LiDAR and cadastral surveys: application to the Greendale Fault, Canterbury, New Zealand (Invited paper EP51E-04)', *2011 Fall Meeting, AGU*, San Francisco, California.

Duman, TY, Emre, O, Dogan, A & Ozalp, S 2005, 'Step-over and bend structures along the 1999 Duzce earthquake surface rupture, North Anatolian Fault, Turkey', *Bulletin of the Seismological Society of America,* vol. 95, no. 4, pp. 1250-62. DOI:10.1785/0120040082

Dutcher, LC & Garrett, AA 1963, 'Geological and hydrologic features of San Bernardino area, California, with special reference to underflow across the San Jacinto fault', *US Geological Survey Water Supply Paper,* vol. 1419. Retrieved 7 February 2012, from Scopus database.

Earle, MM 1980, *A Study of Boi and Mollo, Two Metamorphic Massifs on Timor, Eastern Indonesia*, PhD Thesis, University of London.

Earle, MM 1981, 'The metamorphic rocks of Boi, Timor, eastern Indonesia', in AJ Barber & S Wiryosujono (eds), *The Geology and Tectonics of Eastern Indonesia*, vol. 2, GRDC Spec. Pub, pp. 239-51.

Earle, MM 1983, 'Continental margin origin for cretaceous radiolarian chert in western Timor', *Nature,* vol. 305, pp. 129-30.

Eberhart-Phillips, D, Haeussler, PJ, Freymueller, JT, Frankel, AD, Rubin, CM, Craw, P, Ratchkovski, NA, Anderson, G, Carver, GA, Crone, AJ, Dawson, TE, Fletcher, H, Hansen, R, Harp, EL, Harris, RA, Hill, DP, Hreinsdóttir, S, Jibson, RW, Jones, LM, Kayen, R, Keefer, DK, Larsen, CF, Moran, SC, Personius, SF, Plafker, G, Sherrod, B, Sieh, K, Sitar, N & Wallace, WK 2003, 'The 2002 Denali

Fault earthquake, Alaska: A large magnitude, slip-partitioned event', *Science,* vol. 300, no. 5622, pp. 1113-8.

Ekström, G, Dziewonski, A, Maternovskaya, N & Nettles, M 2009, 'Global Centroid Moment Tensor Catalog'. http://www.globalcmt.org/, 11 December 2009

Elburg, MA, Foden, JD, van Bergen, MJ & Zulkarnain, I 2005, 'Australia and Indonesia in collision: Geochemical sources of magmatism', *Journal of Volcanology and Geothermal Research,* vol. 140, no. 1-3, pp. 25-47. Retrieved 6 July 2012, from Scopus database.

Elliott, AJ, Dolan, JF & Oglesby, DD 2009, 'Evidence from coseismic slip gradients for dynamic control on rupture propagation and arrest through stepovers', *Journal of Geophysical Research - Solid Earth,* vol. 114, no. B2, p. B02313. DOI:10.1029/2008jb005969

Elliott, JR, Nissen, EK, England, PC, Jackson, JA, Lamb, S, Li, Z, Oehlers, M & Parsons, B 2012, 'Slip in the 2010 and 2011 Canterbury earthquakes, New Zealand', *Journal of Geophysical Research,* vol. 117, no. B3, p. B03401. DOI:10.1029/2011jb008868

Ely, KS 2009, *Geochronology of Timor-Leste and seismo-tectonics of the southern Banda Arc*, PhD Thesis, The University of Melbourne.

Ely, KS & Sandiford, M 2010, 'Seismic response to slab rupture and variation in lithospheric structure beneath the Savu Sea, Indonesia', *Tectonophysics,* vol. 483, no. 1-2, pp. 112-24.

Ely, KS, Sandiford, M, Hawke, ML, Phillips, D, Quigley, MC & Reis, JEd 2011, 'Evolution of Ataúro Island: Temporal constraints on subduction processes beneath the Wetar zone, Banda Arc', *Journal of Asian Earth Sciences,* vol. 41, no. 6, pp. 477-93. DOI:10.1016/j.jseaes.2011.01.019

England, P & Houseman, G 1989, 'Extension during continental convergence, with application to the Tibetan Plateau', *Journal of Geophysical research,* vol. 94, no. B12. Retrieved 2 February 2011, from Scopus database.

England, P & Molnar, P 1993, 'Cause and effect among thrust and normal faulting, anatectic melting and exhumation in the Himalaya', in T P.J. & S M.P. (eds), *Himalyan tectonics*, Geological Society Special Publication 74, London, pp. 401-11.

Environment Canterbury 2011, *Well cards*, Environment Canterbury, Christchurch, New Zealand, 7 May 2011. Retrieved 16 Aug 2011, from http://ecan.govt.nz/services/online-services/tools-calculators/pages/well-card.aspx

Escalona, A & Mann, P 2011, 'Tectonics, basin subsidence mechanisms, and paleogeography of the Caribbean-South American plate boundary zone', *Marine and Petroleum Geology,* vol. 28, no. 1, pp. 8-39. Retrieved 6 June 2012, from Scopus database.

Evans, JA, Zalasiewicz, JA & Chopey-Jones, A 2009, 'Facies effects on the behaviour of Nd and Sr isotope systems in turbidite mudrocks during diagenesis', *Sedimentology,* vol. 56, no. 4, pp. 863-72. DOI:10.1111/j.1365-3091.2008.01001.x

Falloon, T, Berry, RF, Robinson, P & Stolz, AJ 2006, 'Whole-rock geochemistry of the Hili Manu peridotite, East Timor: Implications for the origin of Timor ophiolites', *Australian Journal of Earth Sciences,* vol. 53, no. 4, pp. 637-49.

Fedo, CM, Nesbitt, HW & Young, GM 1995, 'Unravelling the effects of potassium metasomatism in sedimentary rocks and paleosols, with implications for paleoweathering conditions and provenance', *Geology,* vol. 23, no. 10, pp. 921-4. Retrieved 12 April 2012, from Scopus database.

Fergusson, CL, Cas, RAF & Stewart, IR 1989, 'Ordovician turbidites of the Hotham Group, eastern Victoria: Sedimentation in deep-marine channel-levee complexes', *Australian Journal of Earth Sciences,* vol. 36, no. 1, pp. 1-12. DOI:10.1080/14400958908527947

Ferranti, L, Oldow, JS & Sacchi, M 1996, 'Pre-Quaternary orogen-parallel extension in the Southern Apennine belt, Italy', *Tectonophysics,* vol. 260, pp. 325-47.

Ferrill, DA, Stamatakos, JA & Sims, D 1999, 'Normal fault corrugation: Implications for growth and seismicity of active normal faults', *Journal of Structural Geology,* vol. 21, no. 8-9, pp. 1027-38. Retrieved 21 August 2011, from Scopus database.

Finnemore, M 2004, *The application of seismic reflection surveying to the characterisation of aquifer geometry and related active tectonic deformation, North Canterbury*, Ph.D Thesis, University of Canterbury.

Fleury, J-M, Pubellier, M & de Urreiztieta, M 2009, 'Structural expression of forearc crust uplift due to subducting asperity', *Lithos,* vol. 113, no. 1-2, pp. 318-30.

Florinsky, IV 1996, 'Quantitative topographic method of fault morphology recognition', *Geomorphology,* vol. 16, pp. 103-19.

Floyd, PA, Leveridge, BE, Franke, W, Shail, R & Dörr, W 1990, 'Provenance and depositional environment of Rhenohercynian synorogenic greywackes from the Giessen Nappe, Germany', *Geologische Rundschau,* vol. 79, no. 3, pp. 611-26. DOI:10.1007/bf01879205

Forsyth, PJ, Barrell, DJA & Jongens, R 2008, 'Geology of the Christchurch area. Institute of Geological and Nuclear Sciences Geological Map 16'. GNS Science, Lower Hutt, New Zealand, p. 1 sheet + 67 p

Fortuin, AR, van der Werff, W & Wensink, H 1997, 'Neogene basin history and paleomagnetism of a rifted and inverted forearc region, on- and offshore Sumba, Eastern Indonesia', *Journal of Asian Earth Sciences,* vol. 15, pp. 61-88.

Frisch, W, Kuhlemann, J, Dunkl, I & Brügel, A 1998, 'Palinspastic reconstruction and topographic evolution of the Eastern Alps during late Tertiary tectonic extrusion', *Tectonophysics,* vol. 297, no. 1-4, pp. 1-15.

Gageonnet, R & Lemoine, M 1958, *Contribution à la connaissance de la géologie de la province Portugaise de Timor*, Lisboa,.

Gallagher, SJ, Wallace, MW, Li, CL, Kinna, B, Bye, JT, Akimoto, K & Torii, M 2009, 'Neogene history of the West Pacific Warm Pool, Kuroshio and Leeuwin currents', *Paleoceanography,* vol. 24. Review

Galloway, WE 1998, 'Siliciclastic Slope and Base-of-Slope Depositional Systems: Component Facies, Stratigraphic Architecture, and Classification', *AAPG Bulletin,* vol. 82, no. 4, pp. 569-95. Retrieved 29 September 2012, from Scopus database.

Ganas, A, Pavlides, S & Karastathis, V 2005, 'DEM-based morphometry of range-front escarpments in Attica, central Greece, and its relation to fault slip rates', *Geomorphology,* vol. 65, no. 3-4, pp. 301-19.

Gapais, D 1989, 'Shear structures within deformed granites: mechanical and thermal indicators', *Geology,* vol. 17, no. 12, pp. 1144-7. Retrieved 16 October 2012, from Scopus database.

Gasperi, JT & Kennett, JP 1993, 'Vertical thermal structure evolution of Miocene surface waters: Western equatorial Pacific DSDP Site 289', *Marine Micropaleontology,* vol. 22, no. 3, pp. 235-54. Scopus database.

Genrich, JF, Bock, Y & Mason, RG 1997, 'Crustal deformation across the Imperial Fault: Results from kinematic GPS surveys and trilateration of a densely spaced, small-aperture network', *Journal of Geophysical Research B: Solid Earth,* vol. 102, no. B3, pp. 4985-5004.

Genrich, JF, Bock, Y, McCaffrey, R, Calais, E, Stevens, CW & Subarya, C 1996, 'Accretion of the southern banda arc to the Australian plate margin determined by global positioning system measurements', *Tectonics,* vol. 15, no. 2, pp. 288-95.

Georgiopoulou, A, Wynn, RB, Masson, DG & Frenz, M 2009, 'Linked turbidite–debrite resulting from recent Sahara Slide headwall reactivation', *Marine and Petroleum Geology,* vol. 26, no. 10, pp. 2021-31. DOI:10.1016/j.marpetgeo.2009.02.013

Getaneh, W 2002, 'Geochemistry provenance and depositional tectonic setting of the Adigrat Sandstone northern Ethiopia', *Journal of African Earth Sciences,* vol. 35, no. 2, pp. 185-98.

Ghisetti, FC & Sibson, RH 2012, 'Compressional reactivation of E–W inherited normal faults in the area of the 2010–2011 Canterbury earthquake sequence', *New Zealand Journal of Geology and Geophysics,* vol. 55, no. 3, pp. 177-84. DOI:10.1080/00288306.2012.674048

Giles, KA & Lawton, TF 2002, 'Halokinetic sequence stratigraphy adjacent to the El Papalote diapir, northeastern Mexico', *American Association of Petroleum Geologists Bulletin,* vol. 86, no. 5, pp. 823-40.

Gingele, FX, De Deckker, P & Hillenbrand, C-D 2001, 'Clay mineral distribution in surface sediments between Indonesia and NW Australia -- source and transport by ocean currents', *Marine Geology,* vol. 179, no. 3-4, pp. 135-46.

Gledhill, K, Ristau, J, Reyners, M, Fry, B & Holden, C 2011, 'The Darfield (Canterbury, New Zealand) Mw 7.1 earthquake of September 2010: a preliminary seismological report', *Seismological Research Letters,* vol. 82, pp. 378-86.

Gledhill, K, Ristau, J, Reyners, M, Fry, B, Holden, C & GeoNet-Team 2010, 'The Darfield (Canterbury) earthquake of September 2010: Preliminary seismological report', *Bulletin of the New Zealand Society for Earthquake Engineering,* vol. 43, no. 4, pp. 215-21.

Goldfinger, C, Nelson, CH & Johnson, JE 2003a, 'Deep-water turbidites as Holocene earthquake proxies: The Cascadia subduction zone and Northern San Andreas Fault systems', *Annals of Geophysics,* vol. 46, no. 5, pp. 1169-94.

Goldfinger, C, Nelson, CH & Johnson, JE 2003b, 'Holocene earthquake records from the Cascadia subduction zone and northern San Andreas fault based on precise dating of offshore turbidites', in *Annual Review of Earth and Planetary Sciences*, vol. 31, pp. 555-77

Goldstein, S, O'Nions, R & Hamilton, P 1984, 'A Sm-Nd isotopic study of atmospheric dusts and particulates from major river systems', *Earth and Planetary Science Letters,* vol. 70, pp. 221-36.

Gordon, AL & Fine, RA 1996, 'Pathways of water between the Pacific and Indian oceans in the Indonesian seas', *Nature,* vol. 379, no. 6561, p. 146.

Gordon, AL, Giulivi, CF & Ilahude, AG 2003a, 'Deep topographic barriers within the Indonesian seas', *Deep-Sea Research Part II: Topical Studies in Oceanography,* vol. 50, no. 12-13, pp. 2205-28.

Gordon, AL & McClean, JL 1999, 'Thermohaline stratification of the Indonesian Seas: Model and observations', *Journal of Physical Oceanography,* vol. 29, no. 2, pp. 198-216.

Gordon, AL, Susanto, RD & Vranes, K 2003b, 'Cool Indonesian throughflow as a consequence of restricted surface layer flow', *Nature,* vol. 425, no. 6960, pp. 824-8.

Gorney, D, Escalona, A, Mann, P, Magnani, MB & Group, BS 2007, 'Chronology of Cenozoic tectonic events in western Venezuela and the Leeward Antilles based on integration of offshore seismic reflection data and on-land geology', *AAPG Bulletin,* vol. 91, no. 5, pp. 653-84. DOI:10.1306/11280606002

Gourlan, AT, Meynadier, L & Allegre, CJ 2008, 'Tectonically driven changes in the Indian Ocean circulation over the last 25 Ma: Neodymium isotope evidence', *Earth and Planetary Science Letters,* vol. 267, no. 1-2, pp. 353-64.

Grady, AE & Berry, RF 1977, 'Some Palaeozoic-Mesozoic stratigraphic-structural relationships in East Timor and their significance to the tectonics of Timor', *Journal of the Geological Society of Australia,* vol. 24, pp. 203-14.

Grunau, HR 1953, 'Zur Geologie von Portugiesisch-Ost-Timor', *Eclogae Geologicae Helvetica,* vol. 46, pp. 29-37.

Grunau, HR 1956, 'Zur Geologie von Portugiesisch-Ost-Timor - review'. Mitteilungen der Naturforshcenden Gesellschaft, Bern

Guccione, MJ, Mueller, K, Champion, J, Shepherd, S, Carlson, SD, Odhiambo, B & Tate, A 2002, 'Stream response to repeated coseismic folding, Tiptonville Dome, New Madrid Seismic Zone', *Geomorphology,* vol. 43, pp. 313-49.

Gustafson, JK 1946, 'Two occurrences of chloritoid as a hydrothermal mineral in igneous rocks', *American Mineralogist,* vol. 31, pp. 313-6.

Haeussler, PJ, Schwartz, DP, Dawson, TE, Stenner, HD, Lienkaemper, JJ, Sherrod, B, Cinti, FR, Montone, P, Craw, PA, Crone, AJ & Personius, SF 2004, 'Surface Rupture and Slip Distribution

of the Denali and Totschunda Faults in the 3 November 2002 M_W 7.9 Earthquake, Alaska', *Bulletin of the Seismological Society of America,* vol. 94, no. 6B, pp. S23-52. DOI:10.1785/0120040626

Haig, DW 2012, 'Palaeobathymetric gradients across Timor during 5.7-3.3Ma (latest Miocene-Pliocene) and implications for collision uplift', *Palaeogeography, Palaeoclimatology, Palaeoecology,* vol. 331-332, pp. 50-9. Retrieved 3 May 2012, from Scopus database.

Haig, DW & McCartain, E 2007, 'Carbonate pelagites in the post-Gondwana succession (Cretaceous - Neogene) of East Timor', *Australian Journal of Earth Sciences,* vol. 54, no. 6, pp. 875-97.

Haig, DW, McCartain, E, Barber, L & Backhouse, J 2007, 'Triassic-lower Jurassic foraminiferal indices for bahaman-type carbonate-bank limestones, Cablac Mountain, East Timor', *Journal of Foraminiferal Research,* vol. 37, no. 3, pp. 248-64.

Haig, DW, McCartain, E, Keep, M & Barber, L 2008, 'Re-evaluation of the Cablac Limestone at its type area, East Timor: Revision of the Miocene stratigraphy of Timor', *Journal of Asian Earth Sciences,* vol. 33, no. 5-6, pp. 366-78.

Halferdahl, LB 1961, 'Chloritoid: Its composition, x-ray and optical properties, stability, and occurrence', *Journal of Petrology,* vol. 2, no. 1, pp. 49-135. Retrieved 9 October 2012, from Scopus database.

Hall, R 2002, 'Cenozoic geological and plate tectonic evolution of SE Asia and the SW Pacific: computer-based reconstructions, model and animations', *Journal of Asian Earth Sciences,* vol. 20, pp. 353-431.

Hall, R 2009, 'Southeast Asia's changing palaeogeography', *Blumea: Journal of Plant Taxonomy and Plant Geography,* vol. 54, no. 1-3, pp. 148-61. Retrieved 23 October 2012, from Scopus database.

Hall, R 2011, 'Australia-SE Asia collision: Plate tectonics and crustal flow', in R Hall, MA Cottam & MEJ Wilson (eds), *The SE Asian Gateway: History and Tectonics of the Australia-Asia Collision*, Geological Society Special Publication 355, London, pp. 75-109.

Hall, R 2012, 'Late Jurassic–Cenozoic reconstructions of the Indonesian region and the Indian Ocean', *Tectonophysics,* vol. 570–571, no. 0, pp. 1-41. DOI:10.1016/j.tecto.2012.04.021

Hall, R, Cloke, IR, Nur'aini, S, Puspita, SD, Calvert, SJ & Elders, CF 2009, 'The North Makassar Straits: What lies beneath?', *Petroleum Geoscience,* vol. 15, no. 2, pp. 147-58. Retrieved 23 October 2012, from Scopus database.

Hall, R & Sevastjanova, I 2012, 'Australian crust in Indonesia', *Australian Journal of Earth Sciences,* vol. 59, no. 6, pp. 827-44. Retrieved 30 October 2012, from Scopus database.

Hall, R & Wilson, MEJ 2000, 'Neogene sutures in eastern Indonesia', *Journal of Asian Earth Sciences,* vol. 18, no. 6, pp. 781-808.

Hantoro, WS, Pirazzoli, PA, Jouannic, C, Faure, H, Hoang, CT, Radtke, U, Causse, C, Best, MB, Lafont, R, Bieda, S & Lambeck, K 1994, 'Quaternary uplifted coral reef terraces on Alor Island, East Indonesia', *Coral Reefs,* vol. 13, no. 4, pp. 215-23. Retrieved 20 June 2011, from Scopus database.

Harris, RA 1991, 'Temporal distribution of strain in the active Banda orogen: a reconciliation of rival hypotheses', *Journal of Southeast Asian Earth Sciences,* vol. 6, no. 3-4, pp. 373-86.

Harris, RA 1992, 'Peri-collisional extension and the formation of Oman-type ophiolites in the Banda arc and Brooks Range', *Ophiolites and their modern oceanic analogues*, pp. 301-25.

Harris, RA 2006, 'Rise and fall of the Eastern Great Indonesian arc recorded by the assembly, dispersion and accretion of the Banda Terrane, Timor', *Gondwana Research,* vol. 10, no. 3-4, pp. 207-31.

Harris, RA 2011, 'The Nature of the Banda Arc–Continent Collision in the Timor Region', in D Brown & PD Ryan (eds), *Arc-Continent Collision*, vol. 1, Springer Heidelberg, Berlin, pp. 163-211.

Harris, RA, Kaiser, J, Hurford, A & Carter, A 2000, 'Thermal history of Australian passive margin cover sequences accreted to Timor during Late Neogene arc-continent collision, Indonesia', *Journal of Asian Earth Sciences,* vol. 18, no. 1, pp. 47-69.

Harris, RA & Long, T 2000, 'The Timor ophiolite, Indonesia: Model or myth?', in Y Dilek, E Moores, D Elthon & A Nicolas (eds), *Ophiolites and Oceanic Crust: New Insights from Field Studies and the Ocean Drilling Program*, Geological Society of America Special Paper 349, pp. 321-30.

Harris, RA, Sawyer, RK & Audley-Charles, MG 1998, 'Collisional melange development: geologic associations of active melange-forming processes with exhumed melange facies in the western Banda orogen, Indonesia', *Tectonics,* vol. 17, no. 3, pp. 458-79.

Harris, RA, Vorkink, MW, Prasetyadi, C, Zobell, E, Roosmawati, N & Apthorpe, M 2009, 'Transition from subduction to arc-continent collision: Geologic and neotectonic evolution of Savu Island, Indonesia', *Geosphere,* vol. 5, pp. 152-71.

Hart, EW & Bryant, WA 1997, 'Fault Rupture Hazard Zones in California: Alquist-Priolo Earthquake Fault Zoning Act with Index to Earthquake Fault Zones Maps'. Californian Department of Conservation, Division of Mines and Geology, p. 47

Hartleb, RD, Dolan, JF, Akyüz, HS, Dawson, TE, Tucker, AZ, Yerli, B, Rockwell, TK, Toraman, E, Çakir, Z, Dikba, A & Altunel, E 2002, 'Surface rupture and slip distribution along the Karadere segment of the 17 August 1999 İzmit and the western section of the 12 November 1999 Düzce, Turkey, earthquakes', *Bulletin of the Seismological Society of America,* vol. 92, no. 1, pp. 67-78. Retrieved 14 October 2012, from Scopus database.

Hartz, EH & Andresen, A 1997, 'From collision to collapse: Complex strain permutations in the hinterland of the Scandinavian Caledonides', *J. Geophys. Res.,* vol. 102, no. B11, pp. 24697-711. DOI:10.1029/97jb02275

Haug, GH & Tiedemann, R 1998, 'Effect of the formation of the isthmus of panama on atlantic ocean thermohaline circulation', *Nature,* vol. 393, no. 6686, pp. 673-6.

Hay, WW 1996, 'Tectonics and climate', *Geologische Rundschau,* vol. 85, no. 3, pp. 409-37.

Hein, FJ & Walker, RG 1982, 'The Cambro-Ordovician Cap Enragé Formation, Québec, Canada: conglomeratic deposits of a braided submarine channel with terraces', *Sedimentology,* vol. 29, no. 3, pp. 309-52. DOI:10.1111/j.1365-3091.1982.tb01798.x

Heirtzler, JR, Veevers, JJ, Bolli, HM, Carter, AN, Cook, PJ, Krasheninnikov, V, McKnight, BK, Proto-Decima, F, Renz, GW, Robinson, PT, Rocker(Jr), K & Thayer, PA 1974, 'Site 262', *Initial Reports on the Deep Sea Drilling Project 27*, pp. 193-278.

Herrington, RJ, Scotney, PM, Roberts, S, Boyce, AJ & Harrison, D 2011, 'Temporal association of arc-continent collision, progressive magma contamination in arc volcanism and formation of gold-rich massive sulphide deposits on Wetar Island (Banda arc)', *Gondwana Research,* vol. 19, no. 3, pp. 583-93. DOI:10.1016/j.gr.2010.10.011

Hinschberger, F, Malod, J-A, Dyment, J, Honthaas, C, Rehault, J-P & Burhanuddin, S 2001, 'Magnetic lineations constraints for the back-arc opening of the late Neogene South Banda Basin (eastern Indonesia)', *Tectonophysics,* vol. 333, pp. 47-59.

Hinschberger, F, Malod, JA, Réhault, JP, Villeneuve, M, Royer, JY & Burhanuddin, S 2005, 'Late Cenozoic geodynamic evolution of eastern Indonesia', *Tectonophysics,* vol. 404, no. 1-2, pp. 91-118.

Hiscott, RN 1984, 'Ophiolitic source rocks for Taconic-age flysch: trace-element evidence', *Geological Society of America Bulletin,* vol. 95, no. 11, pp. 1261-7. Retrieved 27 September 2012, from Scopus database.

Holbrook, J & Schumm, SA 1999, 'Geomorphic and sedimentary response of rivers to tectonic deformation: A brief review and critique of a tool for recognizing subtle epeirogenic deformation in modern and ancient settings', *Tectonophysics,* vol. 305, no. 1-3, pp. 287-306. Retrieved 3 May 2011, from Scopus database.

Holden, C, Beavan, J, Fry, B, Reyners, M, Ristau, J, Van Dissen, R, Villamor, P & Quigley, MC 2011, 'Preliminary source model of the M_W 7.1 Darfield earthquake from geological, geodetic and seismic data', *Ninth Pacific Conference on Earthquake Engineering, Building an Earthquake-Resilient Society, Paper 164, 7 p.* , New Zealand Society for Earthquake Engineering, Auckland, New Zealand.

Hong, E 1997, 'Evolution of Pliocene to Pleistocene sedimentary environments in an arc-continent collision zone: evidence from the analyses of lithofacies and ichnofacies in the southwestern foothills of Taiwan', *Journal of Asian Earth Sciences,* vol. 15, no. 4-5, pp. 381-92. DOI:10.1016/s1367-9120(97)00022-9

Honthaas, C, Réhault, JP, Maury, RC, Bellon, H, Hémond, C, Malod, JA, Cornée, JJ, Villeneuve, M, Cotten, J, Burhanuddin, S, Guillou, H & Arnaud, N 1998, 'A Neogene back-arc origin for the Banda Sea basins: Geochemical and geochronological constraints from the Banda ridges (East Indonesia)', *Tectonophysics,* vol. 298, no. 4, pp. 297-317.

Hooper, DM, Bursik, MI & Webb, FH 2003, 'Application of high-resolution, interferometric DEMs to geomorphic studies of fault scarps, Fish Lake Valley, Nevada-California, USA', *Remote Sensing of Environment,* vol. 84, no. 2, pp. 255-67. Retrieved 4 March 2012, from Scopus database.

Hopper, RW 1942, 'Nederlandsche Pacific Petroleum Maatschappij preliminary reconnoissance report ', *Netherlands Pacific Petroleum Company (unpublished report)*.

Howard, M, Nicol, A, Campbell, J & Pettinga, J 2005, 'Holocene paleoearthquakes on the strike-slip Porters Pass Fault, Canterbury, New Zealand', *New Zealand Journal of Geology & Geophysics,* vol. 48, pp. 59-74

Hu, JC, Hou, CS, Shen, LC, Chan, YC, Chen, RF, Huang, C, Rau, RJ, Chen, KHH, Lin, CW, Huang, MH & Nien, PF 2007, 'Fault activity and lateral extrusion inferred from velocity field revealed by GPS measurements in the Pingtung area of southwestern Taiwan', *Journal of Asian Earth Sciences,* vol. 31, no. 3, pp. 287-302. Retrieved 11 July 2012, from Scopus database.

Hubbard, SM, de Ruig, MJ & Graham, SA 2009, 'Confined channel-levee complex development in an elongate depo-center: Deep-water Tertiary strata of the Austrian Molasse basin', *Marine and Petroleum Geology,* vol. 26, no. 1, pp. 85-112. DOI:10.1016/j.marpetgeo.2007.11.006

Hudnut, KW, Borsa, A, Glennie, C & Minster, J-B 2002, 'High-Resolution topography along surface rupture of the 16 October 1999 Hector Mine, California, Earthquake (M_W 7.1) from airborne laser swath mapping', *Bulletin of the Seismological Society of America,* vol. 92, no. 4, pp. 1570-6.

Ilahude, AG & Gordon, AL 1996, 'Thermocline stratification within the Indonesian Seas', *Journal of Geophysical research,* vol. 101, pp. 12401-9.

Jackson, J & Leeder, M 1994, 'Drainage systems and the development of normal faults: an example from Pleasant Valley, Nevada', *Journal of Structural Geology,* vol. 16, pp. 1041-59.

Jain, V & Sinha, R 2004, 'Fluvial dynamics of an anabranching river system in Himalayan foreland basin, Baghmati river, north Bihar plains, India', *Geomorphology,* vol. 60, no. 1-2, pp. 147-70. Retrieved 3 February 2011, from Scopus database.

Jain, V & Sinha, R 2005, 'Response of active tectonics on the alluvial Baghmati River, Himalayan foreland basin, eastern India', *Geomorphology,* vol. 70, no. 3-4 SPEC. ISS., pp. 339-56.

Jamieson, RA & Beaumont, C 2011, 'Coeval thrusting and extension during lower crustal ductile flow - implications for exhumation of high-grade metamorphic rocks', *Journal of Metamorphic Geology,* vol. 29, no. 1, pp. 33-51. Retrieved 30 October 2012, from Scopus database.

Jarvis, A, Reuter, HI, Nelson, A & Guevara, E 2008, *Hole-filled seamless SRTM data V4.1* International Centre for Tropical Agriculture (CIAT), available from http://srtm.csi.cgiar.org. Retrieved 30 January 2009,

Johnston, CR & Bowin, CO 1981, 'Crustal reactions resulting from the mid-Pliocene to Recent continent-island arc collision in the Timor Region', *BMR Journal of Australian Geology and Geophysics,* vol. 6, pp. 223-43.

Jones, CE, Halliday, AN, Rea, DK & Owen, RM 1994, 'Neodymium isotopic variations in North Pacific modern silicate sediment and the insignificance of detrital REE contributions to seawater', *Earth and Planetary Science Letters,* vol. 127, no. 1–4, pp. 55-66. DOI:10.1016/0012-821x(94)90197-x

Jongens, R, Barrell, DJA, Campbell, JK & Pettinga, JR 2012, 'Faulting and folding beneath the Canterbury Plains identified prior to the 2010 emergence of the Greendale Fault', *New Zealand Journal of Geology and Geophysics (Special issue: Canterbury, New Zealand, 2010-2011 earthquake sequence),* vol. 55, no. 3, pp. 169-76.

Jouannic, C, Hoang, CT, Soepri Hantoro, W & Delinom, RM 1988, 'Uplift rate of coral reef terraces in the area of Kupang, West Timor: Preliminary results', *Palaeogeography, Palaeoclimatology, Palaeoecology,* vol. 68, no. 2-4, pp. 259-72.

Kääb, A 2002, 'Monitoring high-mountain terrain deformation from repeated air- and spaceborne optical data: Examples using digital aerial imagery and ASTER data', *ISPRS Journal of Photogrammetry and Remote Sensing,* vol. 57, no. 1-2, pp. 39-52. Retrieved 11 February 2011, from Scopus database.

Kane, IA, Dykstra, ML, Kneller, BC, Tremblay, S & McCaffrey, WD 2009, 'Architecture of a coarse-grained channel-levée system: The Rosario Formation, Baja California, Mexico', *Sedimentology,* vol. 56, no. 7, pp. 2207-34. Retrieved 1 October 2012, from Scopus database.

Karas, C, Nürnberg, D, Gupta, AK, Tiedemann, R, Mohan, K & Bickert, T 2009, 'Mid-Pliocene climate change amplified by a switch in Indonesian subsurface throughflow', *Nature Geoscience,* vol. 2, no. 6, pp. 434-8.

Karig, DE, Barber, AJ, Charlton, TR, Klemperer, S & Hussong, DM 1987, 'Nature and distribution of deformation across the Banda Arc - Australian collision zone at Timor', *Geological Society of America Bulletin,* vol. 98, no. 1, pp. 18-32.

Kastens, KA 1984, 'Earthquakes as a triggering mechanism for debris flows and turbidites on the Calabrian Ridge', *Marine Geology,* vol. 55, no. 1-2, pp. 13-33.

Keep, M 2000, 'Models of lithospheric-scale deformation during plate collision: effects of indentor shape and lithospheric thickness.', *Tectonophysics,* vol. 326, pp. 203-16.

Keep, M, Barber, L & Haig, DW 2009, 'Deformation of the Cablac Mountain Range, East Timor: An overthrust stack derived from an Australian continental terrace', *Journal of Asian Earth Sciences,* vol. doi:10.1016/j.jseaes.2009.02.001.

Keep, M & Haig, DW 2010, 'Deformation and exhumation in Timor: Distinct stages of a young orogeny', *Tectonophysics,* vol. 483, no. 1-2, pp. 93-111. DOI:10.1016/j.tecto.2009.11.018

Keigwin, L 1982, 'Isotopic paleoceanography of the Caribbean and east Pacific: Role of Panama uplift in late neogene time', *Science,* vol. 217, no. 4557, pp. 350-3.

Kenyon, CS 1974, *Stratigraphy and sedimentology of the Late Miocene to Quaternary deposits in Timor.*, PhD Thesis, University of London.

Kim, H, Arrowsmith, JR, Crosby, CJ, Jaeger-Frank, E, Nandigam, V, Memon, A, Conner, J, Badden, SB & Baru, C 2006, 'An Efficient Implementation of a Local Binning Algorithm for Digital Elevation Model Generation of LiDAR/ALSM Dataset', *Eos Trans. AGU,* vol. 87, no. 52.

King, G & Nábělek, J 1985, 'Role of fault bends in the initiation and termination of earthquake rupture', *Science,* vol. 228, no. 4702, pp. 984-7.

King, GCP 1986, 'Speculations on the geometry of the initiation and termination processes of earthquake rupture and its relation to morphology and geological structure', *Pure and Applied Geophysics,* vol. 124, no. 3, pp. 567-85. Retrieved 2 September 2011, from Scopus database.

Klein, GD 1985, 'The frequency and periodicity of preserved turbidites in submarine fans as a quantitative record of tectonic uplift in collision zones', *Tectonophysics,* vol. 119, no. 1–4, pp. 181-93. DOI:10.1016/0040-1951(85)90038-1

Kneller, B 1995, 'Beyond the turbidite paradigm: Physical models for deposition of turbidites and their implications for reservoir prediction', vol. 94, pp. 31-49

Knesel, KM, Cohen, BE, Vasconcelos, PM & Thiede, DS 2008, 'Rapid change in drift of the Australian plate records collision with Ontong Java plateau', *Nature,* vol. 454, no. 7205, pp. 754-7. Retrieved 27 December 2011, from Scopus database.

Konca, AO, Leprince, S, Avouac, JP & Helmberger, DV 2010, 'Rupture process of the 1999 M_W 7.1 Duzce Earthquake from joint analysis of SPOT, GPS, InSAR, strong-motion, and teleseismic data: A supershear rupture with variable rupture velocity', *Bulletin of the Seismological Society of America,* vol. 100, no. 1, pp. 267-88. Retrieved 17 August 2011, from Scopus database.

Koseluk, RA & Bischke, RE 1981, 'An elastic rebound model for normal fault earthquakes', *Journal of Geophysical research,* vol. 86, no. B2, pp. 1081-90. Retrieved 1 June 2011, from Scopus database.

Kreemer, C, Holt, WE, Goes, S & Govers, R 2000, 'Active deformation in eastern Indonesia and the Philippines from GPS and seismicity data', *Journal of Geophysical Research B: Solid Earth,* vol. 105, no. B1, pp. 663-80.

Kuhnt, W, Holbourn, A, Hall, R, Zuvela, M & Käse, R 2004, 'Neogene History of the Indonesian Throughflow', *AGU Chapman Conference*, American Geophysical Union, Washington, DC, San Diego, CA, pp. 299-320.

Labay, KA & Haeussler, P, J. 2007, *3D visualization of earthquake focal mechanisms using ArcScene*, United States Geological Survey Report 241, 241.

Larkin, RG & Sharp Jr, JM 1992, 'On the relationship between river-basin geomorphology, aquifer hydraulics, and ground-water flow direction in alluvial aquifers', *Geological Society of America Bulletin,* vol. 104, no. 12, pp. 1608-20. Retrieved 8 September 2012, from Scopus database.

Larned, ST, Hicks, DM, Schmidt, J, Davey, AJH, Dey, K, Scarsbrook, M, Arscott, DB & Woods, RA 2008, 'The Selwyn River of New Zealand: a benchmark system for alluvial plain rivers', *River Research and Applications,* vol. 24, no. 1, pp. 1-21. DOI:10.1002/rra.1054

Lawless, JV, Lovelock, BG & Ussher, GN 2005, 'Geothermal Potential of East Timor', *World Geothermal Congress 2005*, Antalya, Turkey.

Lee, YH, Chen, HS, Rau, RJ, Chen, CL & Hung, PS 2006, 'Revealing surface deformation of the 1999 Chi-Chi earthquake using high-density cadastral control points in the Taichung area, central Taiwan', *Bulletin of the Seismological Society of America,* vol. 96, no. 6, pp. 2431-40. DOI:10.1785/0120060055

Lee, YH, Chen, YC, Chen, CL, Rau, RJ, Chen, HC, Lo, W & Cheng, KC 2011, 'Revealing coseismic displacement and displacement partitioning at the northern end of the 1999 Chi-Chi earthquake, central Taiwan, using digital cadastral data', *Bulletin of the Seismological Society of America,* vol. 101, no. 3, pp. 1199-212. DOI:10.1785/0120100156

Lee, YH, Wu, KC, Rau, RJ, Chen, HC, Lo, W & Cheng, KC 2010, 'Revealing coseismic displacements and the deformation zones of the 1999 Chi-Chi earthquake in the Tsaotung area, central Taiwan, using digital cadastral data', *Journal of Geophysical Research-Solid Earth,* vol. 115, B03419, 13pp. Article. DOI:10.1029/2009jb006397

Leeder, MR & Alexander, J 1987, 'The origin and tectonic significance of asymmetrical meander-belts', *Sedimentology,* vol. 34, no. 2, pp. 217-26. Retrieved 3 May 2011, from Scopus database.

Leopold, LP, Wolman, MG & Miller, JP 1964, *Fluvial Processes in Geomorphology*, W.H. Freeman, San Francisco, CA.

Leprince, S, Ayoub, F, Klinger, Y & Avouac, JP 2007a, 'Co-registration of optically sensed images and correlation (COSI-Corr): an operational methodology for ground deformation measurements', *Proceedings of the IEEE International Geoscience and Remote Sensing Symposium (IGARSS 2007)*, pp. 1943-6. DOI:10.1109/IGARSS.2007.4423207

Leprince, S, Barbot, S, Ayoub, F & Avouac, JP 2007b, 'Automatic and precise ortho-rectification, coregistration, and subpixel correlation of satellite images: application to ground deformation measurements', *IEEE Transactions on Geoscience and Remote Sensing,* vol. 45, no. 6 (1), pp. 1529-58.

Li, B, Wang, J, Huang, B, Li, Q, Jian, Z, Zhao, Q, Su, X & Wang, P 2004, 'South China Sea surface water evolution over the last 12 Myr: A south-north comparison from Ocean Drilling Program Sites 1143 and 1146', *Paleoceanography,* vol. 19, no. 1.

Li, ZX & Powell, CM 2001, 'An outline of the palaeogeographic evolution of the Australasian region since the beginning of the Neoproterozoic', *Earth Science Reviews,* vol. 53, no. 3-4, pp. 237-77. Retrieved 7 September 2012, from Scopus database.

Lindsay, J 2010, *Whitebox Geospatial Analysis Tools*, The Centre for Hydrogeomatics, The University of Guelph, Guelph, Canada.

Linthout, K, Helmers, H & Sopaheluwakan, J 1997, 'Late Miocene obduction and microplate migration around the southern Banda Sea and the closure of the Indonesian Seaway', *Tectonophysics,* vol. 281, no. 1-2, pp. 17-30.

Lister, G & Forster, M 2009, 'Tectonic mode switches and the nature of orogenesis', *Lithos,* vol. 113, no. 1-2, pp. 274-91. DOI:10.1016/j.lithos.2008.10.024

Liu-Zeng, J, Wen, L, Sun, J, Zhang, Z, Hu, G, Xing, X, Zeng, L & Xu, Q 2010, 'Surficial slip and rupture geometry on the Beichuan fault near Hongkou during the Mw 7.9 Wenchuan earthquake, China', *Bulletin of the Seismological Society of America,* vol. 100, no. 5 B, pp. 2615-50. Retrieved 10 August 2011, from Scopus database.

Liu, YG, Miah, MRU & Schmitt, RA 1988, 'Cerium: A chemical tracer for paleo-oceanic redox conditions', *Geochimica et Cosmochimica Acta,* vol. 52, no. 6, pp. 1361-71. Retrieved 30 September 2012, from Scopus database.

Lourens, LJ, Hilgen, FJ, Shackleton, NJ, Laskar, J & Wilson, D 2004, 'The Neogene Period', in FM Gradstein, JG Ogg & AG Smith (eds), *Geological Time Scale 2004*, Cambridge University Press, pp. 409-40.

Lowe, DR 1982, 'Sediment gravity flows: II. Depositional models with special reference to the deposits of high-density turbidity currents', *Journal of Sedimentary Petrology,* vol. 52, no. 1, pp. 279-97. Retrieved 11 October 2012, from Scopus database.

Makaske, B 2001, 'Anastomosing rivers: A review of their classification, origin and sedimentary products', *Earth Science Reviews,* vol. 53, no. 3-4, pp. 149-96. Retrieved 16 August 2011, from Scopus database.

Mann, P 2007, 'Global catalogue, classification and tectonic origins of restraining- and releasing bends on active and ancient strike-slip fault systems', in D Cunningham & P Mann (eds), *Tectonics of Strike-Slip Restraining and Releasing Bends*, Geological Society of London Special Publication 290, pp. 13-142.

Marsella, M, Proietti, C, Sonnessa, A, Coltelli, M, Tommasi, P & Bernardo, E 2009, 'The evolution of the Sciara del Fuoco subaerial slope during the 2007 Stromboli eruption: Relation between deformation processes and effusive activity', *Journal of Volcanology and Geothermal Research,* vol. 182, no. 3-4, pp. 201-13. Retrieved 11 February 2011, from Scopus database.

Martin, EE & Scher, H 2006, 'A Nd isotopic study of southern sourced waters and Indonesian throughflow at intermediate depths in the Cenozoic Indian Ocean', *Geochemistry Geophysics Geosystems,* vol. 7. Article

Masoud, A & Koike, K 2006, 'Tectonic architecture through Landsat-7 ETM+/SRTM DEM-derived lineaments and relationship to the hydrogeologic setting in Siwa region, NW Egypt', *Journal of African Earth Sciences,* vol. 45, no. 4-5, pp. 467-77.

Masson, DG, Milsom, J, Barber, AJ, Sikumbang, N & Dwiyanto, B 1991, 'Recent tectonics around the island of Timor, eastern Indonesia', *Marine and Petroleum Geology,* vol. 8, no. 1, pp. 35-49.

McCaffrey, R 1988, 'Active tectonics of the Eastern Sunda and Banda Arcs', *Journal of Geophysical research,* vol. 93, no. B12, pp. 15163-82.

McCaffrey, R 1989, 'Seismological constraints and speculations on Banda Arc Tectonics', *Netherlands Journal of Sea Research,* vol. 24, no. 2/3, pp. 141-52.

McCaffrey, R 1996, 'Estimates of modern arc-parallel strain rates in fore arcs', *Geology,* vol. 24, no. 1, pp. 27-30. DOI:10.1130/0091-7613(1996)024<0027:eomaps>2.3.co;2

McCaffrey, R & Abers, GA 1991, 'Orogeny in arc-continent collision: The Banda arc and western New Guinea', *Geology,* vol. 19, no. 6, pp. 563-6.

McConnico, TS & Bassett, KN 2007, 'Gravelly Gilbert-type fan delta on the Conway Coast, New Zealand: Foreset depositional processes and clast imbrications', *Sedimentary Geology,* vol. 198, pp. 147-66.

McCulloch, MT & Wasserburg, GJ 1978, 'Sm-Nd and Rb-Sr chronology of continental crust formation', *Science,* vol. 200, no. 4345, pp. 1003-11. Retrieved 8 July 2012, from Scopus database.

McLennan, SM 1989, 'Rare earth elements in sedimentary rocks: influence of provenance and sedimentary processes', in BR Lipin & GA McKay (eds), *Geochemistry and mineralogy of rare earth elements*, pp. 169-200.

McLennan, SM, Hemming, S, McDaniel, DK & Hanson, GN 1993, 'Geochemical approaches to sedimentation, provenance, and tectonics', in MJ Johnsson & A Basu (eds), *Processes Controlling the Composition of Clastic Sediments*, Geological Society of America Special Paper 284, Boulder, Colorado, pp. 21-40.

McLennan, SM, McCulloch, MT, Taylor, SR & Maynard, JB 1989, 'Effects of sedimentary sorting on neodymium isotopes in deep-sea turbidites', *Nature,* vol. 337, no. 6207, pp. 547-9. 10.1038/337547a0

McLennan, SM, Taylor, SR, McCulloch, MT & Maynard, JB 1990, 'Geochemical and NdSr isotopic composition of deep-sea turbidites: Crustal evolution and plate tectonic associations', *Geochimica et Cosmochimica Acta,* vol. 54, no. 7, pp. 2015-50. Retrieved 16 September 2012, from Scopus database.

Means, WD 1989, 'Stretching faults', *Geology,* vol. 17, no. 10, pp. 893-6. DOI:10.1130/0091-7613(1989)017<0893:sf>2.3.co;2

Merritts, D, Eby, R, Harris, RA, Edwards, RL & Chang, H 1998, 'Variable rates of Late Quaternary surface uplift along the Banda Arc- Australian plate collision zone, eastern Indonesia', in I Stewart & C Vita-Finzi (eds), *Coastal tectonics*, vol. 146, Geological Society Special Publication, pp. 213-24.

Metcalfe, I 1996, 'Pre-Cretaceous evolution of SE Asian terranes', in R Hall & DJ Blundell (eds), *Tectonic Evolution of Southeast Asia. Geological Society of London Special Publication 106*, pp. 97-122.

Michels, KH, Kudrass, HR, Hübscher, C, Suckow, A & Wiedicke, M 1998, 'The submarine delta of the Ganges–Brahmaputra: cyclone-dominated sedimentation patterns', *Marine Geology,* vol. 149, no. 1–4, pp. 133-54. DOI:10.1016/s0025-3227(98)00021-8

Mikolajewicz, U, Maier-Reimer, E, Crowley, TJ & Kwang-Yul, K 1993, 'Effect of Drake and Panamanian gateways on the circulation of an ocean model', *Paleoceanography,* vol. 8, no. 4, pp. 409-26.

Miller, RG & O'Nions, RK 1984, 'The provenance and crustal residence ages of British sediments in relation to palaeogeographic reconstructions', *Earth and Planetary Science Letters,* vol. 68, no. 3, pp. 459-70. DOI:10.1016/0012-821x(84)90130-4

Mills, CM 2011, *Erosion of a rising mountain belt: the sedimentary cycle within the Seical Catchment, East Timor*, MSc Thesis, University of Melbourne.

Milsom, J & Audley-Charles, MG 1986, 'Post- collision isostatic readjustment in the southern Banda Arc (Timor)', *Collision tectonics*, pp. 353-64.

Molnar, P & Tapponnier, P 1975, 'Cenozoic Tectonics of Asia: Effects of a Continental Collision', *Science,* vol. 189, no. 4201, pp. 419-26.

Moody, L 2012, *Indonesian climate investigations using stable isotopic data from modern, Holocene and Pliocene corals*, MSc Thesis, University of Canterbury.

Moody, L, Quigley, MC & Duffy, B 2011, 'Indonesian palaeoceanographic history using detrital Pliocene corals', in *Geosciences 2011*, vol. Miscellaneous Publication 130A. Geoscience Society of New Zealand, Nelson, New Zealand

Mook, DH & Hoskin, CM 1982, 'Organic determinations by ignition: Caution advised', *Estuarine, Coastal and Shelf Science,* vol. 15, no. 6, pp. 697-9. DOI:10.1016/0272-7714(82)90080-4

Morey, SL, Shriver, JF & O'Brien, JJ 1999, 'The effects of Halmahera on the Indonesian throughflow', *Journal of Geophysical Research C: Oceans,* vol. 104, no. C10, pp. 23281-96.

Morris, JD, Gill, JB, Schwartz, D & Silver, EA 1984, 'Late Miocene to Recent Banda Sea Volcanism, III: Isotopic compositions', *Eos Trans. AGU,* vol. 65, p. 1135.

Mudelsee, M & Raymo, ME 2005, 'Slow dynamics of the Northern Hemisphere glaciation', *Paleoceanography,* vol. 20, no. 4.

Mukoyama, S 2011, 'Estimation of ground deformation caused by the earthquake (M7.2) in Japan, 2008, from the geomorphic image analysis of high resolution LiDAR DEMs', *Journal of Mountain Science,* vol. 8, no. 2, pp. 239-45. DOI:10.1007/s11629-011-2106-7

Mulder, T & Alexander, J 2001, 'The physical character of subaqueous sedimentary density flow and their deposits', *Sedimentology,* vol. 48, no. 2, pp. 269-99. Retrieved 20 October 2012, from Scopus database.

Mulder, T, Syvitski, JPM, Migeon, S, Faugères, JC & Savoye, B 2003, 'Marine hyperpycnal flows: Initiation, behaviorand related deposits. A review', *Marine and Petroleum Geology,* vol. 20, no. 6-8, pp. 861-82. Retrieved 29 September 2012, from Scopus database.

Muller, JR & Harding, DJ 2007, 'Using LIDAR surface deformation mapping to constrain earthquake magnitudes on the Seattle fault in Washington State, USA', *Proceedings of the IEEE Urban Remote Sensing Joint Event, 2007*, pp. 1-7. DOI:10.1109/URS.2007.371789

Murray, RW, Buchholtz Ten Brink, MR, Gerlach, DC, Russ Iii, GP & Jones, DL 1991, 'Rare earth, major, and trace elements in chert from the Franciscan Complex and Monterey Group, California: Assessing REE sources to fine-grained marine sediments', *Geochimica et Cosmochimica Acta,* vol. 55, no. 7, pp. 1875-95. DOI:10.1016/0016-7037(91)90030-9

Mutti, E 1985, 'Turbidite systems and their relations to depositional sequences (gravity flows)', *Provenance of arenites. Proc. Cetraro, Cosenza, 1984*, pp. 65-93. Retrieved 29 September 2012, from Scopus database.

Mutti, E, Lucchi, FR, Seguret, M & Zanzucchi, G 1984, 'Seismoturbidites: A new group of resedimented deposits', *Marine Geology,* vol. 55, no. 1-2, pp. 103-16.

Najman, Y & Garzanti, E 2000, 'Reconstructing early Himalayan tectonic evolution and paleogeography from Tertiary foreland basin sedimentary rocks, northern India', *Geological Society of America Bulletin,* vol. 112, no. 3, pp. 435-49. DOI:10.1130/0016-7606(2000)112<435:rehtea>2.0.co;2

Nathan, SA & Leckie, RM 2009, 'Early history of the Western Pacific Warm Pool during the middle to late Miocene (~ 13.2-5.8Â Ma): Role of sea-level change and implications for equatorial circulation', *Palaeogeography, Palaeoclimatology, Palaeoecology,* vol. 274, no. 3-4, pp. 140-59.

Nesbitt, HW & Young, GM 1982, 'Early proterozoic climates and plate motions inferred from major element chemistry of lutites', *Nature,* vol. 299, no. 5885, pp. 715-7. Retrieved 12 April 2012, from Scopus database.

Nesbitt, HW & Young, GM 1989, 'Formation and diagenesis of weathering profiles', *Journal of Geology,* vol. 97, no. 2, pp. 129-47. Retrieved 12 April 2012, from Scopus database.

Nesbitt, HW, Young, GM, McLennan, SM & Keays, RR 1996, 'Effects of chemical weathering and sorting on the petrogenesis of siliciclastic sediments, with implications for provenance studies', *Journal of Geology,* vol. 104, no. 5, pp. 525-42. Retrieved 16 September 2012, from Scopus database.

Nguyen, N 2011, *Reconstruction of Timor's uplift and ENSO variability during the Pliocene using Palynology* BSc (Hons) Thesis, University of Queensland.

Nguyen, N, Duffy, B, Shulmeister, J & Quigley, MC 2013, 'Rapid Pliocene uplift of Timor', *Geology,* vol. 41, no. 2, pp. 179-82. DOI:10.1130/G33420.1

Nicol, A 1992, 'Tectonic structures developed in Oligocene limestones: implications for New Zealand plate boundary deformation in North Canterbury', *New Zealand Journal of Geology and Geophysics,* vol. 35, pp. 353-62.

Nicol, A 1993, 'Haumurian (c.66-80 Ma) half-graben development and deformation, mid Waipara, north Canterbury, New Zealand', *New Zealand Journal of Geology & Geophysics,* vol. 36, no. 1, pp. 127-30.

Noda, A, TuZino, T, Kanai, Y, Furukawa, R & Uchida, Ji 2008, 'Paleoseismicity along the southern Kuril Trench deduced from submarine-fan turbidites', *Marine Geology,* vol. 254, no. 1-2, pp. 73-90.

Normark, WR, Piper, DJW & Hiscott, RN 1998, 'Sea level controls on the textural characteristics and depositional architecture of the Hueneme and associated submarine fan systems, Santa Monica Basin, California', *Sedimentology,* vol. 45, no. 1, pp. 53-70.

Norris, RJ & Cooper, AF 2001, 'Late Quaternary slip rates and slip partitioning on the Alpine fault, New Zealand', *Journal of Structural Geology,* vol. 23, no. 2-3, pp. 507-20.

Nugroho, H, Harris, RA, Lestariya, AW & Maruf, B 2009, 'Plate Boundary Reorganization in the Active bandA Arc-Continent Collision: Insights from New GPS Measurements', *Tectonophysics,* vol. 479, no. 1-2, pp. 52-65.

Orange, DL 1990, 'Criteria helpful in recognizing shear zone and diapiric melanges: Examples from the Hoh Accretionary Complex, Olympic Peninsula, Washington', *Geological Society of America Bulletin,* vol. 102, pp. 935-51.

Oskin, ME, Arrowsmith, JR, Corona, AH, Elliott, AJ, Fletcher, JM, Fielding, EJ, Gold, PO, Garcia, JJG, Hudnut, KW, Liu-Zeng, J & Teran, OJ 2012, 'Near-field deformation from the El Mayor–Cucapah earthquake revealed by differential LIDAR', *Science,* vol. 335, pp. 702-5.

Ouchi, S 1985, 'Response of alluvial rivers to slow active tectonic movement', *Geological Society of America Bulletin,* vol. 96, pp. 504-15.

Peacock, DCP & Sanderson, DJ 1991, 'Displacements, segment linkage and relay ramps in normal fault zones', *Journal of Structural Geology,* vol. 13, no. 6, pp. 721-33. DOI:10.1016/0191-8141(91)90033-f

Pedley, KL, Barnes, PM, Pettinga, JR & Lewis, KB 2010, 'Seafloor structural geomorphic evolution of the accretionary frontal wedge in response to seamount subduction, Poverty Indentation, New Zealand', *Marine Geology,* vol. 270, no. 1-4, pp. 119-38

Petit, JP 1987, 'Criteria for the sense of movement on fault surfaces in brittle rocks', *Journal of Structural Geology,* vol. 9, no. 5/6, pp. 597-608.

Pettinga, JR, Yetton, MD, Van Dissen, RJ & Downes, G 2001, 'Earthquake source identification and characterisation for the Canterbury Region, South Island, New Zealand.', *Bulletin of the New Zealand Society for Earthquake Engineering,* vol. 34, no. 4, pp. 282-317.

Pickering, KT, Hiscott, RN & Hein, FJ 1989, *Deep marine environments: clastic sedimentation and tectonics*, Unwin Hyman, London; Boston.

Planert, L, Kopp, H, Lueschen, E, Mueller, C, Flueh, ER, Shulgin, A, Djajadihardja, Y & Krabbenhoeft, A 2010, 'Lower plate structure and upper plate deformational segmentation at the Sunda-Banda arc transition, Indonesia', *J. Geophys. Res.,* vol. 115, no. B8, p. B08107. DOI:10.1029/2009jb006713

Platt, JP 1986, 'Dynamics of orogenic wedges and the uplift of high-pressure metamorphic rocks', *Geological Society of America Bulletin,* vol. 97, no. 9, pp. 1037-53. Retrieved 13 June 2011, from Scopus database.

Poole, GC, Stanford, JA, Frissell, CA & Running, SW 2002, 'Three-dimensional mapping of geomorphic controls on flood-plain hydrology and connectivity from aerial photos', *Geomorphology,* vol. 48, no. 4, pp. 329-47. DOI:10.1016/s0169-555x(02)00078-8

Posamentier, HW & Walker, RG 2006, 'Deep-water turbidites and submarine fans', in HW Posamentier & RG Walker (eds), *Facies Models Revisited*, SEPM (Society for Sedimentary Geology) Special Publication 84, Tulsa, Oklahoma, pp. 399-520.

Pouderoux, H, Lamarche, G & Proust, JN 2012, 'Building an 18 000-year-long paleo-earthquake record from detailed deep-sea turbidite characterisation in Poverty Bay, New Zealand', *Natural Hazards and Earth System Science,* vol. 12, no. 6, pp. 2077-101. Retrieved 21 September 2012, from Scopus database.

Pourmand, A, Dauphas, N & Ireland, TJ 2012, 'A novel extraction chromatography and MC-ICP-MS technique for rapid analysis of REE, Sc and Y: Revising CI-chondrite and Post-Archean Australian Shale (PAAS) abundances', *Chemical Geology,* vol. 291, pp. 38-54. Retrieved 27 June 2012, from Scopus database.

Prentice, CS, Crosby, CJ, Whitehill, CS, Arrowsmith, JR, Furlong, KP & Phillips, DA 2009, 'Illuminating Northern California's Active Faults', *EOS,* vol. 90, no. 7, p. 55.

Price, EJ & Burgmann, R 2002, 'Interactions between the Landers and Hector Mine, California, earthquakes from space geodesy, boundary element modeling, and time-dependent friction', *Bulletin of the Seismological Society of America,* vol. 92, no. 4, pp. 1450-69.

Price, NJ & Audley-Charles, MG 1983, 'Plate rupture by hydraulic fracture resulting in overthrusting', *Nature,* vol. 306, no. 5943, pp. 572-5.

Price, NJ & Audley-Charles, MG 1987, 'Tectonic collision processes after plate rupture', *Tectonophysics,* vol. 140, no. 2-4, pp. 121-9.

Prider, RT 1947, 'Chloritoid at Kalgoorlie', *American Mineralogist,* vol. 32, pp. 471-4.

Pubellier, M & Cobbold, PR 1996, 'Analogue models for the transpressional docking of volcanic arcs in the Western Pacific', *Tectonophysics,* vol. 253, no. 1-2, pp. 33-52. Retrieved 30 December 2011, from Scopus database.

Quigley, MC, Bastin, S & Bradley, B in press, 'Recurrent liquefaction in Christchurch, New Zealand during the Canterbury earthquake sequence', *Geology*.

Quigley, MC, Duffy, B, Woodhead, J, Hellstrom, J, Moody, L, Horton, T, Suares, J & Fernandes, L 2012a, 'U/Pb dating of a terminal Pliocene coral from the Indonesian Seaway', *Marine Geology,* vol. 311-314, pp. 57-62.

Quigley, MC, Sandiford, M & Cupper, ML 2007, 'Distinguishing tectonic from climatic controls on range-front sedimentation', *Basin Research,* vol. 19, no. 4, pp. 491-505. DOI:10.1111/j.1365-2117.2007.00336.x

Quigley, MC, Van Dissen, R, Litchfield, N, Villamor, P, Duffy, B, Barrell, D, Furlong, K, Stahl, T, Bilderback, E & Noble, D 2012b, 'Surface rupture during the 2010 M_W 7.1 Darfield (Canterbury) earthquake: implications for fault rupture dynamics and seismic-hazard analysis', *Geology,* vol. 40, no. 1, pp. 55-8. DOI:10.1130/G32528.1

Quigley, MC, Van Dissen, R, Villamor, P, Litchfield, N, Barrell, D, Furlong, K, Stahl, T, Duffy, B, Bilderback, E, Noble, D, Townsend, D, Begg, J, Jongens, R, Ries, W, Claridge, J, Klahn, A,

Mackenzie, H, Smith, A, Hornblow, S, Nicol, R, Cox, S, Langridge, R & Pedley, K 2010a, 'Surface rupture of the Greendale Fault during the Darfield (Canterbury) earthquake, New Zealand: Initial findings', *Bulletin of the New Zealand Society for Earthquake Engineering,* vol. 43, no. 4, pp. 236-42.

Quigley, MC, Villamor, P, Furlong, K, Beavan, J, Van Dissen, R, Litchfield, N, Stahl, T, Duffy, B, Bilderback, E, Noble, D, Barrell, D, Jongens, R & Cox, S 2010b, 'Previously unknown fault shakes New Zealand's South Island', *EOS,* vol. 91, no. 49, pp. 469-70.

Rahiman, TIH & Pettinga, JR 2008, 'Analysis of lineaments and their relationship to Neogene fracturing, SE Viti Levu, Fiji', *Bulletin of the Geological Society of America,* vol. 120, no. 11-12, pp. 1544-55.

Rangin, C, Bellon, H, Benard, F, Letouzey, J, Muller, C & Sanudin, T 1990, 'Neogene arc-continent collision in Sabah, Northern Borneo (Malaysia)', *Tectonophysics,* vol. 183, no. 1, pp. 305-19. DOI:10.1016/0040-1951(90)90423-6

Ratschbacher, L, Frisch, W, Linzer, HG & Merle, O 1991a, 'Lateral extrusion in the eastern Alps, Part 2: structural analysis', *Tectonics,* vol. 10, no. 2, pp. 257-71. Retrieved 16 July 2012, from Scopus database.

Ratschbacher, L, Merle, O, Davy, P & Cobbold, P 1991b, 'Lateral extrusion in the eastern Alps, part 1: boundary conditions and experiments scaled for gravity', *Tectonics,* vol. 10, no. 2, pp. 245-56. Retrieved 16 July 2012, from Scopus database.

Reading, HG & Richards, M 1994, 'Turbidite systems in deep-water basin margins classified by grain size and feeder system', *American Association of Petroleum Geologists Bulletin,* vol. 78, no. 5, pp. 792-822. Retrieved 29 September 2012, from Scopus database.

Reigber, C, Xia, Y, Michel, GW, Klotz, J & Angermann, D 1997, 'The Antofagasta 1995 earthquake: Crustal deformation pattern as observed by GPS and D-INSAR', *Proceedings of the 3rd ERS Symposium on Space at the Service of Our Environment,* , European Space Agency, Florence, Italy, pp. 507-13.

Reyners, M, Eberhart-Phillips, D & Bannister, S 2011, 'Tracking repeated subduction of the Hikurangi Plateau beneath New Zealand', *Earth and Planetary Science Letters,* vol. 311, no. 1–2, pp. 165-71. DOI:10.1016/j.epsl.2011.09.011

Richardson, AN & Blundell, DJ 1996, 'Continental collision in the Banda Arc', in R Hall & DJ Blundell (eds), *Tectonic Evolution of Southeast Asia*, vol. 106, Geological Society of London Special Publication, pp. 47-60.

Rigg, JWD & Hall, R 2012, 'Neogene development of the Savu Forearc Basin, Indonesia', *Marine and Petroleum Geology,* vol. 32, pp. 76-94.

Ring, U, Glodny, J, Thomson, S & Will, T 2010, 'The Hellenic subduction system: High-pressure metamorphism, exhumation, normal faulting and large-scale extension.', *Annual Review Earth and Planetary Sciences,* vol. 38, pp. 45-76. DOI:10.1146/annurev.earth. 050708.170910

Roosmawati, N & Harris, RA 2009, 'Surface uplift history of the incipient Banda arc-continent collision: Geology and synorogenic foraminifera of Rote and Savu Islands, Indonesia', *Tectonophysics,* vol. 479, no. 1-2, pp. 95-110. DOI:10.1016/j.tecto.2009.04.009

Roser, BP & Korsch, RJ 1988, 'Provenance signatures of sandstone-mudstone suites determined using discriminant function analysis of major-element data', *Chemical Geology,* vol. 67, pp. 119-39.

Rosidi, HMD, Suwitodirdjo, K & Tjokosaproetro, S 1981, 'Geologic map of the Kupang-Atambua quadrangles, Timor'. Geological Research and Development Centre, Bandung, Indonesia

Rutherford, E, Burke, K & Lytwyn, J 2001, 'Tectonic history of Sumba Island, Indonesia, since the Late Cretaceous and its rapid escape into the forearc in the Miocene', *Journal of Asian Earth Sciences,* vol. 19, no. 4, pp. 453-79.

Ryan, WBF, Carbotte, SM, Coplan, JO, O'Hara, S, Melkonian, A, Arko, R, Weissel, RA, Ferrini, V, Goodwillie, A, Nitsche, F, Bonczkowski, J & Zemsky, R 2009, 'Global Multi-Resolution

Topography synthesis', *Geochemistry Geophysics Geosystems,* vol. 10, Q03014. DOI:10.1029/2008GC002332

Sacks, PE & Secor Jr, DT 1990, 'Delamination in collisional orogens', *Geology,* vol. 18, no. 10, pp. 999-1002. Retrieved 5 October 2011, from Scopus database.

Sandiford, M 2008, 'Seismic moment release during slab rupture beneath the Banda Sea', *Geophysical Journal International,* vol. 174, no. 2, pp. 659-71.

Sandiford, M 2010, 'Geodynamics: Complex subduction', *Nature Geoscience,* vol. 3, no. 8, pp. 518-20. Retrieved 15 June 2011, from Scopus database.

Santisteban, JI, Mediavilla, R, Lopez-Pamo, E, Dabrio, CJ, Blanca Ruiz Zapata, M, Jose Gil Garcıa, M, Castano, S & Martınez-Alfaro, PE 2004, 'Loss on ignition: a qualitative or quantitative method for organic matter and carbonate mineral content in sediments?', *Journal of Paleolimnology,* vol. 32, pp. 287-99.

Sato, K, Oda, M, Chiyonobu, S, Kimoto, K, Domitsu, H & Ingle, JC 2008, 'Establishment of the western Pacific warm pool during the Pliocene: Evidence from planktic foraminifera, oxygen isotopes, and Mg/Ca ratios', *Palaeogeography Palaeoclimatology Palaeoecology,* vol. 265, no. 1-2, pp. 140-7. Article

Sawyer, RK, Sani, K & Brown, S 1993, 'The stratigraphy and sedimentology of West Timor, Indonesia', *Proceedings of the Indonesian Petroleum Association, Twenty Second Annual Convention*, pp. 533-74.

Schellart, WP & Lister, GS 2005, 'The role of the East Asian active margin in widespread extensional and strike-slip deformation in East Asia', *Journal of the Geological Society,* vol. 162, no. 6, pp. 959-72. DOI:10.1144/0016-764904-112

Schettino, A & Scotese, CR 2005, 'Apparent polar wander paths for the major continents (200 Ma to the present day): A palaeomagnetic reference frame for global plate tectonic reconstructions', *Geophysical Journal International,* vol. 163, no. 2, pp. 727-59.

Schneider, B & Schmittner, A 2006, 'Simulating the impact of the Panamanian seaway closure on ocean circulation, marine productivity and nutrient cycling', *Earth and Planetary Science Letters,* vol. 246, no. 3-4, pp. 367-80.

Schott, FA & McCreary Jr, JP 2001, 'The monsoon circulation of the Indian Ocean', *Progress in Oceanography,* vol. 51, no. 1, pp. 1-123.

Schubert, JK, Kidder, DL & Erwin, DH 1997, 'Silica-replaced fossils through the Phanerozoic', *Geology,* vol. 25, no. 11, pp. 1031-4. Retrieved 9 October 2012, from Scopus database.

Schumm, SA 1985, 'Patterns of Alluvial Rivers', *Annual Review of Earth and Planetary Sciences,* vol. 13, pp. 5-27. Review

Schumm, SA 1986, 'Alluvial river response to active tectonics'.

Shanmugam, G 1997, 'The Bouma Sequence and the turbidite mind set', *Earth-Science Reviews,* vol. 42, no. 4, pp. 201-29. Retrieved 29 September 2012, from Scopus database.

Shanmugam, G 2000, '50 years of the turbidite paradigm (1950s-1990s): Deep-water processes and facies models-a critical perspective', *Marine and Petroleum Geology,* vol. 17, no. 2, pp. 285-342. Retrieved 29 September 2012, from Scopus database.

Shanmugam, G 2006, *Deep-water Processes and Facies Models: Implications for Sandstone Petroleum Reservoirs*, Elsevier, Amsterdam.

Shanmugam, G & Moiola, RJ 1988, 'Submarine fans: Characteristics, models, classification, and reservoir potential', *Earth Science Reviews,* vol. 24, no. 6, pp. 383-428. Retrieved 29 September 2012, from Scopus database.

Shields, G & Stille, P 2001, 'Diagenetic constraints on the use of cerium anomalies as palaeoseawater redox proxies: An isotopic and REE study of Cambrian phosphorites', *Chemical Geology,* vol. 175, no. 1-2, pp. 29-48. Retrieved 30 September 2012, from Scopus database.

Shulgin, A, Kopp, H, Mueller, C, Lueschen, E, Planert, L, Engels, M, Flueh, ER, Krabbenhoeft, A & Djajadihardja, Y 2009, 'Sunda-Banda arc transition: Incipient continent-island arc collision

(northwest Australia)', *Geophys. Res. Lett.,* vol. 36, no. 10, p. L10304. DOI:10.1029/2009gl037533

Sibson, R, Ghisetti, F & Ristau, J 2011a, 'Stress control of an evolving strike-slip fault system during the 2010-2011 Canterbury, New Zealand, earthquake sequence', *Seismological Research Letters,* vol. 82, no. 6, pp. 824-32.

Sibson, RH 1985, 'Stopping of earthquake ruptures at dilational fault jogs', *Nature,* vol. 316, no. 6025, pp. 248-51.

Sibson, RH 1989, 'Earthquake faulting as a structural process', *Journal of Structural Geology,* vol. 11, no. 1/2, pp. 1-14.

Sibson, RH, Ghisetti, FC & Crookbain, RA 2011b, ''Andersonian' wrench faulting in a regional stress field: the 2010 Mw7.1 Darfield (Canterbury, New Zealand) earthquake sequence', in D Healy (ed.), *Stress Controls on Faulting, Fracturing and Igneous Intrusion in the Earth's Crust—Commemorating the Work of Ernest Masson Anderson*, Geological Society of London Special Publication.

Sieh, K, Lilje, A, Lindvall, S, McGill, SF, Mori, J, Rubin, C, Spotila, JA, Stock, J, Thio, HK, Treiman, J, Wernicke, B, Jones, L, Zachariasen, J, Hauksson, E, Hudnut, K, Eberhart-Phillips, D, Heaton, T, Hough, S, Hutton, K & Kanamori, H 1993, 'Near-Field Investigations of the Landers Earthquake Sequence, April to July 1992', *Science,* vol. 260, no. 5105, pp. 171-6. DOI:10.1126/science.260.5105.171

Silver, EA, Reed, D, McCaffrey, R & Joyodiwiryo, Y 1983, 'Back arc thrusting in the eastern Sunda arc, Indonesia: a consequence of arc-continent collision', *Journal of Geophysical Research,* vol. 88, no. B9, pp. 7429-48

Similox-Tohon, D, Sintubin, M, Muchez, P, Verhaert, G, Vanneste, K, Fernandez, M, Vandycke, S, Vanhaverbeke, H & Waelkens, M 2006, 'The identification of an active fault by a multidisciplinary study at the archaeological site of Sagalassos (SW Turkey)', *Tectonophysics,* vol. 420, no. 3-4, pp. 371-87.

Simons, AL 1940, 'Geological investigations in north-east Netherlands Timor', in HA Brouwer (ed.), *Geological Expedition to the Lesser Sunda Islands under the Leadership of H. A. Brouwer*, vol. 1, Noord-Hollandsche Uitgevers Maatschappij, Amsterdam, pp. 107-213.

Simons, M, Fialko, Y & Rivera, L 2002, 'Coseismic deformation from the 1999 Mw 7.1 Hector Mine, California, earthquake as inferred from InSAR and GPS observations', *Bulletin of the Seismological Society of America,* vol. 92, no. 4, pp. 1390-402. Retrieved 11 February 2011, from Scopus database.

Slingerland, R & Smith, ND 1998, 'Necessary conditions for a meandering-river avulsion', *Geology,* vol. 26, no. 5, pp. 435-8. Retrieved 16 August 2011, from Scopus database.

Slingerland, R & Smith, ND 2004, 'River avulsions and their deposits', vol. 32, pp. 257-85

Smith, AG & Pickering, KT 2003, 'Oceanic gateways as a critical factor to initiate icehouse Earth', *Journal of the Geological Society,* vol. 160, no. 3, pp. 337-40.

Smith, WHF & Sandwell, DT 1997, 'Global seafloor topography from satellite altimetry and ship depth soundings', *Science,* vol. 277, pp. 1957-62.

Snow, RS & Slingerland, RL 1990, 'Stream profile adjustment to crustal warping: nonlinear results from a simple model', *Journal of Geology,* vol. 98, no. 5, pp. 699-708. Retrieved 8 February 2011, from Scopus database.

Snyder, DB, Milsom, J & Prasetyo, H 1996a, 'Geophysical evidence for local indentor tectonics in the Banda Arc east of Timor', in DJ Blundell & R Hall (eds), *Tectonic evolution of Southeast Asia*, Geological Society, London, pp. 61-73.

Snyder, DB, Prasetyo, H, Blundell, DJ, Pigram, CJ, Barber, AJ, Richardson, A & Tjokosaproetro, S 1996b, 'A dual doubly vergent orogen in the Banda Arc continent-arc collision zone as observed on deep seismic reflection profiles', *Tectonics,* vol. 15, no. 1, pp. 34-53.

Soh, W 1989, 'Coarse clast dominant submarine debrite, the Mio-Pliocene Fujikawa Group, central Japan', in A Taira & F Masuda (eds), *Sedimentary Facies in the Active Plate Margin*, Terra Scientific Publishing Company, Tokyo, pp. 495-510.

Sohn, YK 2000, 'Depositional Processes of Submarine Debris Flows in the Miocene Fan Deltas, Pohang Basin, SE Korea with Special Reference to Flow Transformation', *Journal of Sedimentary Research,* vol. 70, no. 3, pp. 491-503. DOI:10.1306/2dc40922-0e47-11d7-8643000102c1865d

Sopaheluwakan, J, Helmers, H, Tjokrosapoetro, S & Surya Nila, E 1989, 'Medium pressure metamorphism with inverted thermal gradient associated with ophiolite nappe emplacement in Timor', *Netherlands Journal of Sea Research,* vol. 24, pp. 333-43.

Spakman, W & Hall, R 2010, 'Surface deformation and slab–mantle interaction during Banda arc subduction rollback', *Nature Geoscience,* vol. 3, pp. 562-6. DOI:10.1038/NGEO917

Sprintall, J, Wijffels, SE, Molcard, R & Jaya, I 2009, 'Direct estimates of the Indonesian Throughflow entering the Indian Ocean: 2004–2006', *J. Geophys. Res.,* vol. 114, no. C7, p. C07001. DOI:10.1029/2008jc005257

Srinivasan, MS & Sinha, DK 1998, 'Early Pliocene closing of the Indonesian Seaway: evidence from north-east Indian Ocean and Tropical Pacific deep sea cores', *Journal of Asian Earth Sciences,* vol. 16, no. 1, pp. 29-44.

St.-Onge, G, Mulder, T, Piper, DJW, Hillaire-Marcel, C & Stoner, JS 2004, 'Earthquake and flood-induced turbidites in the Saguenay Fjord (Quebec): A Holocene paleoseismicity record', *Quaternary Science Reviews,* vol. 23, no. 3-4, pp. 283-94.

Stahl, T, Winkler, S, Bebbington, MS, Quigley, MC, Duffy, B & Duke, D in review, 'Schmidt hammer dating of late Quaternary fluvial terraces in New Zealand', *Earth Surface Processes and Landforms*.

Standley, CE & Harris, RA 2009, 'Tectonic Evolution of Forearc Nappes of the Active Banda Arc-Continent Collision: Origin, Age, Metamorphic History and Structure of the Lolotoi Complex, East Timor', *Tectonophysics,* vol. doi:10.1016/j.tecto.2009.01.034.

Stewart, IS & Hancock, PL 1990, 'What Is a Fault Scarp', *Episodes,* vol. 13, no. 4, pp. 256-63. Article

Strachan, LJ & Alsop, GI 2006, 'Slump folds as estimators of palaeoslope: a case study from the Fisherstreet Slump of County Clare, Ireland', *Basin Research,* vol. 18, no. 4, pp. 451-70. DOI:10.1111/j.1365-2117.2006.00302.x

Styron, RH, Taylor, MH & Murphy, MA 2011, 'Oblique convergence, arc-parallel extension, and the role of strike-slip faulting in the High Himalaya', *Geosphere,* vol. 7, no. 2, pp. 582-96. DOI:10.1130/ges00606.1

Suggate, RP 1963, 'The fan surfaces of the central Canterbury Plain', *New Zealand Journal of Geology and Geophysics,* vol. 6, pp. 281-7.

Suppe, J 1984, 'Kinematics of arc-continental collision, flipping of subduction, and back-arc spreading near Taiwan', *Memoir of the Geological Society of China (Taiwan),* vol. 6, pp. 21-33. Retrieved 16 August 2012, from Scopus database.

Talbot, CJ & Von Brunn, V 1987, 'Intrusive and extrusive (micro) melange couplets as distal effects of tidal pumping by marine ice sheet', *Geological Magazine,* vol. 124, pp. 513-25.

Tapponnier, P, Lacassin, R, Leloup, PH, Schärer, U, Dalai, Z, Haiwei, W, Xiaohan, L, Shaocheng, J, Lianshang, Z & Jiayou, Z 1990, 'The Ailao Shan/Red River metamorphic belt: Tertiary left-lateral shear between Indochina and South China', *Nature,* vol. 343, no. 6257, pp. 431-7. Retrieved 16 July 2012, from Scopus database.

Taylor, M, Yin, A, Ryerson, FJ, Kapp, P & Ding, L 2003, 'Conjugate strike-slip faulting along the Bangong-Nujiang suture zone accommodates coeval east-west extension and north-south shortening in the interior of the Tibetan Plateau', *Tectonics,* vol. 22, no. 4, p. 1044.

Taylor, SR & McLennan, SM 1985, *The Continental Crust: its Composition and Evolution. An Examination of the Geochemical Record Preserved in Sedimentary Rocks*, Blackwell Scientific, Oxford.

Teng, LS, Lee, CT, Tsai, YB & Hsiao, LY 2000, 'Slab breakoff as a mechanism for flipping of subduction polarity in Taiwan', *Geology,* vol. 28, no. 2, pp. 155-8. Retrieved 5 October 2011, from Scopus database.

Tjia, H 1981, 'Examples of young tectonism in eastern Indonesia', in A Barber & S Wiryosujono (eds), *The Geology and Tectonics of Eastern Indonesia, Special Publication*, vol. 2, Geological Research and Development Centre, Bandung, Indonesia.

Tobgay, T, Long, S, McQuarrie, N, Ducea, MN & Gehrels, G 2010, 'Using isotopic and chronologic data to fingerprint strata: Challenges and benefits of variable sources to tectonic interpretations, the Paro Formation, Bhutan Himalaya', *Tectonics,* vol. 29, no. 6, p. TC6023. DOI:10.1029/2009tc002637

Torabi, G, Arai, S & Koepke, J 2011, 'Metamorphosed mantle peridotites from central Iran (Jandaq area, Isfahan province)', *Neues Jahrbuch fur Geologie und Palaontologie - Abhandlungen,* vol. 261, no. 2, pp. 129-50. Retrieved 8 October 2012, from Scopus database.

Tripsanas, EK, Piper, DJW, Jenner, KA & Bryant, WR 2008, 'Submarine mass-transport facies: new perspectives on flow processes from cores on the eastern North American margin', *Sedimentology,* vol. 55, no. 1, pp. 97-136. DOI:10.1111/j.1365-3091.2007.00894.x

Trudgill, B & Cartwright, J 1994, 'Relay-ramp forms and normal-fault linkages, Canyonlands National Park, Utah', *Geological Society of America Bulletin,* vol. 106, no. 9, pp. 1143-57. Retrieved 21 August 2011, from Scopus database.

Tullis, J 1983, 'Deformation of feldspars', *Reviews of the American Mineralogical Society,* vol. 2, pp. 297-323.

Uchman, A 1995, 'Taxonomy and palaeoecology of flysch trace fossils: The Marnoso-arenacea Formation and associated facies (Miocene, Northern Apennines, Italy)', *Beringeria,* vol. 15, pp. 1-115.

Unterschutz, J, Creaser, R, Erdmer, P, Thompson, R & Daughtry, K 2002, 'North American margin origin of Quesnel terrane strata in the southern Canadian Cordillera: Inferences from geochemical and Nd isotopic characteristics of Triassic metasedimentary rocks', *Geological Society of America Bulletin,* vol. 114, pp. 462-75.

van Aken, HM, Brodjonegoro, IS & Jaya, I 2009, 'The deep-water motion through the Lifamatola Passage and its contribution to the Indonesian throughflow', *Deep Sea Research Part I: Oceanographic Research Papers,* vol. 56, no. 8, pp. 1203-16. DOI:10.1016/j.dsr.2009.02.001

van der Werff, W 1995a, 'Cenozoic evolution of the Savu Basin, Indonesia: forearc basin response to arc-continent collision', *Marine and Petroleum Geology,* vol. 12, no. 3, pp. 247-62.

Van der Werff, W 1995b, 'Structure and morphotectonics of the accretionary prism along the Eastern Sunda-Western Banda Arc', *Journal of Southeast Asian Earth Sciences,* vol. 11, no. 4, pp. 309-22.

Van Dissen, R, Barrell, D, Litchfield, N, King, A, Quigley, MC, Villamor, P, Furlong, K, Mackenzie, H, Klahn, A, Begg, J, Townsend, D, Stahl, T, Noble, D, Duffy, B, Bilderback, E, Jongens, R, Cox, S, Langridge, R, Ries, W, Dhakal, R, Smith, A, Nicol, R, Pedley, K, Henham, H & Hunter, R 2011, 'Surface rupture displacement on the Greendale Fault during the Mw 7.1 Darfield (Canterbury) Earthquake, New Zealand, and its impact on man-made structures', *Ninth Pacific Conference on Earthquake Engineering, Building an Earthquake-Resilient Society, Paper 186, 8 p.*, New Zealand Society for Earthquake Engineering, Auckland, New Zealand.

Van Dissen, R, Litchfield, N, Quigley, MC, Villamor, P, Barrell, D, Furlong, K, Stahl, T, Duffy, B, Bilderback, E, Noble, D, Townsend, D, Begg, J, Jongens, R, Ries, W, Klahn, A, Mackenzie, H, Smith, A, Nicol, R, Cox, S, Pedley, K & Langridge, R 2010, 'Surface rupture displacement on

the Greendale Fault during the Mw 7.1 Darfield (Canterbury) earthquake, New Zealand', *GeoNZ 2010*, Auckland, New Zealand.

van Marle, LJ 1991, 'Late Cenozoic palaeobathymetry and geohistory analysis of Central West Timor, eastern Indonesia', *Marine and Petroleum Geology,* vol. 8, no. 1, pp. 22-34.

Van Rensbergen, P, Morley, CK, Ang, DW, Hoan, TQ & Lam, NT 1999, 'Structural evolution of shale diapirs from reactive rise to mud volcanism: 3D seismic data from the Baram delta, offshore Brunei Darussalam', *Journal of the Geological Society,* vol. 156, pp. 633-50.

van West, FP 1941, *Geological investigations in the Miomaffo region (Netherlands Timor)*, Noord-Hollandsche Uitg. Mij., Amsterdam,.

Vance, D, Scrivner, AE, Beney, P, Staubwasser, M, Henderson, GM & Slowey, NC 2004, 'The use of foraminifera as a record of the past neodymium isotope composition of seawater', *Paleoceanography,* vol. 19, no. 2, p. PA2009. DOI:10.1029/2003pa000957

Veevers, JJ 1971, 'Shallow stratigraphy and structure of the Australian continental margin beneath the Timor Sea', *Marine Geology,* vol. 11, no. 4, pp. 209-49.

Veevers, JJ, Falvey, DA & Robins, S 1978, 'Timor trough and australia: Facies show topographic wave migrated 80 km during the past 3 m.y', *Tectonophysics,* vol. 45, no. 2-3, pp. 217-27.

Vendeville, BC & Jackson, MPA 1992a, 'The fall of diapirs during thin-skinned extension', *Marine and Petroleum Geology,* vol. 9, no. 4, pp. 354-71. Retrieved 2 February 2012, from Scopus database.

Vendeville, BC & Jackson, MPA 1992b, 'The rise of diapirs during thin-skinned extension', *Marine and Petroleum Geology,* vol. 9, no. 4, pp. 331-54. DOI:10.1016/0264-8172(92)90047-i

Venkatesh, V & Malhotra, PD 1960, 'Chloritoid from Mosaboni, Bihar', *Records of the Geological Survey of India,* vol. 86, no. 3, pp. 545-50.

Villamor, P, Barrell, D, Litchfield, N, Van Dissen, R, Hornblow, S & Levick, S 2011, 'Greendale Fault investigation of surface rupture characteristics for fault avoidance zonation. ', *GNS Science Consultancy Report*, no. 2011-121, pp. 1-58.

Villamor, P, Litchfield, N, Barrell, D, Van Dissen, R, Hornblow, S, Quigley, MC, Levick, S, Ries, W, Duffy, B, Begg, J, Townsend, D, Stahl, T, Bilderback, E, Noble, D, Furlong, K & Grant, H 2012, 'Map of the 2010 Greendale Fault surface rupture, Canterbury, New Zealand: Application to land use planning ', *New Zealand Journal of Geology and Geophysics (Special issue: Canterbury, New Zealand, 2010-2011 earthquake sequence),* vol. 55, no. 3, pp. 223-330.

Vincent, C 2005, *Hydrogeology of the Upper Selwyn Catchment*, MSc (Engineering Geology) Thesis, University of Canterbury.

Vita-Finzi, C & Hidayat, S 1991, 'Holocene uplift in West Timor', *Journal of Southeast Asian Earth Sciences,* vol. 6, no. 3-4, pp. 387-93.

Voll, G 1976, 'Recrystallization of quartz, biotite and feldspars from Erstfeld to the Leventina Nappe, Swiss Alps, and its geological significance', *Schweiz. Mineral. Petrogr. Mitt.,* vol. 56, pp. 641-7.

Von Der Borch, CC 1979, 'Continent - Island arc collision in the Banda Arc', *Tectonophysics,* vol. 54, no. 3-4, pp. 169-93.

von der Heydt, AS & Dijkstra, HA 2011, 'The impact of ocean gateways on ENSO variability in the Miocene', vol. 355, pp. 305-18

Vranes, K, Gordon, AL & Ffield, A 2002, 'The heat transport of the Indonesian throughflow and implications for the Indian Ocean heat budget', *Deep-Sea Research Part II: Topical Studies in Oceanography,* vol. 49, no. 7-8, pp. 1391-410.

Vroon, PZ, Bergen, MJV, Klaver, GJ & White, WM 1995, 'Strontium, neodymium, and lead isotopic and trace-element signatures of the East Indonesian sediments: Provenance and implications for Banda Arc magma genesis ', *Geochimica et Cosmochimica Acta,* vol. 59, no. 12, pp. 2573-98.

Vroon, PZ, Van Bergen, MJ & Forde, EJ 1996, 'Pb and Nd isotope constraints on the provenance of tectonically dispersed continental fragments in east Indonesia', in R Hall & DJ Blundell (eds), *Tectonic evolution of Southeast Asia*, The Geological Society Special Publication No. 106, London.

Vroon, PZ, Van Bergen, MJ, White, WM & Varekamp, JC 1993, 'Sr-Nd-Pb isotope systematics of the Banda Arc, Indonesia: combined subduction and assimilation of continental material', *Journal of Geophysical research,* vol. 98, no. B12, pp. 22,349-22,66. Retrieved 3 October 2012, from Scopus database.

Wade, BS, Pearson, PN, Berggren, WA & Paelike, H 2011, 'Review and revision of Cenozoic tropical planktonic foraminiferal biostratigraphy and calibration to the geomagnetic polarity and astronomical time scale', *Earth Science Reviews,* vol. 104, pp. 111-42.

Walker, RG 1985, 'Mudstones and thin-bedded turbidites associated with the Upper Cretaceous Wheeler Gorge Conglomerates, California: a possible channel-levee complex', *Journal of Sedimentary Petrology,* vol. 5, pp. 279-90.

Walker, RT, Molor, E, Fox, M & Bayasgalan, A 2008, 'Active tectonics of an apparently aseismic region: Distributed active strike-slip faulting in the Hangay Mountains of central Mongolia', *Geophysical Journal International,* vol. 174, no. 3, pp. 1121-37. Retrieved 2 February 2013, from Scopus database.

Wandres, AM, Bradshaw, JD, Weaver, S, Maas, R, Ireland, T & Eby, N 2004, 'Provenance analysis using conglomerate clast lithologies: A case study from the Pahau terrane of New Zealand', *Sedimentary Geology,* vol. 167, no. 1-2, pp. 57-89. Retrieved 29 September 2012, from Scopus database.

Watkinson, IM, Hall, R & Ferdian, F 2011, 'Tectonic re-interpretation of the Banggai-Sula-Molucca Sea margin, Indonesia', in R Hall, MA Cottam & MEJ Wilson (eds), *The SE Asian Gateway: History and Tectonics of the Australia-Asia Collision*, Geological Society Special Publication 355, London, pp. 203-24.

Wdowinski, S & Zilberman, E 1997, 'Systematic analyses of the large-scale topography and structure across the Dead Sea Rift', *Tectonics,* vol. 16, no. 3, pp. 409-24. DOI:10.1029/97tc00814

Wensink, H 1994, 'Paleomagnetism of rocks from Sumba: tectonic implications since the late Cretaceous', *Journal of Southeast Asian Earth Sciences,* vol. 9, no. 1/2, pp. 51-65.

Wensink, H & van Bergen, MJ 1995, 'The tectonic emplacement of Sumba in the Sunda-Banda Arc: paleomagnetic and geochemical evidence from the early Miocene Jawila volcanics', *Tectonophysics,* vol. 250, no. 1-3, pp. 15-30. DOI:10.1016/0040-1951(95)00048-5

Wesnousky, SG 2006, 'Predicting the endpoints of earthquake ruptures', *Nature,* vol. 444, no. 7117, pp. 358-60.

Williams, PR, Pigram, CJ, Dow, DB & Amiruddin 1984, 'Melange production and the importance of shale diapirism in accretionary terrains', *Nature,* vol. 309, no. 5964, pp. 145-6. 10.1038/309145a0

Wilson, D 1989, 'Quaternary geology of northwestern Canterbury Plains. Miscellaneous series map 14'. New Zealand Geological Survey, Department of Scientific and Industrial Research

Winchester, JA & Floyd, PA 1977, 'Geochemical discrimination of different magma series and their differentiation products using immobile elements', *Chemical Geology,* vol. 20, no. C, pp. 325-43. Retrieved 29 September 2012, from Scopus database.

Wood, P, Robins, P & Hare, J 2010, 'Preliminary observations of the 2010 Darfield (Canterbury) Earthquakes: an introduction', *Bulletin of the New Zealand Society for Earthquake Engineering,* vol. 43, no. 4, p. i.

Wronkiewicz, DJ & Condie, KC 1987, 'Geochemistry of Archean shales from the Witwatersrand Supergroup, South Africa: Source-area weathering and provenance', *Geochimica et Cosmochimica Acta,* vol. 51, no. 9, pp. 2401-16. Retrieved 27 September 2012, from Scopus database.

Wyrtki, K 1989, 'Some thoughts about the West Pacific warm pool', *Proc. of Western Pacific International Meeting and Workshop on TOGA COARE*, pp. 99-109.

Yin, A & Kelty, TK 1991, 'Development of normal faults during emplacement of a thrust sheet: an example from the Lewis allochthon, Glacier National Park, Montana (U.S.A.)', *Journal of Structural Geology,* vol. 13, no. 1, pp. 37-47. DOI:http://dx.doi.org/10.1016/0191-8141(91)90099-5

Yin, A & Taylor, MH 2008, 'Non-Andersonian conjugate strike-slip faults: Observations, theory, and tectonic implications', in *Donald D Harrington Symposium on the Geology of the Aegean*, vol. 2. IOP Conf. Series: Earth and Environmental Science. DOI:10.1088/1755-1307/2/1/012026

Yin, A & Taylor, MH 2011, 'Mechanics of V-shaped conjugate strike-slip faults and the corresponding continuum mode of continental deformation', *Geological Society of America Bulletin,* vol. 123, no. 9-10, pp. 1798-821. DOI:10.1130/b30159.1

Yu, H-S & Jiunn Chenn, L 1995, 'Development of the shale diapir-controlled Fangliao Canyon on the continental slope off southwestern Taiwan', *Journal of Southeast Asian Earth Sciences,* vol. 11, no. 4, pp. 265-76. DOI:10.1016/0743-9547(95)00004-c

Zhang, JY, Yin, A, Liu, WC, Wu, FY, Lin, D & Grove, M 2012, 'Coupled U-Pb dating and Hf isotopic analysis of detrital zircon of modern river sand from the Yalu River (Yarlung Tsangpo) drainage system in southern Tibet: Constraints on the transport processes and evolution of Himalayan rivers', *Geological Society of America Bulletin,* vol. 124, no. 9-10, pp. 1449-73. DOI:10.1130/b30592.1

Glossary

broken formation: disrupted pods or lenticular beds, commonly sandstone,. 'floating' in and supported by a shale matrix 25

delamination: The splitting or separating of the upper crust from the lower crust 12

DEM: Digital elevation model 3

extrusion: orogen parallel lengthening, accommodated by pure-shear strike slip faulting, which occurs in response to shortening. 4

Indonesian Throughflow: an ocean current that transports water between the Pacific Ocean and the Indian Ocean through the Indonesian Seaway 1

mantle tomography: A technique for displaying a representation of a cross section through the mantle and crust using earthquake waves 12

massifs: blocks of the earth's crust bounded by faults or flexures and displaced without internal change. 10

mélange: a mappable body of rock characterized by a lack of continuous bedding and the inclusion of fragments of exotic rocks of all sizes, all contained in a fine-grained deformed matrix. 4

slab rupture: the breaking off of oceanic crust from the adjoining passive margin. 12

slip-off terrace: a terrace abandoned during uni-lateral down-slope migration of a river. 5

APPENDIX 1 – STRATIGRAPHIC COLUMNS

Full size stratigraphic columns are provided in the back pocket of this thesis.

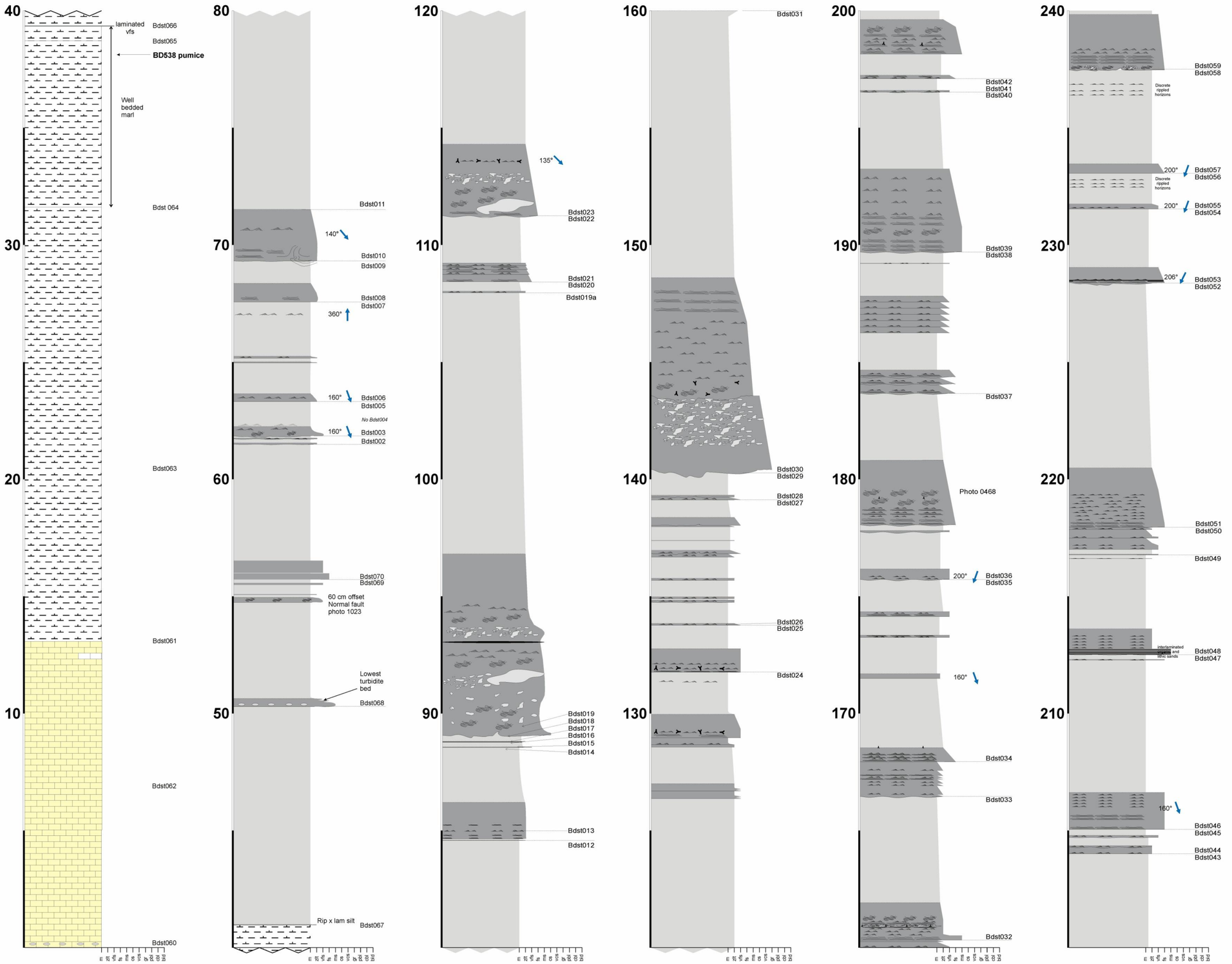

Detailed Stratigraphy and sedimentology of the Viqueque Megasequence.

Column A: Type Section located in the Cuha River southeast from S8° 51.900' E126° 21.844'

Legend

Sedimentary structures

- Ripple cross lamination
- Planar lamination
- Convolute bedding
- Rip up horizon
- Intermlaminated organics
- Large organic 'clasts'

Annotations

- Bdst059 / Bdst058 — Sample locations relative to bedding plane
- 200° — Paleoflow - azimuth and graphic

Contacts

- Gradational
- Sharp planar
- Sharp wavy
- Load casted
- Flame structured

Lithologies

- Foraminiferal chalk
- Marl
- Mudstone
- Turbidite sandstone

Note: Scale varies between columns

Scale 1:50

Detailed Stratigraphy and sedimentology of the Viqueque Megasequence.

Column B: Northern Cuha River section logged southeast from S8° 49.703' E126° 22.456'

Legend

Sedimentary structures

- Ripple cross lamination
- Planar lamination
- Convolute bedding
- Rip up horizon
- Intermlaminated organics
- laminated silt lens
- Large organic 'clasts'

Annotations

- Bdst059 / Bdst058 — Sample locations relative to bedding plane
- 200° — Paleoflow - azimuth and graphic

Contacts

- Gradational
- Sharp planar
- Sharp wavy
- Load casted
- Flame structured

Lithologies

- Foraminiferal chalk
- Marl
- Mudstone
- Turbidite sandstone
- Obscured

Note: Scale varies between columns

Scale 1:100

Detailed Stratigraphy and sedimentology of the Viqueque Megasequence.

Column C: Caiaco River section

logged south from 8°57'18.31"S, 125°19'36.09"E

Legend

Sedimentary structures

- Ripple cross lamination
- Planar lamination
- Convolute bedding
- Rip up horizon
- Cross bedded
- Hummocky cross stratified
- Intermlaminated organics (black) or silt (grey)
- Lens - laminated silt (left) or sand (right)
- Large wood fragments
- Slump

Annotations

- CR58.1-2 / CR58A / CR58 — Sample locations; Paleomag sample; Coarse grained sample; Fine grained sample (palynology/biostratigraphy)
- Photo number and description
- 200° — Paleoflow - azimuth and graphic

Contacts

- Gradational
- Sharp planar
- Sharp wavy
- Load casted
- Flame structured
- Channel

Lithologies

- Foraminiferal chalk
- Marl
- Mudstone
- Turbidite sandstone
- Conglomerate (left) and imbricated conglomerate (right)
- Obscured

Note: Scale varies between columns

Scale 1:125

when printed on a 42" roll